Light-responsive delivery and photothermal enhancement of antimicrobial peptides to combat bacterial wound infections
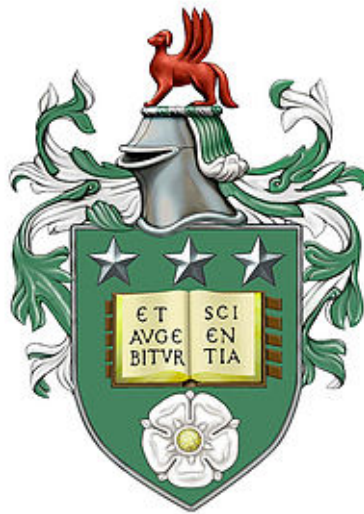
Samuel Charles Tensin Moorcroft

School of Physics & Astronomy

University of Leeds

A thesis for the degree of

Doctor of philosophy

September 17, 2020

The candidate confirms that the work submitted is his own, except where work which has formed part of jointly authored publications has been included. The contribution of the candidate and the other authors to this work has been explicitly indicated below. The candidate confirms that appropriate credit has been given within the thesis where reference has been made to the work of others.

In chapter 4 of this thesis some of the work discussed has appeared in publication as follows:

L. Roach *et al.* Morphological control of the seedless synthesis of gold nanorods using binary surfactants. *Nanotechnology* 2018, 29, 359501

In this publication SM was responsible for particle synthesis and TEM micrograph acquisition.

The work discussed in chapters 5 and 6 of this thesis has appeared in publication as follows:

S. C. T. Moorcroft *et al.* Nanoparticle-Loaded Hydrogel for the Light-Activated Release and Photothermal Enhancement of Antimicrobial Peptides. *ACS Appl. Mater. Interfaces* 2020, 12(22), 24544–24554.

Other publications co-authored during the course of this studentship include:

S. C. T. Moorcroft *et al.* Stimuli-Responsive Release of Antimicrobials Using Hybrid Inorganic Nanoparticle-Associated Drug-Delivery Systems. *Macromol. bioscience* 2018, 18(12), 1800207.

K. Ricketts *et al.* Recommendations for clinical translation of nanoparticle-enhanced radiotherapy. *The British journal of radiology.* 2018, 91(1092), 20180325.

S. Ye *et al.* Exploring high aspect ratio gold nanotubes as cytosolic agents: structural engineering and uptake into mesothelioma cells. Submitted to Small.

This copy has been supplied on the understanding that it is copyright material and that no quotation from the thesis may be published without proper acknowledgement. The right of Andrew James Harvie to be identified as Author of this work has been asserted by him in accordance with the Copyright, Designs and Patents Act 1988.

I

For Mother Dear, Big Poppa and lil Pukey Lukey

Acknowledgements

Abstract

Antibiotic overuse has driven the development of antimicrobial resistance (AMR), whilst a dwindling antibiotic development pipeline has led to the emergence of resistance to "last resort" antibiotics, such as carbapenem. Antimicrobial peptides (AMPs) are emerging as a promising means of treating multidrug resistant bacterial infections, with reduced risk of AMR development due to the AMP efficacy and rapid bactericidal effects. Clinical translation of AMPs is hindered by peptide susceptibility to proteolytic degradation, low biostability and unknown potential for systemic toxicity. Stimuli-responsive AMP delivery systems offer a promising means of circumventing these shortcomings with spatial and temporal control over drug delivery increasing drug pharmacodynamics, thus permitting the use of lower drug doses. Furthermore, the encapsulation of an AMPs inside a delivery vehicle can improve biostability and protect the cargo from proteolytic degradation.

This thesis discusses the development of a prototype poly(ethylene glycol) (PEG) hydrogel wound dressing that contains phospholipid coated gold nanorods (AuNRs) and liposomes loaded with the AMP IRIKIRIK-CONH$_2$ (IK8). Using facile lipid film hydration techniques, liposomes were fabricated to encapsulate lethal doses of IK8 and protect the internalised peptides from protease degradation. The liposomes exhibit negligible leakage until heated to the gel-fluid phase transition temperature in the presence of bacteria. The bulk temperature of the gel can be controlled by varying the intensity of applied continuous wave irradiation that mediates the AuNR photothermal heating profile. Irradiation at 2.1 W cm^{-2} for 10 mins (heating the sample to 55°C) demonstrated triggered delivery of IK8, eliciting bactericidal activity against *Staphylococcus aureus* and *Pseudonomas aeruginosa*. Irradiation at 2.4 W cm^{-2} (heating the sample to 60°C for 10 mins) demonstrated thermal bacteria killing alone, and an additive antibacterial effect in conjunction with the AMP. Through controlling the concentration of IK8-liposomes and the laser irradiation time a single gel can provide bactericidal activity against multiple batches of bacteria.

Additionally, by mixing maleimide-functionalised phospholipid stabilised AuNRs with IK8-loaded liposomes containing the thiolated lipid DPPE-Ptd, AuNR conjugated IK8-liposome (ANCIL) complexes were fabricated that enabled the triggered release of AMPs under pulsed laser irradiation (450 μJ cm^{-2} for 10 mins) without bulk heating. The ANCIL complexes demonstrate a >3-log reduction in viable *S. aureus* compared to non-irradiated equivalents.

Abbreviations

4APM: 4-arm poly(ethylene)glycol-maleimide

AA: Ascorbic acid

AAS: Atomic absorbance spectroscopy

ANCIL: Gold nanorod conjugated IK8-loaded liposome

AMP: Antimicrobial peptide

AuNR: Gold nanorod

AuNP: Gold nanoparticle

BCA: Bicinchoninic acid

CTAB: Cetyl Trimethyl Ammonium Bromide

DLS: Dynamic light scattering

DLPC: 1,2-dilauroyl-sn-glycero-3-phosphocholine

DMET: 2-dimethylaminoethanthiol

DMPE-RhB: 1,2-dimyristoyl-sn-glycero-3 phosphoethanolamine-N-lissamine rhodamine B sulfonyl

DMPG: 1,2-dimyristoyl-sn-glycero-3-phosphoglycerol

DMSO: Dimethyl sulfoxide

DOPC: 1,2-dioleoyl-sn-glycero-3-phosphocholine

DPPC: 1,2-dipalmitoyl-sn-glycero-3-phosphocholine

DPPE-Ptd: 1,2-Dipalmitoyl-sn-Glycero-3-Phosphothioethanol

DPTAP: 1,2-dipalmitoyl-3-trimethylammonium-propane

DSPC: 1,2-distearoyl-sn-glycero-3-phosphocholine

DSPE-mPEG2k: 1,2-distearoyl-sn-glycero-3-phosphoethanolamine-N-[methoxy(polyethylene glycol)-2000]

DSPE-mPEG2k-maleimide: 1,2-distearoyl-sn-glycero-3-phosphoethanolamine-N-[methoxy (polyethylene glycol)-2000]

HAuCl$_4$: Gold chloride

HDF: Human dermal fibroblast

HGN: Hollow gold nanoshell

HPLC: High performance liquid chromatography

IK8: IRIKIRIK-CONH$_2$

LSPR: Longitudinal surface plasmon resonance

LysoPC: 1-stearoyl-2-hydroxy-*sn*-glycero-3-phosphocholine

MBC: Minimal bactericidal concentration

MES: 2-mercaptoethanesulfonate

MHB II: Mueller-Hinton broth II

MIC: Minimum inhibitory concentration

MPPC: 1-palmitoyl-2-hydroxy-*sn*-glycero-3 phosphocholine

NaOL: Sodium oleate

ND: Natural density

PBS: Phosphate buffered saline

PEG: Poly(ethylene) glycol

PEGSH: Poly(ethylene)glycol dithiol

RPE: Reverse Phase evaporation

T_m: Phase transition temperature

TEM: Transmission electron microscopy

WST-1: Water soluble tetrazolium salt-1

Contents

List of Figures

Chapter 1

Introduction

1.1 Overview and thesis outline

Antibiotic remedies have been used for millennia to treat bacterial infections, however chemical treatments, or chemotherapeutics, were not discovered until physician Paul Ehrlich isolated arsphenamine as a treatment for syphilis in the late 19th century.[1] Chemotherapeutic antibiotics have since revolutionised medicine, with their high treatment efficiency and ease of manufacture leading to wide spread usage. However, overuse has driven the development of antimicrobial resistance (AMR) in bacteria, dramatically decreasing antibiotic efficacy and in turn increased the risks of infection related mortalities.[2] Furthermore, a dwindling development pipeline of novel antibiotics has led to bacteria evolving resistance to "last resort" antibiotics such as carbapenem, leaving critically few options for treatment.[3–5] As such, antibiotic alternatives are viewed as a promising means of overcoming resistance. Antimicrobial peptides (AMPs) in particular exhibit potential as antibacterial chemotherapeutics, displaying rapid and high antibacterial efficacy that decreases the likelihood of bacteria acquiring resistance. The path to the clinical translation of AMPs is blocked by their susceptibility to proteolytic degradation, low biostability, and potential to induce systemic toxicity. This thesis discusses the loading of AMPs into stimuli-responsive delivery systems that will protect the encapsulated cargo from protease degradation and ensure peptide stability until the drug is released in response to an exogenous stimulus. Spatial and temporal control allows direct delivery at the infection site increasing the drug pharmacodynamic profile, meaning lower concentrations are required for treatment which in turn decreases the risk of toxicity. Payload release can be triggered upon exposure

to chemical (e.g. changes in pH and ionic strength), physical (e.g. thermal or magnetic) or biological (e.g. proteolytic enzyme) stress. Recent studies on murine models have shown that increasing the localised temperature of an infected wound to 50-60°C effectively kills pathogenic bacteria without detriment to the reepithelialisation process.[6–10] As such, this thesis will employ a thermal release mechanism that will investigate not only AMP efficacy upon delivery to planktonic bacteria but whether thermal bacteria killing can be utilised in conjunction with AMPs. The prevailing mechanisms of drug delivery vehicle heating from external stimuli convert light irradiation or electromagnetic fields into thermal energy through photothermal and magnetothermal mechanisms, respectively. Metallic nanoparticles (e.g. gold, silver, copper) are commonly used as photothermal agents due to the presence of delocalised electrons that can be driven into coherent oscillation by incident radiation, creating a localised surface plasmon resonance (LSPR) condition at specific frequencies of light. Using anisotropic particles, such as gold nanorods (AuNRs), a longitudinal plasmon with a tunable absorbance peak is created, providing enhanced absorbance efficiency compared to the transverse plasmon peak of isotropic particles. The energy absorbed is then dissipated as heat through electron-phonon collisions with the particle lattice. Nanoparticles are also prevalent in magnetothermal heating, requiring superparamagnetic iron oxide nanoparticles (SPIONs). The application of an alternating magnetic field produces a phase lag between the applied field and the SPION magnetization creating a hysteresis loop. The excess energy of the hysteresis is thermally emitted through changes in spin state and through the induced rotation causing friction between the particle and the surrounding fluid, mechanisms known as Néel and Brownian relaxations, respectively. Photothermal heating is significantly more efficient than magnetothermal heating[11,12], as such this thesis will utilise light-responsive triggering mechanisms to enable AMP release. The main limitation of photothermal heating is the low tissue penetration of light irradiation, however this is less of an issue with regard to the treatment of bacterial infections, as lesions in the skin are the most frequent locations of such infections. This means that incident radiation does not have to penetrate through much, if any, tissue to reach the treatment site.

Phospholipids are amphiphilic molecules containing a hydrophilic head group and hydrophobic hydrocarbon tails that enable self assembly into micelle or vesicles formed of a lipid bilayer, otherwise known as liposomes, in aqueous environments. Drug molecules can be loaded into phospholipid structures by simply including the therapeutic in the solution during liposome/micelle fabrication. Phospholipids possess a fundamental gel-fluid phase transition temperature

(T_m), above which the lipid molecules are highly mobile within a bilayer creating a flexible structure, whereas below the T_m the alkyl chains are rigid, reducing lipid mobility creating a thicker and more brittle bilayer. The conformational changes in a liposome enable release of small molecule payloads encapsulated within the lumen. The thermo-responsive nature, as well as the biocompatibility of many phospholipids, mean that liposomes are ideal drug delivery vehicles that release their cargoes only when the T_m is reached. Furthermore, by restricting protease access to encapsulated AMPs, phospholipid structures demonstrate a protective effect against proteolytic degradation.[13,14] Liposomes will therefore be adopted as the AMP encapsulating vehicle that will be used in conjunction with photothermal agents that will enable the localised heating to initiate AMP delivery.

In summary, this thesis discusses the synthesis of AuNR mediated light-responsive delivery systems to provide triggered release from AMP-loaded liposomes, and the potential for combination AMP-photothermal bacteria treatment. IRIKIRIK-CONH$_2$ (IK8) will be used throughout this thesis as the model AMP. IK8 is a broad-spectrum short AMP that forms a β-sheet secondary structure upon interaction with a bacteria membrane to elicit both antimicrobial and antibiofilm properties,[15,16] and is an ideal model drug to demonstrate triggered delivery; it displays high antimicrobial efficacy, its small size should ensure ease of encapsulation, enables demonstration of the protective properties of soft matter delivery systems. This thesis will also explore the incorporation of such systems into a prototype hydrogel wound dressing to aid topical bacterial infection management.

1.2 Aims and objectives

The primary aim of this thesis is to develop light-responsive systems that provide the triggered delivery of AMPs, overcoming the shortcomings hindering AMP clinical translation. The main issues surrounding AMPs are its susceptibility to proteolytic degradation, instability *in vivo* leading to poor biodistribution, and systemic toxicity. Spatial and temporal control over drug delivery delivery increases the pharmacodynamic profile of a drug, meaning lower concentrations are required for treatment, reducing the risk of systemic toxicity. Loading the AMP into a delivery vehicle should also protect the drug until it is released, providing increased stability and restricting protease access. As such, the AMP delivery systems desribed in this thesis must fit the following criteria:

- Exhibit the encapsulation of lethal doses of AMPs and restrict premature leakage that could both reduce treatment efficacy and increase the likelihood of bacterial resistance.

- Protect internalised cargo from protease degradation.

- Provide controllable photothermal heating profiles.

- Demonstrate an adequate release profile in response to light irradiation, delivering lethal AMP doses.

- Ensure encapsulated AMP stability in biologically relevant media (i.e. broth or cell media) to maintain its antimicrobial efficacy.

- Guarantee no toxicity to host cells.

- Maintain colloidal stability both in suspension and in a hydrogel network, over a prolonged period of time.

Thermal treatments of infected wounds on murine models have previously been shown to effectively reduce bacteria concentrations whilst not being of detriment to the wound healing process.[6–10] As such, this thesis aims to investigate the potential of combined photothermal and AMP treatments.

1.3   Overview of results chapters

This thesis contains four distinct results chapters. The first results chapter (**Chapter 4**) discusses the synthesis of AuNRs, investigating how the ratio of the surfactants cetrimonnium bromide (CTAB) and sodium oleate (NaOL) affected the morphology and optical properties of the resultant rod shaped gold crystals. CTAB exhibits an innate toxicity against both mammalian and bacterial cell types, affecting the respiratory pathways and membrane protein functionalities. As such, the surface replacement of this co-surfactant bilayer with phospholipids was also investigated to improve stability, biocompatibility, and reduced cytotoxicity before determining the photothermal properties of these particles under continuous wave laser irradiation.

The second results chapter (**Chapter 5**) is focused on development of IK8-loaded liposomes that triggered cargo release upon light mediated photothermal heating. Initially, the liposome fabrication process was investigated to create homogeneous vesicles that can encapsulate IK8 at several times the minimum inhibitory concentration (MIC) against *Staphylococcus aureus* and *Pseudonomas aeruginosa*. The effects of the liposome composition were then explored to obtain

vesicles that did not exhibit passive leakage but demonstrate an adequate release profile upon heating to the vesicle's gel-fluid phase transition temperature. Finally, the efficacy of the AMP-liposomes to treat planktonic *S. aureus* was assessed when used in combination with AuNRs under laser irradiation. Furthermore, the bacteria killing effects of photothermal heating were evaluated to determine whether it can enhance the antimicrobial properties of the IK8.

The third results chapter (**Chapter 6**) discusses the development of a poly(ethylene glycol) (PEG) hydrogel that incorporated both AMP-loaded liposomes and AuNRs to form the basis of a prototype wound dressing. Hydrogels are widely used as dressings due to their oxygen permeability[17] and high water content (generally >90%) that accelerates the angiogenesis process,[18] prevents cell dehydration[19] and provides a soothing texture that increases patient compliance with the treatment.[20] The first stage of testing was the optimisation of the gelation process through controlling the weight percentage of gel within the network and buffering conditions to control the rate of reaction, before loading the construct with AuNRs and liposomes. The mechanical properties, swelling ratios and retention rates of the particle loaded gels was then characterised. The antimicrobial efficacy of the system was assessed against both Gram-positive and Gram-negative bacteria, before fine tuning the system to determine whether it was possible for a single gel complex to provide treatment against multiple batches of fresh bacteria.

The final results chapter (**Chapter 7**) provides proof of concept for the liposomal delivery of AMPs using a pulsed laser system, to trigger release without generating any bulk heating. Initial developments entailed attempts to synthesise a gold coating on the liposomes before demonstrating the potential for binding phospholipid coated AuNRs onto the liposome surface. The release efficacy of the liposome-AuNR complexes was evaluated by varying the pulse fluence and irradiation time. This ascertained whether the system could provide AMP triggered release to incite bactericidal activity without requiring significant temperature increases.

Chapter 2

Background and Theory

Some of the content within this chapter can be found within the following the following publications: S. C. T. Moorcroft *et al.* 2018. 'Stimuli-Responsive Release of Antimicrobials Using Hybrid Inorganic Nanoparticle-Associated Drug-Delivery Systems' in *Macromolecular Bioscience* **18.12**:1800207

2.1   Pathogenic bacteria and antibiotic resistance

Bacteria are single cellular microorganisms have have adapted and evolved over hundreds of millions of years to thrive in almost every environment on Earth. Classed as prokaryotes, bacterial cells do not have a nucleus but have deoxyribonucleic acid (DNA, molecules that govern cell growth, function, and reproduction) free floating in the cytoplasm in a tangled nucleoid or forming a plasmid ring structure. Alongside the DNA, ribosomes synthesise functional proteins through the assembly of amino acids. The cytoplasm is encapsulated within a cell membrane, of which there are two distinct variations that are categorised using the crystal violet Gram stain. Gram-positive bacteria have a plasma membrane with a thick peptidoglycan pericellular layer, see Figure 2.1, onto which the Gram stain will bind causing a pink/violet colouration under a microscope. Gram-negative bacteria have a thinner peptidoglycan layer and an additional membrane on the outside of the peptidoglycan, however the overall structure is thinner than that of the Gram-positive bacteria. The peptidoglycan layer in the cell wall has a mesh-like structure, allowing molecules smaller than 50 kDa to freely diffuse through the cell wall directly to the plasma membrane. Bacteria cell membranes primarily consist of phosphatidylglycerol

(PG), phosphatidylethanolamine (PE) and cardiolipin complemented with small amounts of phosphatidylcholine (PC), and phosphatidylinositol (PI).[21] PG, cardiolipin and PI all exhibit a negative charge at physiological pH, in addition to this Gram-positive and Gram-negative membranes have negative Lipoteichoic acids and lipopolysaccharides respectively, providing the bacterial membrane with a strong anionic charge. Bacteria cells may also have external structures such as flagella which enable directional motion or pili that anchor the bacterium to surfaces and transfer DNA.
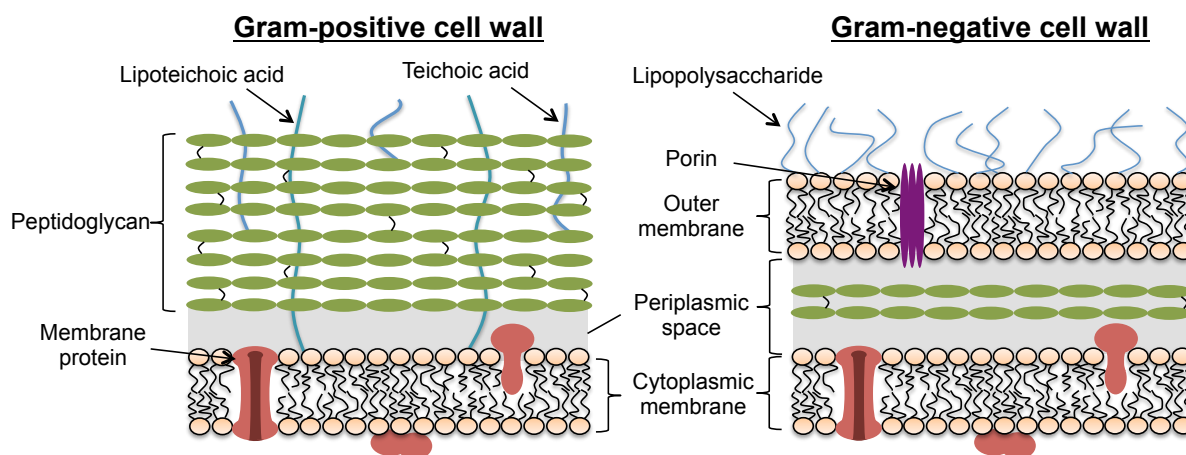
Figure 2.1: The cell walls of Gram-positive and -negative bacteria.

Bacteria are an integral part of the human microbiome providing a vast array of functionalities from aiding digestion to the production of vitamins.[22] These commensal bacteria only cause harm when the host becomes immunocompromised or there is an abnormality in the bacteria's environment, whereas pathogenic bacteria utilise the host's resources, circumventing the immune system and potentially causing trauma. Pathogenic bacteria such as *Staphyloccoci* and *Streptococci* are present in our every day lives without causing any issues, it is only when the immune system is weakened (e.g. through a lesion in the skin) that the opportunistic bacteria pose a threat. In order to effectively survive within a host the bacteria must: 1) make the initial colonisation in the correct *in vivo* environment that provides adequate nutrients, 2) be able to circumvent the immune system, 3) be able to reproduce, 4) be able to relocate to a new host. This induces a high selective pressure on the bacteria meaning only the most resilient species may survive.

Many of the symptoms associated with bacterial infections are in fact physiological responses of the immune system in order to fight of the invading pathogen. Prime examples of this are

the inflammation of an infected wound, due to immune cells attacking the pathogenic bacteria, and fevers that increase the host temperature above the optimal reproductive temperature of the pathogen, stunting the progression of the infection. To elicit immunogenic responses the bacteria have to impair some functionality or harm host cells. This can simply occur through the presence of bacteria, an imbalance between host and bacteria cells in an open lesion can be detrimental to the reepithelialisation process regardless of the contaminant activity, leading to inflammation and slower healing.[23] The physiological response can also be so intense that it is itself toxic. The response to bacteria such as *Mycobacterium tuberculosis* and *Mycobacterium leprae* (bacteria commonly associated with tuberculosis and leprosy) can induce the production of toxic biomolecules by lymphocytes, macrophages, and polymorphonuclear neutrophils host defense cells that can destroy tissues, providing an ideal proliferation environment for resistant bacteria.[24] The harmful activity of many pathogens can substantially exacerbate these issues. Certain bacteria invade host cells, providing a nutrient-rich environment in order to grow and reproduce whilst offering protection against extracellular immune responses. *Rickettsia* for example, are only able to reproduce within the cytosol of eukaryotes, killing the cell in the process.[25] Pathogenic bacteria also produce an array of virulence factors to support their proliferation. These molecules perform a variety of functions; 1) adhesion and colonisation factors initiate the formation of a colony within a host, 2) invasion factors that facilitate the internalisation of the pathogen inside host eukaryotes, 3) capsules and surface components to protect the bacteria from phagocytosis, 4) endotoxins are released upon bacterial lysis inducing toxicity and a large amount of physiological responses.[26]

2.1.1 Biofilms

In nature infectious bacteria rarely survive for long periods of time in isolation, as such many bacteria will form colonies and biofilms that will increase their chances of survival. Biofilms are a collective community of microorganisms enclosed within a matrix of extracellular polymeric substances (EPS), formed by the excretion of a polymeric conglomeration of polysaccharides, lipids, DNA and protein producing a slime containing a high density of cells. The formation of a biofilm creates nutrient and oxygen gradients within the EPS matrix causing cells to switch from a planktonic to biofilm mode of growth. In this state bacteria exhibit decreased metabolic activity and higher doubling rates that can result in a series of phenotypic, metabolic and physiological changes.[27–29] This switch can actuate mechanisms that result in antimicrobial

resistance (AMR), increased virulence and persistence.[30] In combination with EPS restricting of antibiotic availability to sub-lethal doses, these effects can result in significant increases in AMR, potentially increasing the dosage required for treatment by several orders of magnitude.[30] Furthermore, the concentration of persister cells in a biofilm is greatly increased compared to planktonic bacteria, up to 1% in biofilms and approximately 1 in 10^6 in bacterial suspensions.[31] Persister cells are metabolically inactive, spore-like cells that are potentially the main reason for AMR in certain biofilms such as *P. aeruginosa*.[32]

Bacterial biofilms pose the largest burden to infection treatment with 65%[33] to 80%[34] of all microbial and chronic infections attributed to bacterial biofilms. Biofilm formation within an open wound can cause prolonged inflammation that produces excess levels of metalloproteases that degrade the extracellular matrix, a vital component in tissue regeneration. Ultimately this can lead to the development of chronic wounds, particularly in immunocompromised individuals, a common example being diabetic foot ulcers.[35,36] Biofilms also occur within the digestive and respiratory systems, due to the presence of bacteria in food and air respectively, and can produce long lasting diseases such pneumonia in cystic fibrosis suffers, causing a substantial decrease in a patient's quality of life.[37] In addition, biofilm formation on medical implants and catheters is the main cause of nosocomial infection.[38]
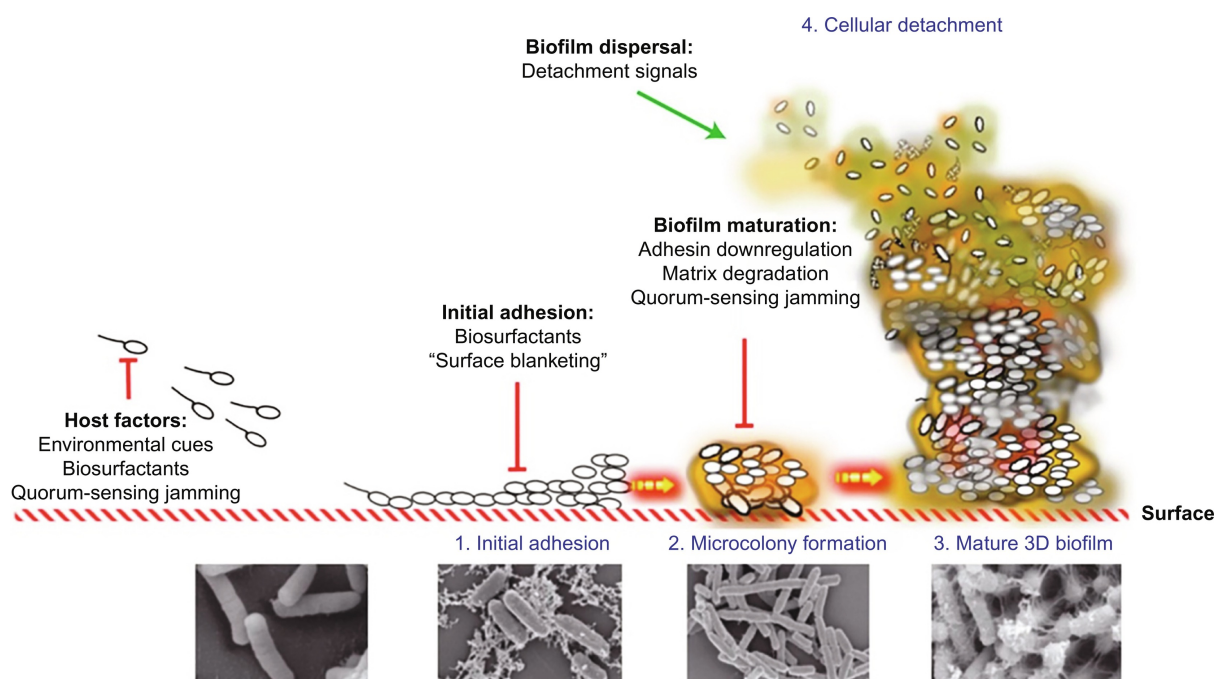
Figure 2.2: Schematic representation of the formation of a biofilm, from the initial adhesion of planktonic bacteria through biofilm maturation to dispersion to form new colonies. Accompanying scanning electron micrographs of the different stages of growth of a *P. aeruginosa* biofilm. Reproduced with permission.[39] Copyright 2018, Elsevier.

Prior to biofilm formation, bacteria will be in a planktonic state, free in a liquid suspension. When under flow a bacterium will approach a surface at which point it can become constrained by both hydrodynamic and physiochemical (electrostatic, Van der Waals and hydrophobic forces) effects.[40] These effects are weak and short lasting (i.e. demonstrate adhesion timescales of minutes), as such the bacterium will then irreversibly bind itself to a surface by enhancing the Van der Waals forces between the surface and the hydrophobic regions of the cell membrane whilst augmenting the binding strength with cell adhesion structures such as pili and lipopolysaccharides.[41] As depicted in Figure 2.2, bacteria will only bind to a surface provided the environment is optimal for its survival (i.e. a rich source of nutrients, moist, the correct temperature and adequate oxygen levels if the bacteria is aerobic), leading to higher cell densities in specific regions. At this point the bacteria will start to excrete a mixture of DNA and lipids to form the basis of the EPS, and initiating microcolonisation. The bacterial cells begin to communicate through the production and detection of extracellular signalling molecules, known as quorum sensing. Quorum sensing allows synchronisation between cells to regulate phenotype expressions to govern the behaviour of the colony as a whole.[42,43] At this point the bacteria in the colony will begin to produce polysaccharides that form the bulk of the EPS.[44] As the bacteria switch to their biofilm mode of growth the cell doubling rate increases causing rapid biofilm growth, until a mature 3D biofilm is formed. The mature biofilm will then start to disperse, releasing cells into the surrounding medium such that they initiate the biofilm formation elsewhere.

2.1.2   Mechanisms of action of antibiotics

Antibiotics primarily target the synthesis pathways of the cell wall, nucleic acids, and proteins, Figure 2.3, to kill the bacteria directly (bactericidal) or inhibit proliferation (bacteriostatic).[45] Many antibiotics have concentration dependent antibacterial action, providing bacteriostatic activity at low concentrations and bactericidal effects at high concentrations.

Cell wall targeting antibiotics primarily disrupt peptidoglycan synthesis, leading to bacteria lysis. The peptidoglycan layer is formed of glycan saccharides cross-linked via glycine residues of the D-alanyl D-alanine portion of side chain peptides, that is facilitated by penicillin binding proteins (PBPs).[46] β-lactam antibiotics (penicillins, cephalosporins, monobactams, carbapenems and carbacephems)[47] mimic D-alanyl D-alanine causing the PBP to bind to the antibiotics, inhibiting cell wall synthesis.[45] Conversely, glycopeptides (e.g. vancomycin and teicoplanin)

bind to the D-alanyl D-alanine portion of the saccharide bridging peptides, impeding PBPs and hindering cell wall synthesis.[48]

Quinolone antibiotics prevent bacterial DNA replication that leads to both bacteriostatic and bactericidal effects. Fluoroquinolones (e.g. ciprofloxacin, delafloxacin, gemifloxacin, levofloxacin, moxifloxacin, norfloxacin, and ofloxacin) are the most commonly prescribed quinolone, that provide broad-spectrum antimicrobial activity through the inhibition of bacteria DNA gyrase.[49] Gyrase enzymes catalyse the ATP-dependent negative super-coiling that terminates the DNA double coil.[50] Fluoroquinolones bind to the gyrase sub unit relating to the nicking of the DNA, interfering with the DNA cutting and sealing.

Antibiotics that inhibit protein biosynthesis by targeting the 30S and 50S ribonucleoprotein subunits of the bacterial 70S ribosome. Simply put, protein synthesis occurs through the binding of messenger RNA (mRNA) to the 30S ribosome subunit, the 50S subunit then promotes the addition of amino acids to form a protein chain before release factors activate the peptidyltransferase function of the ribosome, releasing the complete protein.[51] Aminoglycosides (e.g. streptomycin, kanamycin, and gentamicin) and tetracyclines (e.g. chlortetracycline, doxycycline, and minocycline) both target the 16S subunit of the 30S ribosome RNA (r-RNA) that binds to the Shine-Dalgarno sequence of the mRNA initiating the protein synthesis.[52,53] Aminoglycoside binding to the 16S subunit causes the misreading and premature termination of translation of mRNA, whereas tetracyclines inhibit binding of transfer RNA to the ribosome stopping the initiation of protein synthesis. Macrolides (e.g. erythromycin, azithromycin, and clarithromycin) and oxazolidinones (e.g. Linezolid, and tedizolid) target the 23S r-RNA of the 50S ribosome subunit, that is associated with the peptidyl transferase which form the amine bonds between the amino acids.[54–56] The antibiotic molecules binding to the 23S r-RNA results in prematurely releasing incomplete peptide chains from the ribosome.
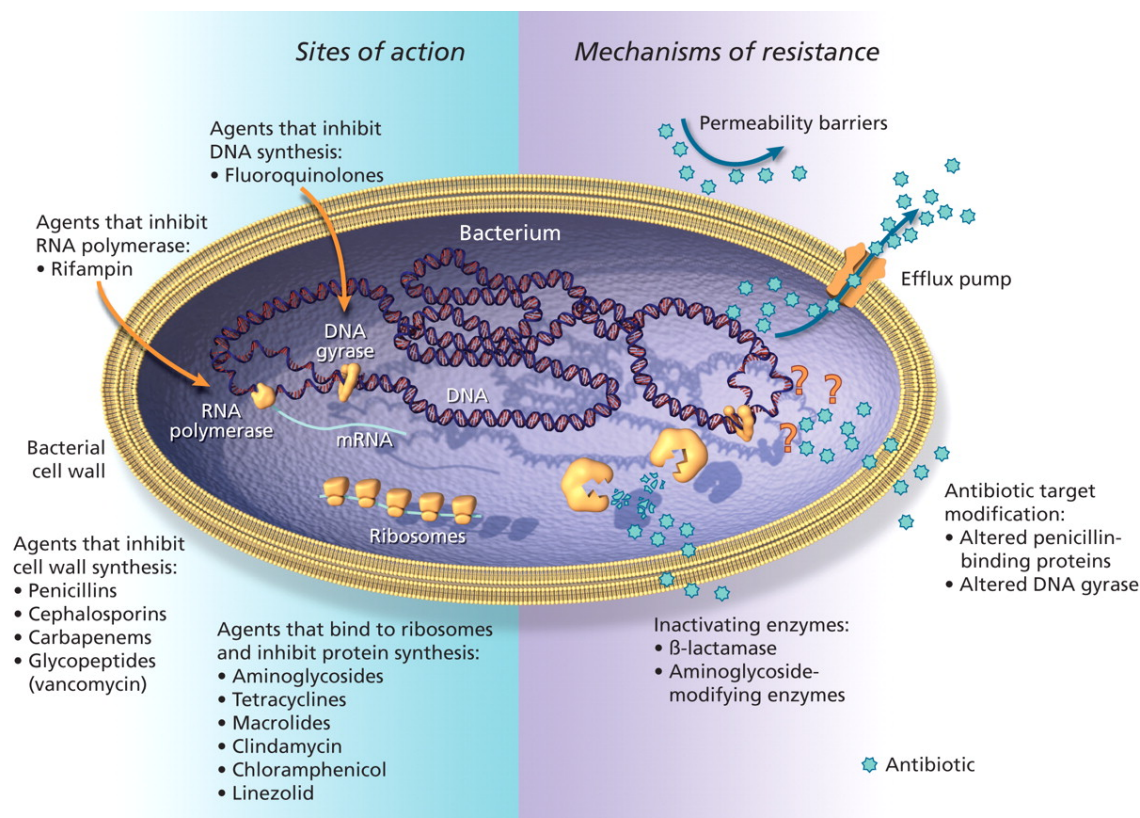
Figure 2.3: Common mechanisms of action of antibiotics and the mechanisms of resistance to combat them. Reproduced with permission.[57] Copyright 2009, CMAJ Group.

2.1.3 Mechanisms of antimicrobial resistance

There are four major biochemical mechanisms of antibiotic resistance; enzymatic interaction/-modification of the drug molecule, altering the target site, utilising efflux pumps to remove internalised drugs, and altering the cell membrane composition to decrease drug permeability. The antibiotic targets within a bacterial cell and the AMR mechanisms that protect the bacteria are depicted in Figure 2.3.

Firstly, resistant bacteria can produce enzymes that will alter or degrade an antibiotic disabling its antimicrobial activity. One of the most well studied examples is the resistance against β-lactam antibiotics. β-lactams bind to the D-Ala-D-Ala substrates responsible for crosslinking the peptidoglycan components within the cell wall, disrupting the cell wall integrity which ultimately leads to cell lysis.[58] As such bacteria have evolved to excrete β-lactamase enzymes that cleave the β-lactam rings rending the molecule inactive.[59]

Another cause of resistance is through alterations in the primary site of action for the antibiotic, meaning the drug will no longer have affinity to the binding site and as such it cannot perform

its activity. Possibly the most commonly known of drug resistant bacteria *methicillin-resistant Staphylococcus aureus* (MRSA), contains the *mecA* gene that facilitates the the synthesis of an altered penicillin-binding protein (PBP2a) that inhibits the binding of all β-lactam antibiotics.[60] This effect has also been observed in initially β-lactam susceptible *Streptococcus pneumoniae*, that gain resistance through alterations in peptidoglycan synthesising enzymes, thus lowering the affinity to the penicillin molecule.[61,62]

The final two resistance mechanisms restrict access of the antibiotic molecule to its action site. Efflux pumps are membrane spanning proteins that remove potentially toxic molecules from the cytoplasm and expel them from the cell. It's believed these proteins were initially devised as a mechanisms to remove disruptive amphiphilic compounds from the cell, as such these proteins evolved to remove a wide range of harmful products, it should therefore be of no surprise that efflux pumps evolved to remove harmful antibotics.[63] There are five main bacterial antibiotic specific super-families of efflux pump associated with antibiotic resistance; Small multidrug resistance (remove lipophilic and multicationic subtrates), ATP-binding cassette (removes amphiphilic, neutral, cationic, and anionic substrates), Multi-antimicrobial extrusion protein family (remove organic and cationic substrates), Resistance nodulation division (remove amphiphilic and charged substrates), and Major facilitator superfamily (amphiphilic and mono- or dicationic substrates).[63–66] Each protein family utilises a different molecule expulsion mechanism allowing targeting of a variety of molecular properties, as such this efflux pumps have been observed to increase resistance against a wide range of antibiotics. Access to the antibiotic binding site is also blocked by mutations in the outer cell membrane to decrease antibiotic permeability. Hydrophilic compounds, such as β-lactams, gain access into the cell through pore-forming proteins (porins) that regulate molecule internalisation,[67] whereas hydrophobic antibiotics, such as macrolides, diffuse into the lipid bilayer of the membrane.[68] By changing the membrane lipid and protein composition the antibiotic permeability can be severely restricted.[68,69] Furthermore, alterations in membrane permeability can be coupled with other mechanisms, such as antibiotic degrading enzyme secretion, to significantly increase multidrug resistance.[70]

Horizontal gene transfer is the primary means of passing along antimicrobial resistance. Mutations in the DNA of one bacterium that increase the chance of survival against an antibiotic may be passed to other bacteria leading to the rapid spread of resistance. This DNA transfer is achieved in three ways; plasmid conjugation, natural transformation by extracellular DNA, and

transduction by bacteriophages.[71] Plasmid conjugation is performed through the direct transfer of a small portion of the donor cell genome to the recipient via a sexual pilus that requires cell-to-cell contact.[72] Natural transformation occurs through the excretion of plasmids containing the resistant DNA, which is internalised by alternate bacteria under environmental stress.[73] The third means of resistance transfer requires the use of bacteriophages, viruses that target bacteria cells in order to reproduce. A bacteriophage will bind to a bacteria membrane before injecting their genome into the cell, commandeering the metabolic pathways and utilising the cell's energy for DNA replication and production of capsid proteins that encase the DNA.[74] Upon assembly of the new phages, the cell nucleoids and plasmids are broken apart creating DNA debris before the the bacterium lyses releasing the new virus particles. Antibiotic resistance is transferred when DNA debris that encodes the resistance mechanism is accidentally encapsidated, subsequently transferring the DNA when that virus infects another bacterium.[75]

2.2 Antimicrobial peptides

Antimicrobial peptides (AMPs), otherwise known as host defence peptides (HDPS), are short chains of amino acids, generally 5-50 residues in length, that are an integral part of the immune system in all life forms, performing a wide breadth of functions as depicted by Figure 2.4.[76–78] Taking AMPs alone, such is the diversity of the structures that they demonstrate activity against bacteria, parasites, yeast, fungi, and viruses, with a range of techniques to disarm each pathogen. AMPs are mostly comprised of a mixture of cationic and hydrophobic residues that provide attraction to the anionic membrane of bacteria (-130 to -150 mV) and enable structural organisation into secondary structures that enhance efficacy.[15,79–81] The plasma membrane of eukaryotic cells mainly consist of zwitterionic (neutral) phospholipids meaning mammalian cells are less negatively charged (-90 to -110 mV) and as such are targeted less.[80,82]
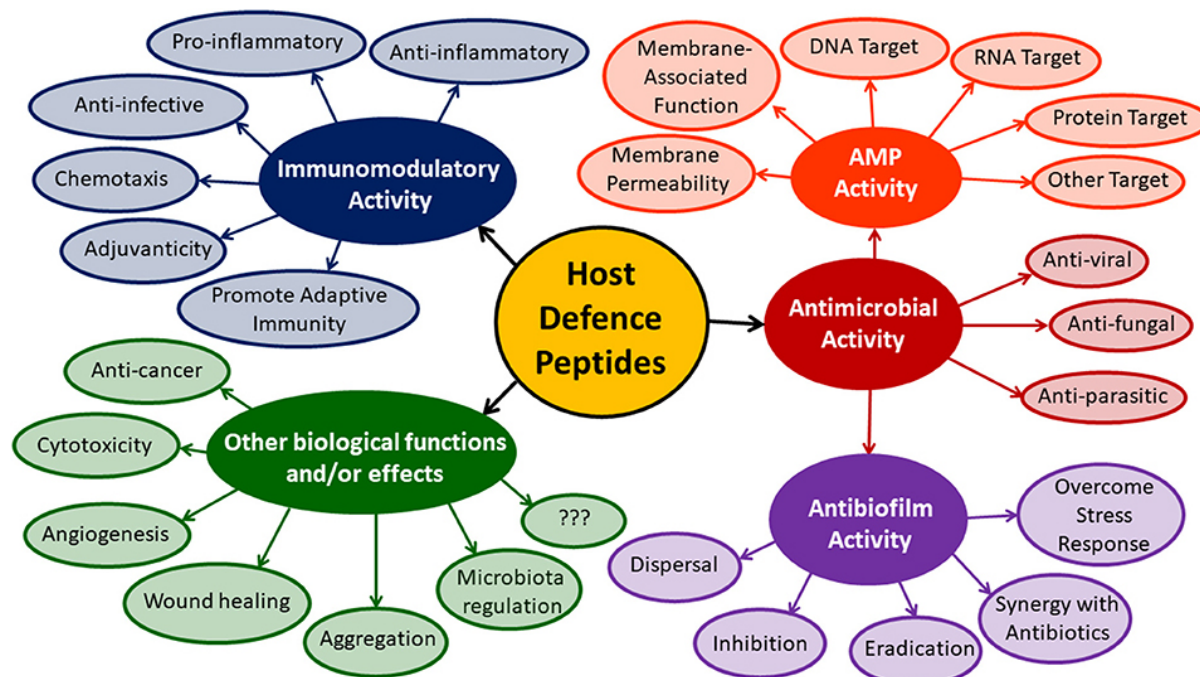
Figure 2.4: The wide array of functions host defence peptides play, with antimicrobial peptides only one branch of the versatile biomolecules. Reproduced with permission under a CC-BY license.[76]

AMPs have been touted as a key weapon in the antimicrobial arsenal to combat the ever-growing issue of multidrug resistance. The primary antibacterial mechanism of AMPs is through membrane disruption, which in turn promotes cytoplasmic leakage. This brute approach provides a decreased chance of resistance development, and offers broad-spectrum activity. As discussed in section 2.1.3, resistance to traditional antibiotics can be acquired through the uptake of foreign DNA through horizontal gene transfer[83] or through a variety of genetic mutations, altering a range of functions or properties of the cell.[84] Such resistant mechanisms are possible due to the low metabolic cost of mutation, whereas the brute membrane disruption of many AMPs is believed to reduce the risk of drug resistance due to the higher metabolic cost of membrane repair than the rate at which the damage is inflicted.[15] Despite the significant decrease in the chances of bacterial resistance development to AMPs, resistant mechanisms have been identified against natural HDPs. The most common means of acquiring resistance that have been observed *in vivo* are the modification of the cell surface structures and the usage of efflux transporters.[85] Bacteria cell membrane modification occurs by altering the anionic lipopolysaccharide and lipoteichoic acids of Gram-negative and Gram-positive cell membranes respectively, and through acylation of phosphatidylglycerol headgroups, to reduce the anionic charge of the membrane suppressing the electrostatic attraction of the cationic AMPs.[86] Efflux pumps are transmembrane proteins

used to expel toxic substances from the bacteria cytoplasm, and are a leading cause of antibiotic resistance.[65] AMP resistance through the secretion of additional proteases has also been observed in a small number of studies.[85] Frighteningly, AMP resistance development has the potential to further decrease bacterial susceptibility to classic antibiotics,[87] however the risk of AMP resistance is significantly lower than that of antibiotics and there is also evidence that using synthetic AMPs minimizes the risk further.[88]

2.2.1 AMP membrane disruptive mechanisms of action

Despite studying the properties of AMPs for three decades the complexity of interactions means that the specific antimicrobial mechanisms are still not fully understood.[89] There are currently four prevailing theories as to how cationic peptides interact with the bacterial membrane; the Barrel-stave model, the Toroidal pore model, the Carpet model, and the Detergent model. The simplest models for the AMP antimicrobial activity, the Barrel-stave and Toroidal pore models, describe the formation of a transmembrane pore. In the barrel-stave model, peptides lie in within polar headgroups of the lipids within the upper leaflet of the bilayer before rotating such that they are perpendicular to the bilayer. This encourages lateral peptide interactions, causing the formation of a peptide-stabilised pore, Figure 2.5A. This model requires the formation of secondary structures (α-helices or β-sheets), that match their hydrophobic regions to the hydrophobic core of the bilayer creating a hydrophilic lumen through which diffusion of polar solvents can flow.[90,91] Similarly to the Barrel-stave model the Toroidal pore model causes pore formation, however in the toroidal model the pores are not stabilised but are transient and dynamic. The AMP will directly insert itself perpendicularly to the membrane disrupting the lipid arrangement. This in turn rearranges the lipid molecule orientation, making it energetically favourable to form a radius of curvature between the bilayer leaflets, such that the lipid headgroups aid the hydrophilic regions of the AMP combine forming a pore lumen, see Figure 2.5B. It is entirely possible that upon degeneration of the pore the AMP is translocated across the cell membrane allowing targeting of the cytoplasmic materials.[92]

A) Barrel-stave model   **B) Toroidal pore model**

C) Carpet model   **D) Detergent model**
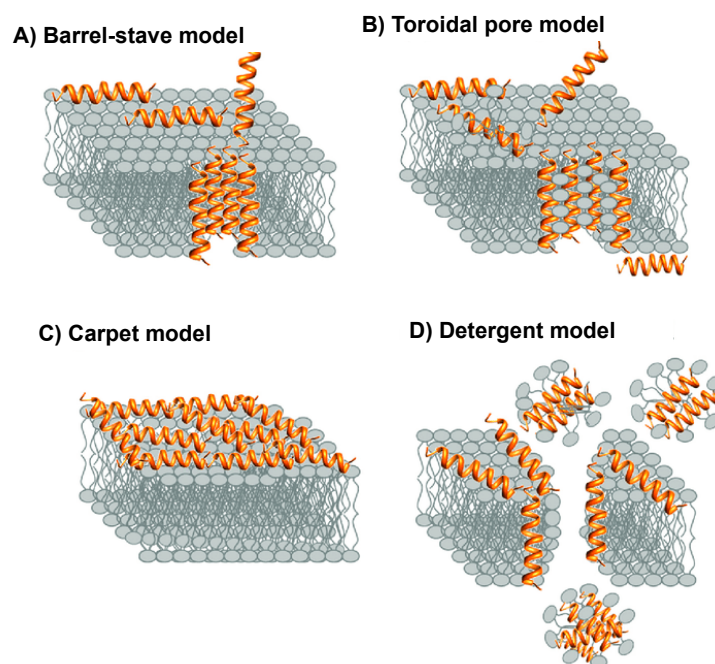
Figure 2.5: Schematic representations of the four most accepted models describing the interactions between antimicrobial peptides and a lipid bilayer. A) The barrel-stave model, AMPs form secondary α-helix or β-sheet structures producing a transmembrane pore. B) The Toroidal pore model, AMPs insert themselves into the bilayer with little order, causing transient and dynamic pore formation. C) The carpet model, AMPs lie within the membrane outer leaflet causing lipid packing disruption and allowing leakage. D) The detergent model, at high concentrations AMPs cause mass disruption leading to membrane disintegration. Adapted with permission under a CC-BY license.[93]

AMPs are also able to interact with a membrane without pore formation. In the carpet model AMPS are adsorbed onto the outer leaflet parallel to the membrane, Figure 2.5C. Upon reaching a critical concentration, the peptides "carpet" the membrane causing unfavourable interactions with the lipids, compromising the membrane integrity. Since the carpet model requires no peptide-peptide interactions or peptide insertion into the bilayer a large proportion of AMPs are expected to interact with membranes in this way.[94,95] The detergent, or aggregation, model become relevant upon further increasing the AMP concentration such that the membrane disruption is substantial enough that the bilayer will disintegrate with the lipids forming micelle, Figure 2.5D. It is probable that an individual AMP is likely to act through several mechanisms due to the wide range of parameters that will affect the AMP-lipid interactions (i.e. the structural properties of the membrane, the lipid:AMP ratio, the topology, and AMP aggregation).[96] As such the Shai–Matsuzaki–Huang (SMH) model was developed as a way of describing the mechanism of most membrane active AMPs and integrates three of the fundamental mechanisms.[82,97,98] Initially the AMP will be adsorbed onto the surface of the lipid bilayer through

electrostatic attraction between the cationic residues of the AMP and the anionic cardiolipin
and phosphatidylglycerol lipids within the membrane, as described by the carpet model (Fig-
ure 2.6A). The AMP will then insert itself into the upper leaflet of the bilayer (Figure 2.6B),
pushing the lipids apart and increasing the total surface area of the leaflet. This in turn causes
the layer to become thinner and imparts a strain force throughout the membrane. Upon sub-
stantial membrane disruption, rather than having the alkyl-tails of the lipids exposed to the
aqueous environment the hydrophobic forces impose a radius of curvature between the leaflets
of the bilayers causing the formation of toroidal pores (Figure 2.6C). The transient nature of
these pores means that the bilayer will reform, however some of the AMP will be translocated
onto the bottom leaflet (Figure 2.6D). At this point the AMPS on both sides of the bilayer can
cause the formation of micelle, leading to disintegration of the membrane as described by the
detergent model (Figure 2.6E), or the AMPs can diffuse into the bacteria cytoplasm.
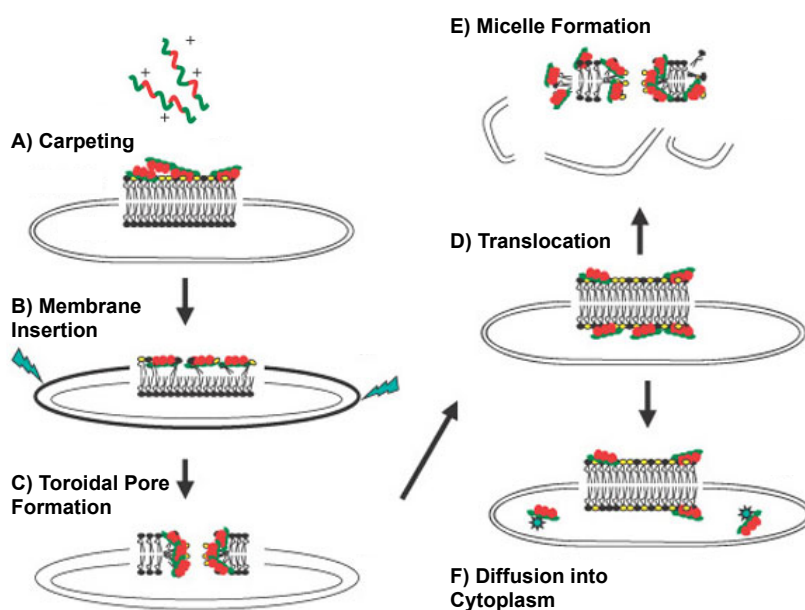
Figure 2.6: Schematic representations of the Shai-Matsuzaki-Huang (SMH) model of the mech-
anism of action of antimicrobial peptides (AMPs). A) Through electrostatic attraction AMPs
adsorb onto outer leaflet of a lipid membrane, causing initial disruption of the bilayer as de-
scribed by the carpet model. B) The AMP inserts itself into the bilayer causing thinning of
the outer leaflet. The surface area of the outer leaflet is then increased causing a stain force
within the bilayer, denoted with jagged arrows). C) It becomes energetically favourable to
form a radius of curvature within the bilayer causing the formation of transient toroidal pores.
D) AMPs are translocated across the membrane, at which point either E) the lipid will form
micelle leading to membrane disintegration (the detergent model), or F) AMPs will diffuse into
the cytoplasm. Adapted with permission.[82] Copyright 2002, Nature.

These models are general descriptions of how a large proportion of AMPs will interact with a

bacterial membrane, however many AMPs interact through more unique mechanisms. Nisin for example, anchors itself to Lipid II, a peptidoglycan precursor in the cell wall, before inserting into the membrane.[99,100] The limited mobility of the Lipid II-nisin complexes causes aggregation and eventually vesiculation. Similar effects have been observed in plant defensins, however they tend to target phospholipids and fungus-specific sphingolipids.[101] As such, the wide scope of AMPs acting through a variety of specific and non-specific mechanisms means that there is still a great deal about the antimicrobial activities of AMPs that is still unknown.

2.2.2 The challenges facing AMP clinical translation

Despite the significant benefits of AMPs as a treatment for multi-drug resistant microorganisms, few have made it to clinical trails and even fewer have demonstrated efficacy in human patients. The largest challenges facing the clinical translation of AMPs is that of instability *in vivo* and low bioavailability.[102] Preclinical studies often overstate the therapeutic potential of AMPs due to the *in vitro* test being performed in ionic conditions that are not representative of physiological conditions and potentially more importantly tests are generally performed in the absence of proteolyic enzymes.[103] The fundamental susceptibility of AMPs to proteases, such as trypsin and peptin, have restricted the means of application to topical uses only as the peptide half-life is too short to demonstrate efficacy with systemic delivery through oral or parenteral means.[104] Systemic delivery of AMPs is also hindered by the rapid removal of peptides through the renal system and the lack of understanding of the AMP biodistribution requires cytotoxic dosages to provide treatment of an infection.[105] A frequently used means of alleviating these issues is through chemical modification, of which the most common approaches are; cyclization to improve metabolic stability or bind bioactive groups, replacement of non-integral residues with amino acids known to increase stability, and N-/C-terminus modifications to avoid targeting by proteases.[102,106] One such modification is the inclusion of poly(ethylene) glycol (PEG) in the AMP structure, or PEGylation, which does not affect the antimicrobial efficacy but increases both the half-life in blood and the cytocompatibility, whilst reducing non-specific cellular uptake.[107,108]

Another critical issue of AMP clinical translation is that of systemic toxicity. AMPs have been shown to demonstrate hemolytic activity and cause long term toxic side effects.[109,110] In order to reduce the cytotoxic effects many novel AMPs are being synthesised with an emphasis on decreasing the number of residues. Synthetic short chain analogues of natural AMPs have shown

toxicity levels over 300 times lower than their endogenous counterparts.[111,112] Using shorter chain AMPs also reduces both material costs and synthesis time, whilst providing the added benefit of minimising the likelihood of immunogenicity.[15] Reducing the peptide chain length whilst maintaining antimicrobial efficacy is difficult, however it can be achieved by altering the residue sequencing to change the stereochemistry, creating secondary α-helical or β-sheet structures that augment the bactericidal properties.[15,16,113,114]

2.2.3   Conventional drug delivery systems for controlled release treatment of pathogenic bacteria

To overcome the therapeutic challenges facing AMP clinical translation, AMPs may be loaded into biocompatible delivery vehicles that will improve the pharmacokinetics and pharmacodynamics by increasing stability and protecting encapsulated peptides from proteolytic degradation.

2.2.3.1   Liposomes and lipid nanostructures

Liposomes are artificial vesicles consisting of a lipid bilayer that encloses an aqueous compartment. The lipid bilayers self-assemble into an energetically favourable structure with the hydrophilic headgroups exposed to the aqueous environment, sandwiching a bilayer of hydrophobic acyl chains, which offer a favourable environment for the encapsulation of hydrophobic molecules. Liposomes are the most widely researched nanoscale antimicrobial delivery system,[115–117] primarily due to their ability to increase the biocompatibility, bioavailability, and safety profiles of encapsulated antimicrobial materials.[118]

With regard to AMPs, Ron-Doitch *et al.* demonstrated an increase in the cytocompatibility by encapsulating cathelicidin LL-37 (100 μM) within liposomes (DSPC/DSPE-mPEG-2k/cholesterol, molar ratio 20:1:10) and inoculating keratinocyte HaCaT cells with the AMP-loaded vesicles.[119] After 24 hours the cells were adversely affected by free LL-37 (100 μM) with an >80% viability decrease, however the liposomal formulation containing the equivalent AMP concentration only resulted in a 20% reduction in viability. As such the isolation of drugs inside delivery vehicles can restrict interaction with peripheral tissues reducing toxic effects.
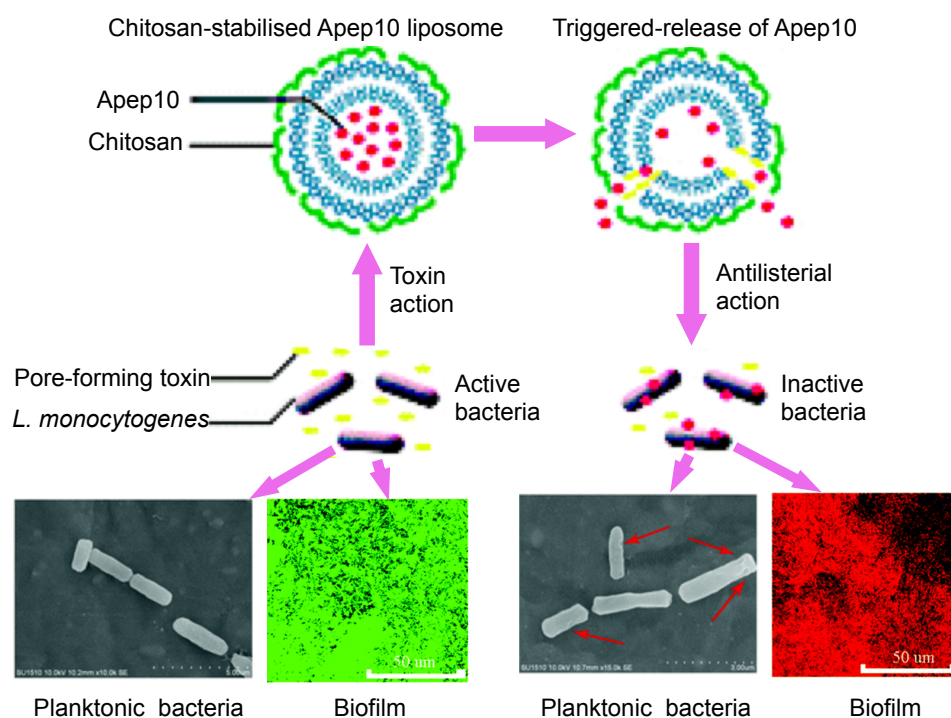
Figure 2.7: Schematic representation of Apep10 loaded liposomes coated in chitosan, that provide release of peptides upon pore formation from bacterial toxins. Scanning electron micrographs display the Apep10 degradation of planktonic *Listeria monocytogene* membranes (indicated with red arrows) and LIVE/DEAD staining of a *L. monocytogene* biofilm demonstrates a change from a mature viable (green) biofilm before treatment to a dead biofilm (red). Reproduced with permission.[120] Copyright 2016, Royal Society of Chemistry.

The bioavailability of AMPs may also be increased through liposomal encapsulation. Using an *in vivo* pharmacokinetic study Li *et al.* demonstrated the encapsulation of the cyclic lipopeptide daptomycin (DAP) within liposomes (soy phosphatidylcholine/sodium cholate, 17:1 mol ratio) enabled DAP to accumulated at bacteriostatic concentrations even after permeating through 5 layers of dermal and subcutaneous tissues.[121] The liposomes provided controlled release of the DAP with maximum concentrations observed in each tissue within 2.5 hours and ensured bacteriostatic concentrations in all 5 soft tissues 24 hours after administration to the dermis. By altering the liposomal lipid composition the release of encapsulated AMPs may be controlled to produce antimicrobial activity over several days. For example, Imran *et al.* demonstrated the controlled release of nisin from liposomes (1,2-dioleoyl-*sn*-glycero-3-phosphocholine [DOPC]) that induced progressively larger reductions in the *Listeria monocytogenes* bacterial load over the course of 72 hours.[122] Conversely, the liposome composition may be altered to encourage more rapid delivery. Many bacteria secrete pore forming toxins that target lipid bilayers, causing eukaryotic cell death. Pu *et al.* harnessed this by loading APep10 into chi-

tosan coated liposomes (1,2-dipalmitoyl-*sn*-glycero-3-phosphocholine [DPPC]/1,2-dimyristoyl-*sn*-glycero-3-phosphoglycerol [DMPG]/cholesterol, molar ratio 2:1:1) that release over 60% of their payload in the presence of *L. monocytogenes* in 5 hours, and nearly 100% after 24 hours, whereas the liposomes exhibit negligible release in phosphate buffered saline (PBS) in the same time frame.[120] Furthermore, 30 mg ml^{-1} of the liposome formulation produced eradication of both planktonic and biofilm *L. monocytogenes* in 10 and 24 hours respectively (see Figure 2.7). The liposomal encapsulation of AMPs has also been shown to increase the drug efficacy. Through the encapsulation of nisin into Phospholipon 90G/phytosphingosin (molar ratio 5:1) liposomes there was a four-fold reduction in drug concentration required to inhibit glucan-biofilm synthesis by *Streptococcus mutans* compared to free nisin;[123] resulting in complete inhibition of biofilm growth after 6 h using the liposome formulation, as opposed to free nisin at equivalent concentrations that lost inhibitory activity in the same time period. An increase in treatment efficacy has also been demonstrated *in vivo*. Polymyxin B (PB) encapsulated within DPPC and cholesterol liposomes showed a decrease in bacterial load of multidrug resistant *P. aeruginosa* in a lung tissue model compared to free PB, 3.9- and 8.0-log colony forming units (CFUs) g^{-1} respectively, and prolonged the survival rates of murine models by ~14% (an additional 8 hours) compared to a PB solution.[124]

Alternative lipid based delivery systems such as solid lipid nanoparticles (SLNs) and nanostructured lipid carriers (NLCs) have also been used to provide controlled release of AMPs.[125–127] SLNs are composed of a matrix of solid lipids encased in a surfactant, whereas NLCs are droplets of fluid lipids and a surfactant coating. Moreno-sastre *et al.* demonstrated that colistin loaded NLCs exhibit excellent stability with no decrease in antimicrobial efficacy after a year in storage, whereas colistin-loaded SLNs lost their antimicrobial activity after only 3 months.[127] The NLC encapsulation of colistin sulfate also demonstrates increased antibiofilm activity compared to the free drug, when used to treat *P. aeruginosa* biofilms obtained from cystic fibrosis patients.[125] Furthermore, the antimicrobial efficacy of an AMP-NLC complex may be augmented through co-loading the AMP with antibiotics. This effect was explored by Lewies *et al.* who loaded nisin Z and melittin into NLCs with a variety of antibiotics in order to determine the fractional inhibitory concentrations when treating *E. coli*.[126] The most potent combination was found to be nisin Z used in combination with novobiocin, interestingly the bactericidal activity of nisin Z was also complimented using the non-antibiotic chelating agent ethylenediaminetetraacetic acid (EDTA). In 2018 Groo *et al.* developed a unique NLC containing AP138-loaded reverse

micelle to demonstrate protection against protease degradation and provide controlled release to treat Gram-positive and Gram-negative bacteria.[13] Upon incubating both the AP138-NLC complex and free AP138 with the proteolytic enzyme trypsin it took over double the amount of time to degrade 90% of the encapsulated AMP compared to the peptide in solution, >120 mins and 60 mins respectively. The same construct provided complete bacteria eradication of both *S. aureus* and MRSA within 18 hours of incubation with each bacterial suspension.
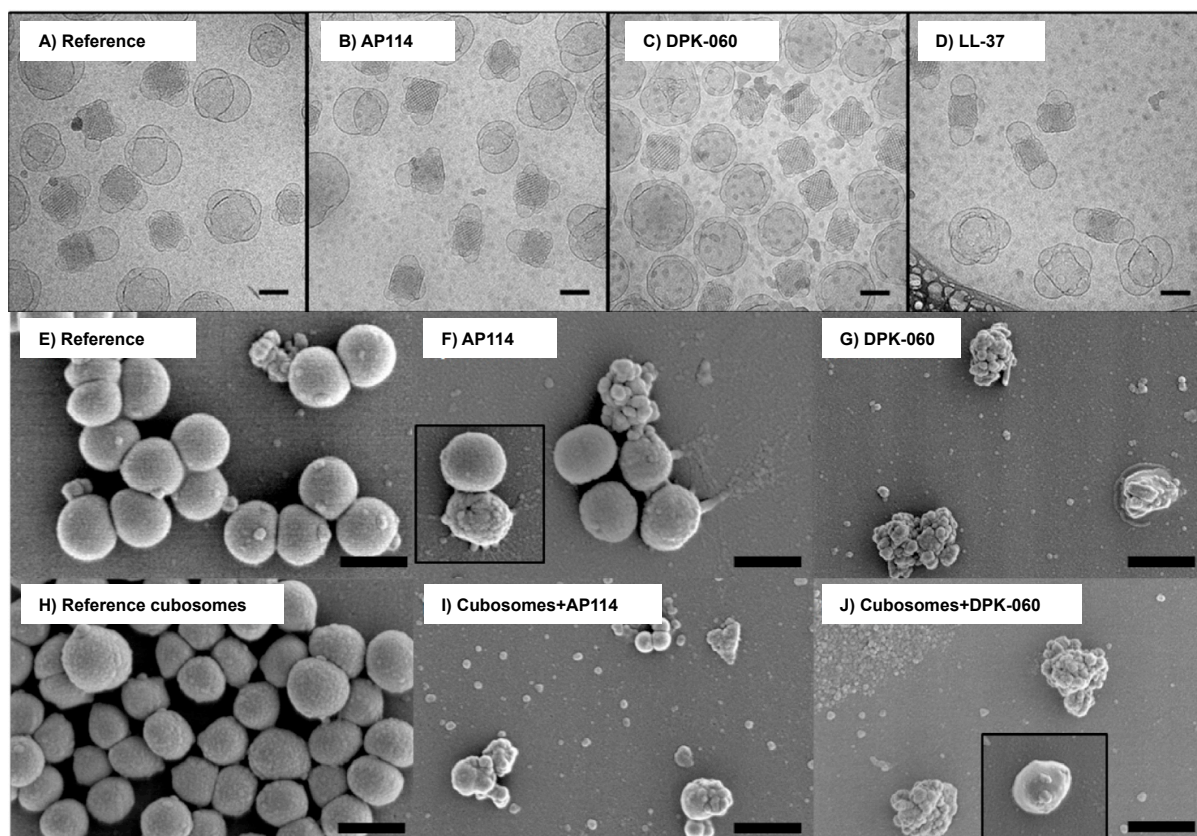
Figure 2.8: Transmission electron micrographs of (A) blank cubosomes, and cubosomes loaded with (B) AP114, (C) DPK-060 and (D) LL-37 AMPs. Scale bars equal 100 nm. Scanning electron micrographs of MRSA incubated for 10 hours with free AMPs (E-G) and AMP-loaded cubosomes (H-J). Scale bar equals 1 μm. Adapted with permission.[128] Copyright 2017, Elsevier.

Lipid stabilised liquid crystalline nanoparticles, are gaining attention as AMP delivery vehicles due to their high stability that allows protection and delivery of AMPs in enzyme-rich environments such as the mouth.[14] Boge *et al.* have investigated the incorporation of three different AMPs (AP114, DPK-060, and LL-37) in to cubosomes (Figures 2.8A-D) and hexosomes (cubic and hexagonal 3D structures) achieving encapsulation efficiencies between 40-90% and 94-98% respectively.[129] Hexosomes of glycerol monooleate (GMO)/oleic acid were found to be too stable, demonstrating no change in morphology upon internalisation of AMPs and

little AMP release, substantially increasing the MIC against *S. aureus* and MRSA. AMP incorporation into cubosomes (GMO alone) induced a slight radius of curvature that increased with peptide hydrophobicity. The use of cubosome vehicles was observed to increase the AMP efficacy against *S. aureus, Escherichia coli* and MRSA.[128] Scanning electron micrographs of the MRSA cells show that the AMP-loaded cubosomes (Figures 2.8I,J) produced a greater degree of membrane disruption than the free peptide (Figures 2.8F,G), and that the non-functionalised cubosomes did not affect the bacteria (Figure 2.8H). The cubosome formulation protected all 3 AMPs from *Pseudomonas* elastase (PE) and human neutrophil elastase.[130]

2.2.3.2   Hydrogels and polymer systems

Hydrogels are water-swollen three-dimensional networks exhibiting viscoelastic properties governed by the characteristics of the subunits and the means and degree to which the subunits are bound.[131] The high water content of hydrogels means that they are ideal vehicles for hydrophilic drugs that allow control of the molecular diffusion and release by altering the solute size compared to the pore size between polymer chains, the polymer chain mobility, and the electrostatic interactions between the solute and the polymer chain.[132] The controlled release of molecules from a polymeric hydrogel is often not just controlled by the diffusive motion of a molecule but is affected by erosion, swelling and dissolution of the network.[133] Rajan *et al.* fabricated gels comprised of 8arm-PEG-thiol crosslinked with 4arm-PEG-NHS that demonstrated a biphasic release of the relatively hydrophobic cyclic peptide subtilosin; for 12 hours gels of 4 and 6 wt% released the AMP at 3.96 and 4.04 μg h^{-1} respectively, before dropping to 0.28 and 0.24 μg h^{-1} for the next 108 h.[134] The release was deemed to be non-Fickian (i.e. the characteristic solute diffusion time was comparable to the polymer relaxation time), and as such was governed by both the AMP diffusion through the network and the polymer relaxation. Furthermore, the AMP-loaded gel only exhibited antimicrobial activity against the pathogenic *Gardnerella vaginalis*, with only a small increase in the MIC compared to the free drug (7.2 to 12 μg ml^{-1}), without imparting any adverse effects upon 4 types of lactobacilli (*L. acidophilus, L.gasseri, L. plantarum, and L. vaginalis*) that play a key part in the vaginal microflora. The release kinetics from a gel can also be affected by the polymer charge and the ionic strength of the environment. Anionic microgels made from poly(ethyl acrylate/methacrylic acid (MAA)/1,4-butandiol diacrylate) with electrostatically adsorbed cationic AMPs LL-37 and DPK-060, exhibit high retention at 10 mM NaCl concentrations ($\sim$10-20% release of both AMPs), whereas at higher NaCl concentrations

(150 mM) the ionic buffering reduces the polymer-AMP electrostatic attraction increasing the release profiles, ~30-40% and ~60-70% for LL-37 and DPK-060 respectively.[135] This system was also used to demonstrate how the gel charge density affects its protective properties. The gel containing a higher proportion of anionic MAA, 60% rather than 26.5%, exhibited significantly higher protection of LL-37 against PE degradation than both the low MAA content microgel and the free peptide.

AMPs can also be immobilised within/onto hydrogels through chemical modification of AMPs, by binding to functional groups within a polymer.[136,137] Cleophas *et al.* first demonstrated as such by synthesising a series of AMP HHC10 analogues containing thiol groups to anchor to poly(ethylene glycol)diacrylate-based hydrogels using thiol-ene chemistry.[136] The thiol functionalised HHC10 analogue with the highest antimicrobial efficacy (inverso-CysHHC10) was subsequently conjugated to the network which demonstrated complete bacteria killing against *S. aureus*, *S. epidermis* and *E. coli*. Through polymer conjugation AMPs can have prolonged efficacy, increased stability and can be modified to provide multi-functionality.[138]

An interesting property of hydrogels is that they can form interpenetrating networks with apolar polymers currently used to fabricate plastics in medical devices. Klein *et al.* developed a novel hybrid catheter material comprised of an interpenetrating network of silicone elastomer (polydimethylsiloxane) host polymer accompanied by poly(2-hydroxyethyl methacrylate)-co-poly(ethylene glycol) methyl ether acrylate hydrogel as a guest polymer, onto which the plectasin derivate NZ2114 adsorbed.[139] This novel catheter system demonstrated effective inhibition of MRSA biofilm growth within a continuous flow system used to emulate blood flow (Figure 2.9). The plectasin NZ2114 retention was high enough that a 2-log MRSA CFU reduction was still observed even after 6 days of continuous flow of PBS prior to testing.
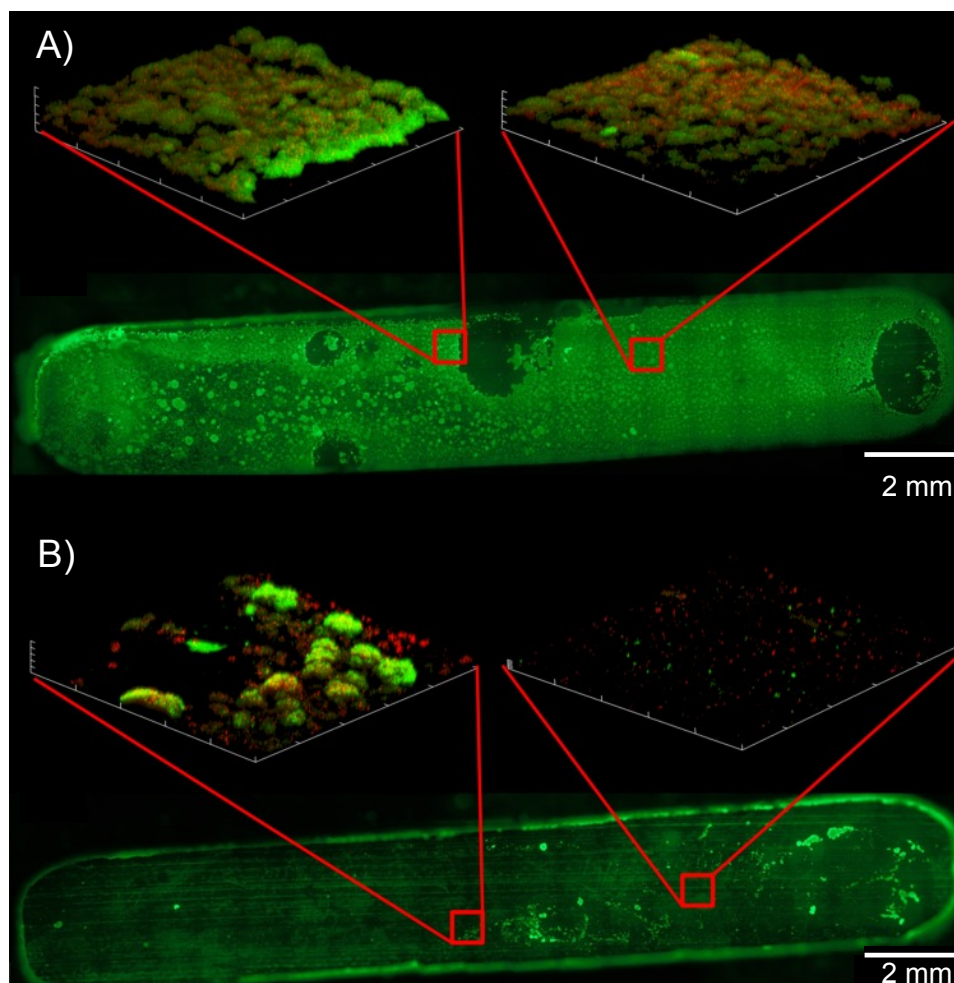
Figure 2.9: Microscopy images of MRSA biofilms grown on a catheter made from an interpenetrating network of a silicone elastomer (polydimethylsiloxane) and the a poly(2-hydroxyethyl methacrylate)-co-poly(ethylene glycol) methyl ether acrylate hydrogel loaded without (A) and with (B) the AMP, plectasin NZ2114. Biofilms were imaged using a LIVE/DEAD BacLight bacterial viability kit producing green and red fluorescence depending on whether the bacteria were alive or dead respectively. Adapted with permission.[139]

Polymers may also used to fabricate micro- or nanogel particles, that can be loaded with AMPs. Polymeric nanoparticles offer most of the same benefits as macroscopic hydrogel delivery vehicles (i.e. controlled release, protection against degradation, prolonged activity, and increased biocompatibility)[140–142] whilst allowing parenteral or oral administration. For example, Casciaro *et al.* fabricated poly(vinyl alcohol) stabilised poly(lactide-*co*-glycolide) nanoparticles for use as an aerosol to treat lung infections of cystic fibrosis sufferers.[143] The nanoparticles encapsulating the AMPs Esc(1-21) or its diastereomer Esc(1-21)-1c were administered to murine models infected with *P. aeruginosa* through intratracheal inoculation, demonstrating a statistically significant decrease in the CFUs observed in the bronchoalveolar lavage, compared to treatment with the free peptides. Interestingly, the total number of inflammatory cells (including macrophages,

neutrophils, and lymphocytes) in the bronchoalveolar lavage was also observed to increase upon treatment with ESC(1-21)-NPs, whereas this was not seen using the particles or AMP alone.

Electrospun nanofibres have also been utilised to produce controlled release of AMPs. Electrospinning is a technique whereby a charged polymer solution is drawn out into a fibril through attraction to a surface with an opposing charge, this results in a highly porous mesh with a large fibre surface area.[144] The innate polymer charge required to produce electrospun fibres can be adopted to electrostatically adsorb cationic AMPs to the fibre surface. This has been demonstrated by Amariei *et al.* to adhere ϵ-polylysine to anionic fibres of poly(vinyl alcohol)-poly(acrylic acid). These fibres were used to create a mesh dressing that demonstrated inhibition of bacterial fouling after 14 days of incubation in *S. aureus*, *S. epidermis* and *E. coli* broths (Figure 2.10).[145] Nanofibres have also been utilised by the food industry with nisin-loaded amaranth protein isolate-pullulan nanofibres displaying pH dependent controlled release of the AMP.[146] After 12 hours at a neutral pH the nanofibres release ~40% of the loaded-nisin, whereas in an acidic environment (pH 3.4) the fibres released ~80% of the AMP. This produced total eradication of *Salmonella Typhimurium*, *L. monocytogenes* and *Leuconostoc mesenteroides* after 20-100 h in acidic apple juice whereas total bacteria killing required 120-170 h on the neutral surface of Panela cheese.
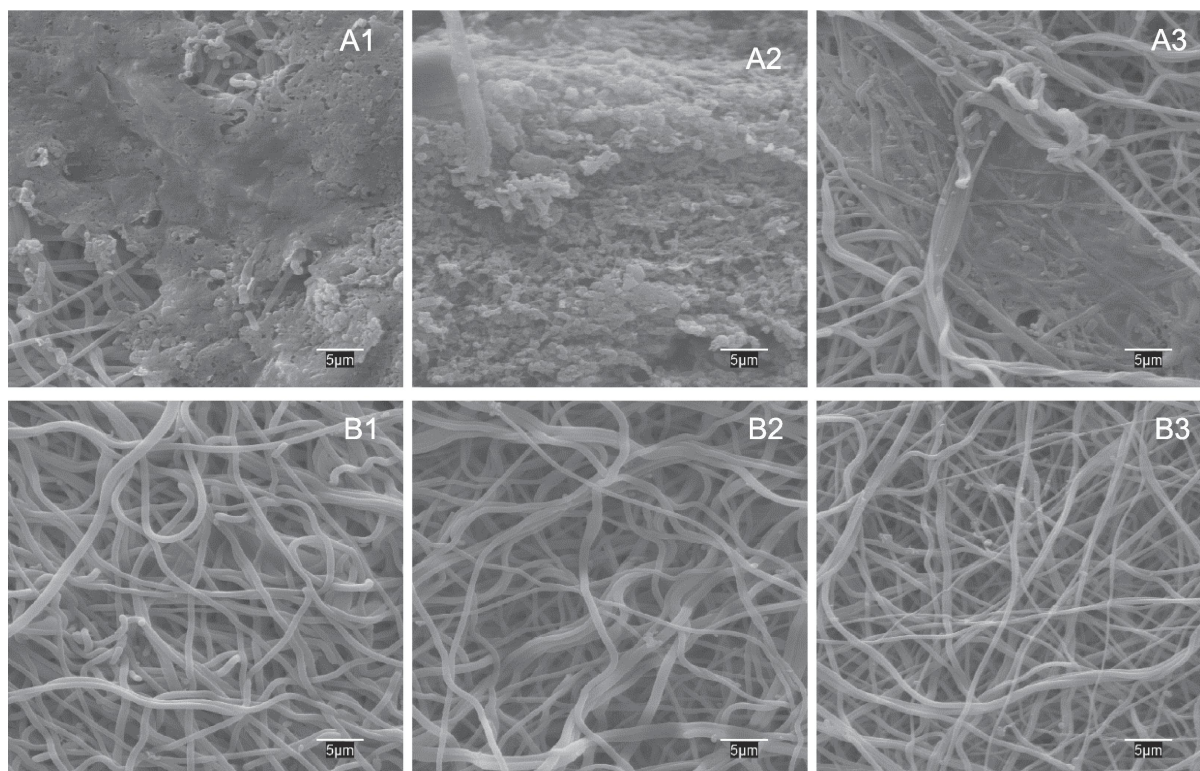
Figure 2.10: Scanning electron micrographs of (A) non-functionalised and (B) ϵ-polylysine loaded poly(vinyl alcohol)-poly(acrylic acid) nanofiber dressings after a 14 day incubation with *S. aureus* (A1, B1), *S. epidermis* (A2, B2) and *E. coli* (A3, B3). Scale bars are 5 μm. Reproduced with permission.[144]

2.3   Optical properties of gold nanoparticles

2.3.1   The Drude model and skin depth of penetrating light

Before broaching the subject of plasmonics it is important to discuss the behaviour of electrons within metals. The high electric and thermal conductivities, as well as many optical effects of metals may be attributed to the high density of delocalised, or 'free' electrons, that can propagate through a metallic lattice with little resistance. The high density of electrons means that the spacing between the electron energy levels is very small compared to the the thermal excitation, $K_B T$, at room temperature.[147] As such, the interactions of electrons with electromagnetic forces may be modelled by Maxwell's equations, and ignore many of the quantum mechanical phenomena of nanoscale structures with low electron densities, such as semiconductors. This allows the application of Drude's model as an approximation to the propagation of electrons through a material. Based on Lorentz' oscillating dipole theory; electron motion acts as if it were attached by a spring to an atomic nucleus and undergoing oscillatory motion driven by

an applied electromagnetic field.[148–150] Drude's model is a classical representation of a damped, driven harmonic oscillator in which electrons are driven to oscillate by an external electric field (e.g. light). The lack of a restoring force means there is no natural resonant frequency. Using this model the dielectric function of the free electron gas as a function of an applied electric field can be stated as

$$\epsilon(\omega) = 1 - \frac{\omega_p^2 \tau}{\omega^2 \tau + i\omega} \tag{2.1}$$

where τ is the relaxation time for a free electron gas ($\sim 10^{-14}$ s at room temperature) and ω_p is the plasma frequency of a free electron gas and is defined as

$$\omega_p^2 = \frac{ne^2}{\epsilon_0 m^*} \tag{2.2}$$

where n is the free electron density, e is the charge of an electron and m^* is the effective mass of an electron. The real and complex components of the dielectric function, $\epsilon(\omega) = \epsilon_1(\omega) + i\epsilon_2(\omega)$, are given by

$$\epsilon(\omega) = 1 - \frac{\omega_p^2 \tau}{1 + \omega^2 \tau} + i \frac{\omega_p^2 \tau}{\omega(1 + \omega^2 \tau^2)} \tag{2.3}$$

This model predicts that the metals are reflective when the frequency of incident radiation is lower than the plasma frequency ($\omega < \omega_p$), as $\epsilon_1(\omega)$ is ~ 1 meaning no light can propagate through the material. Conversely, when the frequency of the incident radiation is greater than the the plasma frequency ($\omega > \omega_p$) then $\epsilon_1(\omega)$ tends to zero, meaning the light is not retarded and the material is transparent. Irradiation at low frequencies, when $\omega\tau \ll 1$ and $\epsilon_2 \gg \epsilon_1$, the refractive index ($n$) and the extinction coefficient (k) are approximately equal, allowing the complex refraction index, $\epsilon^{1/2} = n + ik$, to be rearranged and substituted directly into the equation for the absorption coefficient,

$$n \approx k = \left(\frac{\omega_p^2 \tau}{2\omega} \right)^{1/2}$$
$$\alpha = \frac{2\omega}{c} k = \left(\frac{2\omega_p^2 \tau \omega}{c^2} \right)^{1/2} \tag{2.4}$$

Using the Beer-Lambert law of absorbance, $I = I_0 e^{-x\alpha/2}$,[151] the intensity of the light can be seen to decrease exponentially with the penetration depth, providing a material with a characteristic retardation length scale known as the skin depth, that is the inverse of the absorption coefficient.

The electromagnetic excitation of electrons in conductive materials is therefore restricted to a thin layer at the surface, shielding the electrons in the bulk material from the incident radiation. This result means that when radiation is applied the conductive structures of equivalent size to the skin depth, the light can drive the coherent oscillation of all delocalised electrons. This forms a longitudinal charge density wave, known as a polariton, that drives an electromagnetic wave that propagates along the nanoparticle surface. This resultant wave is called a localised surface plasmon (LSP).[152]

2.3.2   Localised surface plasmons - Mie theory

A plasmon is a quasiparticle (a collective excitation that can be modelled as an individual particle) that is formed when coherently oscillating electrons are driven at their resonance frequency. Plasmons are driven by the E-field component of incident light, which has a skin depth of up to ~50 nm in gold meaning that all electrons within a nanoparticle may be excited creating a localised surface plasmon. As shown in Figure 2.11 excited electrons coordinate to oppose the applied electrical field forming an oscillating dipole that is dampened by electron scattering, thus providing the resonance condition for maximum absorbance.
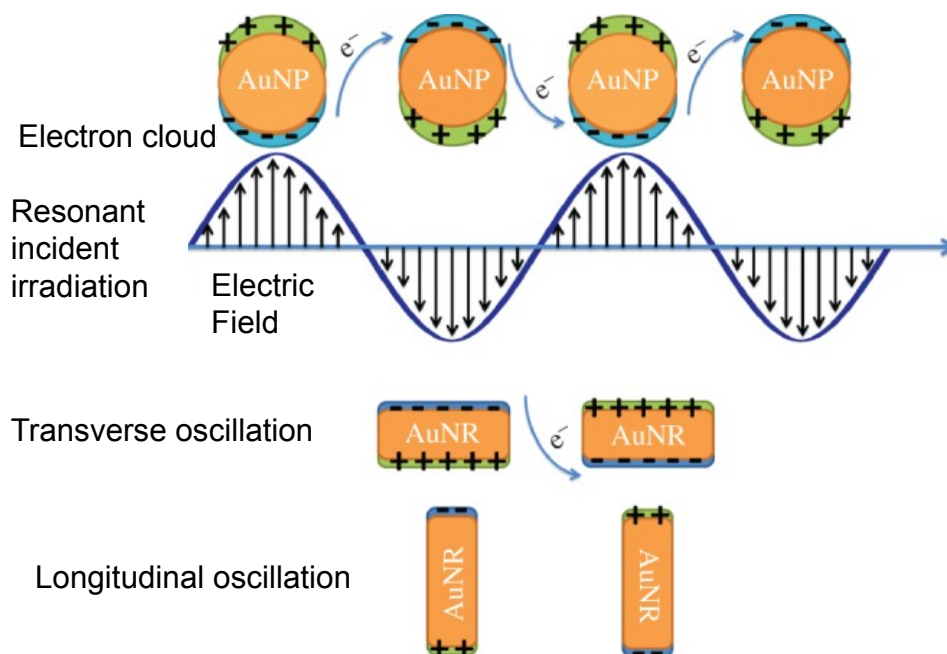
Figure 2.11: A schematic representation of the oscillations of the free electrons within the nanoparticle structures and the resulting electric field it induces. For spherical particles this can be seen in only the transverse axis, whereas asymmetric nanoparticles, such as gold nanorods, produce E-fields along both the transverse and longitudinal axes. Reproduced with permission.[153] Copyright 2013, The Royal Society.

The absorption and scattering of the E-field upon interaction with a metallic nanoparticle can be modelled by solving Maxwells equations for a singular sphere being acted upon by a plane wave in a homogenous medium, known as Mie theory.[154] The scattering properties are defined by two perpendicular polarisation functions,

$$S_1(\theta) = \sum_{n=1}^{\infty} \frac{2n+1}{n(n+1)} \{a_n \pi_n(cos\theta) + b_n \tau_n(cos\theta)\}$$
$$S_2(\theta) = \sum_{n=1}^{\infty} \frac{2n+1}{n(n+1)} \{b_n \pi_n(cos\theta) + a_n \tau_n(cos\theta)\}$$
(2.5)

The functions π_n and τ_n are angle dependent functions related to first degree Legendre polynomials.

2.3.3   Localised surface plasmons - Gans' Solution

In 1912 Gans published a solution to augment Mie theory by including scattering from oblate or prolate ellipsoids, rather than just a sphere.[155] This solution models the splitting of the localised surface plasmons into two distinct modes that vary as a function of the ellipsoid aspect ratio.[156] Whilst this model is designed for ellipsoids the solutions are in agreement with the absorption profiles of cylindrical hemi-spherically capped gold nanorods (AuNRs).[157] The Gans solution splits the polarisability along each axis to give

$$\alpha_{x,y,z} = \frac{4\pi}{3} a_x a_{y,z}^2 \frac{\epsilon_p - \epsilon_m}{\epsilon_m + P_{x,y,x}(\epsilon_p - \epsilon_m)}$$
(2.6)

Where ϵ_p and ϵ_m represent the real components of the permittivity of the particle and medium respectively, a_x is the length of the major axis and $a_{y,z}$ is the length of the minor axes, Figure 2.12A, and $P_{x,y,z}$ denotes the shape factor along each axis in relation to the eccentricity of the ellipsoid. As such, the scattering and absorbance cross-sections of the ellipsoid are determined:

$$\sigma_{scattering} = \frac{k^4}{6\pi} \left(\frac{|\alpha_x|^2}{3} + \frac{|\alpha_y|^2}{3} + \frac{|\alpha_z|^2}{3} \right)$$
$$\sigma_{absorption} = k Im \left\{ \frac{\alpha_x}{3} + \frac{\alpha_y}{3} + \frac{\alpha_z}{3} \right\}$$
(2.7)

This produces two distinct plasmonic absorption peaks for the ellipsoidal particles, the transverse plasmonic peak at ∼550 nm and a longitudinal plasmonic peak at longer wavelengths as seen in Figure 2.12B. The transverse absorption peak is a result of plasmon propagation along

the ellipsoid circumference, and as the aspect ratio of the ellipsoid increases the peak decreases in intensity and is slightly blue shifted. Conversely, upon increasing the ellipsoid aspect ratio the longitudinal peak, the plasmon propagation along the major axis, is seen to increase in intensity and is substantially red shifted. This indicates that the absorption spectra of an ellipsoidal nanoparticle, or nanorod, may be tuned to provide a resonance peak in the visible to near-infrared (NIR) range, simply be altering the particle morphology.
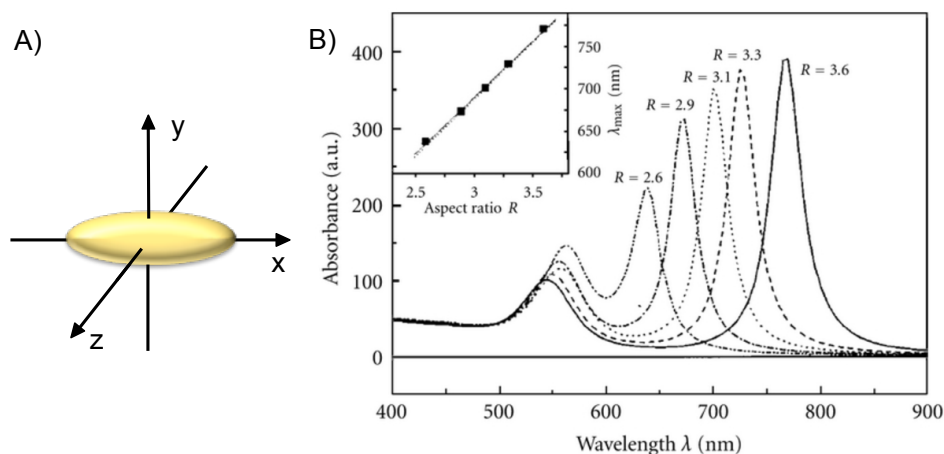
Figure 2.12: A) An ellipsoid in a cartesian coordinate system. B) The simulated spectra of gold ellipsoids of increasing aspect ratio (R) calculated using Gans solution. Inset: the relation between the peak absorption wavelength and the aspect ratio. Reproduced with permission.[158]

2.4   Photothermal heating
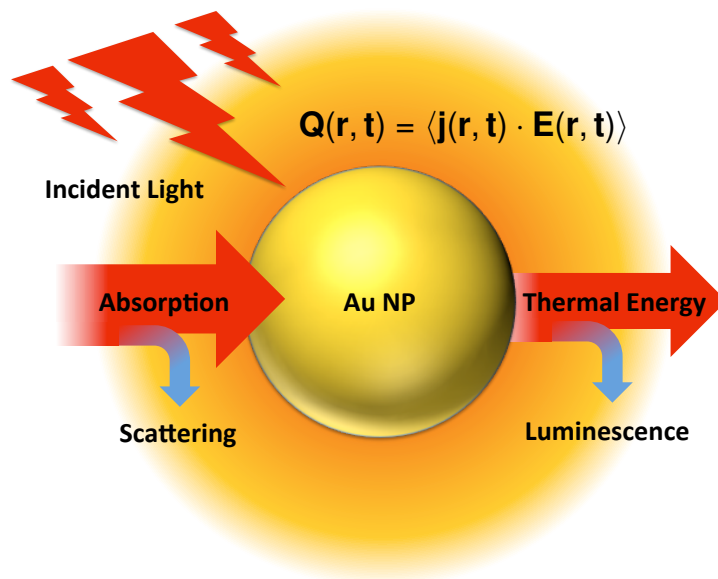
Figure 2.13: The photothermal effect occurs when energy is absorbed from incident light with little scattering. Of the energy absorbed, approximately 99% is thermally radiated with the excess energy lost through photoluminescence. The thermal energy dissipated from Au NP, Q(r,t), may be calculated by taking the time dependent average of the current density, j(r,t), by the electric field from the applied light source, E(r,t).

Photothermal heating is the phenomena by which electromagnetic energy applied to a photothermal agent is absorbed and the energy is reemitted as thermal radiation. In the case of metallic nanoparticles, when exposed to light of a resonant wavelength, governed by the particle size and anisotropy, the incident photons can couple with the electrons within the metal lattice driving the formation of a plasmon. This energy can then be dissipated through either scattering or absorbance, it can be assumed that nearly all of the absorbed energy is transferred into thermal radiation. The generation of heat occurs in a three step process; (1) the absorption of the photon by free electrons takes approximately ∼100 fs, (2) heat is generated within the nanoparticle through electron-phonon scattering with the crystal lattice (> 85%) or through electron-electron scattering (< 15%), taking approximately 0.1-10 ps, (3) thermalisation occurs between the nanoparticles and the surrounding medium through phonon-phonon scattering taking up to 1 ns.[159–161] To reach a quasi-stationary temperature profile within a particle of ∼10 nm in diameter, takes approximately 2 ps and upon irradiation timescales above several ns it can be assumed that that there is a continuous heat flow radially away from the particle surface. The heating of a particle can be assumed to be uniform throughout the lattice and is described

by

$$\rho_p c_p V_p \frac{\delta T_p}{dt} = \frac{1}{4} I(t) \sigma_{abs} S_p - j S_p \tag{2.8}$$

where ρ_p, c_p, V_p and S_p, are the particle's density, specific heat capacity, volume and surface area, t is time, T is temperature, I(t) is the irradiation density, σ_{abs} is the absorption coefficient and j is the energy flux density away from the particle surface. When the timescale of irradiation is greater than the the thermal dissipation time, $t_T \sim r_p^2/4\alpha_p$, where r_p and α_p are the particle radius and thermal diffusivity, the quasi-stationary temperature at a distance r in a spherical coordinate system originating at the centre of the particle is

$$T(r) = T_\infty \left\{ 1 + \frac{r_p}{r} \left[\left(\frac{T_p}{T_\infty} \right)^{a+1} - 1 \right] \right\}^{\frac{1}{a+1}} \tag{2.9}$$

where a is a constant and assuming a temperature-dependent media thermal conductivity, k, is $k = k_\infty (T/T_\infty)^a$ where k_∞ and T_∞ are the thermal conductivity of the liquid and the temperature at an infinite radius, respectively.[162] This equation is useful to model the temperature due to an individual nanoparticle however it does not describe the thermal output of a bulk AuNP suspension. The thermal power output of a solution of AuNPs, otherwise known as the specific absorption rate (SAR, W m^{-3}), is the sum of the power output from each particle individually,

$$SAR = N \times \sigma_{abs} \times I = \mu_{np} \times I \tag{2.10}$$

where N is the number of AuNPs per m^3, σ_{abs} is the AuNP absorbance cross-section, I is the laser fluence and μ_{np} is the absorption coefficient of the AuNP solution. This shows that the only information required to identify the thermal power output are the solution absorbance and the laser fluence. To obtain the temperature increase within an isolated AuNP solution the SAR is divided by the specific heat capacity of the medium, c, multiplied by the mass of the solution:

$$\Delta T = \frac{SAR}{C \times m} \tag{2.11}$$

In a non-isolated system the temperature increase is also hindered by heat diffusion into the surroundings and potentially melting/morphological changes in the AuNP altering the absorbance cross-section.

2.4.1   Localised heating through pulsed-laser irradiation

Light deposition into photothermal agents on timescales equivalent or less than the thermalisation rate can lead to localised temperature increases of several hundred degrees. The temperature of a nanoparticle during a heating pulse is

$$T_p = T_\infty + \frac{I\sigma_{abs}r_p}{4k_\infty}(1 - e^{-Bt}) \qquad (2.12)$$

where B is $B = 3k_\infty/\rho_p c_p r_p^2$. Neglecting the loss of heat during irradiation and expanding the exponential function gives the maximum temperature at the end of the pulse duration,

$$T_{max} = T_\infty + \frac{3I\sigma_{abs}t_p}{4\rho_p c_p r_p} \qquad (2.13)$$

where t_p is the pulse width. Subsequently, the temperature of a particle is cooling after the pulse is:

$$T_p = T_\infty + (T_{max} - T_\infty)exp\left(\frac{-3k_\infty(t - t_p)}{\rho_p c_p r_p^2 T_\infty}\right) \qquad (2.14)$$

This equation again demonstrates that at the end of the pulse width (t=t_p) the exponential equals one and as such the particle temperature is at it's maximum. The exponential decrease in temperature after the pulse width (t> t_p), means that even at fast repetition rates in the range of kHz there is a long duration of time, relative to t_p, in which the particle is at thermal equilibrium with the surrounding medium (T_p=T_∞) meaning there is no bulk heating. It is worth noting that the thermalisation time after the pulse is approximately equal for all nanoparticles that have absorbed equal quantities of energy independent of the pulse width, see Figure 2.14. This figure also depicts the significance of the pulse duration, simply by depositing the equivalent amount of energy at one hundredth the pulse width the particle is heated by an additional $\sim 700°$C.
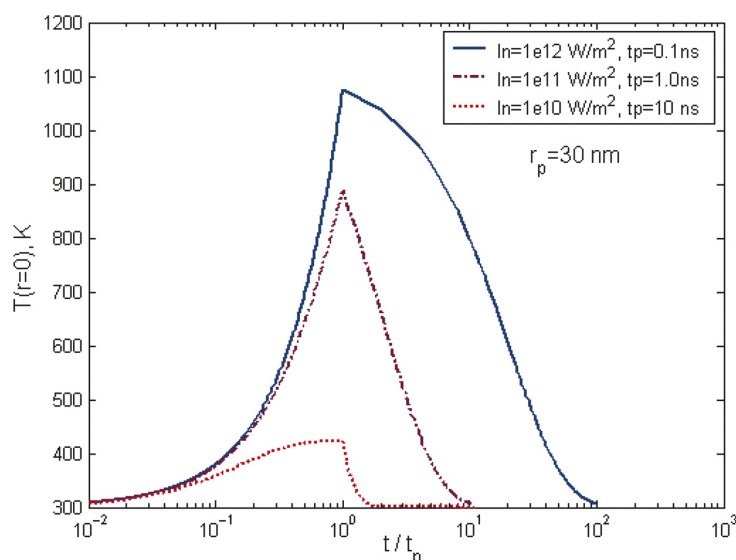
Figure 2.14: The simulated temperature of gold nanoparticles under irradiation from a pulse laser when maintaining an equal energy absorption but varying the pulse width. Reporduced with permission.[161] Copyright 2009, Taylor & Francis.

2.4.2   Photothermal heating effects on AuNPs and its medical applications
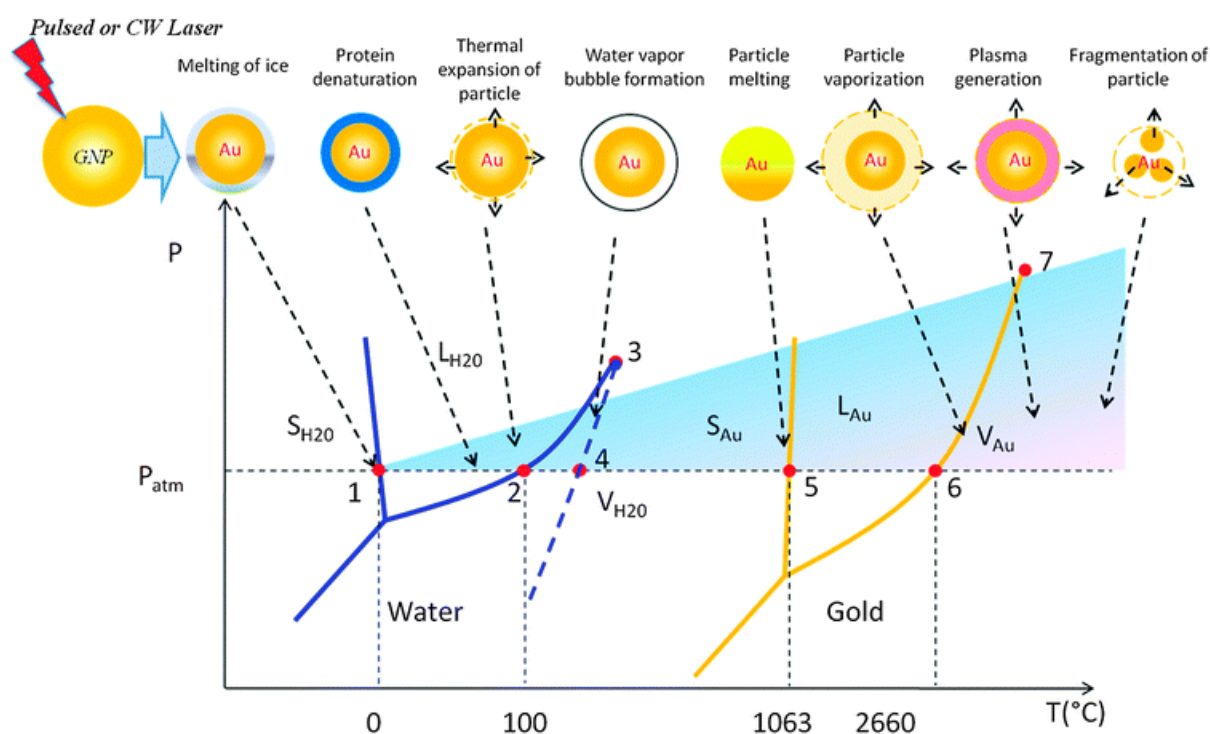
Figure 2.15: The phase diagrams of water and gold and the corresponding thermophysical effects of gold nanoparticles upon photothermal heating as the laser power is increased from left to right. The equilibrium thermodynamic states of water and gold are displayed as solid lines, with each thermodynamic state, solid (S), liquid (L) and vapour (V) displayed for both materials. The non-equilibrium spinodal curve of water is depicted by the blue dashed line. The blue slope indicates the rise in pressure surrounding the gold nanoparticle as the laser intensity is increased. Reproduced with permission.[163] Copyright 2011, Royal Society of Chemistry.

The laser irradiation of metallic nanoparticles and the subsequent thermal heating have been shown to produce a wide array of effects, see Figure 2.15. Through control of the energy deposited into the AuNP structure the photothermal heating can achieve temperatures greater than 1000°C on the femtosecond timescale. To provide macroscopic bulk heating of temperatures below 100°C a continuous wave laser may be used to deposit energy into the system such that the system can reach a quasi-stationary temperature, balancing the constant thermal output of the particles with the thermal diffusivity away from the material. Within medical research, bulk photothermal heating has primarily been used for anti-cancer therapies, the fine temperature control afforded by photothermal therapy can elevate the temperature within a tumour to 42-43°C to incite cell necrosis.[164] The high absorption cross-section of AuNRs has made them particularly desirable as photothermal agents in this field, lowering the laser intensities and nanoparticle concentrations to achieve thermal ablation, and have demonstrated anti-tumour photothermal effects *in vivo*.[165–170][166] To achieve temperatures significantly higher than 100°C, nano- or femto-second pulsed-lasers must be used to deposit large amounts of energy. Neodymium-doped yttrium aluminum garnet (Nd:YAG) lasers are the most common pulsed laser used in medical research and are capable of delivering ∼100 mJ typically over 2-10 ns with repetition rates of 10-30 Hz. Using lasers with a pulse width, the duration of an individual pulse, of ≤ nanosecond timescales means that the excitation rate is greater than the thermalization rate of the absorbing material; as such the energy can be dissipated fast enough such that the lattice cannot approach a thermal equilibrium to provide a constant thermal output.[171,172] This means that gold nanoparticles are able generate temperatures of over 1000°C very locally without inducing any bulk heating within the sample. The high thermal gradients can induce interesting effects, such as the creation of photoacoustic pulses and nano- or microbubble generation and cavitation. At temperatures above 100°C AuNPs begin to expand and contract creating stress that is dissipated into the surroundings as a pressure wave.[173] This effect has been utilised as a medical imaging technology whereby the acoustic wave generated by the AuNP propagates through the soft tissues before detection using an ultrasound transducer.[174] When the surface temperature of an AuNP is above the spinodal limit of water the liquid in the immediate vicinity to the AuNP is vapourised, creating a thin layer of gas at the AuNP surface.[175–177] This layer forms the nucleus of a nanobubble as further evaporation occurs causing the formation of a transient vapour cavity, the size of which is determined by both the AuNP diameter and the laser fleunce.[178,179] Upon collapse of the bubble a stress wave

is released into the surroundings, the effects of which have been shown to increase the permeability of phospholipid vesicles and mammalian cells.[180,181] As shown by Figure 2.15, through photothermal heating the temperature within an AuNP can exceed the melting temperature of bulk gold, however melting effects of AuNPs have been observed at significantly lower temperatures. This is due to the thermal energy within the lattice surpassing the binding energy between the surface Au atoms allowing migration of said atoms from areas of high curvature to surfaces that are more energetically favourable.[182,183] The high curvature of the hemi-spherical tips of AuNRs are particularly susceptible to such migration effects,[159,184–187] with thermal reshaping of AuNRs observed at temperatures as low as 50°C, however the rate of melting is seen to increase with temperature.[188,189] The melting effects of AuNPs are not just dependent upon the morphology but are also affected by the particle size, larger particles reshape more readily than smaller particles, and the surface coating.[189–191]

2.5   Incorporation of NPs into delivery vehicles

To date, the soft matter drug-delivery systems that have been combined with inorganic NPs for the stimuli-responsive release of cargoes include the liposomes, polymersomes, hydrogels, and hybrids of these systems. This section will describe the methods of NP incorporation into liposomal and hydrogel drug-delivery systems, the factors affecting NP-loading efficiencies, and how the incorporation of NPs within the drug carriers could affect the overall stability and drug release from the delivery systems. Despite the large body of research performed utilising NP-polymersome complexes[192–195] this section will focus on nanoparticle incorporation into liposomes and hydrogel structures due to their prevalence as AMP delivery vehicles compared to polymer vesicles. Each method of production described in this section has been used to demonstrate NP-stimulated release of antibiotics or dyes (Table 2.1).

2.5.1   Liposomes

The use of NPs with liposomes is the one of the most widely investigated among the various antimicrobial delivery systems.[117] As seen in Figure 2.16, the four primary means of NP association with liposomes include: (A) the entrapment of NPs within the lipid bilayer, (B) NP encapsulation within the aqueous core of the liposomes, (C) the adsorption of the NPs onto the lipid bilayer, and (D) the addition of free NPs to liposomes.
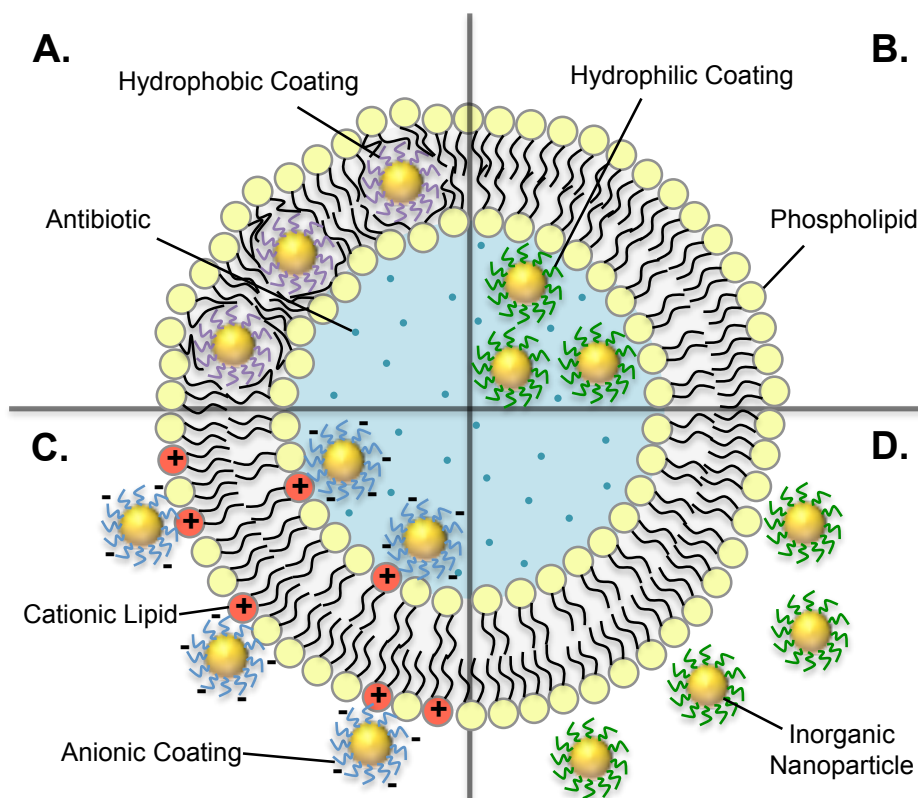
Figure 2.16: The four primary means of inorganic nanoparticle (NP) association with liposomes for the stimuli-responsive release of antibiotics. Inorganic NPs with the indicated surface functionalizations can be incorporated (A) within the lipid bilayer through hydrophobic interactions, (B) within the aqueous core by hydrogen bonding, (C) adhered to the surface of the lipid bilayer through electrostatic attractions, or (D) mixed freely with liposomes.

2.5.1.1   Nanoparticle encapsulation within the lipid bilayer

The lipophilic property of the lipid bilayer core has been utilised to produce liposomes with lipid bilayers containing a variety of hydrophobic NPs, Figure 2.16A.[196,197] The conventional thin-film hydration method is commonly used for the encapsulation of hydrophobic NPs within a lipid bilayer. In this method, a mixture of lipids and hydrophobic NPs is dispersed in an organic solvent, which is evaporated to form a dry lipid film. Subsequently, an aqueous solution is added to the film, causing the spontaneous formation of lipid bilayers. These bilayers often stack to form multilamellar vesicles that can be converted to monodispersed unilamellar vesicles using mechanical agitation involving sonication or extrusion of the mixture through a membrane of predetermined pore size. Another popular route for the encapsulation of hydrophobic NPs within lipid bilayers is the reverse phase evaporation (RPE) process.[198] RPE is performed through the addition of water to an organic solvent containing dissolved lipids and the NPs, before gradually evaporating away the organic solvent to produce lipid vesicles with

the hydrophobic NPs incorporated within the lipid bilayers.[199]

The insertion of a NP within a lipid bilayer has been found to affect the properties of the membrane, which could affect the stability of the drug-loaded liposomes during preparation and storage. The inclusion of hydrophobic NPs within a lipid bilayer could alter the permeability of the membrane depending on whether the temperature is above or below the fluid-gel phase transition temperature (T_m) of the lipids.[200–202] Park *et al.* showed that at a temperature below the T_m (41°C for 1,2-dipalmitoyl-sn-glycero-3-phosphocholine (DPPC)), an increase in the concentration of 3-4 nm hexanethiol-capped Ag NPs added to the lipids (from 0 to 400 ppm), increased the fluidity of the lipid bilayers in the liposomes produced.[200] This was identified through an increase in fluorescence anisotropy values from 0.08 to 0.09 monitored using the fluorescent probe diphenylhexatriene. Above the T_m, however, a decrease in fluorescence anisotropy from 0.106 to 0.097 was observed, suggesting a decrease in the bilayer fluidity. In a subsequent study, the authors incorporated increasing amounts of 3-4 nm Au NPs within DPPC lipid bilayers and observed a consistent trend.[201] A decrease in anisotropy indicates that the bilayer membrane is becoming more disordered and is thus exhibiting more fluid behaviour. The inclusion of both Ag and Au NPs therefore appears to stabilise lipid bilayers at above the T_m and decrease the stability below the T_m.

2.5.1.2 Nanoparticle encapsulation within the aqueous core of the liposome

Hydrophilic NPs are typically incorporated within the aqueous core of liposomes via the thin-film hydration method, which involves the re-hydration of a lipid film with an aqueous solution containing the NPs to induce liposome formation.[203,204] This method of bulk liposome production suffers from high polydispersity and low encapsulation efficiencies, and as such new techniques have been developed to overcome these issues. The RPE method for instance, can produce liposomes with aqueous volume to lipid ratios that are 30 times higher than those produced through lipid film hydration and sonication,[205] and has therefore been used to maximise NP encapsulation within the aqueous compartments of liposomes.[206] As the aqueous core of the liposome offers a large volume for the encapsulation of NPs, a wide variety of NP morphologies can be held within the liposome. Lajunen *et al.* demonstrated this through encapsulating both Au nanostars (60 nm in diameter) and nanorods (25 nm by 60 nm) within DPPC/1,2-distearoyl-*sn*-glycero-3-phosphocholine (DSPC) and DPPC/1-stearoyl-2-hydroxy-*sn*-glycero-3-phosphocholine (LysoPC)/1,2-distearoyl-sn-glycero-3-phosphoethanolamine-N-[methoxy(polye thy-

lene glycol)-2000] (DSPE-mPEG2k) liposomes.[206] However, the encapsulation efficiency of the NPs was not quantified in this study, with changes in the UV-vis spectra provided as the only evidence for successful NP encapsulation. The application of near infrared (NIR) radiation to the thermosensitive liposomes initiated a photothermal response, causing a temperature increase that led to the phase transition of the lipid bilayer to a leaky liquid crystalline phase inducing leakage of the fluorescent reporter molecule calcein. The indiscriminate nature of encapsulation allows for a wide range of NPs with distinct properties to be chosen for specific applications. For example, in the light-stimulated release of therapeutics, the liposomal encapsulation of anisotropic Au NPs such as Au nanorods, Au nanostars, and Au nanoprisms with strong absorbance in the NIR region, where tissues and biological fluids minimally absorb, allows for deeper light penetration through human tissues.[207–209] However, further technique development is required to provide confidence in the encapsulation of anisotropic NPs, as there is little direct evidence, through TEM imaging, to indicate that large scale uniform incorporation of the NPs into the liposomes has been achieved.

The encapsulation efficiency of NPs within the aqueous cores of liposomes has been found to be greatly dependent on several factors such as the total amount of lipids used and the initial amount of NPs added to prepare the liposomes.[203,204] Wijaya and Hamad-Schifferli systematically varied the amount of lipids and NPs used in the preparation of liposomes via the RPE method to investigate lipid-NP phase behaviours.[203] When the DPPC lipid concentration was fixed between 23-27 mg ml^{-1}, a step-wise decrease in the concentration of 12 nm Fe_3O_4 NPs (from 105 to 12 mg ml^{-1}) resulted in morphological changes from a mixture of perforated bilayer/NP-loaded vesicles to empty/NP-loaded vesicles, before finally yielding spherical high density NP-loaded vesicles. In a subsequent study by Bealle et al., it was demonstrated that by using an even lower lipid concentration of 2.5 mg ml^{-1} (DPPC/DSPC 90/10 mol%), the addition of increasing amounts of γ-Fe_2O_3 NPs (from 3 to 313 mg ml^{-1} in iron content) progressively led to the formation of more spherical liposomes that were more densely packed with magnetic NPs as seen under the transmission electron microscope (TEM).[204] This study also stated that the NP size affects the packing density within the liposome, as ascertained using the magnetophoretic mobilities of individual liposomes. The volume fractions of encapsulated 7 and 9 nm diameter NPs were 33±3% and 24±4%, respectively. However, the initial concentration of NPs added during liposome formation was not provided. Taken together, these studies demonstrate that the concentrations of both the lipid and NP used in the formulation of the

liposomes must be optimised to give efficient NP encapsulation.

2.5.1.3 NPs adsorbed onto the liposome bilayers

Another route for NP-liposome association is the adsorption of hydrophilic NPs onto the inner or outer lipid bilayer-aqueous interface of the liposomal structure, Figure 2.16C. This process has been achieved through the electrostatic interactions that occur between oppositely charged lipid bilayers and NPs as well as through the direct synthesis of NPs on the bilayer surface.[210–214] The adsorption of charged NPs on the outer surface of liposomes provides an additional benefit of increasing liposomal stability due to electrostatic repulsions between NP-decorated liposomes of the same charge, which prevents liposomal fusion.[215–218] Phosphatidylcholines, which possess a zwitterionic headgroup containing a negatively charged phosphate and a positively charged choline, are the most commonly used lipids used to form liposomes. Despite the net neutrality of the headgroup, there is a dipole, allowing the electrostatic attraction of charged nanoparticles.[215,219] The positive charge at the terminus of the phosphatidylcholine lipid headgroup results in anionic NPs being more greatly attracted to zwitterionic lipid bilayers than cationic NPs. For the stabilisation of liposomes, however, it has been suggested that the weakly binding cationic NPs are preferable due to the reduced likelihood of NPs forming strong bridges between adjacent liposomes, hence reducing the clustering and fusion of the liposomes. This has been examined through the use of single particle diffusion to observe the motion of 1,2-dilauroyl-*sn*-glycero-3-phosphocholine (DLPC) liposomes stabilised with cationic and anionic polystyrene NPs.[216] It was found that liposomes stabilised with anionic NPs on the outer surface tended to form large dense lipid clusters in which the individual liposomes were unable to move, whereas liposomes stabilised with the same ratio of cationic NPs retained their diffusivity, hence indicating enhanced colloidal stability. However, as the zeta-potentials of the NPs were not provided, the difference in binding strengths may have been due to the difference in NP charge densities.
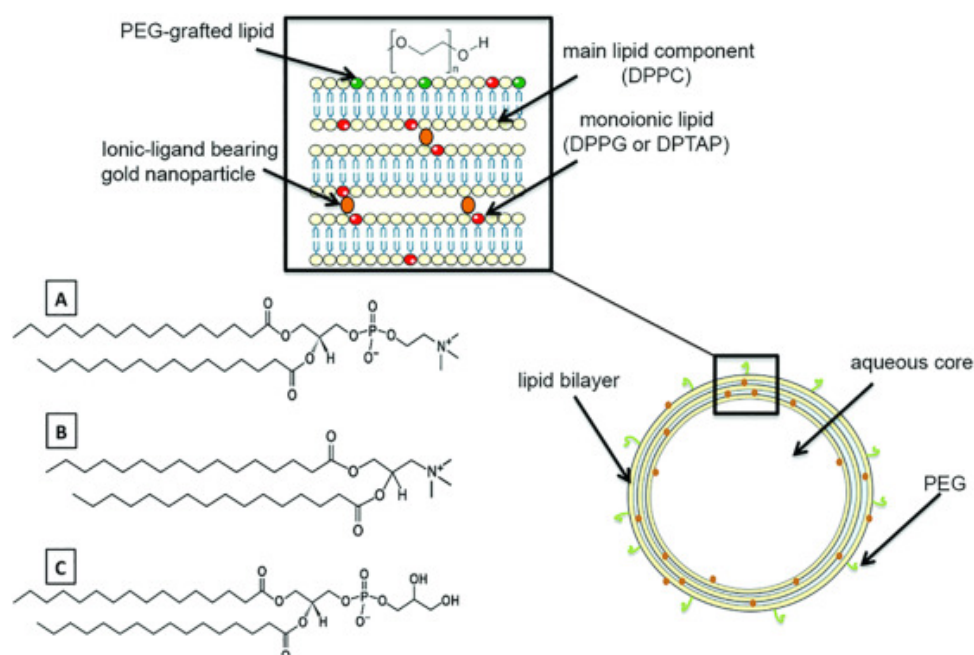
Figure 2.17: Liposome-NP colloid formed via electrostatic interactions between oppositely charged lipids and Au NPs at the aqueous–bilayer interface within a multilamellar structure (inset). The lipid structures presented are A) DPPC, B) DPTAP, and C) DPPG. Reproduced with permission.[220] Copyright 2017, Elsevier.

Dichello et al. also explored the use of electrostatic interactions between oppositely charged NPs and lipids within a liposomal formulation to incorporate Au NPs at the bilayer-aqueous interfaces on the inside of the liposomes, Figure 2.17.[220] Briefly, the liposomes were formed using the RPE process where an aqueous dispersion of the NPs is added to the lipids dissolved in an organic solvent, which is evaporated before sonication and extrusion of the mixture to form homogenous unilamellar vesicles with NPs adsorbed to the inner surface of the liposome. Interestingly, the encapsulation efficiency of cationic 2-dimethylaminoethanthiol (DMET) coated Au NPs in anionic liposomes (DPPC: DPPG; molar ratio 6.1:0.7) determined using microwave-plasma atomic emission spectroscopy was found to be significantly higher compared to the encapsulation of anionic 2-mercaptoethanesulfonate (MES) coated Au NPs within cationic liposomes [DPPC: 1,2-dipalmitoyl-3-trimethylammonium-propane (DPTAP); molar ratio 6.1:0.8] with encapsulation of 7.3±2.6% vs. 3.1±1.5% of the initial gold added, respectively. In another approach by Volodkin et al., the addition of pre-aggregated Au NPs to positively charged carboxyfluorescein-loaded liposomes was used to form liposome-NP complexes with strong NIR absorbance.[221] After laser irradiation, an increase in the fluorescent signal was observed under the confocal laser scanning microscopy, which indicates lysis of the liposomes and release of the fluorescent dye. In contrast, the liposome-NP complexes formed from the addition of

single non-aggregated AuNPs to dye-loaded liposomes did not give any dye release upon laser irradiation due to the poor absorbance of the single AuNPs in the NIR region.

The surface decoration of liposomes with NPs may also be achieved through the selective reduction and deposition of metal atoms at the liposome surface.[213,214,222–225] Rengan *et al.* utilised DSPC/cholesterol (8:2 molar ratio) liposomes as a template for the deposition of a layer of gold via the reduction of Au^{3+} ions by ascorbic acid.[213] Following irradiation with a 750 nm diode laser (650 mW) for 15 mins, the Au-coated calcein-loaded liposomes released 85% of the encapsulated dye, as opposed to 10% release without the Au NP coating. Irradiation for 30 mins showed complete liposome degradation producing 5 nm Au NPs, which can be excreted by the kidneys by virtue of its size. A similar approach was also employed in another study, where the liposomes were coated in a layer of poly-L-histidine which is capable of chelating metal ions, before the addition of the Au salt and the reducing agent hydroxylamine.[222] This produced complete Au coverage over the liposome forming a nanocontainer. The structural integrity of the nanocontainer was enhanced by the gold shell as observed by negligible leakage of encapsulated carboxyfluorescein after 24 days. The nanocontainers appeared stable under laser irradiation at 4 mJ cm^{-2} independent of the laser wavelength used. However, at laser powers greater than 4 mJ cm^{-2}, the nanocontainers degraded; with maximum dye released observed upon irradiation using a 20 mJ cm^{-2} laser.

2.5.1.4 Free nanoparticles added to liposome dispersions

Lastly, the co-administration of free NPs with drug-loaded liposomes represents the simplest means of utilising NPs for stimuli-responsive drug delivery as this can be achieved simply through the mixing of preformed liposomes and NPs.[180,226] Liposomes can also be designed to further augment their cargo release efficiency in response to an external stimulus. In the study by Guo *et al.*, the thermoresponsive poly(N-isopropylacrylamide-co-butylmethacrylate) (PNIPAM-BMA) copolymer was adsorbed onto the surface of calcein-loaded DPPC liposomes and mixed with Au NPs to provide 'on-demand' release of the cargo through a thermally induced two stage mechanism.[226] Under NIR irradiation, the heat generated by the Au NPs first causes contraction of the adsorbed PNIPAM-BMA polymers to give the first stage of membrane disruption and dye release below the T_m DPPC (41°C). As the temperature increases above T_m, the permeability of the phospholipid bilayer is enhanced as it undergoes solid gel-to-liquid crystal transition, thereby giving rise to the second stage of dye release.

Whilst the addition of free NPs to liposomal dispersions has shown promise for the light acti-
vated release of cargoes, the proximity of the NPs to the drug carrier has been found to greatly
influence release efficiency. Wu *et al.* investigated the use of hollow Au nanoshells (HGNs) that
were encapsulated within, tethered to, or freely dispersed in the liquid medium with DPPC
liposomes for the triggered release of encapsulated carboxyfluorescein via transient microbubble
cavitation-induced membrane disruption following irradiation with femtosecond pulses of NIR
light.[180] When the HGNs are irradiated with a pulsed laser, a temperature gradient is formed
around the HGNs which induces the formation of microbubbles that grows and collapses to
provide transient mechanical disruption of lipid membranes. For the most efficient membrane
permeabilization by light-induced microbubble cavitation, the HGNs must be at an optimal
distance from the lipid membrane. It was found that the HGNs directly tethered to the li-
posomes via a thiol-PEG-lipid linker provided the most efficient release of carboxyfluorescein
(93%), followed by the encapsulated HGNs (71%), and lastly the free HGNs (35%) after pulsed
laser irradiation.

2.5.2 Hydrogels incorporating NPs

NP-incorporated hydrogels are commonly prepared either by the direct addition of an aque-
ous NP dispersion to the polymer mixture before gel formation, or through the re-hydration
of a preformed dehydrated gel using a NP dispersion allowing NP diffusion into the swelling
polymer matrix, with both methodologies providing entrapment of large masses of NPs.[227,228]
An alternative means of NP incorporation into a hydrogel is through the synthesis of particles
within the network. This is commonly performed by the absorption of a metal salt solution
within a gel before addition of a reducing agent. Gupta *et al.* incorporated SPIONs into a
hydrogel through the hydration of a poly(vinyl alcohol)-g-poly(2-hydroxyethyl methacrylate)
(PVA-g-PHEMA) based hydrogel in a solution containing a mixture of ferrous and ferric salts
(0.5 and 0.6 M respectively).[229] The swollen gel was then dried at room temperature before
being placed into a 10% v/v NaOH or NH_4OH alkaline solution causing the precipitation of
magnetite NPs. Depending upon the PVA-PHEMA ratio, the SPIONs accounted for 6-15% of
the total mass of the gel. Metal ions can also bind with carboxyl groups loaded onto polymer
chains forming nucleation sites, where upon introduction of a strong reducing agent, NPs can
grow anchored to the hydrogel network.[230] As such, the dimensions and porosities of the gel,
as well as the concentrations of ions and reducing agents, may be tuned to obtain specific NP

morphologies.[231]
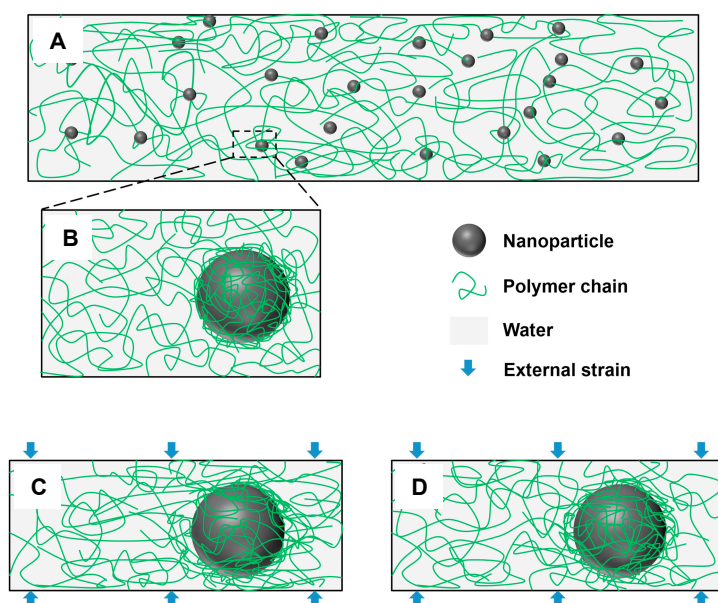
Figure 2.18: Schematic illustrating the effects of compression on the interphase between a NP and a hydrogel. A) NP-loaded hydrogel. B) An interphase is formed around the NP, comprising of a higher polymer density at the NP surface. C) Under instantaneous compression, the polymer density at the interphase is decreased. D) Under sustained compression, the interphase recovers as the gel relaxes with an increased polymer density at the surface of the NP. Reproduced with permission.[232] Copyright 2017, Elsevier.

The incorporation of NPs within a gel network can alter the mechanical properties of the hydrogel. The presence of NPs within a hydrogel causes a dense localised region of entangled polymer chains to surround the NP, known as an interphase (Figure 2.18A and 2.18B).[232,233] The interphase has a heightened hyperelastic stress and increased viscoelastic properties in terms of relaxation time and residual stress retention; as such the interphase will reform under continuous compression (Figures 2.18C and 2.18D). The relaxation time of this interphase is hindered most using high polymer to NP ratios. The increased viscoelasticity allows the production of hydrogels that can be molded under the application of a shear stress and provides rapid self-healing upon the removal of the external stress.

2.5.3   NP incorporated liposome-hydrogel hybrid systems

In addition to the liposomes, polymersomes, and hydrogel systems described earlier, NPs have also been incorporated into hybrid systems comprised of different combinations of materials for the stimuli-responsive release of therapeutics. These systems exploit the advantageous ca-

pabilities of separate materials to further enhance the total therapeutic effects. Gao *et al.* demonstrated the benefits of a dual delivery system by loading cationic liposomes, which are stabilised electrostatically with carboxyl-modified gold NPs, into an acrylamide hydrogel, cross-linked using poly(ethylene glycol) dimethacrylate (PEGDMA).[217] By varying the concentration of the crosslinker PEGDMA, it was found that both the viscoelastic properties of the hydrogel and the gold NP loaded liposome release rate was altered. The NP-adsorbed liposomes would remain stable until encountering an acidic environment triggering NP disassociation from the cationic liposome, allowing the liposome to fuse to an *S. aureus* membrane inducing bactericidal effects. This system therefore provides a tuneable sustained release of both liposomes and NPs, a multi-therapeutic delivery mechanism. Liposomes may also be chemically bonded to the hydrogel network structure providing vesicle lesion upon high shear forces across the hydrogel structure.[234] NP conjugated therapeutics may therefore be encapsulated within the liposomes and would therefore be protected from enzymatic degradation by the hydrogel whilst ensuring low diffusive drug loss.This system therefore provides an adaptable means of delivery of inherently antimicrobial or antibiotic-loaded liposomes for triggered bactericidal effects.

2.6   Light responsive treatments of pathogenic bacteria

2.6.1   Mechanisms for the light-responsive release of antimicrobial agents from NP-incorporated delivery systems
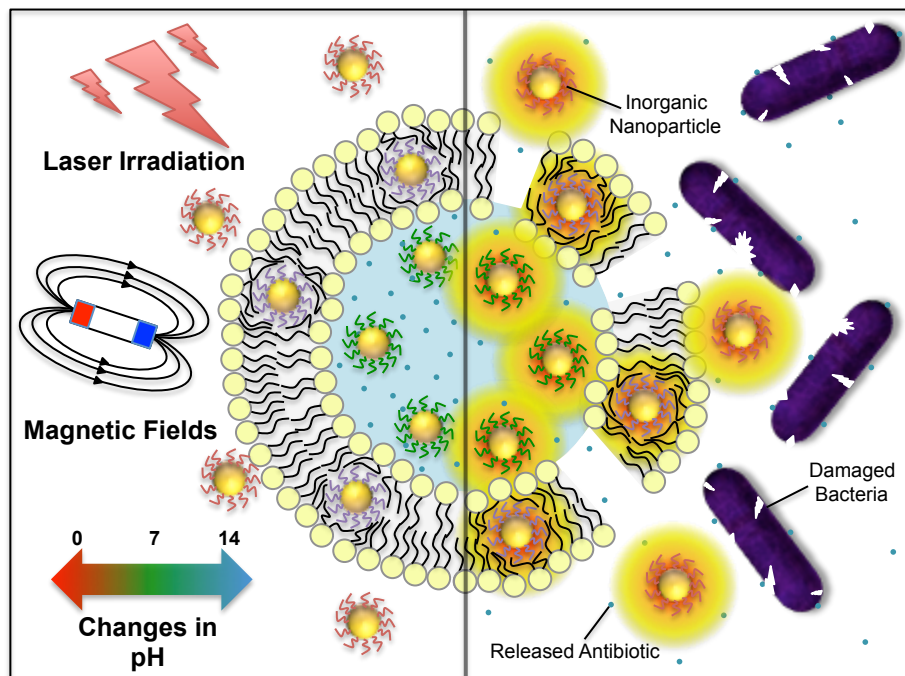
Figure 2.19: Remotely applied or local stimuli that are commonly utilised to induce conformational changes and disruption in the inorganic nanoparticle-associated drug delivery systems, thereby triggering the selective release of loaded antibiotics to combat pathogenic bacteria at infection sites.

The advantage of utilising inorganic NPs as a stimuli-responsive element within drug delivery systems lies in their ease of synthesis and functionalisation, highly tunable optical properties, excellent biocompatibility, and the ease of incorporation into the drug delivery systems. These aspects avoid the need for often complicated and costly synthetic protocols to impart stimuli-responsive moieties to lipids and polymeric systems. The incorporation of NPs into delivery systems is also useful to trigger the release of antimicrobials for sustained or instantaneous release during infections, Figure 2.19. AuNPs have been utilised to provide delivery antibiotics and fluorescent dyes in response to light, magnetic fields and changes in pH, as described in Table 2.1. However, discussion is restricted to triggered release due to photothermal heating and bubble cavitation effects.

Table 2.1: Inorganic NP-incorporated systems demonstrating NP-stimulated release of antibiotics or dye molecules.

Delivery system	NP location	NP type	Trigger mechanism	Released molecule	Ref.
Liposome	Within the bilayer	AuNP	Photothermal	Calcein	235,236
		SPION	Magnetothermal	Calcein	194
		AuNP	Bubble cavitation	Calcein	237
	Within the aqueous core	AuNP	Bubble cavitation	Allophycocyanin & R-phycoerythin	238
		Au nanorod	Photothermal	Calcein	206,239
		AuNP	Photothermal	Calcein	240
	Adsorbed onto the surface	AuNP	Photothermal	Fluorescein	241
		AuNP	Photothermal	Carboxyfluorescein	222
		AuNP	pH-responsive	Doxycyline	210
		Au nanocage	Bubble cavitation	Carboxyfluorescein	180
		Au nanoshell	Photothermal	Fluorescein	223
		AuNP	Photothermal	Carboxyfluorescein	221
	Free with dispersion	AuNP	Photothermal	Calcein	226
Polymersome	Within the bilayer	AuNP	Photothermal	Sulforhodamine & 8-hydroxyl-1,3,6 -pyrenetrisul acid	194
		AuNP	Photothermal	Lysozyme	242
		SPION	Magnetic field	Methicillin	243
		SPION	Magnetothermal	Calcein	244
		AgNP	Photothermal	Ofloxacin	245
Hydrogel	In the network	SPION	Magnetothermal	Ciprofloxacin	229,246
		SPION	Magnetothermal	Vancomycin	247,248

The unique optical properties of inorganic NPs have been respectively harnessed for the photothermal release of therapeutics from drug delivery systems due to the ease of achieving selective disruption of the drug carriers by the external application of a laser. The generation of heat from activated inorganic NPs incorporated within the drug delivery systems also enhances the antibacterial efficiency of the delivered antibiotics through synergistic thermal ablative effects.[223,249]

Photothermal heating can be used to deposit thermal energy to a localised area or throughout the drug carrier, thereby causing the destruction of the encapsulating material to trigger release of the loaded therapeutics.[223,244,250] An early demonstration on the use of photothermal effects to release antibacterial agents from drug carriers was shown by Radt et al.[242] In their study, lysozyme crystals and 6 nm Au NPs were embedded within a polyelectrolyte shell built from the layer-by-layer deposition of negatively charge poly(sodium 4-styrenesulfonate) and positively

charged poly(allylamine hydrochloride). The capsules were first irradiated with a 10 ns pulsed laser (λ = 1064 nm) at 50 mJ cm^{-2} for 5 mins at a frequency of 10 Hz before being added to a suspension of *Micrococcus lysodeikticus.* Due to the release of lysozymes from photothermally degraded capsules, rapid bacterial digestion was observed, with an associated decrease in the extinction value at, 450 nm, decreased from 0.8 to 0.3 within 50 min, indicating a significant decrease in bacterial viability. The extinction spectra for the photothermally degraded capsules were identical to that obtained for the mechanically crushed capsules, hence indicating highly efficient photothermal-mediated release of lysozymes from the capsules. In contrast, no changes in the extinction spectra were observed for the non-irradiated mixture of intact capsules. In another approach, Ag NPs were embedded within a poly(butyl methacrylate-co-acrylamide-co-methacrylic acid) hydrogel to provide controlled release of the model antibiotic ofloxacin following irradiation with a 405 nm laser for 15 s at the 10, 30, and 50 min mark after the start of the experiment.[199] After 70 min, a significantly higher amount of ofloxacin (> 80% of total mass) was found to be released at both pH 7.4 and 1.2 when compared to the non-irradiated samples. The enhanced drug release was attributed to the cross-linked polymeric hydrogel system swelling as the temperature rose above its volume phase transition temperature after laser irradiation.

Transient optically induced photothermal effects have also been exploited for the mechanical disruption of drug carriers through micro- or nano-bubble cavitation without the involvement of bulk heating.[194,222,241] In the study by Wu *et al.*, femtosecond pulsed laser irradiation of liposomes encapsulating hollow gold nanoshells (HGNs) or mixed with free HGNs triggered the release of encapsulated carboxyfluorescein above a threshold of ~1.5 W cm^{-2} without the induction of permanent liposomal damage or drastic temperature increases to the bulk solution, thus suggesting that the triggered dye release occurred due to transient cavitation effects.[180] The authors suggested that at sufficiently high temperatures, the water molecules surrounding the HGN vaporise to form a gaseous cavity that violently expands and collapses, analogous to the transient cavitation effects of microbubbles in response to applied ultrasound.[251–253] The collapse of the vapour bubble subsequently emits a shock wave that propagates through the surrounding medium to transiently disrupt liposome membranes thus releasing the encapsulated cargo. This theory was further supported by the lack of dye release seen when a continuous wave laser was used to irradiate the HGN/liposome complexes even at a high power density of 89 W cm^{-2}. Under continuous wave irradiation, HGNs are always near thermal equilibrium with

the surrounding medium and are therefore unable to generate the thermal gradient required for bubble cavitation.

2.6.2   AuNP mediated photothermal killing of bacteria

Recently, several studies have been published describing the photothermal treatment of bacterial infections. For decades photothermal and photodynamic therapies have been in development for the treatment of cancerous tumours, however in response to the growing demand for alternative treatments to combat AMR, research focus has shifted to the photothermal treatment of bacterial infections. Heat can kill bacteria through disruption of the cell membrane, melting fatty acids and denaturing proteins,[254] and as of yet little to no resistance to photothermal treatment has been observed in bacteria.[255] Due to the substantial array of studies in this field discussion will concentrate only the photothermal treatment of bacteria using AuNPs, however alternative nanoscale photothermal agents comprised of alternative metals/metallic compounds,[6,256–263] photoactive polymers[7,264–269] and carbon structures[270–276] have all demonstrated antimicrobial efficacy.

Although there are several studies employing free AuNP suspensions to cause thermal bacteria killing[277–280] the most common means of utilising AuNPs to incite antimicrobial photothermal heating is through the adsorption of the photothermal agent to the bacteria prior to irradiation. A growing number of studies have adapted the AuNR surface coating to provide electrostatic attraction to bacterial membranes only in an acidic infection environment.[8,281–283] Hu *et al.* (2018) developed a polydopamine (PDA) coated gold AuNR system functionalised with glycol chitosan (GCS), and loaded with DAP, DAP-GCS-PDA@AuNRs, to provide synergistic photothermal and chemotherpeutic antimicrobial activity, Figure 2.20.[284] GCS has a variable charge depending on the pH, such that upon entering the acidic infection environment the polymer becomes positively charged providing electrostatic attraction toward the anionic components in the bacterial membrane. The charge between the chitosan molecules causes electrostatic repulsion, extending the polymer chains and partially releasing some of the DAP. This demonstrated antimicrobial activity against MRSA, the effects of which were augmented through irradiation at the AuNR plasmonic peak (0.5 W cm^{-2} at 808 nm for 7 mins). *In vivo* testing of subcutaneous abscesses inoculated with MRSA showed that the dual photothermal and chemotherapeutic approach resulted in a 98.5% reduction in bacterial colonies, whereas the pH-triggered release of DAP (DAP-GCS-PDA@AuNR + pH 6.3) and photothermal heating (GCS-PDA@AuNR +

NIR) antimicrobial effects alone resulted in 35% and 50% bacterial reductions respectively. The *in vivo* testing of an equivalent GCS-PDA@AuNR system loaded with Ag^+ ions (Ag^+-GCS-PDA@AuNRs) demonstrated the same synergistic antimicrobial effect upon NIR irradiation resulting in a 0.9% bacteria survival rate, a statistically significant decrease compared to the individual photothermal (GCS-PDA@AuNR + NIR) and Ag^+ ion (Ag^+-GCS-PDA@AuNRs + pH 6.3) treatments, survival rates of 37.9% and > 70% respectively.[285]
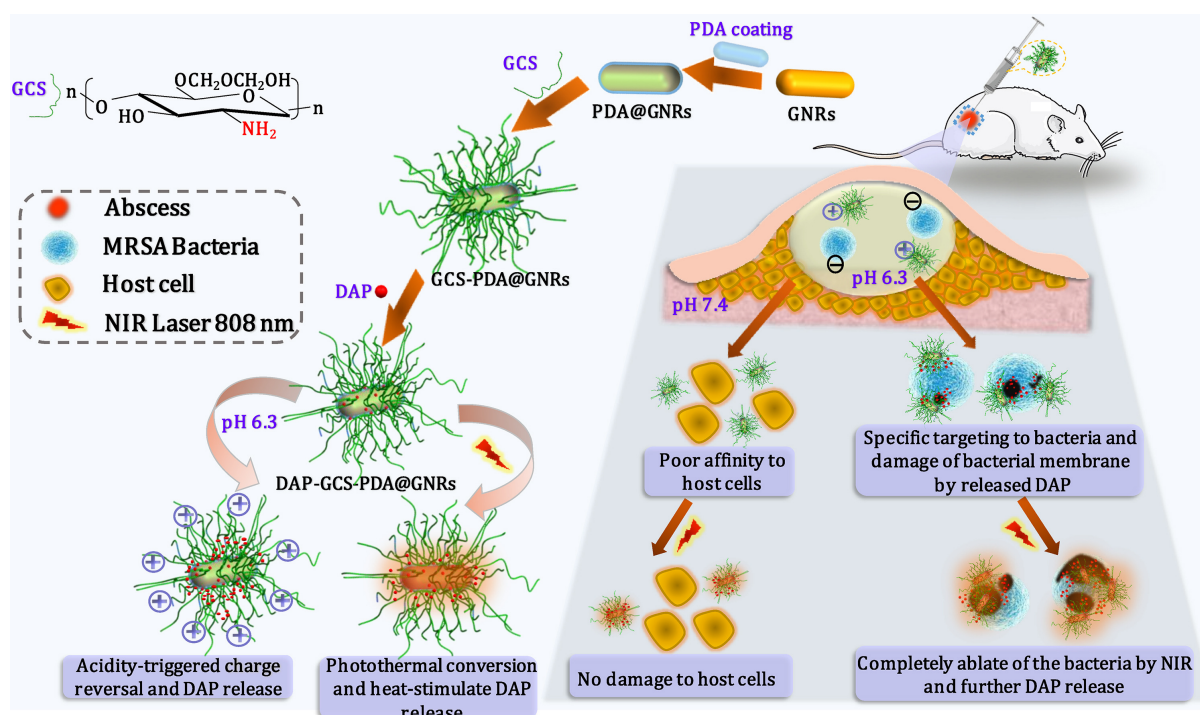
Figure 2.20: Schematic representation of the step-by-step functionalisation of gold nanorods (GNRs) with polydopamine (PDA) and glycol chitosan (GSC) before loading the structure with daptomycin (DAP). The multi-stimulus responsive DAP release is then depicted, with acidic environments (pH = 6.3) and NIR irradiation (0.5 W cm^{-2} at 808 nm for 7 mins) induced heating causing conformational changes in the GSC, allowing DAP diffusion into the surrounding region. The intention of this system is to provide a two-step antimicrobial action, the initial pH change from an infectious environment will not only release DAP but create a positive charge on the GSC providing electrostatic attraction to anionic bacteria membranes, at which point NIR radiation is applied to incite photothermal bacteria killing. Reproduced with permission.[284] Copyright 2018, Applied Materials Today.

Rather than simply relying on electrostatic interactions for targeting many recent studies have demonstrated active targeting using biological materials such as DNA,[286] antibodies[249,287–291] and antibiotics.[292,293] In 2009 Huang *et al.* developed an iron oxide-gold (Fe_3O_4@Au NP) loaded "Nanoegg" that possessed both photothermal and magnetic capabilities.[293] The Nanoeggs were functionalised using vancomycin to target the D-Ala-D-Ala moieties of peptides residing within the bacteria walls. Upon the application of a magnetic field the bacteria covered in Nanoeggs

aggregated at which point NIR radiation (250 mW cm^{-2} at 808 nm for 5 mins) was applied to produce photothermal killing at 60°C. Interestingly, all bacteria exhibited a decrease in the survival fraction upon NIR irradiation in the aggregated state compared to being free in suspension. A novel approach for the active targeting of AuNPs to bacteria by adapting phage therapy was demonstrated by Peng *et al.* through the conjugation of AuNRs to the thiol modified bacteriophage, M13KE-SH.[294] Bacteriophages are viruses that specifically target bacteria with no known effects upon mammalian cells.[74] As such, AuNRs will readily bind to the thiol groups of the filamentous bacteriophage creating a "phagorod" complex (Figure 2.21A). Transmission electron microscopy (TEM) images of the phagorod show the targeting and aggregation of AuNRs on the membranes of *E. coli* bacterium whereas the AuNRs alone show no specific interaction, Figures 2.21C and B respectively. The high specificity of the Phagorod targeting was demonstrated by treating a *P. aeruginosa* biofilm grown in the presence of the epithelial Madin-Darby Canine Kidney II (MDCKII) cells. MDCKII cells and the *P. aeruginosa* biofilm were sequentially cultivated into a well plate, before additional of the Phagorods and irradiation for 10 mins (3 W cm^{-2}, 808 nm) heating the sample to ~75°C. Using a SYTO9 and propidium iodide (PI) live/dead assay, a reduction of ~98% in the bacteria viability was observed (2.21D and E), whereas there was only a ~16% decrease in the MDCKII viability, demonstrating the specificity of the AuNR binding. Interestingly, the photothermal effects also destroyed the the phage base eliminating the possibility of phage reproduction and reducing the risks over the dosage control, a factor hindering clinical translation.[295]
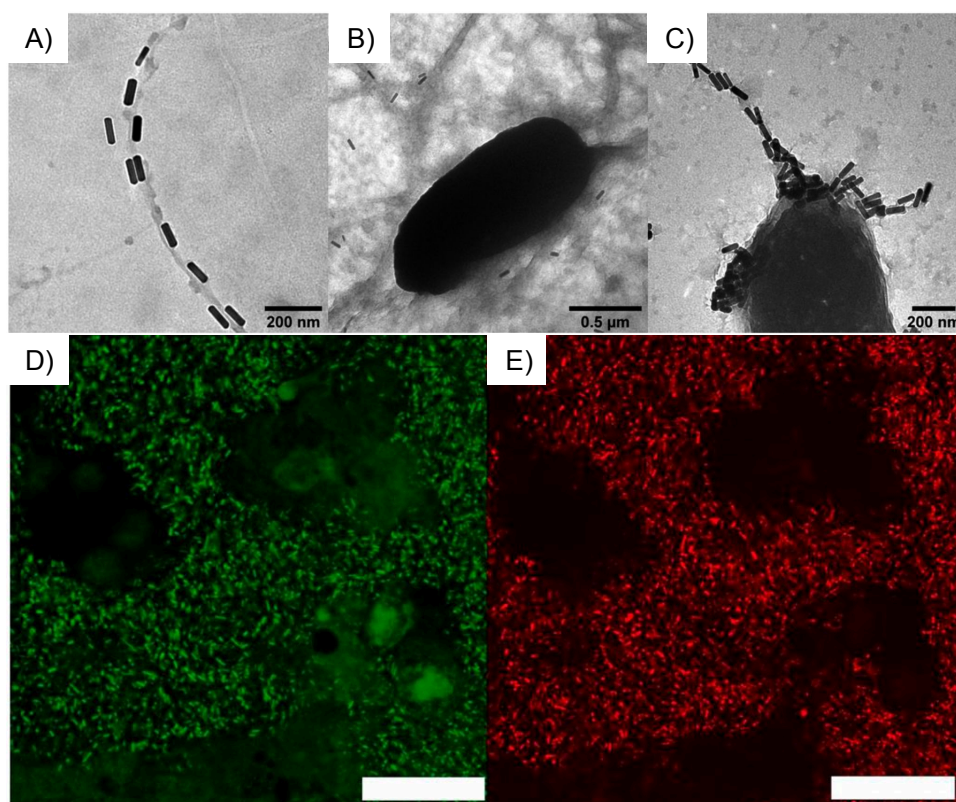
Figure 2.21: TEM images of A) AuNRs adhered to the bacteriophage (M13KE-SH) as it forms a filament B) AuNRs mixed with *E.coli*, and C) M13KE-AuNRs binding to the bacterium. D) and E), fluorescence microscopy images of a *P. aeruginosa* biofilm grown on epithelial Madin-Darby Canine Kidney II cells, before and after treatment with M13KE-AuNRs and NIR irradiated for 10 mins (3 W cm^{-2}, 808 nm). Bacteria were stained with a SYTO9 and propidium iodide (PI) Live/dead assay, to identify the ratio of live (green) and dead (red) cells.(scale bar: 30 μm). Adapted with permission.[294].

Antibody functionalised particles have also demonstrated a synergistic photothermal bactericidal effect whilst providing triggered delivery of antibiotics. Meeker *et al.* synthesised gold nanocages (AuNCs) functionalised with DAP (DAP@AuNCs).[249] The irradiation of AuNCs (1.67 W cm^{-2} at 808 nm for 10 mins) in the presence of a *S. aureus* resulted in an instantaneous reduction of bacterial viability below the plate reader sensitivity (20 CFU ml^{-1}), however after 24 hours the bacteria concentration rebounded to that of the untreated control, indicating incomplete bacterial eradication. Irradiation of the bacterial sample containing Dap@AuNCs however produced instantaneous bactericidal effects with a complete 6-log reduction observed with no viable bacteria detected after 24 hours, indicating that the photothermal and antibiotic effects worked synergistically. This construct was also applied to LAC (a stain of MRSA) in both planktonic and biofilm forms. Complete bactericidal effects were observed against the planktonic LAC immediately after irradiation with no bacteria growth over 24 hours. LAC biofilms

exhibited initial photothermal resistance with only a 4-log reduction, however complete bactericidal effects were observed after 24 hours. The addition of the staphylococcal antibody aSpa onto the AuNC surface enabled targeting that increased the immediate photothermal bactericidal effects by inducing a complete 7-log reduction in bacteria viability within the biofilm. Zhang *et al.* showed a similar synergistic effect through the loading of kanamycin (kana) into hollow spherical AuNPs functionalised with the imaginatively named anti-*E.coli* antibody.[288] *E. coli* suspensions treated with the hollow AuNPs irradiated for 10 mins (200 mW cm^{-2} at 650 nm), kana alone and irradiated kana-loaded hollow AuNPs exhibited bacterial survival rates of 90%, 87% and 50% respectively.

Recently there has been growing interest in loading AuNRs into hydrogel systems to formulate potential wound dressings that provide light-responsive antibacterial properties.[10,296–298] The first instance of antimicrobial AuNR-gels was demonstrated by Jo *et al.* whom loaded CTAB-stabilised AuNRs into an alginate gel.[296] The incorporation of the AuNRs into the gel did not affect the optical properties of the particles and exhibited photothermal heating to 50°C in 30 s and 70°C after 90 s under NIR irradiation (0.45 W at 808 nm). Using the live/dead stain SYTO 9, a 60% decrease in *E. coli* viability within a biofilm was observed after only 30 seconds of irradiation, however there was no increase in antibacterial activity for longer irradiation times. This was attributed to the decreasing thermal profile within the biofilm, with the majority of the viable bacteria located in the furthermost region from the AuNR-gel. The affects of the heating on the bacteria membrane are clearly observed when imaging using scanning electron microscopy, with bacteria within thermally treated biofilm exhibiting significant blebbing and vesiculation (Figure 2.22B) compared to the smooth membranes of bacteria in the untreated biofilm (2.22A). The experiment was replicated using Alamar blue to determine the metabolic activity of the biofilm after photothermal treatment. After 30 s irradiation a 25% reduction in bacterial metabolic activity was observed, rising to 84% after a 60 s irradiation. This is significantly higher than the 60% reduction in *E. coli* viability depicted by the SYTO 9, which relies on membrane disruption to induce the colour change, indicating that the antimicrobial activity of photothermal heating is not solely through membrane damage. AuNRs have also been incorporated into clinically approved gels. Al-Bakri and Mahmoud loaded phospholipid (DSPE-PEG-SH) AuNRs into a Pluronic® F127 gel, a block co-polymer used in novel drug delivery systems and tissue engineering.[10,299] Under laser irradiation (3 W cm^{-2}, 805 nm for 15 mins) the gel exhibited heating to 62°C using 0.125 mM AuNRs. The heating

demonstrated a 4.5-log reduction in *P. aeruginosa* CFUs in a biofilm. The AuNR-gels have also demonstrated antimicrobial efficacy *in vivo*. Abdou mohamed *et al.* loaded mPEG-SH AuNRs into a thermosensitive n-vinylpolycaprolactam polymer that provided a photothermal mediated increase of 30°C under laser irradiation (0.65 W cm^{-2} at 785 nm). Upon testing on planktonic bacteria a difference in the thermal sensitivity between Gram-negative and Gram-positive bacteria was observed, with 94-96% reductions in the viability of Gram(-ve) *E. coli* and *Acinetobacter baumannii*, and a 65% reduction in the Gram(+ve) *Enterococcus faecalis*. *In vivo* testing performed by placing the AuNR-gel in direct contact with a biopsy punch on the dorsum of a murine model inoculated with 1–2 × 10^6 CFU of *E. coli*, demonstrated a 98% reduction in bacteria viability upon laser irradiation for 40 mins (ΔT = 30°C). The treatment showed no detrimental affects on the wound healing process with complete re-epithelialisation occurring in the same time frame as the non-infected wounds.
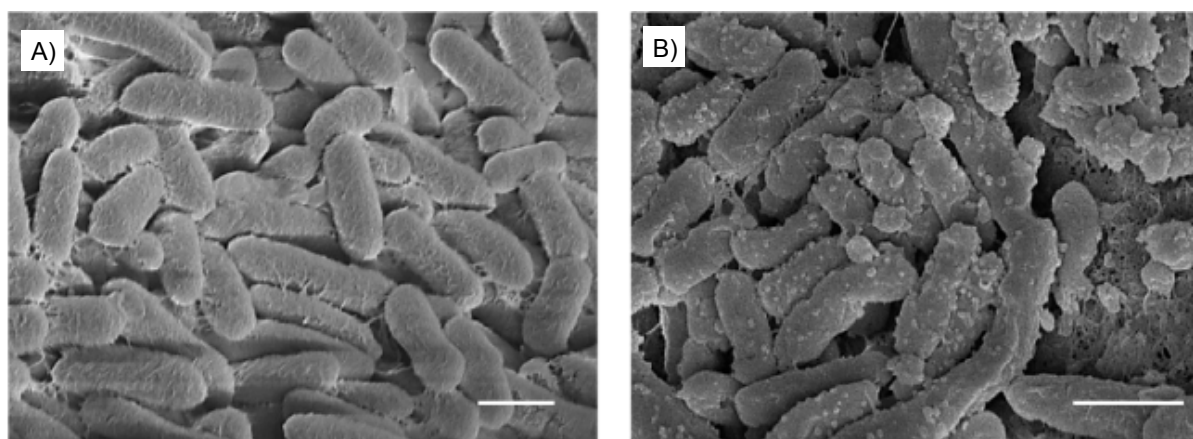
Figure 2.22: Scanning electron microscopy micrographs of *E. coli* biofilms A) without and B) with photothermal heating from an AuNR-loaded alginate gel (0.45 W, 808 nm for 30 s). Scale bars are 1 μm. Adapted with permission.[296] Copyright 2013, IOP Publishing.

Biofilm formation on the surface of medical devices/implants has been identified as a leading cause in nosocomial infections.[300,301] As such, AuNPs have also been utilised to provide photothermal antimicrobial activity on functionalised surfaces to denote the potential for implementation on surgical apparatus. Khantamat *et al.* demonstrated this by binding gold nanoshells onto a poly(amidoamine) dendrimer coated polydimethylsiloxane (PDMS) surface. An *E. faecalis* biofilm was then grown on to the Au nanoshell coated surface, achieving ∼70% coverage before irradiation for 10 mins (2.5 W cm^{-2}, 810 nm) heating the surface to 73°C and resulting in complete bacteria eradication. Yang *et al.* used electrostatic attraction to deposit positively charged cetrimonium bromide (CTAB) stabilised AuNRs onto a treated titanium surface after

the layer-by-layer addition of cationic 3-aminopropyltrimethoxysilane and anionic poly(styrene) sulfonate.[302] Laser irradiation at 0.5 W cm^{-2} (808 nm for 20 mins) heated the sample to 49°C, which is lower than the temperatures required for thermal ablation in the majority of studies but still resulted in antibacterial rates of 62%, 67%, 26% and 32% against *E.coli, P. aeruginosa, S.aureus* and *S. epidermidis* respectively. Similarly, Au nanostars (AuNSs) bound to glass surfaces using a 3-mercaptopropyl-trimethoxy silane coating have demonstrated a >90% *S. aureus* cell reduction from a biofilm upon irradiation for 30 mins (0.12 W cm^{-2}, 808 nm).[303] de Miguel *et al.* took this one step further by demonstrating the first instance of antimicrobial photothermal heating from a medical implant that is currently on the market; adhering citrate-stabilised AuNRs onto a polypropylene monofilament surgical mesh from B. Braun Surgical, S.A. (Optilene Mesh LP), that is widely used in hernia repair.[304] The AuNRs adhesion was performed by oxygen plasma activation of the polypropylene mesh that was dipped into pure ethylene diamine to coat the surface in activated amine-groups that, upon submersion in the AuNR solution, anchor the particles to the mesh. As shown in the Figure 2.23A inset, the AuNRs display a homogeneous distribution on the mesh surface with no substantial aggregation after drying. A *S. aureus* biofilm was grown onto the mesh, Figure 2.23B, before irradiation at fluences of 12-16 J cm^{-2} for 40, 100 or 300 ms. Irradiation at 14 J cm^{-2} in 40 ms resulted in a 99.4% biofilm reduction, 15 J cm^{-2} in 100 ms a 99.3% reduction and 16 J cm^{-2} in 300 ms a 99.5% reduction. Despite the deposition of higher energies the bactericidal activity was unaffected, meaning either that the rate of energy deposition is more important than the total energy deposition or that the thermal or that there was no substantial difference in the heating profiles between pulses of 14 J cm^{-2} in 40 ms and 16 J cm^{-2} in 300 ms. The bacteria were also treated with a live/dead stain for quantification of the cell viability, when irradiated at 14 and 15 J cm^{-2} for 300 ms. Control samples, Figure 2.23C and F, showed thick biofilms on the mesh surface with no decrease in viability, whereas the sample irradiated at 14 J cm^{-2} (Figure 2.23D and G) showed an increase in the proportion of dead bacteria but a significant decrease in the total number of bacteria. The sample irradiated at 15 cm^{-2} (Figure 2.23E and H) showed even fewer bacteria adhered to the mesh, but a lower proportion of dead bacteria, Figure 2.23I. The decrease in bacteria is attributed to the biofilm desorption from the mesh surface due to the thermal denaturation of adhesive exopolysaccharides. As such, the proportion of dead bacteria is not decreased with increasing fluence from 14 to 15 J cm^{-2}, as the dead bacteria are more likely to have been removed from the mesh than the live bacteria.
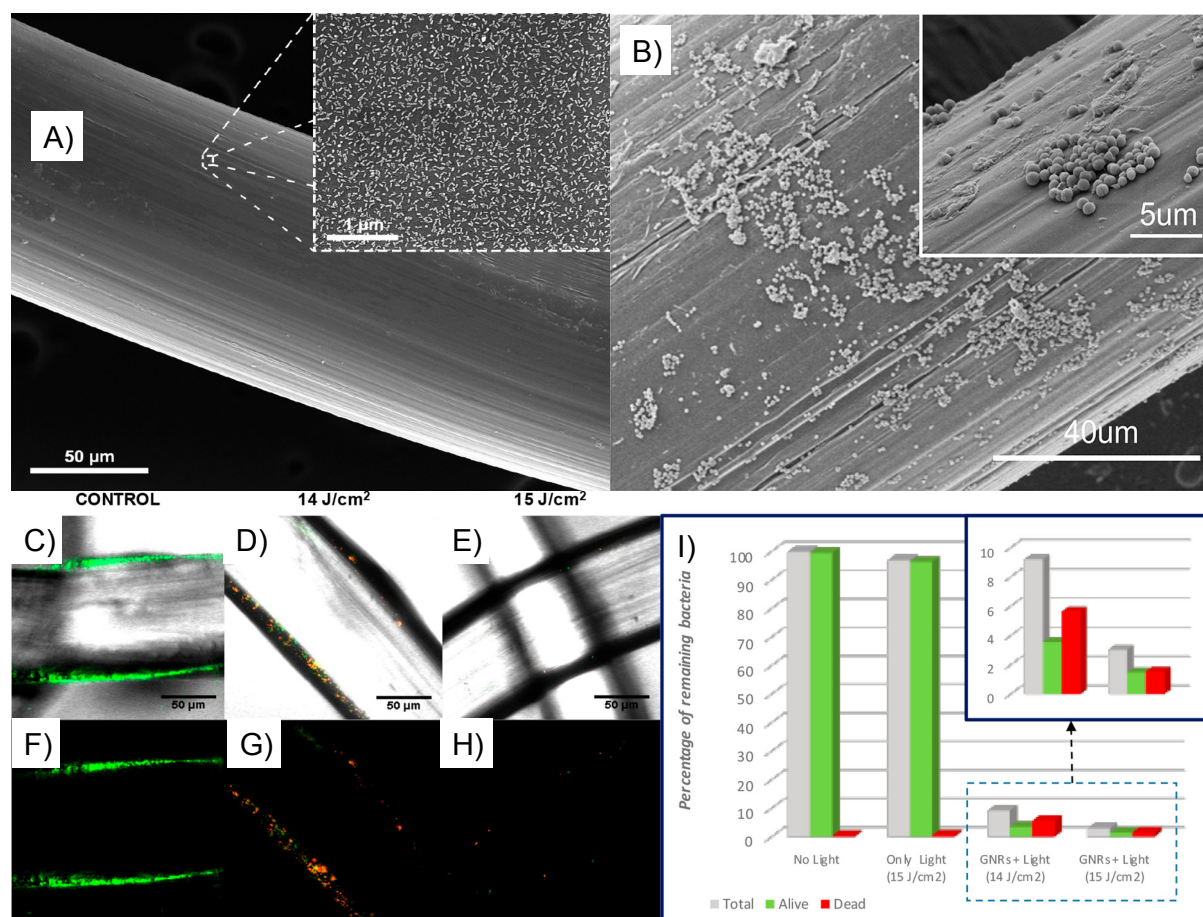
Figure 2.23: Scanning electron micrographs of a polypropylene monofilament surgical mesh from B. Braun Surgical, S.A. (Optilene Mesh LP), coated in A) citrate-stabilised AuNRs and B) a *S. aureus* biofilm. C-H) Fluorescence confocal microscopy images of the mesh surface with bacteria labelled using a live/dead stain (green/red colouration). Bright field images (C-E) are included above the fluorescence images (F-H) to clarify the positions of the mesh, scale bars are equal to 50 μm. Images are of a control mesh with AuNRs but no irradiation (C,F), and meshes irradiated for 300 ms at laser fluences of 14 and 15 J cm^{-2} (D,G and E,H respectively). I) The total percentage of bacteria remaining on the mesh after irradiation, compared to the non-irradiated control, and the proportions of the remaining bacteria that are alive and dead. Adapted with permission.[304] Copyright 2019, American Chemical Society.

The recent advances in the photothermal treatment of pathogenic bacteria indicate that this chemotherapeutic free approach to infection management has the potential for clinical usage. Furthermore, the photothermal enhancement of classical antibiotic efficacy is an exciting prospect that could enable a reduction in the drug dosage required for treatment, possibly reducing the risks of resistance development. This therefore offers two significant pathways for future research; demonstration of reduced resistance in combination chemo-photothermal therapies, and investigating whether photothermal therapies can be used in conjunction with antibiotic alternatives (AMPs, bacteriophages) to further reduce the risks of resistance development. The

work covered in this thesis will attempt to answer the latter question by analysing the whether photothermal bacteria killing can compliment the antimicrobial capabilities of AMPs.

Chapter 3

Experimental techniques

3.1 Lipid preparation and liposome fabrication

Upon arrival, lipids were dissolved in chloroform before aliquoting into 200 mg ml^{-1} glass vials. The chloroform was then extracted by drying under nitrogen for one hour, until an opaque lipid film was formed on the walls of the vial. These vials were stored in a -80°C freezer until use, at which point the lipids were resuspended in chloroform. To fabricate multilamellar lipid vesicles (MLVs), lipids were mixed in the desired proportions and added to a round bottom flask. Lipid mixtures were always prepared in relation to the molar percentage (mol%) of each lipid required within the liposome bilayer. The chloroform was then evaporated through drying under nitrogen for an hour. Next, the flask was added to a water bath, preheated to 10°C above the gel-fluid phase transition temperature of the most abundant lipid, before the addition of an aqueous solution and left to gently mix for an hour. The MLVs were homogenised through extrusion by passing the sample through a 0.4 μm polycarbonate membrane 11 times, the extruder was preheated to the same temperature as the water bath.

3.1.1 Fabrication of calcein loaded liposomes

Calcein loaded liposomes were fabricated through the hydration of the lipid film using a solution of 0.1 M calcein dissolved in phosphate buffered saline (PBS). The liposomes were subsequently extruded at above the gel-fluid phase transition temperature and placed in a fridge at 4°C. A Sephadex G-50 size chromatography column was prepared by mixing the Sephadex G-50 powder with Milli-Q at 10 mg ml^{-1}, before 10 ml of the suspension was added to an empty

filtration column. Bubbles were removed from the column by firming striking the tube with a spatula, before being left to rest for two hours. PBS was then gently flowed through the column until twice the volume of the column had passed through the gel. The calcein-liposome suspension was then added to the surface of the gel and was gently eluted using PBS. When the solution exiting the column became slightly coloured, the solution was then collected in 0.5 ml increments.

3.1.2   Fabrication of AMP loaded liposomes

IK8 loaded MLVs were fabricated as previously described with the hydrating solution comprised of IK8 dissolved in PBS, Figure 3.1. After extrusion the liposomes were placed in a fridge at 4°C. A 15 kDa regenerated cellulose Spectra/Por membrane was left to hydrate in Milli-Q water for 30 mins before the liposomes were added to the dialysis membrane. The sample was then added to a 2 litre bucket of Milli-Q and left to dialyse for 48 hours. The water was replaced after 2, 18 and 26 hours. The liposome sample was then removed from the dialysis membrane and added to an eppendorf to be stored at 4°C.
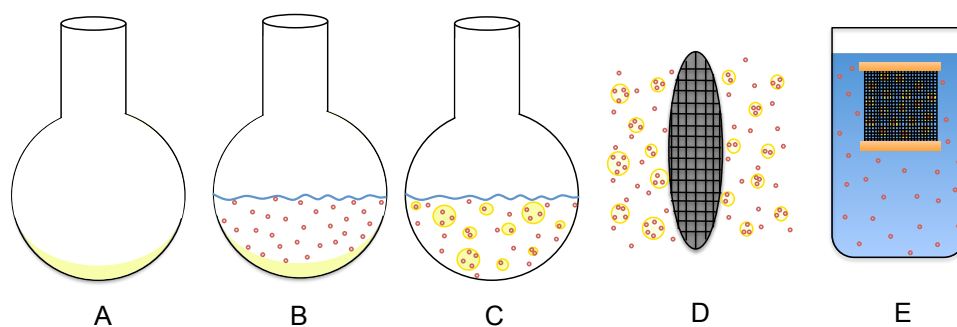
Figure 3.1: Schematic of liposomes fabrication using a lipid-film hydration and cleaning protocol. A) Formation of a thin lipid-film in a round bottom flask, by nitrogen drying lipids dissolved in chloroform. B) Hydration of the lipid-film using a solution containing the material to be encapsulated. C) Liposomes are formed by gently mixing the solution at above the gel-fluid phase transition temperature of the lipids in solution. D) Liposomes are homogenized using extrusion, whilst heated above the lipid gel-fluid phase transition temperature. E) Unencapsulated materials are removed through dialysis.The sample is placed into a dialysis membrane (pore size > 5 times the material to be removed) and placed into a 2 litre bucket of Milli-Q for 48 hours, replacing the water after 2, 18 and 26 hours.

3.2   Liposome characterisation

3.2.1   Dynamic light scattering

Dynamic light scattering (DLS) was performed using a Zetasizer Nano ZS with a 4 mW He-Ne laser at 633 nm and a measurement angle of 173°. Typically 10 μl of sample was diluted into 1 ml of buffer, or Milli-Q, and analysed within polystyrene cuvettes. Samples were measured thrice and the average size distribution was taken.

DLS is a technique used to determine the size distribution of particles in solution. A monochromatic laser source is used to irradiate the particles creating a scattering pattern, made from the constructive and destructive interference of light from each particle scattering event. As the particles diffuse with Brownian motion the intensity of the scattering pattern fluctuates and information regarding the dynamic motion of the particles is obtained by observing the scattering intensity fluctuations, otherwise known as the autocorrelation function, over time.[305,306]For a monodisperse sample the autocorrelation function, g(t), can be defined as a single exponential

$$g(t) = e^{-q^2 Dt} \tag{3.1}$$

with a time decay that is determined by the translational diffusion coefficient of a particle, D, and the length of the scattering vector q, where $q = \frac{4\pi n}{\lambda} sin\frac{\theta}{2}$.[307] The hydrodynamic radius of the solute, R, can be extracted from this equation by relating the translational diffusion coefficient to the Stokes-Einstein equation

$$D = \frac{k_B T}{6\pi\eta R} \tag{3.2}$$

where k_B is Boltzmann's constant, T is the absolute temperature and η is the viscosity of the suspension medium.

3.2.2   Single particle tracking

Single particle tracking is a technique used to determine the size and concentration of a solute. Unlike DLS that observes ensemble averages, single particle tracking measures the scattering off individual particles and tracks their motion through a medium. As such, a known number of

particles can be analysed within a given volume allowing the calculation of the concentration.

Within this thesis all single particle tracking measurements were performed using a Malvern Nanosight NS300. Samples were diluted 10,000 times in buffer, or Milli-Q, and were inserted into a microfluidic chamber affixed on top of a laser module. The sample was then irradiated with a 50 mW laser at 532 nm, and the scattered light from each particle was observed using a microscope with 20 times objective lens. A 60 second video was then recorded whereby nanoparticle tracking analysis software analysed the Brownian diffusion the particles and obtained the radius from the Stokes-Einstein equation 3.2. The concentration was ascertained by measuring the number of particles that flowed into the imaging area, of known volume, and multiplied by the initial dilution factor. Three videos were taken of each sample from which the average size distribution and concentration were obtained.

3.2.3 Zeta-potential measurements
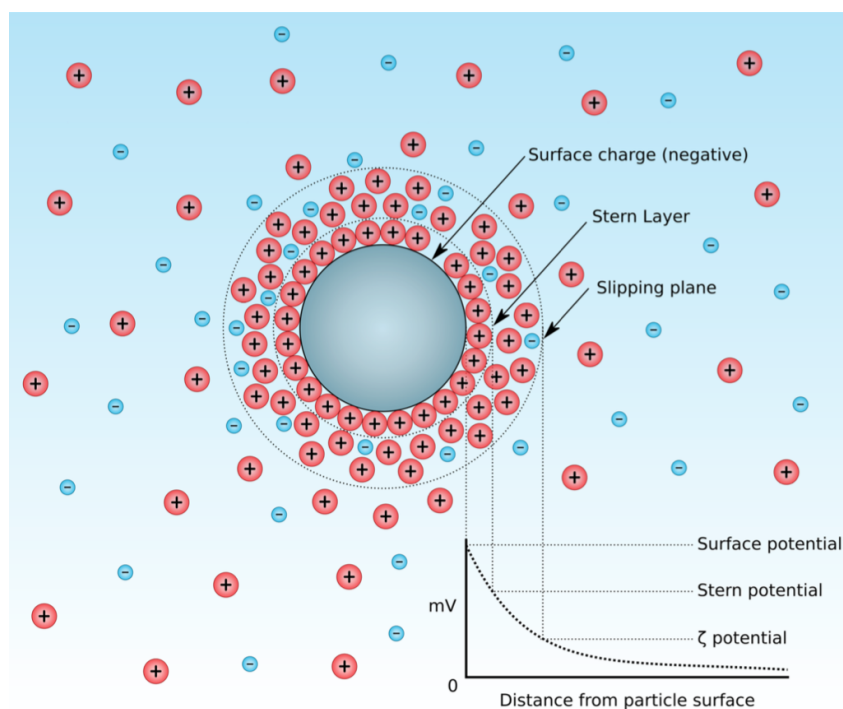
Figure 3.2: A charged particle will attract ions of the opposite charge from within the surrounding medium, binding them tightly to form the stern layer. As the electrostatic attraction decreases beyond the stern layer the density of bound ions decreases to the point at which the ions diffuse freely around the particle, this boundary is the slipping plane. It is the potential at the slipping plane that defines the zeta-potential.[308]

In polar solutions a particle's colloidal stability may be controlled by the surface charge. This is due to the electrostatic repulsion between the particles keeping them dispersed throughout the

medium and inhibiting aggregation or flocculation. The zeta-potential is a means of determining the strength of the electrostatic repulsion between adjacent similarly charged particles and is defined as the potential difference between the dispersion medium and the stationary layer of fluid attached to the particle, Figure 3.2.[309] The zeta-potential is also highly dependent upon the ionic strength and pH of the solution, with each variable potentially screening the the particle charge, hence reducing the zeta-potential, which can cause particle agglomeration. Particles with zeta-potentials greater than $\pm$ 30 mV are generally considered as moderately stable in low ionic strength solutions however these particles may agglomerate over long time periods, particles with charges greater than $\pm$ 60 mV are considered extremely stable and thus can withstand high electrolyte concentrations.[310,311]

Zeta-potentials are commonly determined using electrophoresis, the motion of a dispersion in response to an applied electric field. An oscillating electric field is applied across the dispersion and the particles migrate toward the electrode of opposing charge the velocity of which is proportional to the magnitude of the zeta-potential.[312] The particle velocity is then measured using laser Doppler anemometery, whereby a monochromatic laser beam is used to irradiate the sample, causing Rayleigh scattering that produces an interference pattern. The change in the interference pattern due to the motion of the particles is used to generate a correlation function from which the electrophoretic mobility is calculated. The zeta-potential (ζ) is then extracted using Henry's equation:

$$U_E = \frac{2\varepsilon\zeta f(ka)}{3\eta} \tag{3.3}$$

where U_E is the electrophoretic mobility, ε is the dielectric constant of the medium, f(ka) is Henry's function (k is the debye-length and a the particle radius), and η is the medium viscosity. Henry's function can be assumed to be 1 under the Debye-H$\ddot{u}$ckel approximation (a < 1/k) and 1.5 using Smoluchowski's model (a $\gg$ 1/k).[313,314]

3.2.4   Calcein leakage

Liposome leakage was determined using the fluorescent dye calcein, Figure 3.3A. Fluorescence occurs when an orbital electron of a molecule absorbs a photon causing it to move into a higher energy state, and upon returning to the ground state the electron emits a photon. At

concentrations > 1 mM the innate fluorescence of calcein is self-quenched through excited electron transfer to molecules in the ground state, rather than re-emitting the energy as a photon (See Figure 3.3B).[315,316] Liposomes encapsulating calcein at high concentrations produce very little fluorescence until they leak causing a decrease in the concentration of encapsulated dye and providing a fluorescent response.
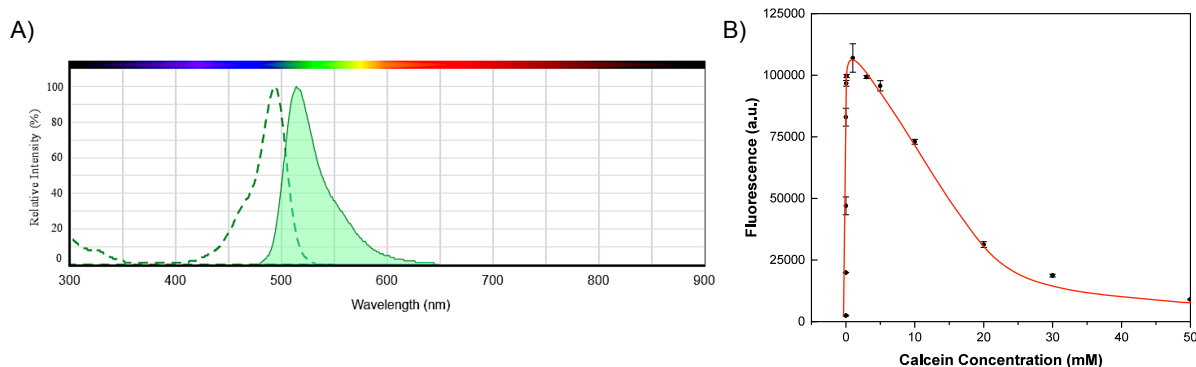
Figure 3.3: A) The excitation (dashed line, peak at 496 nm) and emission (solid line, peak at 515 nm) spectra of calcein.[317] B) The fluorescence of calcein with concentration, demonstrating the self-quenching effects above 1 mM.

Calcein loaded liposomes were diluted 100 times in buffer before addition of 100 μl to an opaque 96-well plate, along with 100 μl of either MHBII, fibroblast growth media or more buffer. The initial fluorescence was measured (EX/EM, 496 nm/515 nm), and the plates were placed in an incubator preheated to 37°C, after which the fluorescence was measured daily. 1% Triton X-100 was added to control wells on day 0 and at the end of the experiment to determine the maximum fluorescence and to ensure the calcein fluorescence was constant. Six replicates wells of each sample were measured. The liposome leakage was calculated using

$$Leakage(\%) = 100 \times \frac{(F_{Sample} - F_{Background}) - (F_{Initial} - F_{Background})}{(F_{Maximum} - F_{Background}) - (F_{Initial} - F_{Background})} \qquad (3.4)$$

3.2.5 Thermally induced calcein release

To determine the thermal release profile, liposomes were heated beyond their gel-fluid phase transition temperature and the proportion of calcein released was quantified. 200 μl of calcein-loaded liposomes, diluted 100 times in PBS, was added to an opaque 96-well plate. The initial fluorescence of the sample was measured before the plate was then placed into an incubator preheated to 25°C. Thermocouples were places into wells containing 200 μl of PBS to observe

the solution temperature. Once the temperature within the wells was within 1°C of 25°C the plate was left for a further 5 mins. The fluorescence was again measured, whilst the incubator temperature was increased to 30°C. The plate was placed into the incubator and once more maintained at within 1°C of 30°C for 5 mins, before again measuring the fluorescence. This process was repeated increasing the temperature in 5°C increments up to 65°C. The percentage of calcein released was calculated using Equation 3.4. 1% v/v Triton X-100 was added to control wells at the start of the experiment, as well as to heated wells at the end of the experiment to provide the total release fluorescence value and to ensure that this value did not change over the course of the experiment.

3.2.6 IK8 encapsulation efficiency

3.2.6.1 High performance liquid chromatography

High-performance liquid chromatography (HPLC) was used to quantify the IK8 concentration. IK8-liposomes were fabricated as described in section 3.1.2. The encapsulation efficiency (EE) of IK8 was determined post dialysis to ensure no peptide external to the liposomes remained. 10 μl of the liposome sample was added to an equal volume of DMSO, to lyse the vesicles releasing the encapsulated IK8, before dilution in Milli-Q to 300 μl. The sample was fed into a 4.6 x 250 mm Insertil ODS-SP column in an acetonitrile gradient (acetonitrile/water ratio at 0.01 mins 13:87, at 10 mins 100/0) at a rate of 2 μl min^{-1}. The column led into a UV-vis spectrometer where the absorbance was read at 220 nm. A peak corresponding to the IK8 was observed after 2.26 mins, Figure 3.4A. The concentration of AMP was determined by integrating beneath the peak and comparing to a predetermined concentration calibration curve, Figure 3.4B. The EE was determined as:

$$EE(\%) = Dilution factor \times 100 \times \frac{M_{Final}}{M_{Initial}} \tag{3.5}$$

where M_{Final} is the final mass of IK8 after dialysis and $M_{Initial}$ is the mass of IK8 used during the hydration of the lipid film.
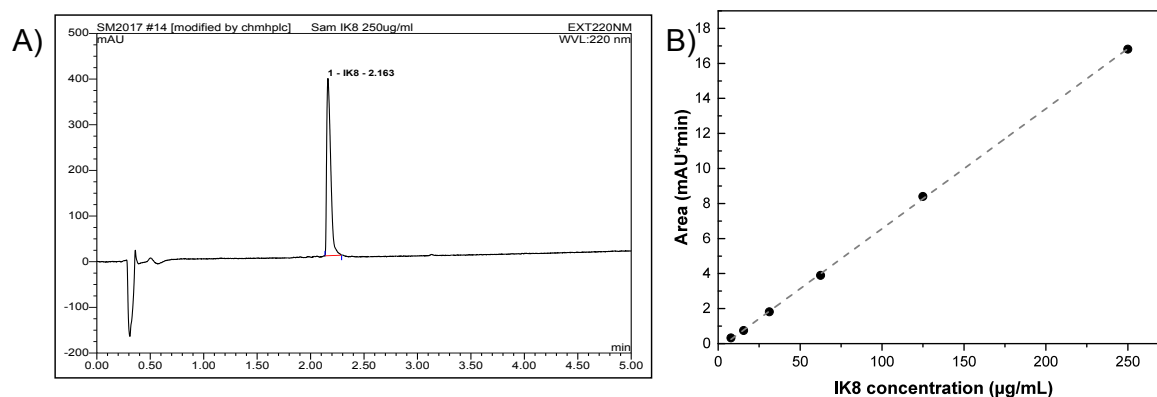
Figure 3.4: A) A HPLC graph used to quantify the concentration of IK8 within a sample. The distinctive peak of IK8 can be seen at 2.26 mins. B) A calibration plot of IK8 obtained using HPLC.

3.2.6.2   Bicinchoninic acid protein assay

IK8 quantification in Chapter **Results chapter 3**, was performed using the bicinchoninic acid (BCA) protein assay. The BCA assay utilises a two stage process to quantify the amount of peptide within a sample.[318] Firstly, Copper(II) sulphate is reduced to Cu^{1+} (cupric cation) by the chelation of the copper with a protein in a basic envronment containing potassium tartare, known as a biuret reaction. The number of cupric cations that form is directly proportional to the quantity of amine bonds between the amino acids of the peptide. The second step of the reaction occurs when two BCA molecules react with a cupric cation to form a structure that absorbs strongly at 562 nm.

The assay was performed by initially mixing Reagents A and B (50:1) of the Pierce™BCA Protein Assay Kit. 175 μl of the assay was then added to 25 μl of the peptide sample in a clear bottomed 96-well plate. The plate was incubated at 37°C for 30 mins before the absorbance at 562 nm was measured. The background absorbance of the assay in the absence of peptides was subtracted from the sample absorbance.

3.2.7   Protection of encapsulated peptides from protease degradation

The efficacy of liposomal protection of encapsulated AMPS from proteolysis was assessed through the addition of protease to solutions containing free IK8 and IK8-loaded liposomes. This protocol was adapted from Banerjee and Onyuksel (2012).[319] 10 μl of trypsin (50μg ml^{-1}) was added to 1 ml of 0.1 mg ml^{-1} of IK8 dissolved in Milli-Q and to liposomes encapsulating

the equivalent mass of peptide. The solutions were then left to incubate at room temperature. After 1 hour 150 μl of the sample was extract and 10 μl of a 40% w/w glacial tricholoacetic acid was added to inactive the trypsin. This was repeated each hour for 5 hours. 5% v/v DMSO was added to the samples containing liposomes to release the encapsulated peptide before the concentration of IK8 remaining was quantified using HPLC, as described in section 3.2.6.

3.3 Gold nanoparticle synthesis

All glassware was cleaned by sonication of a 10% Decon90 solution for 30 mins, followed by a thorough rinsing using Milli-Q water and further sonication of Milli-Q for 30 mins. Additional cleaning was then performed by soaking glassware in aqua regia for 30 mins. Aqua regia is formed by mixing HNO_3 and HCl at a 1:3 ratio. The strong oxidising activity and Cl^- ions dissolve metals removing any remnants of gold that may act as nucleation sites during the reduction of Au^{+3} during the AuNP synthesis. The glassware was then rinsed thoroughly with Milli-Q before being placed in an oven at 80°C overnight. All glassware was allowed to cool to room temperature before any synthesis.

3.3.1 Binary surfactant stabilised AuNR synthesis

AuNRs were synthesised in a large 0.5 l one-pot syntheses. Initially 250 ml of Milli-Q was heated to 70°C using a water bath before the addition of CTAB and NaOL, 48 mM and 12.5 mM respectively, and stirred vigorously until the surfactants were completely dissolved, before allowing to cool to 30°C. The solution was continuously stirred as 250 ml of $HAuCl_4$ (1 mM), 12 ml $AgNO_3$ (4 mM), 2.5 ml HCl (11.8 M), 3.75 ml ascorbic acid (AA, 85.8 mM) were added sequentially, allowing 5 mins of continuous mixing in between addition of each solution. Lastly, the speed of stirring was increased to 1200 rpm and 0.375 ml of ice-cold $NaBH_4$ (10 mM) was rapidly injected. The stirring was stopped immediately and the solution was maintained at 30°C for 4 hours. The binary surfactant stabilised AuNRs were then pelleted through centrifugation at 17,000 g for 30 mins. The supernatant was disregarded and the AuNR pellet was dispersed in Milli-Q. The AuNR solution was then stored in the dark at room temperature.

3.3.2 Replacement of the AuNR binary surfactant coating with a phospholid bilayer

3.3.2.1 PEGylated phospholipid bilayer

Prior to the phospholipid functionalisation of AuNRs a solution containing lipid SUVs was prepared. A lipid mixture of DSPC/DSPE-mPEG2k (95/5 mol%) in chloroform was added to a round bottom flask before removal of the solvent through drying under nitrogen until only a translucent lipid film remained. The thin-lipid film was then hydrated for 1 hour using Milli-Q to produce a MLV solution containing 10 mg ml^{-1} of lipid. The lipid solution was then tip sonicated for 2 hours to produce SUVs which were sized using DLS, and provided the vesicles were > 50 nm they were used for the binary surfactant replacement. 10 ml of binary surfactant stabilised AuNRs at 60 μg ml^{-1}, cleaned once with centrifugation, were centrifuged a second time and the pellet was dispersed in 3 ml of the SUV suspension. The mixture was then placed into a refrigerated bath sonicator for 24 hours. The AuNRs were then centrifugated at 9,000 g for 15 mins and redispersed into 3 ml of a fresh 10 mg ml^{-1} SUV suspension. This process was repeated three times, following the final centrifugation process the pellet was dispersed in Milli-Q. In order to remove excess lipid the NRs were cleaned via centrifugation once more and again dispersed in Milli-Q.

3.3.2.2 Maleimide-functionalised phospholid bilayer

The replacement of the binary surfactant bilayer with maleimide-functionalised phospholipids was performed identically to the PEGylated phospholipid replacement as previously described, however the final round of SUVs were fabricated with 1% of the DSPE-mPEG2k substituted for DSPE-mPEG2k-maleimide.

3.3.3 Polystyrene sulfonate functionalisation of binary surfactant AuNRs

Binary surfactant AuNRs, twice cleaned using centrifugation, at 60 μg ml^{-1} were collated into a 1.5 l beaker and stirred vigorously. An equal volume of 10 mg ml^{-1} polystyrene sulfonate (PSS) dissolved into Milli-Q with 5 mM NaCl was then added to the AuNRs. The solution was then left to mix for 24 hours before centrifugation (9,000 g, 30 mins), removal of the supernatant, and resuspending the pellet in a 1 mg ml^{-1} PSS solution. This was repeated twice with the final pellet resuspended in Milli-Q.

3.3.4   Synthesis of AuNP coated liposomes

The synthesis of AuNP coated liposomes was adapted from work by Rengan *et al.*, as described by Figure 3.5.[213,214] Liposomes were fabricated as described in section 3.1 to ∼350 nm and were diluted to 2 mg ml^{-1} in PBS. 200 μl of the liposome suspension was then mixed with 100 μl of 1-10 mM HAuCl$_4$, before the addition of 400 μl of AA. This produced a rapid colour change that was dependent on the morphology of the NP that was synthesised. The mixture was then left for an hour before cleaning using centrifugation (500 g, 30 mins), the supernatant was removed and the pellet dispersed in Milli-Q.

+ Chloroauric acid
+ Ascorbic acid
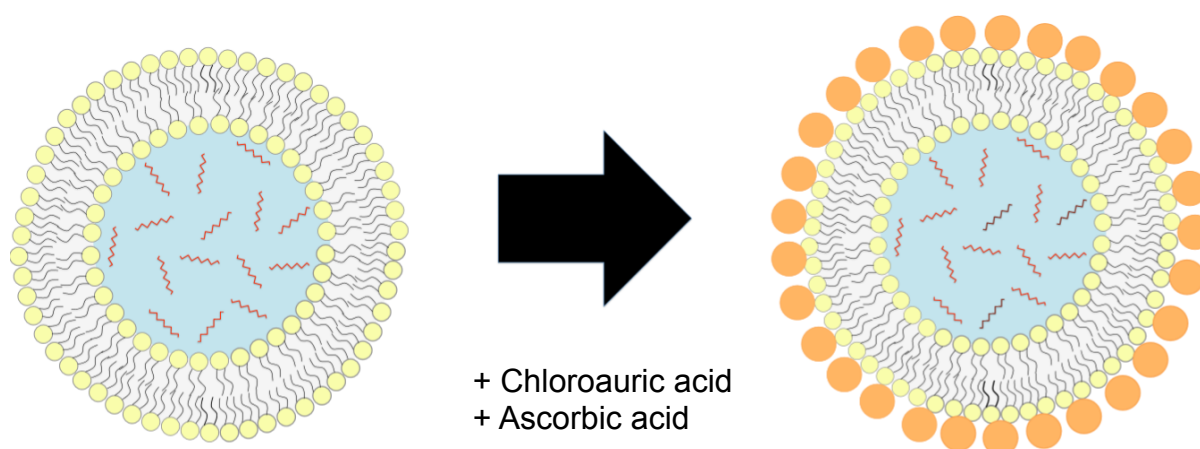
Figure 3.5: A schematic representation of the synthesis of AuNPs onto the surface of a liposome.

3.3.5   Adhering AuNPs to thiolated liposomes

Liposomes were fabricated containing DPPE-Ptd, a lipid molecule functionalised with a sulphur atom to allow the formation of thiol bonds. Liposomes (67/30/2/1 mol%, DSPC/cholesterol/DSPE-PEG2k/DPPE-Ptd) were fabricated to ∼350 nm through thin-lipid film hydration and extrusion through a 400 nm extrusion membrane, as described in section 3.1.2. AuNPs were synthesised by mixing equal volumes of 5 mM HAuCl$_4$ with 5 mM AA in Milli-Q, resulting in a rapid colour change to a deep red. After the colour change equal volumes of the AuNP and DPPE-Ptd suspensions (10 mg ml^{-1}) were mixed and left overnight.

3.3.6   Adhering maleimide-functionalised phospholipid AuNRs to thiolated liposomes

Phospholipid AuNRs functionalised with 1 mol% DSPE-mPEG2k-maleimide (200 μg ml^{-1} of Au), were mixed with an equal volume of liposomes containing 1 mol% DPPE-Ptd (10 mg

ml^{-1}) and left overnight. The following day the solution was centrifuged (9,000 g, 30 mins), the supernatant was disregarded and the pellet suspended in Milli-Q.

3.4 NP characterisation

3.4.1 UV-Vis-NIR spectroscopy

Ultra-violet/visible/near-infra-red absorption spectroscopy was utilised to determine the sample absorption of monochromatic light at wavelengths between 400-1,000 nm. The plasmonic properties of AuNPs provide characteristic absorption spectra that are dependent upon the particle size and morphology, meaning absorption spectroscopy can be particularly useful in giving initial indications of sample quality.

The absorbance spectrum is obtained by varying the wavelength of applied light using a monochromator, and measuring light intensity once it has passed through the sample. The spectrum of a 'blank' well containing only the dispersion medium is simultaneously measured with any sample to provide a background subtraction from the particle absorbance spectrum. Absorbance spectra were obtained using a PerkinElmer Lambda 35 spectrophotometer.

3.4.2 Transmission electron microscopy

Electron microscopy was used throughout this thesis to provide visual identification of AuNPs and liposomes. Electron microscopy was required due to the Abbe diffraction limit restricting the resolution of an optical microscope. This is described using the Abbe equation:

$$d = \frac{\lambda}{2nsin\theta} \tag{3.6}$$

where d is minimum imaging resolution, λ is the wavelength of applied radiation, n is the refractive index of the medium and $sin\theta$ is the angle of convergence. Therefore, for light in the visible wavelengths ($\sim$ 400-700 nm) with a reasonable numerical aperture ($\sim$0.9) the Abbe resolution is in the order of several hundred nanometers, making optical imaging unsuitable for the analysis of nanoscale structures. However, due to particle-wave duality electrons have a De Broglie wavelength, Equation 3.7, which allows for a dramatic reduction in the imaging spot size, circumventing the Abbe resolution limit.[320]

$$\lambda = \frac{h}{mv} \tag{3.7}$$

where h is the planck constant, m and v are the rest mass and velocity of the electron respectively.[321] This means that the resolution of the microscope is governed by the velocity of the electrons.[322] Transmission electron microscopy (TEM) utilises a potential difference to accelerate electrons that are focused to a beam using a pair of condensing lenses. The beam is then trimmed using an aperture before striking the sample. The electrons incident to the sample are scattered by atomic nuclei or absorbed, whereas the other electrons can pass through the grid unimpeded. This creates a 2D rendering of the sample which is captured using a charge coupled device camera.

Throughout this thesis TEM imaging was performed using a Tecnai G2 Spirit TWIN/BioTWIN with an acceleration voltage of 120 kV. Image processing and analysis was performed manually using Fiji.

TEM samples were prepared through the addition of 5 μl of AuNRs ($\sim$600 μg ml^{-1}) in Milli-Q onto a carbon-coated 400-mesh copper grid (Electron Microscopy services, CF400-Cu). The samples were allowed to dry at room temperature before gently blowing across the surface of the grid. The low density of liposomes make visualising them using he TEM can be very difficult, and as such a negative-stain was applied to increase the sample density making the vesicles easier to identify.[323] The liposome samples were diluted 1,000 times before 5 μl was added to the TEM grid and held near a heat source for 30 seconds. The sample was then wicked away using blot paper before 5 μl of 2% uranyl acetate was added to the grid. The negative stain was then immediately wicked away, before this process was repeated thrice with Milli-Q to remove excess stain. The sample was then left to dry at room temperature.

3.4.3   Atomic absorption spectroscopy

Atomic absorption spectroscopy (AAS) uses the unique absorption profiles of atoms in order to both identify and quantify the concentrations of an element within a sample. Gold concentrations were determined using a Varian 240FS atomic absorbance spectrometer (AAS). The NR sample was initially dissolved into aqua regia and diluted in Milli-Q, before being fed into a nebulizer where the solution is vaporised. The sample was then fed into the flame atomizer

fuelled by an air-acetylene mixture igniting a flame with a temperature 2,300°C.[324] Monochromatic light at 242.8 nm, the resonance absorbance wavelength of atomized gold, was shone into the sample and the absorbance was measured. The concentrations of Au within a sample after a AuNR synthesis was determined through comparison to a calibration plot, Figure 3.6.
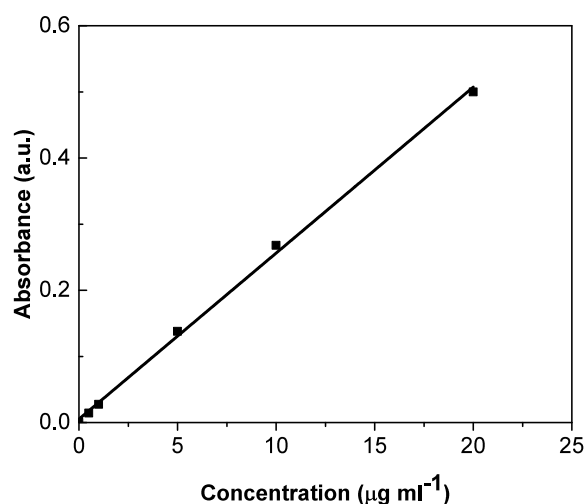
Figure 3.6: The absorbance of increasing concentrations of atomized gold, 0-20 ppm, at 242.8 nm using atomic absorption spectroscopy. This calibration plot of Au concentration was used to quantify the mass of particles after an AuNR synthesis.

3.5   Laser optical set-ups

3.5.1   Continuous wave laser

A custom-made laser rig was designed in order to provide automated irradiation of a 96-well plate, Figure 3.7. The system provided control of the irradiation area through the use of an XY-stage that could move a well plate to align the desired well with the laser beam. The duration of irradiation could also be regulated through the use of a solenoid shutter to block the beam. A cabinet incubator afforded temperature control within the enclosed rig casing to maintain samples at a desired temperature when not under irradiation. The entire path of the beam was enclosed in black piping to ensure there was no chance of potentially dangerous laser exposure.
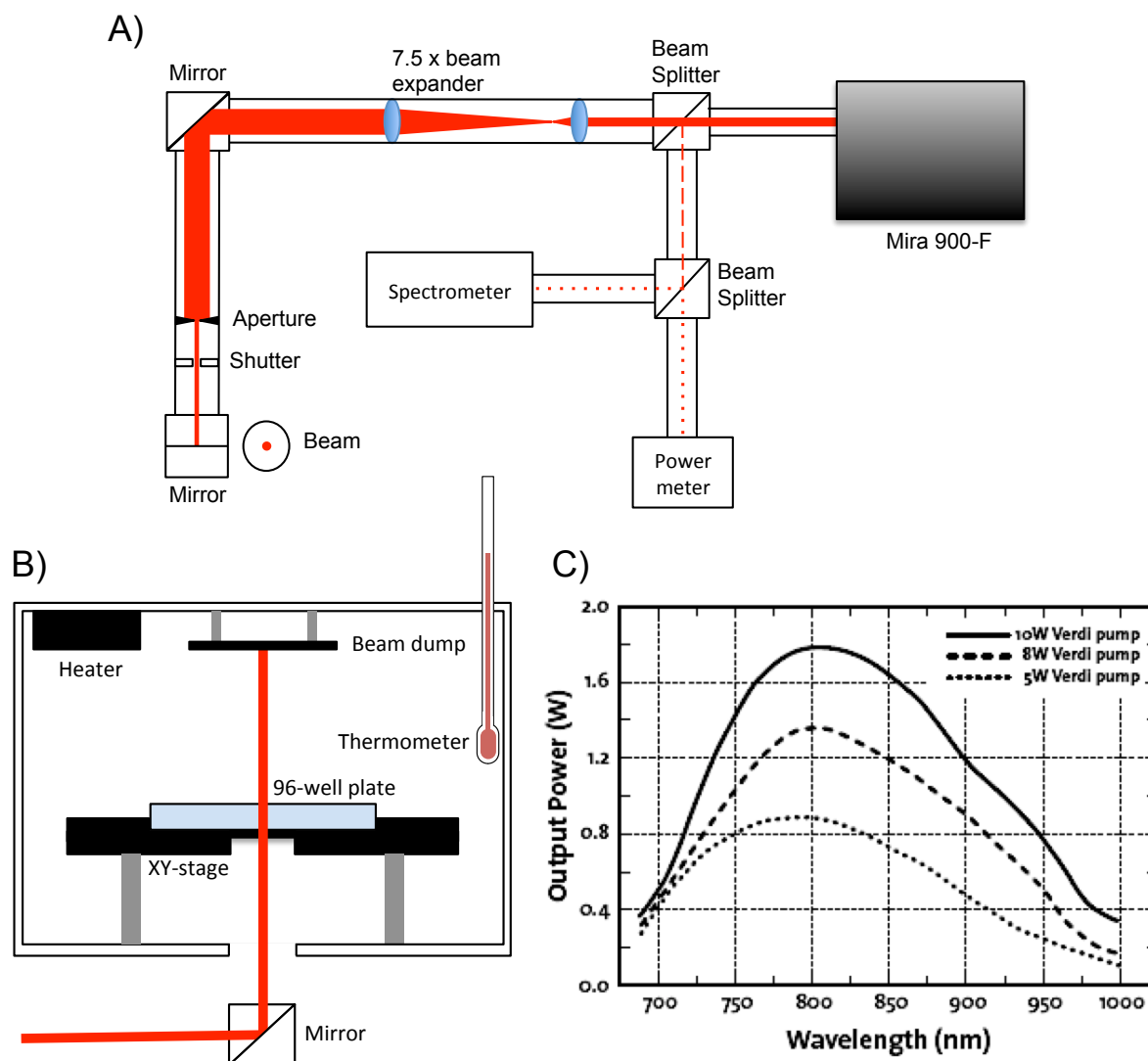
Figure 3.7: A) A schematic representation of the optical set-up directing and shaping the beam into the sample box during photothermal experiments. B) Schematic of the beam as it is directed past the XY-stage, into a 96-well plate before striking the beam dump. C) The maximum power out-put between 680-1,000 nm of the Mira 900-F laser connected to different pumps. The 10 W Verdi pump was used in this laser system.[325]

A Coherent Mira 900-F provided the laser source connected to a 10 W Verdi pump. This Ti:Sapphire femtosecond pulse laser was utilised in a continuous wave mode, with a tunable wavelength between 700–980 nm and a 0.6 mm beam diameter. Upon exiting the laser cavity the beam was passed through a polarised beam splitter where 1% of the beam is redirected to a fibre-coupled Ocean Optics Flame spectrometer and a Thorlabs PM100D power meter with a S120C photodiode power sensor. The remaining 99% of the initial beam was expanded 7.5 times such that the full-width half-maximum of the Gaussian beam intensity was 6 mm, the diameter of a well in a 96-well plate, with the beam periphery removed using a 6 mm aperture. A

solenoid shutter then provided remote control of the beam application to a sample (the shutter was coupled to an interlock to block the beam if the box enclosing the sample was open). A mirror then redirected the beam vertically into the box and into a sample before striking the beam dump attached to the lid of the box. Inside the chamber a Prior H128 motorised XY-stage, fitted with a standard 96-well plate mount, allowed the positioning of a well-plate along the beam path to irradiate a sample. The temperature within the enclosure was maintained at 37°C using a IncuKit cabinet incubator heater, while the temperature within a well-plate was monitored using thermocouples connected to an 8-channel Pico Technology TC-08 Thermocouple Data Logger.

3.5.2 Pulsed laser system

A pulsed laser beam was produced by a Surelite$^{\text{TM}}$OPO Plus neodymium-doped yttrium aluminum garnet (Nd:YAG) laser connected to a 532 nm SL I-10 pump source, Figure 3.8. The beam produced can be tuned between 700-2500 nm with a 10 Hz repetition rate and a 5 nanosecond pulse duration. After leaving the laser cavity the beam was passed into a beam splitter where 10% was redirected into a fibre-coupled Ocean Optics Flame spectrometer. The remaining 90% of the beam passed through a natural density (ND) filter between 0-4, an increase in the ND of 1 will reduce the fluence by 90%. The beam was then passed into a quartz curvette containing the sample, before striking the beam dump at the back of the curvette holder.
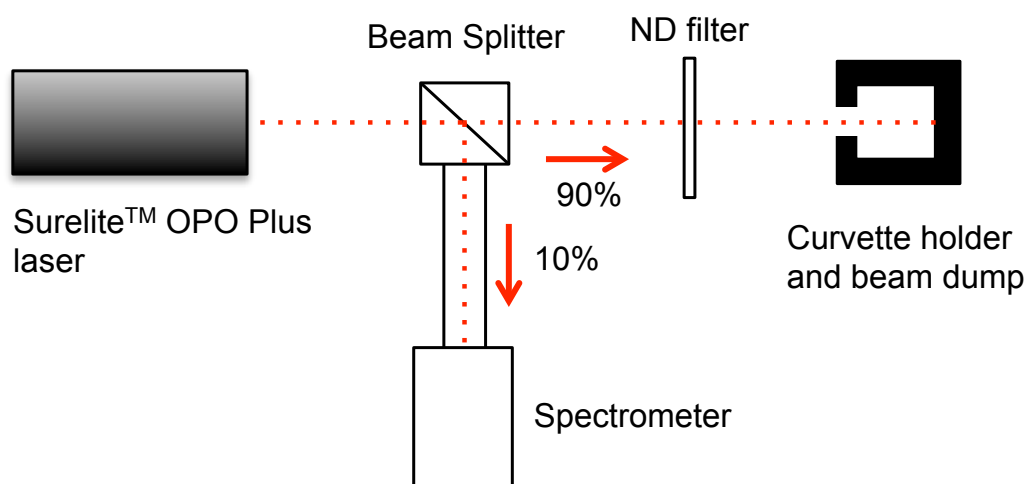
Figure 3.8: Schematic of the optical pulsed laser set-up. A Surelite$^{\text{TM}}$OPO Plus tunable laser was directed into a beam splitter where 10% of the beam was redirected into a spectrometer. The remaining 90% of the beam was then passed through a natural density filter of 0-4 before striking the sample within a quartz curvette that was placed into the holder.

3.6 Hydrogel fabrication and characterisation
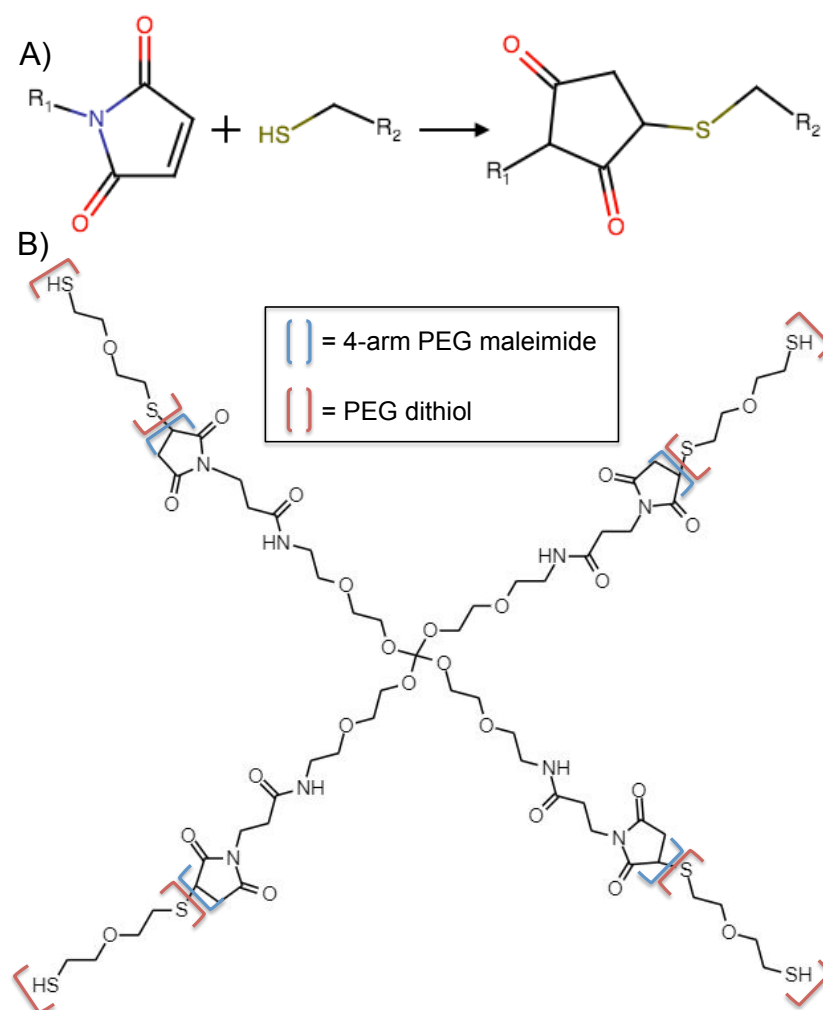
Figure 3.9: A) Schematic of the Michael type addition between a maleimide group and a thiol. B) Schematic of the 4APM

The hydrogel was composed of a four-arm PEG maleimide (4APM, 20 kDa) cross linked with PEG dithiol (3.4 kDa), see Figure 3.9B. The 'click' reaction between the maleimide and thiol groups was formed using a michael type addition, Figure 3.9A, providing control over the reaction rate using the buffer pH and salt concentration.[326] The gel was fabricated by separately dissolving the 4APM and PEG dithiol into 10 mM citrate buffer (pH 6) followed by mixing to initiate gelation. The mass of each component was determined by the desired final gel wt%, whilst maintaining a 1:1 ratio of maleimide to thiol groups. The PEG ditiol was injected directly into the middle of the 4APM solution and the mixture was continuously withdrawn into and ejected from a pipette until the gel was formed stopping the solution from being withdrawn. The duration of the mixing was defined as the gelation time. IK8-loaded liposomes and AuNRs

were incorporated into the gel by mixing the particle suspensions into the 4APM solution prior to the addition of the PEG dithiol.

3.6.1 Liposome and AuNR retention

The retention of liposomes and AuNRs within the hydrogel was determined by incubating the gels with buffer and measuring the leakage of the particles daily. 50 μl PEG gels containing both liposomes and AuNRs were fabricated into opaque 96-well plates and 150 μl of citrate buffer was added to the gels after gelation. To quantify the amount of AuNRs lost from the gel the supernatant absorbance at 860 nm, the longitudinal absorbance wavelength of the AuNRs, was measured. The liposome retention was assessed by including the dye Texas Red within the liposome bilayer, thus providing them with a measurable fluorescence (EX/EM, 561 nm/594 nm). The Texas Red was included by the addition of 0.5 wt% Texas Red to the lipid mixture, prior to the formation of the thin lipid film, the rest of the fabrication protocol was unchanged. The absorbance and fluorescence of the citrate buffer was measured before addition to the gels, and the absorbance and fluorescent values were obtained for the gels on day 0. After 24 hours the supernatant was added to a clean well and the absorbance and fluorescence were both measured, after which the solutions were added back to the gels. The liposome and AuNR release was determined using the equation

$$Release(\%) = 100 \times \frac{X_{Sample} - X_{Buffer}}{X_{Initial} - X_{Buffer}} \tag{3.8}$$

where X is the fluorescence when of the liposomes (EX/EM, 561 nm/594 nm) or the absorbance of the AuNRs (860 nm).

3.6.2 Rheology

The mechanical properties of the IK8-liposome and AuNR loaded gels was assessed using an Anton Paar modular compact rheometer 302. The storage and loss moduli (G' and G" respectively) of the gels was obtained through applying a constant strain of 1% to the gel and by applying a 1% strain at frequencies of 0.1-100 Hz. A 500 μl gel was fabricated on the bottom plate of the rheometer that was preheated to 37°C. Immediately after gelation the 25 mm diameter top plate was lowered to 1 mm above the bottom plate before initiating the measurement. Silicon oil was applied to the periphery of the rheometer plates to restrict evaporation from the

hydrogel.

3.6.3   Swelling ratio

The swelling ratio is the fractional increase in the weight of the hydrogel due to the absorption of water.[327] PEG gels of 2.5, 5 and 10 wt% were fabricated into the eppendorfs, before freeze-drying. The gels were then weighed before 1 ml of Milli-Q was added. After 10, 30, 60, 120, 180 and 240 mins the excess Milli-Q was removed and the gel was weighed again. The swelling ratio was then calculated using:

$$SR = \frac{W_1 - W_2}{W_2} \qquad (3.9)$$

Where W_1 is the weight of the swollen gel and W_2 is the initial weight of the gel before hydration.

3.6.4   Photothermal heating

The photothermal response of the AuNR loaded gels was determined using the Mira 900 laser system as previously described (Section 3.5). 50 μl hydrogels containing AuNRs were fabricated in 96-well plates and subjected to laser irradiation at varying intensities. The photothermal response was measured using thermocouples fixed into the lid of a well plate. To assess the reproducibility of the photothermal heating profile the gels were also subjected to multiple rounds of heating with a 10 minute cooling period between the irradiation cycles.

The photothermal bulk heating produced by the pulsed laser system was determine by filming the samples during irradiation using a thermal camera.

3.6.5   Calcein release from liposomes loaded in gels

Calcein-loaded liposomes were diluted 100 times into citrate buffer and the fluorescence was compared to liposomes diluted in the same amount of Milli-Q, to ensure that the buffer itself did not trigger the release of the encapsulated dye. The liposomes in citrate buffer were then used to dissolve the 4APM before the fabrication of a 50 μl hydrogel in a clear bottom 96-well plate, as described at the beginning of section 3.6. The fluorescence was measured to determine whether the formation of the gel structure impacted the liposome integrity. The gel was then topped up to 200 μl with either buffer, MHB II or a a suspension of 0.5 McFarland standard

78

bacteria diluted a further 100 times. The fluorescence was then measured immediately before incubation at 37 °C, the fluorescence was then measured daily. 1% Triton X-100 was mixed with control samples at the start and end of the experiment to ensure that the maximum fluorescence did not change.

3.7 Cell culture

Cell culture was performed under sterile conditions in a class II A1 biosafety cabinet. All consumables were autoclaved at 131°C for 30 mins unless purchased sterile. All cell culture in this thesis was performed upon human dermal fibroblast (HDF) cells. Cells were incubated at 37°C in 5% CO_2 and a high humidity environment, cells were split at 1:3 upon reaching 80% confluency, approximately every 4 days. Cell splitting was performed by aspirating the spent fibroblast growth media from a flask before gently rinsing with sterile PBS. The flask was then covered in a trypsin/ethylenediaminetetraacetic acid (EDTA) solution and incubated for 5 mins ensuring detachment of all adhered cells. The trypsin was then deactivated through the addition of 5 ml media and centrifuged at 220 x g for 5 mins. The supernatant was discarded and the cell pellet dispersed in 3 ml media. A 10 μl sample was removed and diluted in an equal volume of trypan blue, before addition to a Neubauer haemocytometer. The number of cells in each quadrant of the haemocytometer was counted and the average was taken to calculate the cell concentration. The ratio of bright blue alive cells to the dark dead cells was also measured to determine the cell viability. The concentration was kept at 1 x 10^6 cells per ml, prior to dilution in the flask, and the viability was maintained above 95%. The remaining cells not added to the haemocytometer were seeded into new T75 flasks with 12 ml of fresh media.

The HDF cells were frozen for long term storage by concentrating 2 x 10^6 cells into a cryovial with fibroblast growth media and 10% sterile DMSO. The cryovials were then placed into a Mr Frosty Freezing Container that was filled with IPA and placed in a -80°C freezer overnight, before long term storage in liquid nitrogen. Cells were utilized for toxicity assays between 6-12 passages, after which the cells were discarded.

3.7.1 Cell viability assays

Cell viability assays were performed using the WST-1 cell proliferation reagent. The cytotoxicity of IK8, AuNRs and the 4APM-PEG dithiol hydrogel was assessed on HDF cells. 100 μl

of fibroblast growth media containing HDF cells in were seeded into a 96-well plate at a concentration of 7 x 10^4 cells per well, before incubation at 37°C for 24 hours. Post-incubation the media was replaced with 90 μl of growth media and 10 μl of Milli-Q containing either 32 μg ml^{-1} of IK8 or 48 μg ml^{-1} of lipid coated AuNRs and incubated for 24 hours. The media was then aspirated and the cells were gently rinsed twice with sterile PBS before the addition of fresh media containing 10% v/v of the cell viability reagent WST-1, and incubated for a further 2 hours. An equal volume of the media containing 10% v/v WST-1 was added to wells containing no cells to account for the background absorbance by the WST-1 reagent. The media was transferred to wells that did not contain cells and the absorbance was measured at 440 and 660 nm. The cell viability is conveyed as a percentage of untreated control cells. The relative viability was calculated using:

$$Viability(\%) = 100 \times \frac{(OD_{440nm} - OD_{660nm})_{Sample} - (OD_{440nm} - OD_{660nm})_{Background}}{(OD_{440nm} - OD_{660nm})_{Media} - (OD_{440nm} - OD_{660nm})_{Background}} \quad (3.10)$$

The cytotoxicity of the PEG hydrogel and the PEG gel containing IK8-liposomes and AuNRs was performed as previously described with the addition of a prefabricated 10 μl gel to the HDF cells. The gels were fabricated on top of a glass slide wrapped in Parafilm$^{\text{TM}}$tape, such that the gel droplet formed could slide across the surface. These gels could then simply be tipped into the wells containing the HDF cells.

3.8 Microbial handling techniques

All microbial handling was performed under sterile conditions in a Monmouth Guardian MSC T800 biohood (inlet and downflow air velocities of 0.8 and 0.4 m sec^{-1}). Before any microbial work the biohood was cleaned using Distel disinfectant diluted in Milli-Q, 1:10, and 70% ethanol. All microbial handling equipment was purchased sterile, autoclaved at 121°C for 30 mins or filtered through a 0.2 μm membrane. All equipment entering the hood was coated with 70% ethanol. Once finished, the biohood was cleaned using 70% ethanol and sterilised with a UV lamp for 20 mins. The bacteria used for experimentation are *S. aureus* (NCTC 12981) and *P. aeruginosa* (NCTC 12903).

3.8.1   Preparation of MHB II and MHB agar II plates

All glassware was cleaned with a solution 10% Decon-90 in Milli-Q and placed into a sonic bath for 30 mins, before rinsing thoroughly with Milli-Q and being left to dry at 80°C in an oven. Cation-adjusted Mueller-Hinton broth 2 (MHB II) was prepared by weighing MHB II powder on a balance scale, 22 g l^{-1}, before pouring into a glass flask. The corresponding volume of Milli-Q was measured out into a volumetric flask before addition to the MHB II powder. The mixture was then mixed vigorously until no large agglomerates of the powder remain. The lid of the flask was then opened such that it was resting on top of the flask and held in place using autoclave tape. The flask was then autoclaved at 10-15 lbs pressure at 121°C for 10 mins. Once cool the lid was screwed tightly and the flask was placed into a 4°C fridge.

MH agar II plates were prepared by first weighing Mueller-Hinton agar II (MH agar II) powder into a glass flask, and dissolved in Milli-Q (38 g l^{-1}). Autoclave tape was used to hold the loose lid in place and the flask was autoclaved at at 10-15 lbs pressure at 121°C for 10 mins. Once cool enough to touch, the lid was screwed on and the flask was placed into the biohood. Sterile petri dishes were then laid out and 15 ml of the MH agar II solution was dispensed into each dish using a sterile 25 ml polystyrene serological pipette and pipette controller. Any bubbles in the plate were extracted to ensure a solution of homogenous thickness and smooth surface. The plate lids were rested on the side of the petri dish, ensuring not to cover more than 25% of the plate, otherwise condensation began to form as some of the hot liquid evaporated from the dish. The plates were left to cool for 5 mins until the transparent solution became completely opaque and was no longer warm, before they were then inverted and placed into a refrigerator at 4°C. All agar plates were used within 2 weeks of fabrication and were checked to ensure there was no condensation on the lids that could in increase chances of infection.

3.8.2   Bacteria growth and making stocks

Frozen bacteria stocks were warmed up until no ice crystals remained in the cryotube. A petri dish containing MH agar II was placed in the biohood and left for 10 mins to reach room temperature. 20 μl of the bacteria stock was then added to a spot $\sim$1 cm from the edge of the plate. An inoculating loop was then used to drag the solution in a zig-zag pattern across one quarter of the plate. Another zig-zag pattern crossing the first was drawn into the quarter adjacent to the end of the first. This was repeated until all four quarters had been inoculated.

The dish was then inverted and placed into a 37°C incubator overnight. The following morning 3-5 isolated colony forming units (CFUs) were touched with a pipette tip and placed into 10 ml of MHB II. The suspension was incubated at 37°C and shaken at 300 rpm for 6 hours. The bacteria suspension then diluted in MHB II to achieve an optical density at 600 nm (OD_{600}) of 0.07. An OD_{600} value of 0.07 correlates with a turbidity of 0.5 McFarland standard, as ascertained using a Pro-lab diagnostic latex bead standard, which is comparable to a bacterial suspension of approximately 1.5 x 10^8 CFU ml^{-1}. 0.9 ml of the bacteria suspension was then added to a cryovial followed by 0.1 ml 100% sterile glycerol. The solution was then slowly mixed and added to a -80°C freezer.

3.8.3   MIC testing and CFU quantification

The minimum inhibitory concentration (MIC) of a drug is the concentration of antimicrobial required to completely inhibit any visible growth of a bacteria in solution over an 18-hour incubation. MICs are widely used to determine resistance development and to determine the efficacy of an antimicrobial agent *in vitro*.

A frozen bacteria stock was grown to 0.5 McFarland standard, as described in Section 3.8.2, before a further 100-fold dilution in MHBII. The antimicrobial agent was dissolved into sterile PBS at 20 times the highest concentration required for testing on the bacteria, before being diluted ten times in MHBII. A serial dilution in MHB II was then performed, halving the antimicrobial concentration at each dilution. 0.1 ml of the bacteria suspension and 0.1 ml of the antimicrobial agent solution were mixed in a corning costar 96-well plate, six repeats were made for each concentration. Controls containing 10% PBS and 100% MHB II with no drug ensured the PBS did not affect bacteria proliferation, while wells containing 0.2 ml of bacteria-free MHB II ensured handling procedures were aseptic. The OD_{600} values were measured immediately after treatment and after an 18-hour incubation at 37°C. The MIC was determined as the minimum concentration of antimicrobial that showed no increase in the sample OD_{600}, indicating that there is no increase in turbidity and in turn no bacteria proliferation.

To quantify the number of CFUs, all bacteria suspensions treated with the same concentration of antimicrobial were collated and mixed. This solution was then subjected to a ten-fold serial dilution six times. On the reverse of a sterile MHBII agar plate a cross was used to divide the plate into 4 equal sections, each labelled to indicate each dilution between 10^3 and 10^6. 20

μl of the corresponding bacterial sample dilution was added to each section and, using sterile L-shaped spreader, spread evenly across the segment. This was performed in triplicate for each sample. The sample plates were then inverted and placed into an incubator at 37°C for 18 hours, a blank plate that was not inoculated with bacteria was incubated alongside the sample plates to ensure no wild bacteria contaminated the plates. The following day the number of individual CFUs in each section was counted and the quantity of bacteria was calculated using

$$CFU ml^{-1} = CFUs \times Dilution factor \times 50 \tag{3.11}$$

Distel disinfectant diluted 100 times was added to contaminated plates and falcon tubes to kill of any remaining bacteria. This was left for 24 hours before the dead bacteria were poured down the sink and the tubes and petri dished autoclaved before disposal.

3.8.4 Treatment of bacteria with IK8-liposomes in suspension

Bacteria were grown to 0.5 McFarland standard and diluted a further 100 times. IK8-liposomes were diluted in MHB II and a serial dilution was performed halving the concentration of IK8 from 16 to 2 times the MIC. Lipid coated AuNRs were diluted to 192 μg ml^{-1} in MHB II. 50 μl of both the AuNRs and IK8-liposomes were mixed and added to 100 μl of the bacteria suspension in a 96 well plate. The plate was then placed in an incubator, preheated to 37°C and shaking at 300 rpm, for 1 hour before being irradiated at 860 nm for 10 mins at laser intensities between 1.8 - 2.8 W cm^{-2}. The sample OD$_{600}$ values were measured and the plate was then placed back into the incubator for 18 hours. The OD$_{600}$ was again measured to provide and indication of the bacteria proliferation before the bacteria was collated for quantification of viable CFUs ml^{-1} using microdilution and agar plating techniques.

3.8.5 Treatment of bacteria with IK8-loaded liposomes and AuNRs within a hydrogel

Three distinct gels were fabricated in order to test different antimicrobial properties properties. A gel containing only AuNRs was used to test the antimicrobial effects of photothermal heating. The second gel contained AuNRs and the MIC of free IK8, to demonstrate the antimicrobial effects of the AMP when delivered alongside the photothermal heating. The third gel contained AuNRs and IK8-loaded liposomes, to demonstrate the triggered delivery of the AMP. All gels

were fabricated into wells of a 96-well plate to a total of 50 μl. The wells were topped up to 100 μl with MHB II before the addition of 100 μl of bacteria, 1x10^6 CFU ml^{-1}. After 1 h of incubation wells were irradiated with 860 nm laser, at intensities between 1.8 and 2.8 W cm^{-2}, for 10 min. The plate was then incubated overnight before quantification of the bacteria CFU ml^{-1}. The treated bacteria was then compared to the concentration of bacteria in an untreated control sample in order to determine the number of log reductions in viable bacteria.

3.8.6 Repeated treatment of bacteria with an IK8-loaded liposomes and AuNR containing hydrogel

This experiment was performed similarly to that described in section 3.8.5. Hydrogels containing 2.5 x MIC of IK8 and AuNRs were fabricated into a 96-well plate. They were then innoculated with 100 μl of 100 times diluted 0.5 McFarland standard of bacteria and the well was topped up to 200 μl with MHB II. After incubation for one hour the wells were irradiated at 2.1 or 2.4 W cm^{-2} for 5 mins. The plates were then left to incubate for 18 hours before measuring the change in OD$_{600}$ value and the subsequent removal of the bacteria suspension for quantification. Instead of treating the gels with Distel, they were rinsed with 150 μl of sterile PBS before being inoculated with 100μl of fresh bacteria (1x10^6 CFU ml^{-1}) and left to incubate for an hour. The samples were then irradiated for 10 mins, ensuring the same laser intensity over both treatments. The plates were then left to incubate for another 18 hours before the second batch of bacteria was removed for quantification.

3.8.7 Pulsed laser induced release of IK8 for the treatment of *S. aureus*

Equal volumes of IK8-loaded thiol-functionalised liposomes (DSPC/cholesterol/DSPE-mPEG2k /DPPE-Ptd, 67/30/2/1 mol% at 10 mg ml^{-1}) and maleimide-functionalsied phospholipid AuNRs (DSPC/DSPE-mPEG2k/DSPE-mPEG2k-maleimide, 95/4/1 mol% at 200 μg ml^{-1}) were mixed and left overnight. The following day the sample was pelleted (9,000 g, 30 mins) and dispersed in fresh Milli-Q. The AuNR-liposome complex was then added to a quartz curvette, that had been sterilised with a 70% ethanol solution and allowed to dry in a biological hood. The sample was then irradiated for 10 mins at a fluence of 450 μJ cm^{-2} with a repetition rate of 10 Hz at 738 nm. The Sample was then diluted in MHB II to approximately 4 times the MIC of IK8 against *S. aureus*. 100 μl of the sample was then added to a 96-well plate along with an equal volume of MHB II containing 0.5 McFarland standard of *S. aureus* diluted a further

100 times. Control samples of IK8-loaded liposome-AuNR complexes, the IK8-loaded thiolated liposomes and maleimide-functionalised phospholipid AuNRs (100 μg ml^{-1}) were also added to the bacteria to determine whether the system itself affected the *S. aureus* viability without the pulsed laser irradiation. The samples was then left to incubate for 18 hours before a serial microdilution was performed and the bacteria samples spread onto MH II agar plates. The next day the number of CFUs was counted.

3.9　Statistical analysis

All statistical analysis was performed using two-tailed student's t-testing. Results where considered as statistically significant when P < 0.05, all significant results are denoted with asterisks with the probability range denoted in the corresponding figure caption. Unless otherwise stated error bars indicate the standard deviation.

Chapter 4

Synthesis and characterisation of gold nanorods

Some of the content within this chapter can be found within the following the following publication:

L. Roach *et al.* 2018. 'Morphological control of the seedless synthesis of gold nanorods using binary surfactants' in *Nanotechnology* 29:359501

Motivation:

Throughout this thesis gold nanorods (AuNRs) have been utilised as photothermal agents to produce heating effects that can provide triggered delivery of antimicrobial peptides. AuNRs have been chosen as they provide the highest absorption cross-section of any gold nanoparticle (AuNP). This provides highly efficient photothermal light-to-heat energy conversion which, coupled with the ease of surface functionalisation and tunable optical properties, make AuNRs ideal for medical applications.

In this chapter we will discuss the controlled synthesis of AuNRs, the replacement of the stabilising centrimonium bromide (CTAB) and sodium oleate (NaOL) with phospholipids, and the photothermal properties of AuNRs under continuous wave laser irradiation. AuNR characterisation was performed using UV-vis spectroscopy, TEM imaging and atomic absorption spectrometry. We will also compare the surface functionalisation on AuNR colloidal stability in different media and determine their toxicity against *S. aureus*.

4.1   Binary surfactant AuNR synthesis

The one-pot synthesis of the binary surfactant AuNRs was based upon work from Lai *et al.* (2014), however the work presented in this thesis expands upon the range of surfactants in order to demonstrate morphological control over the AuNRs.[208,328] The AuNR synthesis protocol is described in detail in section 3.3.1. The AuNRs were synthesised in a solution containing the surfactants CTAB and NaOL, the mild reducing agent ascorbic acid (AA) and silver nitrate. Initially, a $HAuCl_4$ solution was added to the surfactant mixture turning the solution a dark yellow as the CTA^+ molecules started to form complexes with the $[AuCl_4]^-$ ions.[329] To this solution $NaHO_3$, HCl and ascorbic acid (AA) were sequentially added. Upon the addition of AA the solution became transparent as the Au^{3+} ions were reduced to Au^{1+}. The final rapid injection of ice-cold $NaBH_4$ caused an initial red plume as the strong reducing agent reduced the Au^{+1} to Au^0, causing the rapid nucleation of nanospheres that form the seeds from which the anisotropic deposition of gold occurs to form AuNRs. The solution was then maintained at 30°C for 4 hours, during which time the characteristic brown AuNR colouration developed. The AuNR suspension was then pelleted using centrifugation (9,000 x g, 30 mins), and the supernatant was removed and replaced with Milli-Q. The solution could then be stored for several months before use, with very little change to the AuNR optical properties. The binary surfactant bilayer stabilising the AuNR however required replacement or coating with polyelectrolytes due to the propensity of the NRs to aggregate after more than one centrifugal cleaning step, Figure 4.1D. In order for CTAB and binary surfactant AuNRs to retain colloidal stability a critical ratio of 740,000:1 of CTAB molecules in solution to AuNRs is required, after one cleaning step CTAB-NaOL stabilised AuNRs demonstrated no change in optical properties 18 months after synthesis, Figure 4.1E.[330] As the amount of excess CTAB is solution is reduced with each pelleting cycle CTAB is removed from the AuNR surface to equilibriate with the surrounding medium causing a decrease in the AuNR zeta-potential that contributes to the aggregation.[331] The binary surfactant AuNRs had zeta-potentials of +68.5 ± 13.4 mV, +31.6 ± 12.3 mV, +22.0 ± 4.2 mV after the first, second and third cleaning step.
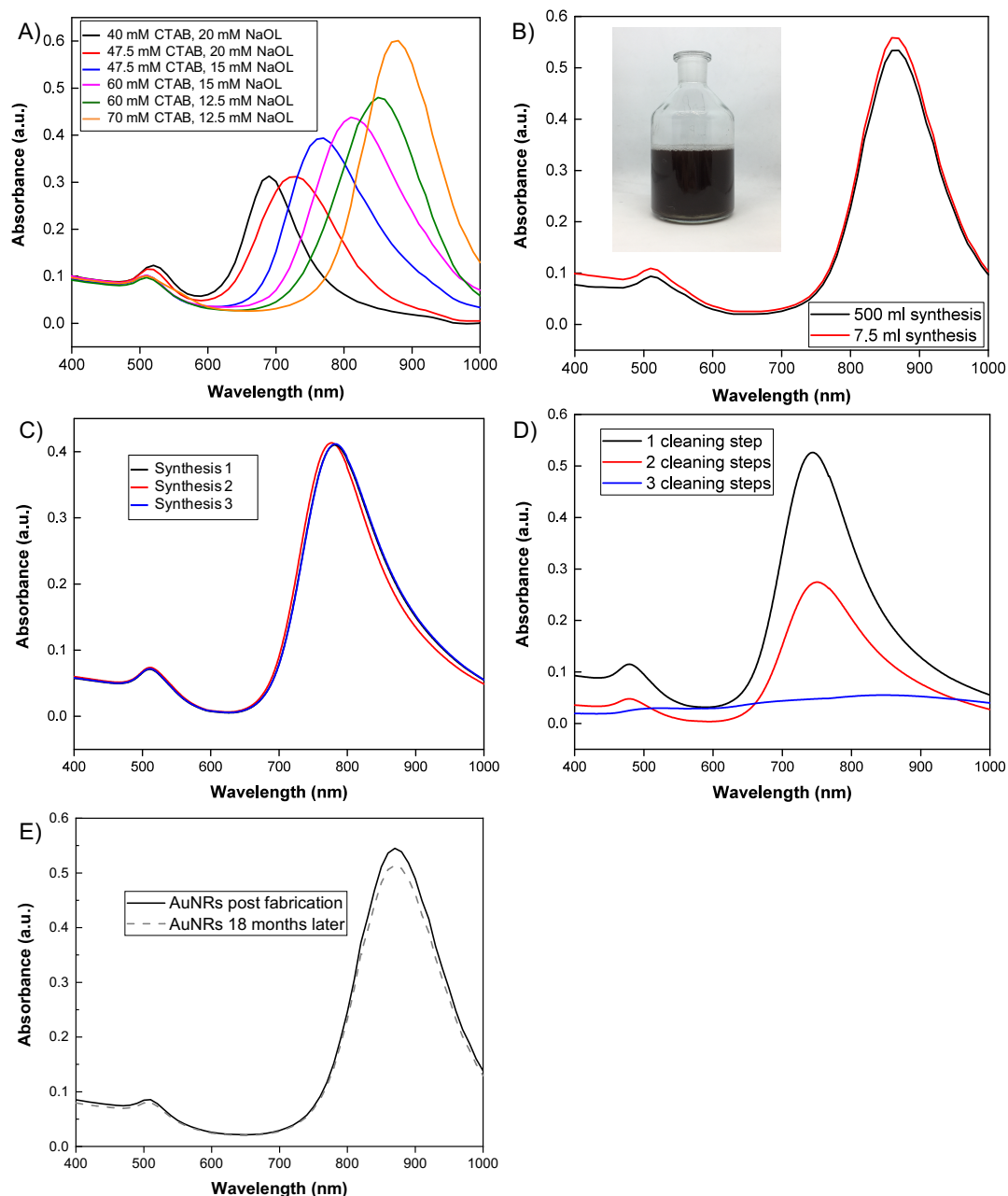
Figure 4.1: A) The longitudinal absorbance peak of AuNRs could be finely controlled by varying the concentration of CTAB and NaOL. B) AuNR production could be scaled up to 0.5 litres, with little detriment to the particle quality. An image of after the 0.5 litre synthesis is inset. C) Absorbance spectra of 2 different batches of AuNRs made with the same CTAB to NaOL concentrations. D) The effects of centrifugal cleaning upon binary surfactant AuNR stability. E) Absorbance spectra of AuNRs immediately after synthesis (solid black) and after 18 months (dashed grey).

This synthesis process was found to be highly versatile, allowing fine tuning of the longitudinal plasmon band between between 650-1,000 nm, Figure 4.1A, by controlling the concentrations of CTAB and NaOL in the growth solution. In general, as the CTAB to NaOL ratio increased the longitudinal plasmonic peak was red shifted. The protocol also exhibited excellent reproducibil-

ity, Figure 4.1C, and scalability with the maximum synthesis attempted at 0.5 litres, Figure 4.1B, this was only limited by the volume of the receptacles available.

The control of the longitudinal plasmon peak through varying the concentrations of CTAB and NaOL was extensively investigated by L. Roach.[208] Figure 4.2A plots the longitudinal surface plasmon peak absorbance as a function of the surfactant concentrations, depicting a region with high AuNR yield (>98%), between 27.5-70 mM CTAB and 12.5-20 mM NaOL. Beyond this parameter space the sample quality diminishes rapidly. Using TEM imaging, the effect of the ratio of surfactants upon the AuNR dimensions was investigated. Firstly, Figure 4.2B depicts that an increasing CTAB to NaOL ratio produced a significant increase in the AuNR length, whereas only a small increase in the width. This resulted in AuNRs with aspect ratios of ~2.5 and ~3.0, at 1:1 to 3.5:1 CTAB:NaOL ratios respectively, correlating to plasmonic absorption peak wavelengths at 650 and 800 nm; meaning an increase in the AuNR aspect ratio produced a red-shift in the longitudinal peak. The validity of these results is reinforced by observing the converse conditions, as shown in Figure 4.2C. Increasing the NaOL to CTAB ratio from 1:5 to 2:5 produced a decrease in the aspect ratio from ~4.0 to ~2.7, which correlated to peak wavelengths of 900 and 725 nm respectively. The observed increase in the aspect ratio producing a red-shift in the longitudinal absorption peak is in line with the literature.[332,333] The significant effects on the AuNR dimensions by utilising binary surfactants as opposed to CTAB alone are attributed to an increased packing density within the bilayer. The inclusion of anionic NaOL into a CTAB bilayer screens the electrostatic repulsion between cationic CTAB headgroups, decreasing the area per molecule. The increased bilayer packing density decreases the Au ion permeation, and given studies of the molecular dynamics of CTAB indicate similar densities on the {100} and {110} facets (i.e. both the AuNR sides and ends), the growth rate is reduced isotropically. The lateral Au deposition is already blocked by the Ag layer on the sides of the AuNR meaning the growth rate at the ends of the rod is reduced to a greater extent than on the sides; the higher the NaOL to CTAB ratio the smaller the aspect ratio.
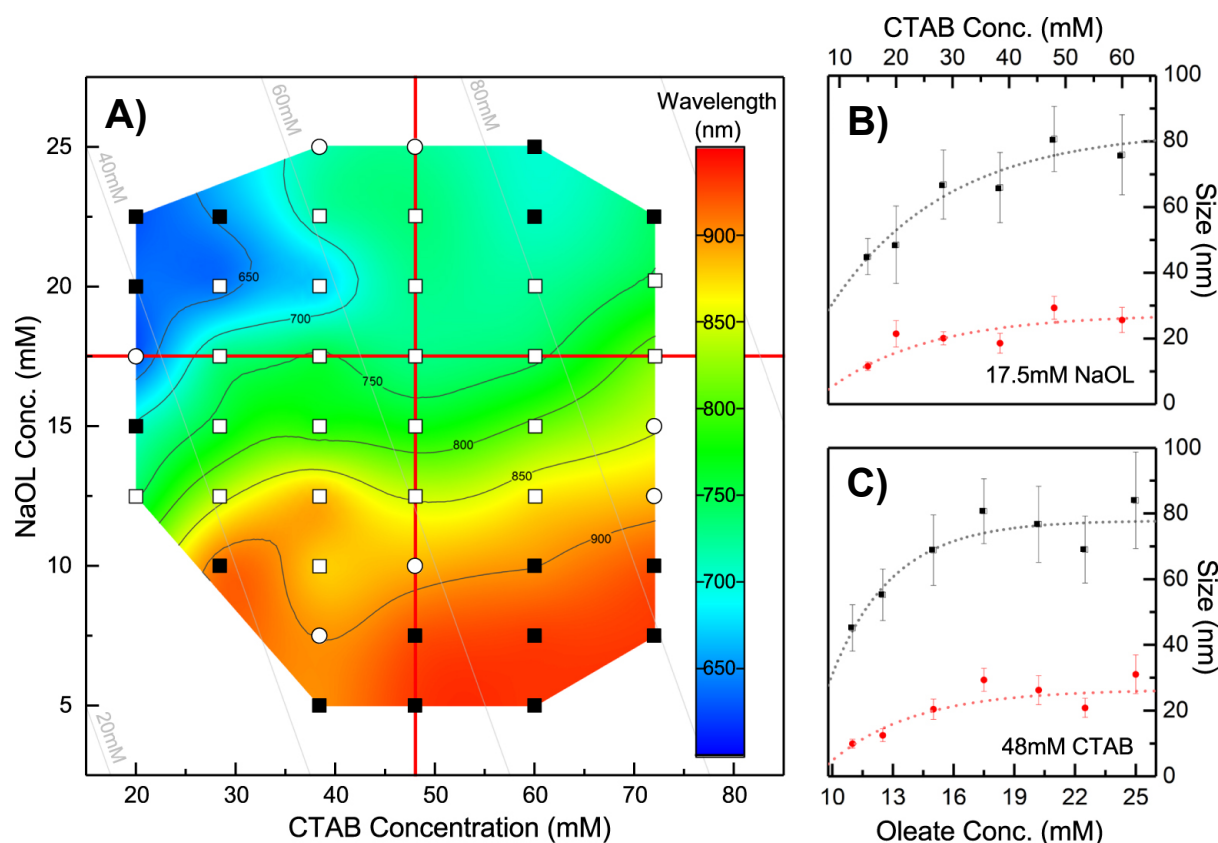
Figure 4.2: A) The effect of the CTAB and NaOL surfactant concentrations upon the longitudinal plasmon absorbance wavelength, holding all other components constant. The AuNR yield for each synthesis is denoted by the shape of the point; □ >98% AuNRs, ◯ >90% AuNRs and ■ <90% AuNRs. B) The morphological effects of varying the CTAB concentration, whilst holding NaOL constant at 17.5 mM. Black points represent the AuNR length along the major axis and red points are the AuNR width along the minor axis. C) The effect on AuNR length (black) and width (red) when holding the CTAB at 48 mM and varying the NaOL concentration.[208] Figure created by Dr. Lucien Roach.

4.2 Phospholipid replacement of binary surfactants as stabilising agents on AuNRs

CTAB is essential for promoting the anisotropic growth of AuNRs and therefore has been used in the initial synthesis. However, it has been found that CTAB stabilised AuNRs are not suitable for biological applications, demonstrating high levels of toxicity against both bacterial and mammalian cells.[334–337] CTAB derives its toxicity from two effects; 1) the cationic surfactant can interact with phospholipids to disrupt biological membranes, 2) the CTA^+ molecule can halt/stop the production of the ATP synthase enzyme thereby inhibiting ATP production and eventually leading to cell death.[338–340] Biocompatible alternative surfactants (e.g. peptides) demonstrate potential as directional agents to induce the uniaxial growth of AuNRs however

further synthesis optimisation is required before these are viable.[341] As such, to reduce toxicity of the CTAB-coating a surface ligand exchange is performed to replace the CTAB layer with more biocompatible phospholipids. Phospholipids are a key component within the cellular membrane and are widely regarded as non-toxic.[342] Zwitterionic PC lipids are commonly the most abundant lipid used in particle coating, however a mixture of PC and cationic or anionic charged lipids is usually required to prevent aggregation.[343] In our liposome-AuNR system we are attempting to keep both components neutrally charged so as to reduce interactions with both the delivered AMP and the bacteria itself. As such, we decided to include PEGylated-PE lipid that will provide steric hinderance to avoid aggregation, whilst only providing a slight negative charge.[344]
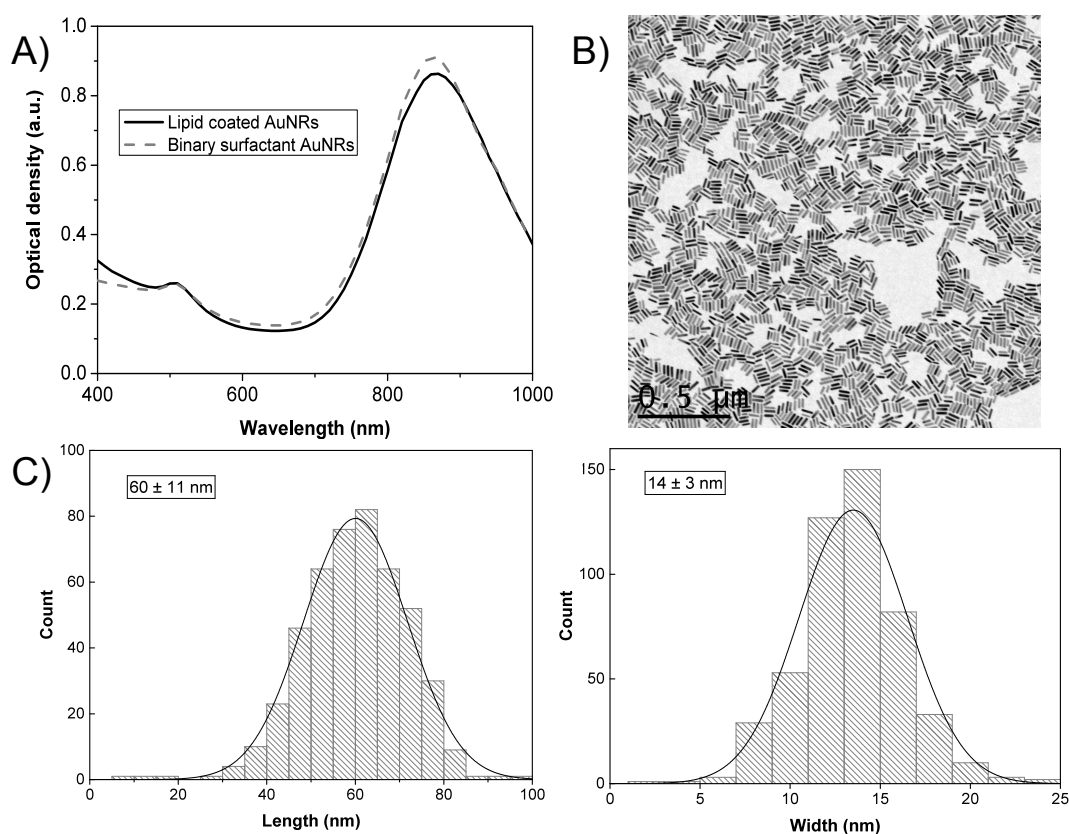
Figure 4.3: A) The absorbance spectra of AuNRs before (solid line) and after (dashed line) the phospholipid replacement of the binary surfactant bilayer. B) TEM image of AuNRs after the surface exchange of the binary surfactants CTAB-NaOL with DSPC:DSPE-PEG2k. C) The length (left) and width (right) distributions of the phospholipid coated AuNRs (n= 431).

The phospholipid surface exchange protocol was based on that of Matthews *et al.*, the key difference being the sonication time was significantly increased.[345] Briefly, 1 ml samples of AuNRs (75 μg ml^{-1}) cleaned once through centrifugation were pelleted a second time and

dispersed into 300 μl of a 10 g L^{-1} SUV suspension (<100 nm) comprised of DSPC:DSPE-PEG2k (19:1 mol ratio). The suspension was then placed into a cooled bath sonicator for 24 hours. This process was repeated three times, after the final sonication the sample was pelleted and dispersed into Milli-Q. Absorbance spectra and TEM images of the lipid coated AuNRs show no aggregation or morphological changes were induced through the replacement procedure, Figure 4.3A and C, indicating a successful exchange with the CTAB-NaOL bilayer, which otherwise would have demonstrated considerable aggregation after just two centrifugation cleaning steps. The phospholipid surface exchange protocol also showed little effect on the optical properties of the AuNRs, Figure 4.3B.

4.3 Colloidal stability of phospholipid stabilised AuNRs in Mueller-Hinton Broth II

To determine whether the phospholipid surface functionalisation could enhance the stability of the AuNRs in biologically relevant media the DSPC:DSPE-PEG2k AuNRs were added to MHB II and the UV-vis spectra was measured after 24 hours. The lipid coated rods demonstrated no significant change in their optical properties, retaining the peak absorption at 860 nm, Figure 4.4. This compared favourably with the cationic CTAB-NaOL coated AuNRs, which rely upon electrostatic repulsion for stability, which showed substantial aggregation, indicating that steric hindrance, associated with the lipid coating, offers is a more effective means of ensuring stability.
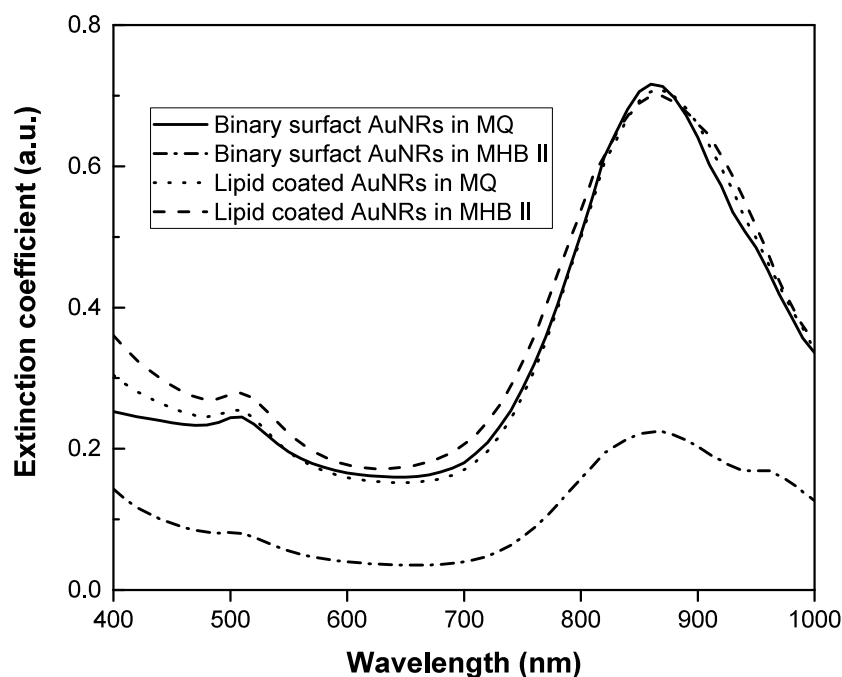
Figure 4.4: The absorbance spectrum of binary surfactant and lipid-coated AuNRs after incubation in Milli-Q or MHB II for 24 hours.

4.4 AuNR toxicity to *S. aureus*

The AuNR effects on bacteria viability were next investigated. CTAB-NaOL, poly(styrene sulfonate) (PSS) and phospholipid coated AuNRs at gold concentrations between 16-250 μg ml^{-1} were added to *S. aureus* suspensions and incubated for 18 hours. The samples were then centrifuged at 200 x g for 5 mins to pellet the bacteria, the AuNRs in the supernatant were then discarded and the pellet redispersed in 200 μl of MHB II. This process was repeated thrice. The optical density of the *S. aureus* suspension was then measured at 600 nm (OD$_{600}$) to determine whether the AuNRs affect the bacteria proliferation. The OD$_{600}$ is used to determine the concentration of a bacteria sample at low densities where the bacteria grow linearly, bacteria do not absorb light at 600 nm meaning the OD$_{600}$ is related purely to scattering effects. Therefore, in the linear growth region the bacterial concentration is linearly proportional to the OD$_{600}$.

As predicted the CTAB-NaOL coated AuNRs demonstrated the highest toxicity with inhibition of growth at 63 μg ml^{-1}, Figure 4.5. The PSS coated AuNRs, included to observe whether the AuNRs stabilised with an anionic polymer showed any difference to the cationic CTAB, exhibited increasing antimicrobial effects on the *S. aureus* proliferation with Au concentration, however the minimum inhibitory concentration was not reached. The phospholipid coated

AuNRs only started to affect the bacteria proliferation at 250 μg ml^{-1}, clearly indicating that the phospholipid coating was less toxic than the alternatives and that non-toxic concentrations of the CTAB-NaOL bilayer remain in the AuNR solution.
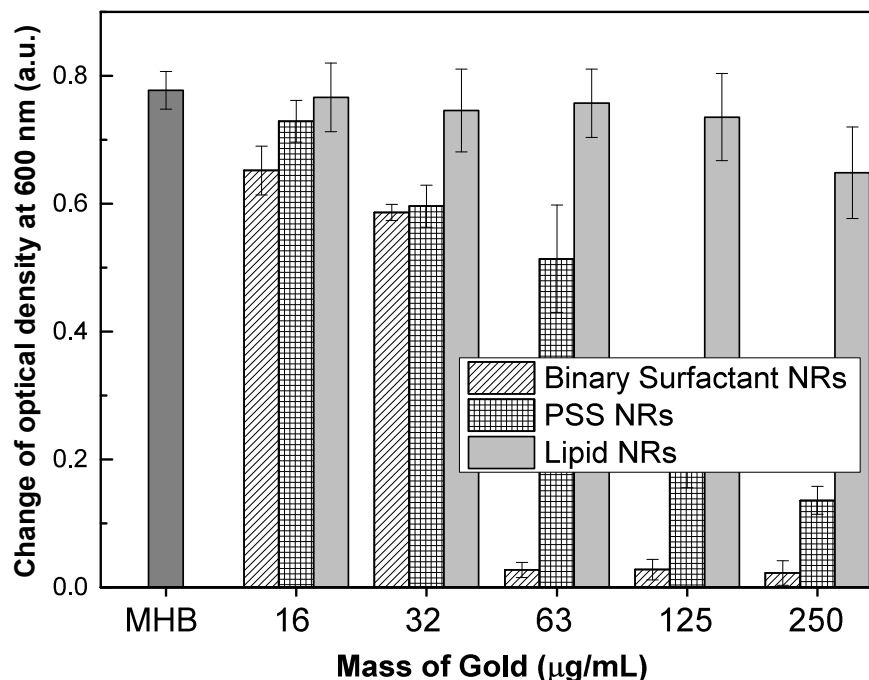
Figure 4.5: The change in optical density of *S. aureus* bacteria when incubated with increasing concentrations of CTAB-NaOL (diagonal slashed), PSS (hashed) and phospholipid (grey) stabilised AuNRs for 18 hours. Results are the average of 6 replicates.

The phospholipid stabilised AuNRs offer lower toxicity to mammalian cells, increased colloidal stability in ionic media, a substantial change in zeta-potential (+60 mV to ∼-2-4 mV), and a lack of antimicrobial activity, compared to the binary surfactant AuNRs; this indicates that the vast majority of the positively charged and toxic CTAB has been removed from the AuNR surface. As such, the phospholipid AuNRs enable the study of the antimicrobial effects of delivered AMPs and photothermal heating without the particles affecting the bacteria viability.

4.5 Photothermal heating from phospholipid coated AuNRs
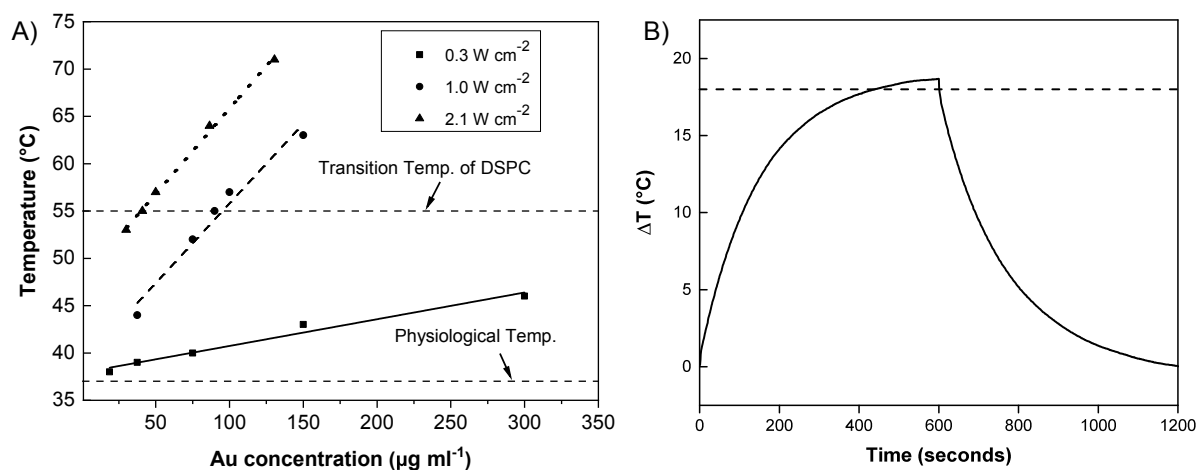
Figure 4.6: A) The temperature of a 200 μl solution containing increasing concentrations of gold, when irradiated at 860 nm for 10 mins at 0.3 W cm^{-2} (squares), 1.0 W cm^{-2} (circles) and 2.1 W cm^{-2} (triangles). B) The photothermal heating profile when 200 μl of AuNRs at 90 μg ml^{-1} was irradiated at 860 nm, for 10 minutes at 1 W cm^{-2}, starting from a base temperature of 37°C. The dashed line indicates 55°C, the T$_m$ of DSPC.

The photothermal heating generated from the phospholipid coated AuNRs was investigated in order to ensure that the the phase transition temperature of DSPC could be reached, 55°C, to trigger the release of encapsulated materials. Liposomes exhibit maximum release of encapsulated materials 1-2°C below the phase transition temperature of the vesicle, due to enhanced small molecule permeability at the grain boundaries between the different lipid phase domains. As such, the Au concentration and laser intensities were optimised to determine how each parameter affected the maximum photothermal temperature increase.[346–348] 200 μl of AuNRs was added to the wells of a clear bottom 96-well plate and irradiated with a continuous wave laser at 860 nm (the longitudinal plasmon peak) with intensities between 0.3-2.1 W cm^{-2} for 10 mins. Thermocouples were placed in the wells in order to observe the temperature increase and to ensure that the solutions all started at a base temperature of 37°C. It was found that after 5 mins of irradiation the bulk temperature within the well would be close to the maximum temperature achievable at a given AuNR concentration and laser intensity, and as such could be maintained within $\pm$ 1°C of a target temperature for a further 5 mins, Figure 4.6B. Initially AuNRs were irradiated at 0.3 W cm^{-2}, the ANSI laser intensity limit for the application of a continuous wave laser directly to the skin for 10-1000 s, however even at 300 μg ml^{-1} of AuNRs the maximum temperature that could be reached was 46°C, significantly lower than the phase transition temperature of DSPC, Figure 4.6A.[349] Increasing the laser intensity to 1 W

cm^{-2} and above showed a significant increase in achievable temperatures, such that using laser intensities of 1 and 2.1 W cm^{-2} heating to 55°C was achieved upon irradiation AuNR solutions of 90 and 35 μg ml^{-1} respectively. It is preferable to utilise a higher laser power with low Au concentrations to obtain a desired photothermal mediated temperature increase as this could potentially reduce both the system toxicity and the cost of fabrication.

Conclusion

In this chapter we have described the one-pot synthesis of binary surfactant stabilised AuNRs, with tunable optical absorption properties, and exceptional scalability and reproducibility. We also demonstrate the replacement of the binary surfactant coating with phospholipid bilayers of DSPC/DSPE-mPEG2k (95 mol%) with little detriment to the optical properties. The steric hinderance provided by the PEGylated lipids within the phospholipid coating provided enhanced stability in Meuller-Hinton broth II compared to AuNRs stabilised through electrostatic repulsion provided by CTAB. The lipid stabilised AuNRs also exhibited only a small decrease in *S. aureus* viability even at the highest concentration of AuNRs, 250 μg ml^{-1} of Au, compared to binary surfactant that induced complete bacteriostatic effects at 63 μg ml^{-1}, and PSS stabilised AuNRs that showed a significant reduction in bacteria viability at Au concentrations of 125 μg ml^{-1} and above. Finally, the photothermal heating effects from the AuNRs achieved a maximum temperature of 70°C that at a laser intensity of 2.1 W cm^{-2}. The photothermal heating profile of the AuNR solution demonstrated a rapid temperature increase for the first five minutes followed by a < 2°C increase over the following five minutes, meaning the temperature can be controlled to within ±1°C of a target temperature by varying the AuNR concentration.

The superior colloidal stability and biocompatibility of phospholipid stabilised AuNRs meant that these particles where taken forward for inclusion in within the photothermal responsive triggered delivery systems developed in the future results chapters.

Chapter 5

Development of a gold nanorod and antimicrobial peptide loaded liposome system to provide light-stimulated release to treat *S. aureus*

Some of the content within this chapter can be found within the following the following publications:

S. C. T. Moorcroft *et al.* Nanoparticle-Loaded Hydrogel for the Light-Activated Release and Photothermal Enhancement of Antimicrobial Peptides. *ACS Appl. Mater. Interfaces* 2020, 12(22), 24544–24554.

[350]

Motivation:

Despite the significant advantages of AMPs over traditional antibiotics their clinical translation has been hindered by their instability *in vivo*, susceptibility to proteolytic degradation and toxicity.[351] As such, we propose the use of a liposomal delivery system to offer spatial and temporal control over the release of AMPs, alleviating the issues of instability in ionic media,

reducing systemic toxicity by both encapsulating the drug and decreasing the administered concentration, whilst providing protection against proteases. The incorporation of human pancreatic polypeptides into sterically-stabilised lipid micelle has previously demonstrated protection against protease degradation, with the micelle providing approximately a 2.5-fold enhancement of the peptide stability when in the presence of the proteolytic enzyme trypsin.[319,352] It is hypothesised that the encapsulation of AMPs within the aqueous core of liposomes would provide a similar protective effect whilst utilising the many benefits of liposomes such as; the potential for high encapsulation efficiency, biocompatibility, increased drug bioavailability and versatility to incorporate different functionalities by varying the lipid composition.[353–355] Liposomal drug delivery can be achieved through stimuli-responsive triggered release where a large dose of the drug is released rapidly in response to an exogenous stimulus or a change in the environmental conditions. Whilst there are benefits of using both means of release, triggered delivery offers a greater degree of spatial and temporal control over the release kinetics.[356–358] This is advantageous when delivering antimicrobials as it minimises premature leakage into healthy peripheral tissue and reduces the chances of delivering sub-lethal doses to local microflora that can increase the likelihood of the bacteria developing resistance.[84] Whilst many exogenous stimuli-responsive systems have been developed for anticancer chemotherapeutics, to our knowledge no such systems have been adapted for the delivery of AMPs to treat bacterial infections. The unique properties of inorganic NPs in response to exogenous stimuli (magnetic fields for iron oxide NPs and light irradiation for Ag, Cu and Au NPs), mean that the incorporation or co-delivery of antimicrobial-loaded soft matter systems can offer a simple means of stimuli-responsive release. Traditionally, stimuli-responsive mechanisms have been integrated into a soft matter systems through the inclusion of responsive-biomaterials and -polymers, however such materials can be difficult to synthesise, the scaling-up of production can be challenging and the intrinsic properties of the delivery system may be compromised.[359–361]

This chapter will discuss the development of leakage free liposomes that release encapsulated cargoes in the presence of bacteria when heated to their gel-fluid phase transition temperature (T_m). These liposomes are subsequently loaded with IRIKIRIK-CONH$_2$, a model AMP, to demonstrate protection against protease degradation and, upon mixing with phospholipid stabilised gold nanorods (AuNRs), elicit bactericidal activity under laser induced photothermal heating, see Figure 5.1. Furthermore, this system was used to investigate the potential for photothermal killing of bacteria and whether it can be used in conjunction with the AMP delivery,

as a combination therapy.
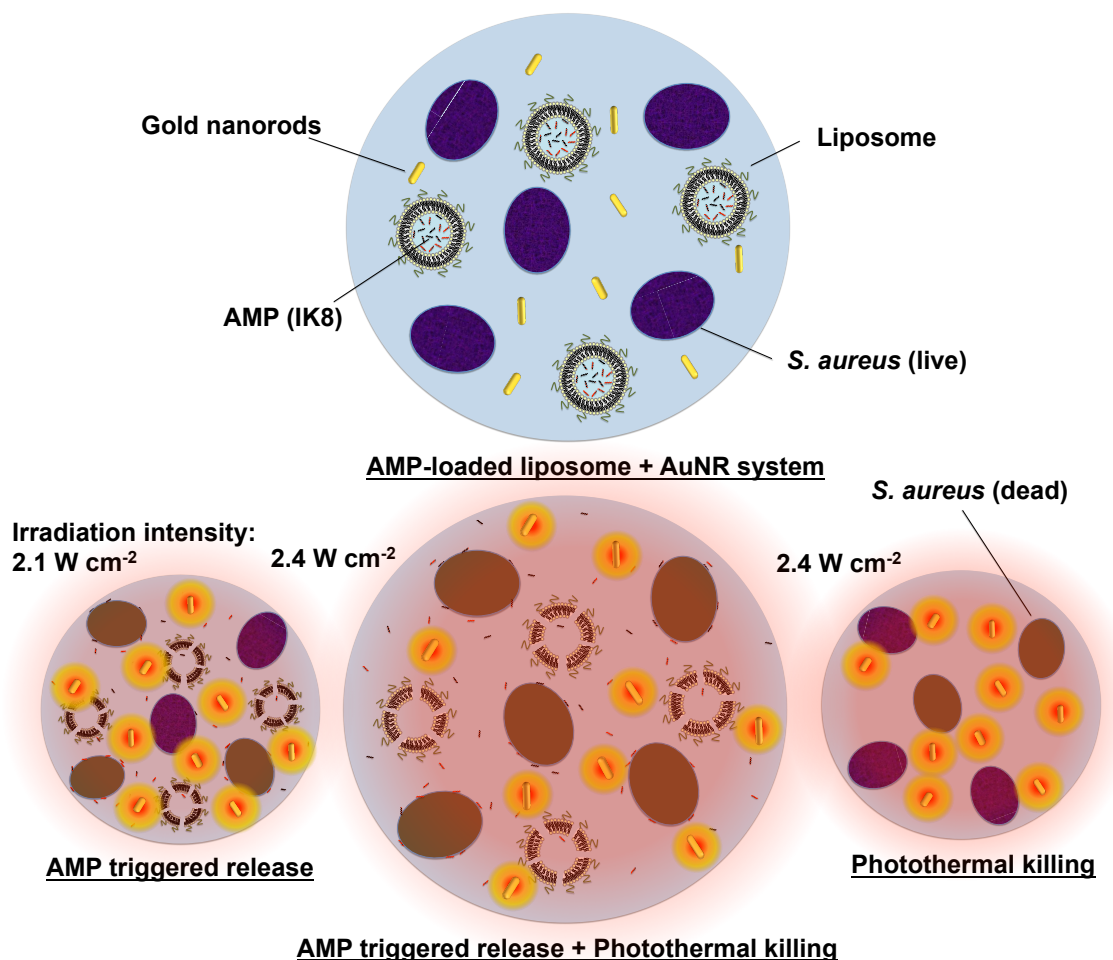
Figure 5.1: : Schematic representation of the AMP-loaded liposome and gold nanorod system, to provide bactericidal activity against *S. aureus* through AMP triggered release at low laser intensities (bottom left), photothermal killing at higher laser in the absence of AMPs (bottom right), and a combination treatment of triggered AMP release and photothermal killing at higher laser intensities (bottom centre).

5.1   Optimising the liposome fabrication protocol

The initial liposome composition, DSPC/cholesterol/DSPE-PEG2000 (65/30/5 mol%), was based on work described by Ron-Doitch *et al.* (2016) where the AMPs LL-37 and indolicidin were encapsulated within liposomes that demonstrated no aggregation over a year post fabrication.[119] This lipid formulation is also similar to work by Thet *et al.* (2013), whereby vesicles of DSPC/cholesterol/DPPE (68/30/2 mol%) show high resistance to dye leakage induced by *S. aureus*.[362] Phosphatidylcholine lipids are commonly utilised as the most abundant lipids in these formulations due to their inertness, bio-compatibility and well defined physical

properties.[363] DSPC in particular proved to be popular in drug delivery systems due to its long
(18 carbon) and saturated hydrocarbon tails that decrease liposome permeability by increasing
the bilayer thickness and providing high lipid packing densities, compared to their unsaturated
counterparts.[364] Increasing the chain length of hydrocarbons also increases the gel-fluid phase
transition temperature, and reduces leakage of encapsualted materials in the presence of bacteria.[365,366] Cholesterol was included within the liposomes to stiffen the lipid bilayers and in turn
reduce premature leakage. Cholesterol sits within the alkyl chains of the lipids, increasing the
ordering and decreasing passive leakage.[367–369] The DSPE-PEG2000 provides steric hindrance
between the liposome and foreign objects, increasing their colloidal stability. The inclusion
of hydrophilic chains also has shown to increase in encapsulation efficiency of polar materials
within the liposome lumen.[370]

The first step in optimising the liposome formulation process was to determine how the homogenisation step affected the liposome size and dispersity. The liposomes were fabricated
using the conventional thin-lipid film hydration technique, whereby a lipid film was hydrated
with a buffer and mixed for an hour whilst maintained at above the phase transition temperature of the most abundant lipid (DSPC, $T_m = 55°$). This forms a polydisperse suspension of
multilamellar vesicles (MLVs) that require homogenisation, which is primarily achieved through
mechanical agitation using ultrasound waves or by extrusion through a porous membrane. Liposomes comprised of DSPC/cholesterol/DSPE-PEG2000 (65/30/5 mol%) were placed into an
ultrasonic bath or tip sonicated for 10 mins and the resulting liposomes had diameters of 150
$\pm$ 30 nm and 80 $\pm$ 20 nm, respectively. Liposomes homogenised using extrusion were passed
through a 0.4 μm polycarbonate membrane 7, 11 or 15 times to investigate whether the number
of extrusion steps influenced the size distribution of the resultant liposomes. The liposomes
were sized using Nanosight.
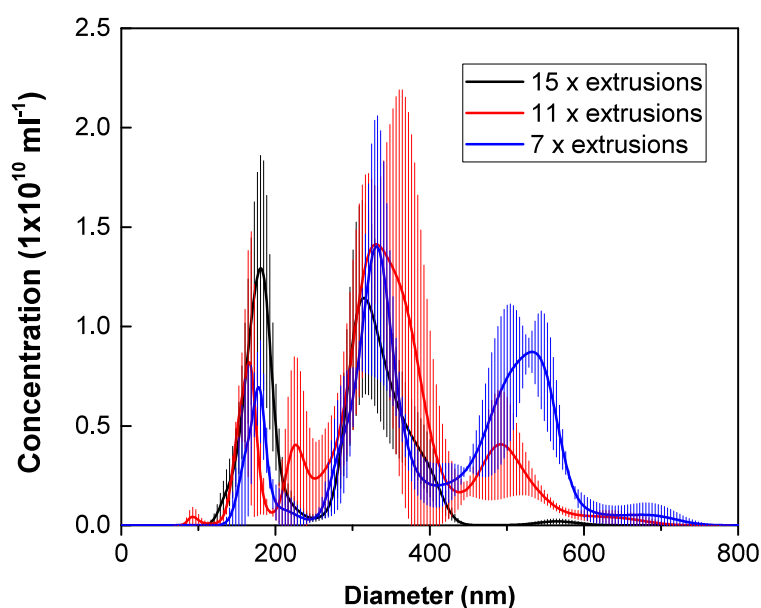
Figure 5.2: Liposome size when varying the number of times the solution is passed through a 400 nm extrusion membrane. Results are the average of 3 independent experiments.

Table 5.1: The proportion of liposomes the are below 250 nm, between 250 to 400 nm and above 400 nm, depending on the number of times the solution was passed through a 400 nm membrane.

No. of extrusion steps	< 250 nm	250 - 400 nm	> 400 nm
7	11%	42%	47%
11	18%	60%	22%
15	38%	58%	4%

The Nanosight data, Figure 5.2, depicts three distinct liposome populations with peaks between 100-200 nm, 250-400 nm and 400-600 nm. The proportion of liposomes in each size bracket is dependent upon the number of extrusion steps, Table 5.1. The largest proportion of liposomes fall within 250-400 nm for samples that had been extruded 11 or 15 times, 60% and 58% respectively, whereas the sample extruded 7 time had the highest proportion of liposomes between 400-600 nm, 47%. The proportion of liposomes larger than 400 nm was seen to decrease significantly with a 43% reduction between 7 and 15 extrusion steps, clearly indicating that the liposomes larger than the membrane pore size are being disrupted. Conversely, the number of liposomes smaller than 250 nm was seen to increase with the number of extrusion steps. These results are in agreement with the extrusion model described by Patty *et al.* (2003) where the liposome homogenisation is modelled upon the motion of bubbles blown through a circular orifice.[371] The model claims that MLVs larger than the pore diameter clog the membrane

until the shear forces acting upon the vesicle cause the surface tension to surpass the rupture tension. This rupturing causes the outer layers of the vesicle to become detached and reform into new liposomes, repetition of this process causes the formation of unilamellar vesicles. The proportion of liposomes beneath the membrane pore size, 400 nm, is seen to increase with the extrusion steps as the larger liposomes are broken up the lipids reform into vesicles smaller than the membrane pore size. The proportion of liposomes in the 250-400 nm region does not however increase going from 11 to 15 extrusion cycles, this is attributed to the majority of the lipids detached from the largest liposomes reforming into liposomes significantly smaller than the pore size. As such, all further liposomes were formulated using 11 extrusion steps in order to provide maximum control over the vesicle size.

5.2 Optimising liposome composition to reduce leakage and increase thermoresponsive release efficacy

In order to ensure that the liposome formulation was optimised such that the cholesterol content and the ratio of DSPC to DPPC were investigated to determine how this affected the stability, leakage and size.

5.2.1 The effects of cholesterol on liposome leakage

Cholesterol was investigated first due to it's ability to regulate the membrane fluidity and mechanical strength, which in turn affects the membrane permeability.[368] Cholesterol increases the structural integrity of a bilayer by sitting within the hydrocarbon chains. When present in high concentrations this can introduce conformational ordering of the lipid chains that reduces the membrane permeability, Figure 5.3. The cholesterol content within the vesicles was varied between 0-30 mol% to identify whether there is an optimum proportion at which there is little leakage at physiological temperatures (37°C), but still provide release of encapsulated materials when heated to the liposome gel-fluid phase transition temperature. The leakage was assessed by encapsulating the self-quenching dye calcein within the liposome lumen and determining the fluorescence increase upon release.
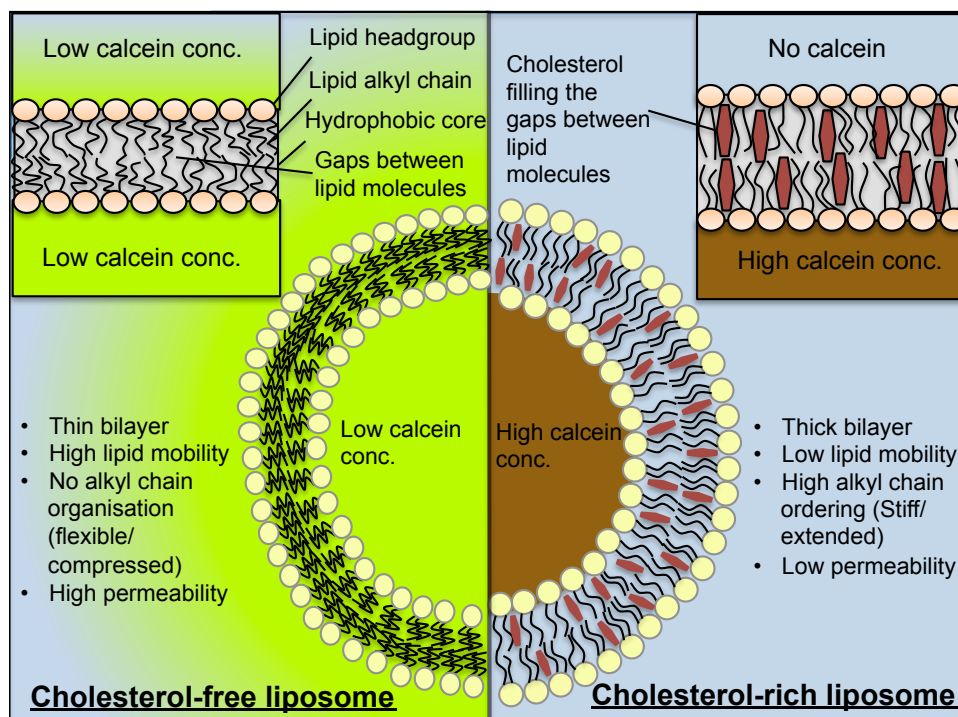
Figure 5.3: A schematic representation of cholesterol-free and -rich liposomes, loaded with the self-quenching dye calcein, as well as the effects that cholesterol imparts on the lipids within a bilayer and how this affects the membrane permeability.
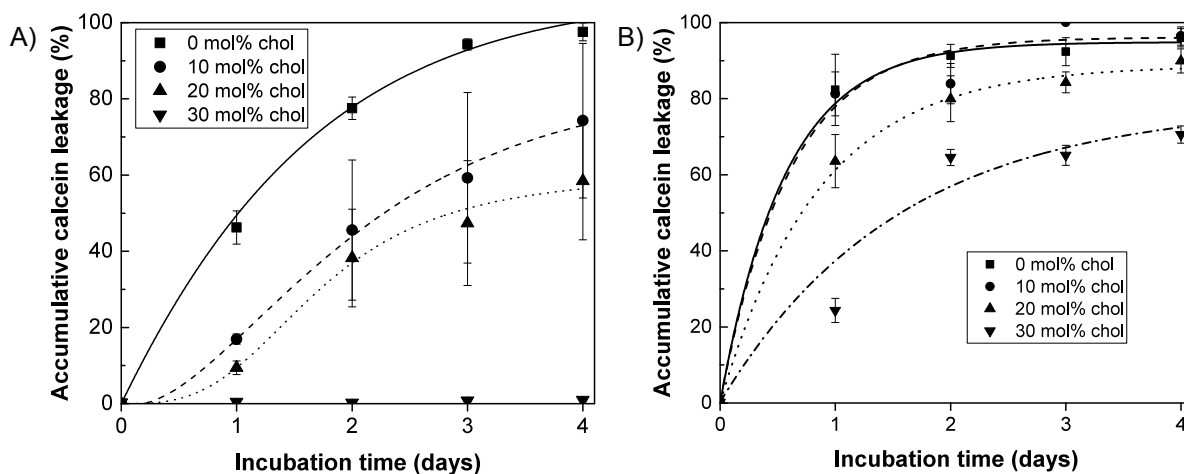
Figure 5.4: A) Calcein leakage from liposomes containing varying amounts of cholesterol when incubated at 37°C in MHB II. B) Calcein leakage of from liposomes when incubated in MHB II initially containing $1x10^6$ *S. aureus* CFU ml^{-1}. Results are the average of 6 replicates.

The calcein leakage from liposomes maintained at 37°C for 4 days showed a dependence upon the cholesterol content, Figure 5.4A. As the cholesterol content was increased from 0 to 30 mol% the amount of leakage was seen to decrease from 100% to 2% > leakage after 4 days. An increase in the cholesterol content also resulted in a decrease in the calcein leakage when incubated with a *S. aureus* suspension, however significant leakage was observed in all samples, Figure 5.4B.

The liposomes containing 30 mol% cholesterol exhibited leakage of 24% and 64% after the first and second days respectively. Pathogenic bacteria are known to secrete an array of virulence factors and pore forming toxins that target the lipid membranes of mammalian cells,[372–374] and as such are known to induce leakage from liposomes.[362,375–377] This induced leakage may be unavoidable but minimising premature release is important to ensure the system maintains antimicrobial efficacy, as well as limiting the release of sub-lethal doses that could driving resistance development, ultimately rendering the treatment futile.

The 30% cholesterol liposome leakage was also assessed in a variety of environments. The vesicles were incubated at 37°C in PBS, a 5mM IK8 solution in PBS and 5×10^3 human dermal fibroblast (HDF) cells in fibroblast growth media, the fluorescence was measured daily. HDFs were chosen due to there abundance in the wound healing environment, contributing to the reepithelialisation process by forming an extracellular matrix to aid wound closure, and regulating both inflammatory and proliferative stages of wound healing.[378]
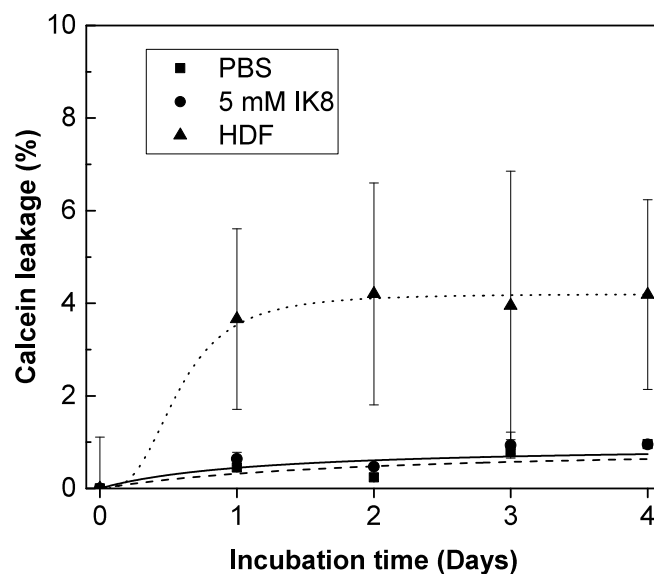
Figure 5.5: The leakage from calcein-loaded liposomes was determined by measuring the sample fluorescence when incubated at 37°C in PBS (squares), 5 mM IK8 (circles), and human dermal fibroblasts (HDF, triangles). Error bars indicate standard deviation (n=6).

The 30% cholesterol liposomes demonstrated negligible leakage after 4 days in all of the environments, Figure 5.5. When incubated with 5 mM IK8 in PBS negligible leakage, <1% is observed indicating that the IK8 does not interact with liposomes, clearly indicating that minimal liposomal disruption by IK8 occurred when encapsulated within the liposome lumen. It is

also important that the HDF cells did not induce leakage, $< 5\%$ after 4 days, as this means that the cells will not cause premature leakage upon implementation of this system into a wound dressing.

These results indicate that liposomes with higher cholesterol content are preferable due to its affects on the liposome permeability, both with and without bacteria. The enhancement of the membrane structural properties can however be detrimental to the lipid thermoresponsivity. Lipid bilayers can exist in two states; a gel phases, below the T_m, where interactions between the hydrocarbon chains are dominated by Van der Waals interacting reducing lipid mobility, and a fluid phase, above the T_m, where lipid molecules have enough kinetic energy to overcome these interactions and become highly mobile. In the fluid phase the hydrocarbon chains become more disordered leading to a reduction in bilayer thickness and an enhanced membrane permeability.[379,380] However, the highest rate of release is observed at the liposome the phase transition temperature.[346] This is attributed to the increased permeability at the boundaries between the gel and fluid phase domains. At temperatures slightly below the phase transition temperature there are a large number of small isolated domains with a large perimeter and as such maximising the total regions where permeability is highest.[347,348]

5.2.2 The effect of cholesterol on liposome thermo-responsive release

To obtain thermal release profile of the liposome compositions the vesicles were loaded with calcein and the fluorescence was measured after 5 mins of incubation at 25°C before repeating this process raising the temperature in 5°C increments up to 60°C, Figure 5.6B. 1% Triton X-100 was added to control samples to ascertain the maximum fluorescence value, and to all test samples to ensure the calcein fluorescence was not affected during the heating.
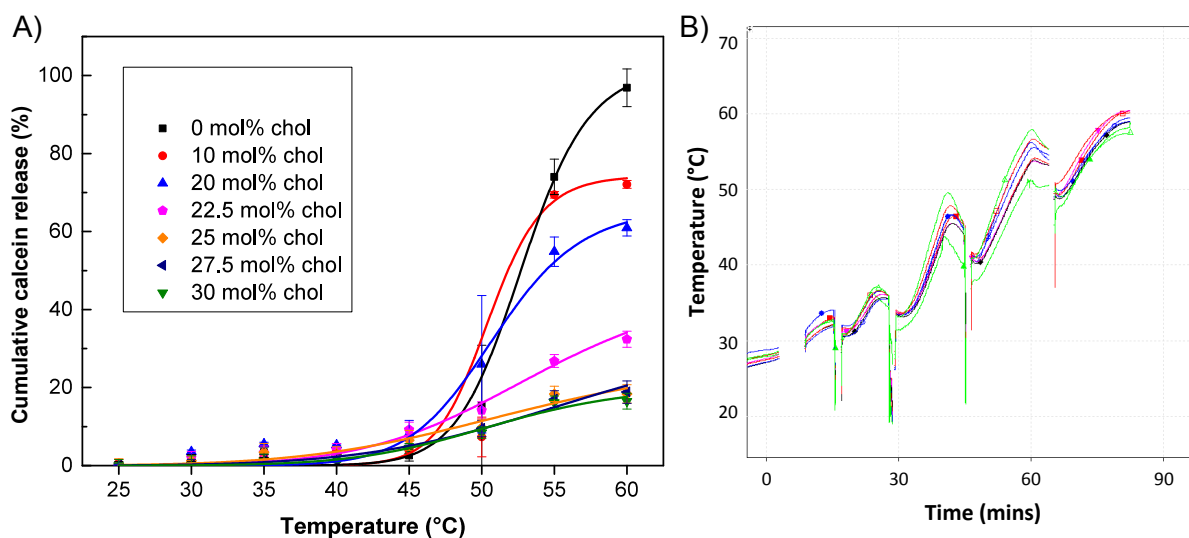
Figure 5.6: A) The thermal release profile of calcein encapsulated within liposomes containing varying concentrations of cholesterol. Liposomes were heated from 25-60°C in 5°C increments measuring the fluorescence after 5 mins at each temperature. Results are the average of 6 replicates. B) The corresponding thermal profile within the wells when increasing the temperature within the incubator.

Figure 5.6A displays the the cumulative calcein release at each temperature and shows that regardless of the cholesterol content, little calcein was released at temperatures below 45°C. The most dramatic increase in fluorescence was observed after incubation at 55°C, the transition temperature of DSPC. A decrease in total calcein released is observed as the cholesterol content increases from 0-25 mol%, at which point the release profiles of liposomes with cholesterol above 25 mol% become indistinguishable from one another. In order to attempt to release the remaining dye the liposomes were heated to 60°C for up to 2 hours, but showed no substantial increase in fluorescence after heating for longer than 5 minutes. The liposomes with cholesterol content greater than 20 mol% were also heated up to 100°C however they showed no additional release beyond 60°C. In both circumstance the sample evaporated rapidly, it is likely that the liposomes degraded at temperatures higher than 60°C, however the decrease in sample volume would have ensured that the calcein remain at self-quenching concentrations even if the liposomes released the dye.

The significant reduction in thermal release at high cholesterol content is attributed to the formation of a liquid-ordered phase in which the phase transition temperature is significantly reduced.[379,381] Redondo-Morata *et al.* observed the diminishing phase transition using the differential scanning calorimetry where the vesicles with 20% cholesterol content exhibited a

dramatically reduced phase transition and liposomes containing 30% cholesterol displayed a broad and small peak such that little phase transition is observed, at contents higher than this no phase transition can be identified, Figure 5.7.[382] This effect has also been shown to almost completely inhibit the release of calcein from DMPC vesicles held at their transition temperature, 24°C.[379]
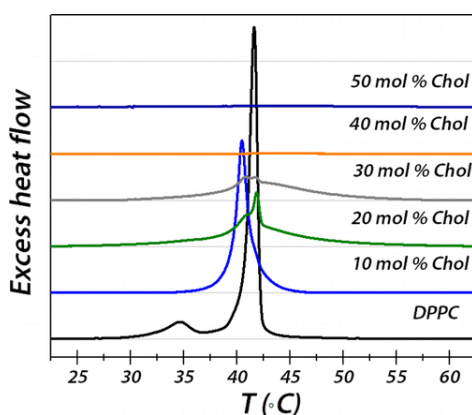
Figure 5.7: Differential scanning calorimetry thermograms of DPPC liposomes containing 0-50 mol% cholesterol, when suspended in 10 mM HEPES, 20 mM MgCl$_2$, and 150 mM NaCl, pH 7.4. Reproduced with permission.[382] Copyright 2012, American Chemical Society.

5.2.3   Substituting DSPC for DPPC to increase the thermal release profile

Another attempt at increasing the release profile of the vesicles was performed by substituting 25-75% of the DSPC for Dipalmitoylphosphatidylcholine (DPPC). The acyl chain length of the phosphatidylcholine lipid directly influences the drug retention capabilities of the vesicles they form with longer chains providing reduced bilayer permeability, therefore replacing a portion of the DSPC with DPPC, hydrocarbon chain lengths of 18- and 16-carbons respectively, may increase the permeability.[383] This however proved to be unsuccessful in increasing the quantity of calcein released, liposomes containing 25, 50 and 75 mol% DPPC released $17 \pm 14\%$, $18 \pm 9\%$ and $17 \pm 3\%$ of encapsulated calcein when incubated at 55°C for 5 mins. This result strongly suggests that cholesterol is the dominant factor governing the liposome thermal release profile. Including DPPC within the liposome composition may yet be useful at a later date due to the lower transition temperature of DPPC (41°C) making the temperature required for optimum release more easily obtainable.

5.2.4 Liposome cargo release when heated to the T_m in the presence of *S. aureus*

The lack of success in finding a suitable liposome composition that sufficiently releases the encapsulated materials only at the transition temperature led to the investigation of alternative method to achieve thermoresponsive release. Certain pore forming toxins (such as actinoporins) exhibit preferential insertion into a lipid bilayer at the boundary between phase domains where there is a lower interfacial energy, otherwise known as the line tension.[384] Upon successful insertion of a toxin molecule into the membrane, additional toxins oligomerise to form secondary pore structures that allow small molecule leakage.[385] As such, it was hypothesised that upon heating to the liposome T_m, despite the reduction in phase transition properties and consequently the gel-fluid domains, there would be an increase in the pore forming toxin activity enabling the release of an encapsulated payload. To investigate this calcein loaded liposomes were incubated with *S. aureus* for an hour before heating for 5 minutes to observe whether embracing the bacteria induced liposome disruption can lead to possible thermal release.
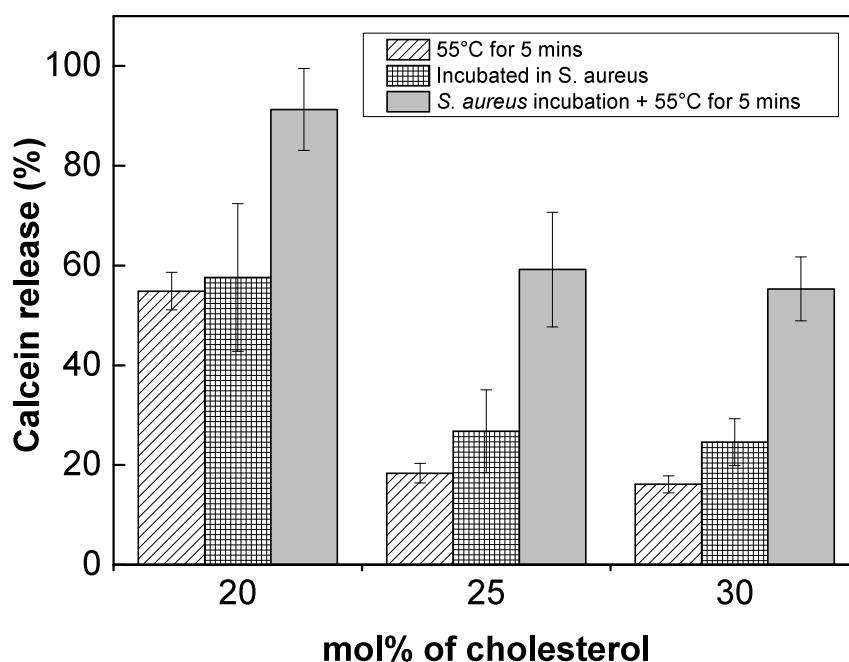
Figure 5.8: Calcein release from liposomes containing 20-30 mol% cholesterol, upon heating to 55°C for 5 mins (diagonal striped), incubation with *S. aureus* (hashed) and heating to 55°C in the presence of the bacteria (solid grey). 100% calcein release was determined through the addition of 1% Triton X-100 to the liposome samples in each environment on day 0. Results are the average of two experiments each with three replicates.

An increased calcein release was observed when heating the liposomes to the T_m in the presence of *S. aureus*. All liposomes between 20-30 mol% cholesterol demonstrated a substantial increase in release compared to those incubated at the T_m or with bacteria individually, Figure 5.8. The 30% cholesterol liposomes, that exhibit the least premature leakage, exhibited $55 \pm 6\%$ of the dye release, substantially more than from heating or the bacteria individually, 16% and 25% respectively. These results infer that heating the liposome to its T_m increases the the pore forming capabilities of the bacterial toxins allowing release of the encapsualted materials. As such, 30 mol% cholesterol liposomes demonstrate high retention of encapsulated materials and an adequate release profile and were therefore taken forward for testing as AMP reservoirs.

5.3 IK8 antimicrobial efficacy and liposomal encapsulation

5.3.1 Determining the MIC of IK8 against *S. aureus* and *P. aeruginosa*

Before determining the best means of liposome fabrication to increase the IK8 encapsulation efficiency, the MIC of IK8 against the pathogenic bacteria must be determined to ensure encapsulation of lethal dosages is possible.
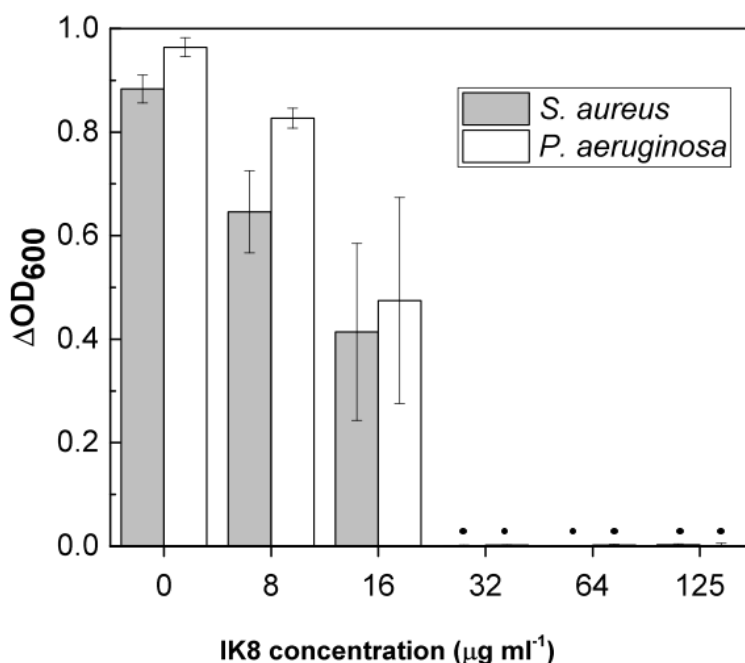
Figure 5.9: The change in the OD_{600} of *S. aureus* and *P. aeruginosa* after an 18 h incubation with increasing concentrations of IK8. The minimum inhibitory concentration (MIC) is the concentration at which there is no increase in turbidity indicating no bacteria proliferation. Black circles indicate the change in $OD_{600} < 0.01$. Results are the average of 6 replicates.

Both *S. aureus* and *P. aeruginosa* both exhibit no proliferation when treated with 32 μg ml^{-1} of IK8, Figure 5.9. The MIC value against *P. aeruginosa* is equal to that published by Ong *et al.* (2013).[15] The MIC value obtained against *S. aureus* is half the published value, this discrepancy can be attributed to the different strains of the bacteria upon which the peptide was tested. Antimicrobial activity is categorised as bactericidal if its mechanism of action directly kills bacteria, or bacteriostatic if the drug inhibits bacteria proliferation thus leading to bacteria eradication. A drug is deemed bactericidal if there is a 3-log reduction in the CFU ml^{-1} of a bacteria when inoculated with the drug at the MIC. As such, *S. aureus* and *P. aeruginosa* were inoculated with 32 μg ml^{-1} of IK8 before incubation for 18 hours and spreading onto agar plates. This produced 5- and 6-log CFU ml^{-1} reductions in *S. aureus* and *P. aeruginosa* respectively, indicating that the IK8 mechanism of action is bactericidal.

5.3.2 Liposome IK8 encapsulation efficiency

The encapsulation efficiency is defined as the proportion of the initial drug added to the lipid film that is contained within the final liposome suspension post removal of non-encapsulated drug. The IK8 encapsulation efficiency was calculated using the following equation,

$$EE(\%) = Dilution factor \times 100 \times \frac{M_{Final}}{M_{Initial}} \tag{5.1}$$

where M$_{Final}$ is the final mass of IK8 after dialysis and M$_{Initial}$ is the mass of IK8 used during the hydration of the lipid film. The encapsulation efficiency of IK8 by the liposomes was assessed by varying both the lipid mass used to form the initial thin film and the concentration of peptide used during the lipid film hydration. Firstly, the dependence of the encapsulation efficiency upon the mass of the lipid film was investigated by increasing the lipid mass from 1 to 20 mg, whilst maintaining the concentration of the hydrating peptide solution, 1 mg ml^{-1}. The excess IK8 was then removed through dialysis for 48 hours before the liposomes were lysed using DMSO and the concentration of peptide was quantified using reverse-phase HPLC, Figure 5.10C. Increasing the mass of the lipid film from 1 to 20 mg in turn increased the encapsulation efficiency from 6 $\pm$ 1 % to 38 $\pm$ 13 %, Figure 5.10A. A lipid film mass of 10 mg was deemed optimal due to the encapsulation of 24 $\pm$ 4% of the initial peptide, $\sim$7.5 times the MIC against *S. aureus* and *P. aeruginosa*. Although lipid films of 15 and 20 mg provided greater encapsulation efficiencies 32 $\pm$ 10 % and 38 $\pm$ 13 % respectively, these samples exhibited significantly higher

sample-to-sample variability (between 4 independent samples) than the 10 mg lipid films. The greater variability in encapsulation efficiency would make controlling the concentration of IK8 administered to bacteria more difficult.
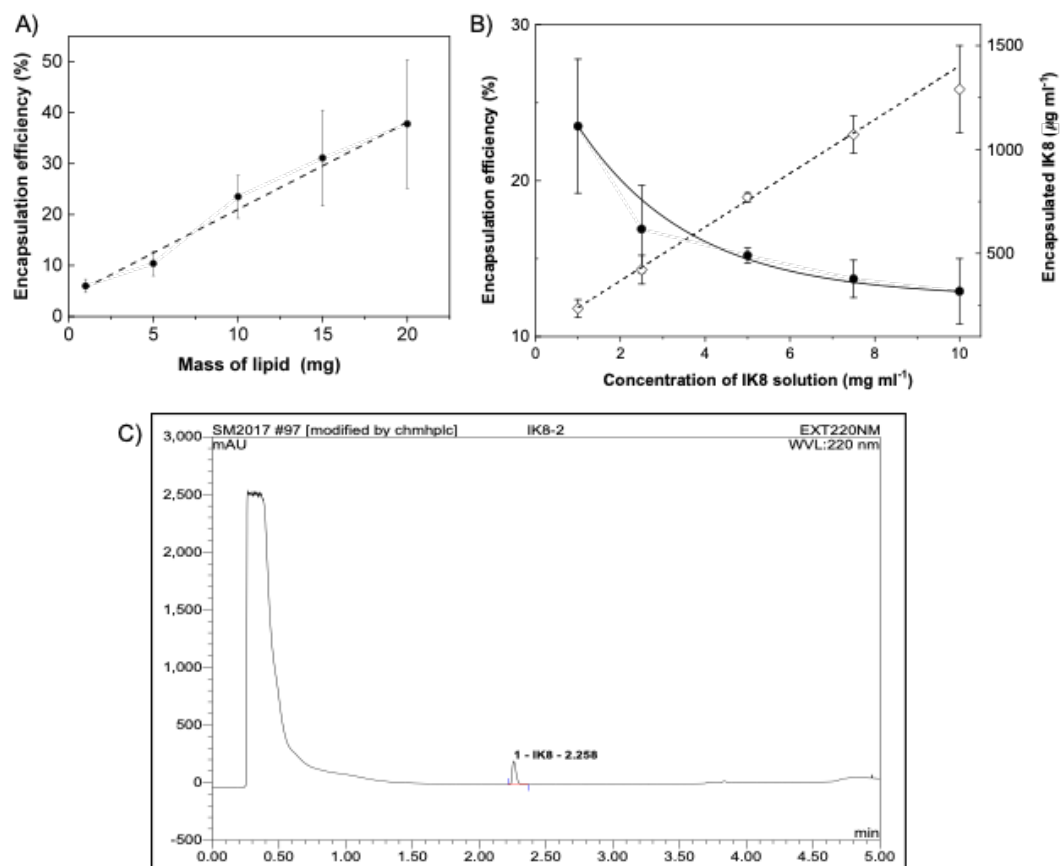
Figure 5.10: A) The encapsulation efficiency of IK8 as the mass of lipid used to form the lipid film was increased when hydrated with a 1 mg ml^{-1} IK8 solution. B) The encapsulation efficiency (solid circles) and capacity (hollow diamonds) when varying the concentration of IK8 in the solution used to hydrate a 10 mg lipid film. C) An example of a HPLC trace used to determine the concentration of IK8 encapsulated within a liposome sample diluted 30 times. Results from both A) and B) are the average of 4 independent experiments.

The next step was to investigate how increasing the IK8 concentration affected the encapsulation efficiency when hydrating a 10 mg lipid film. An increase in the AMP concentration from 1 to 10 mg ml^{-1} resulted in a decrease in the encapsulation efficiency from $24 \pm 4\%$ to $13 \pm 2\%$ (Figure 5.10B), however the total encapsulation capacity was seen to increase, 235 ± 43 to 1290 ± 210 μg ml^{-1}. A 5 mg ml^{-1} IK8 solution deemed the optimum concentration as this enabled encapsulation of 770 ± 21 μg ml^{-1}, $15 \pm 1\%$ of the initial peptide added, approximately 24 times the MIC against both *S. aureus* and *P. aeruginosa* (32 μg ml^{-1}), and demonstrated significantly less sample-to-sample variability in encapsulation efficiency than using higher IK8

concentrations to hydrate the lipid film.

5.3.3   IK8 encapsulation within cationic liposomes

The encapsulation of IK8 within liposomes containing cationic lipids 1,2-dipalmitoyl-3-trimethylammonium-propane (DPTAP) was next investigated. The intention being that the cationic lipids would provide electrostatic repulsion to the cationic IK8 to inhibit leakage. This would allow a reduction in the cholesterol content within the liposome bilayer and hence could increase the thermal responsivity of the liposome and in turn increase the release efficiency.

The IK8-loaded cationic liposomes were formed through thin lipid film hydration however a portion of the DSPC was replaced with DPTAP, whilst maintaining constant proportions of cholesterol and DSPE-PEG2k (30 and 5 mol% respectively). The inclusion of DPTAP provided the liposomes with a positive zeta-potential, with increasing positivity as the proportion of DPTAP also increased, Table 5.2. The DPTAP did not appear to affect the IK8-loaded liposome formation, with all samples having an initial average diameter between 350-400 nm. However, after one day the cationic liposomes showed a substantial increase in diameter, with those containing a higher proportion of DPTAP growing more, whereas the liposomes without DPTAP did not. Control samples of liposomes containing 5% DPTAP that were fabricated without IK8 demonstrated no change in diameter over 24 hours, 372 ± 38 nm to 379 ± 53 nm, meaning that the increase in liposome size only occurred with samples containing IK8 and indicating that the AMP is the cause of the structural instability.

Table 5.2: The initial charge and the morphological stability of IK8-loaded cationic liposomes.

DPTAP (%)	Zeta-potential (mV)	Avg. diameter (nm)	Avg. diameter after 1 day (nm)
0	-5.9 ± 3.9	365 ± 36	364 ± 40
5	+24.8 ± 8.2	395 ± 84	416 ± 115
10	+36.3 ± 3.7	393 ± 86	589 ± 220
20	+40.4 ± 6.4	387 ± 76	779 ± 266

Table 5.3: The initial encapsulation capacity of DPTAP containing liposomes and the peptide leakage after one and two days.

DPTAP (%)	Encapsulation efficiency	Leakage after 1 day	Total leakage after 2 days
0	23.5%	1%	1%
5	20.2%	84.5%	85.8%
10	17.1%	86.6%	91.2%
20	6.0%	84.1%	85.0%

The effect of including DPTAP on the liposome leakage was next investigated. IK8-loaded

liposomes containing 0-20% DPTAP were fabricated and cleaned of excess peptide by passing the sample through an Amicon®Ultra-4 Centrifugal Filter Unit (M_w cutoff = 10 kDa). This removed half of the supernatant each time which was replaced with fresh buffer, the process was repeated 10 times. The effects of DPTAP on the liposome leakage were assessed by incubating the samples at 37°C for 24 or 48 hours, before cleaning with centrifugal filters, as previously described, and disrupting the remaining liposomes with DMSO (5% v/v) and using HPLC to quantify the remaining IK8 concentration. After one day of incubation all liposomes containing DPTAP encapsulated less than 14% of the IK8 the same liposomes contained immediately post fabrication, indicating that over 86% of the peptide had leaked out of the vesicles, Table 5.3. Liposomes without DPTAP exhibited ~1% leakage under the same conditions. The encapsulation efficiency was also seen to decrease as the positive charge on the liposome increased, from 24% to 6% as the zeta-potential changed from -6 to +40 mV. This indicates that there is electrostatic repulsion between the liposome and the peptide, that could be affecting both the encapsulation efficiency and the structural integrity. As such, it was decided that cationic lipids should not be included within the liposome composition.

5.4   IK8-loaded liposome colloidal stability

The colloidal stability of the IK8-loaded liposomes was tested to ensure that the vesicles did not agglomerate or distort during storage in a fridge at 4°C. DLS measurements of liposomes loaded with 0.8 mg ml^{-1} were taken over the course of three weeks after fabrication.

Post fabrication, the immediate liposome diameter was 365 ± 36 nm and after three weeks 385 ± 42 nm, Figure 5.11. The polydispersity index (PDI) also showed very little change with values of 0.12 ± 0.05 and 0.17 ± 0.04, at days 0 and 21 respectively, a homogeneous sample with a PDI value of ≤ 0.2 is generally considered as monodisperse.[386] As such, the IK8-loaded liposomes showed excellent colloidal stability over the three-week observation period.
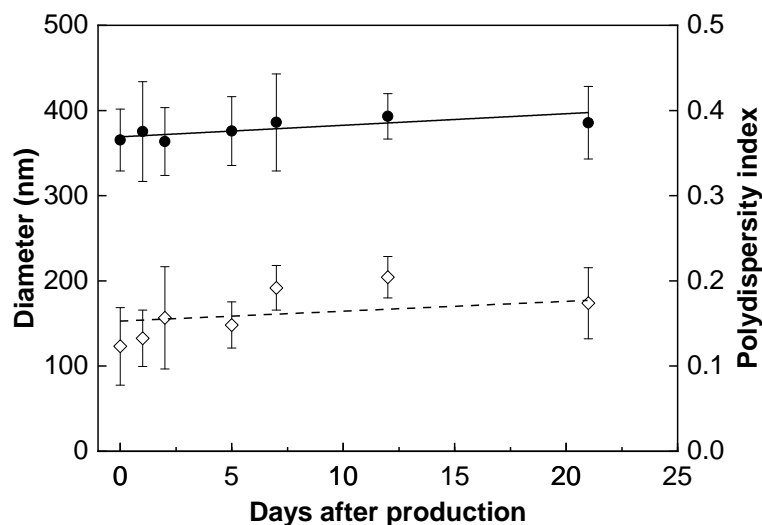
Figure 5.11: The diameter (solid circles) and polydispersity index (hollow diamonds) of IK8-loaded liposomes held when stored in a fridge at 4°C. Results are the average of 4 independent experiments, and lines correspond to linear fits.

5.5 IK8-loaded liposome antimicrobial effects

The antimicrobial properties of the IK8-liposomes was assessed by adding varying amounts of vesicles (containing 0.5, 1, 2 and 4 times the MIC) that were intact, lysed with 5% v/v DMSO, or vesicles heated to 55°C for 5 mins, to a *S. aureus* suspension. Intact vesicles were added to the bacteria to ensure that the bacteria induced leakage of IK8 would not inhibit proliferation, such that the desired thermally induced release is negated. The liposomes lysed using DMSO were added to the bacteria to determine whether the maximum release of IK8 from the liposomes would be substantial enough to provide antimicrobial effects. The liposomes heated to 55°C (± 1°C for 5 mins) immediately prior to the addition to the bacteria, determined whether the thermally induced release of IK8 could reduce bacteria proliferation. After incoulation with the liposomes the bacteria samples were incubated at 37°C for 18 hours before they were centrifuged (200 x g, 5 mins) to pellet the bacteria and leave the liposomes in solution, the supernatant was then discarded and the bacteria resuspended in MHBII before the OD_{600} was measured.
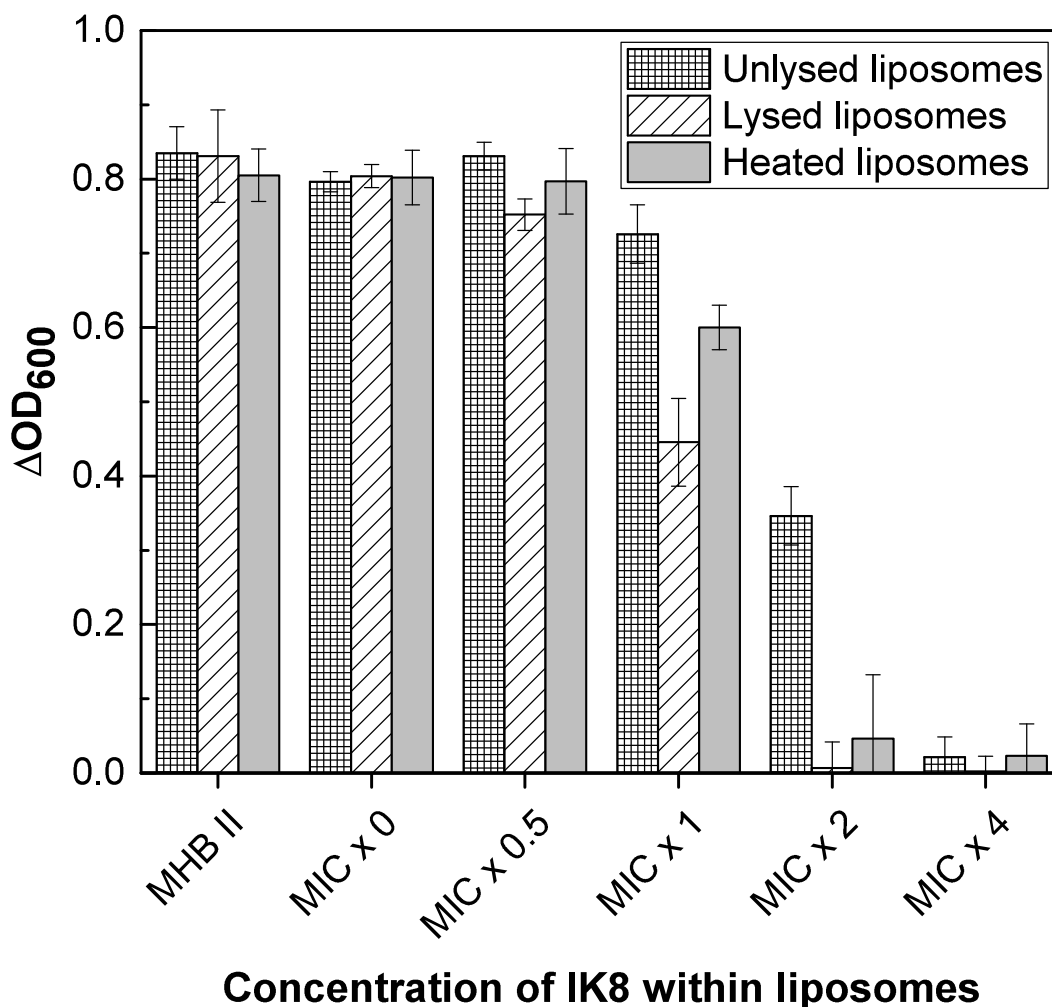
Figure 5.12: *S. aureus* proliferation upon inoculation with IK8-loaded liposomes that have been lysed using DMSO, heated to 55°C for 5 minutes an hour after addition to the bacteria, or intact vesicles, as compared to the proliferation of the bacteria in Mueller-Hinton broth. Results are the average of 2 independent experiments, each with 6 replicates.

From Figure 5.12 several conclusions can be drawn. Firstly, the lysed liposomes containing the MIC x 2 of IK8 showed complete inhibition of *S. aureus* proliferation. Lysed liposomes containing 1 x MIC showed only partial restriction of growth indicating that the entire content of the liposomes was not adequately released to perform the antimicrobial activity. As such, in order to stop any growth of *S. aureus* the bacteria must be treated with liposomes containing between 1-2 times the MIC. Secondly, the thermally triggered release of IK8 only showed increased antimicrobial activity compared to the unlysed liposomes when loaded with 1 and 2 times the MIC. The heated liposomes containing the MIC x 2, showed near total restriction of proliferation, however insufficient quantities of IK8 were released upon heating of 1 x MIC

liposomes to have any significant effect on the bacteria growth. Thirdly, the bacteria induced leakage of IK8 from the unlysed liposomes containing 2 x MIC gave rise to a significant decrease in bacteria proliferation, and the leakage from the liposomes containing the MIC x 4 produced complete restriction of growth. Finally, neither the the addition of liposomes containing no IK8 (MIC x 0) or the heating of the bacteria to 55°C for 5 mins produced any effects on the bacteria proliferation. The results from Figure 5.12 demonstrate that the IK8-loaded liposomes are able to provide thermal sensitive release of AMPs to induce antimicrobial activity whilst restrict some of the bacteria induced leakage. Moving forward, 2 times the MIC was the optimal concentration of liposome encapsulated IK8, enabling complete inhibition of bacteria proliferation upon liposomal release of AMP and significant bacterial growth without vesicle heating or lysis.

5.6 Liposome protection of IK8 from protease degradation
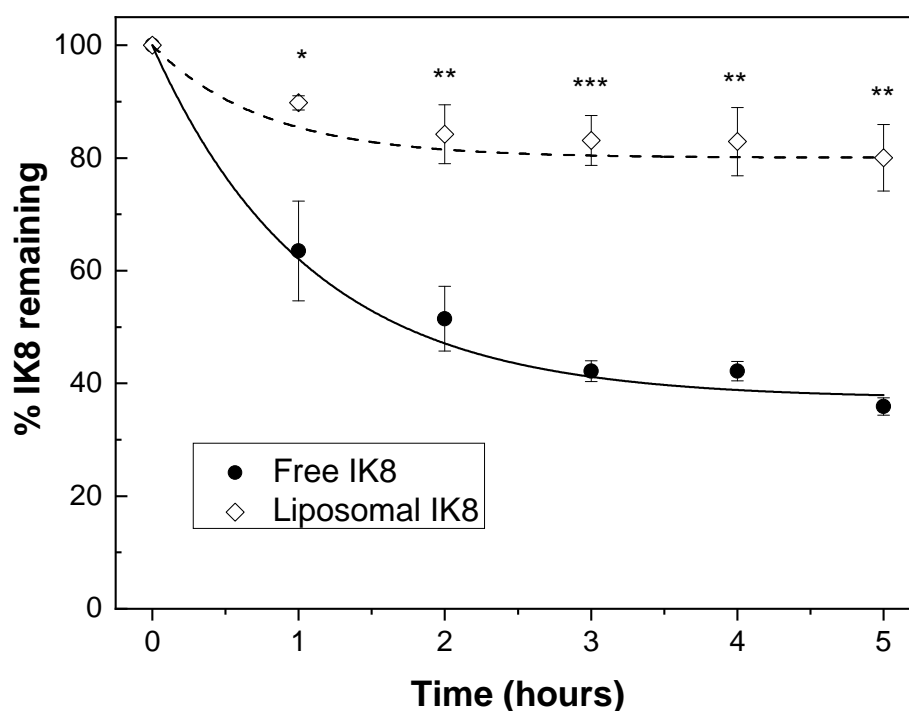
Figure 5.13: The proportion of IK8 remaining when free in solution (solid circles) or encapsulated within liposomes (hollow diamonds) upon the addition of 0.5 μg ml^{-1} of the protease trypsin. Results are the average of three independent experiments. Two-tailed T-testing was performed between free and encapsulated IK8 quantities remaining at each time point, p-values indicate; * < 0.05, ** < 0.01, *** < 0.001.

The final stage of the liposome testing was to assess whether the liposomal encapsulation of IK8 provided protection against enzymatic degradation. AMP are highly susceptible to proteolysis, meaning the internalisation inside a vehicle could protect the drug molecule to ensure that lethal concentrations are retained until the treatment is required. IK8-loaded liposomes and IK8 free in solution were incubated with 0.5 μg ml^{-1} of the protease trypsin (approximately double the concentration in the blood of a healthy adult)[387] for 5 hours with a sample extracted hourly, the trypsin was deactivated using a 40% tricholoacetic acid and the concentration of AMP quantified using HPLC. Figure 5.13 shows that after 5 hours over double the concentration of IK8 encapsulated within liposomes was intact compared to the free IK8, 80 $\pm$ 6 % and 36 $\pm$ 2 % respectively. The lipid bilayer encapsulating the IK8 therefore provides a protective barrier that restricts the access of protease to the AMP, thus allowing treatment infection environments that are often rich in such proteolytic enzymes, such as an open wound.[388]

5.7 IK8 and phospholipid-stabilised AuNR toxicity to fibroblast cells

Considering the cytotoxicity of any medical delivery device is important, however, it is of even more significance when being used to treat a wound that is susceptible to infection. Hindering the regenerative process through increasing the toxicity to mammalian cells leaves the wound vulnerable to infection and increases the risks of a wound becoming chronic.[389–391] As such, the cytocompatibility of both IK8 and the phospholipid-stabilised AuNRs was assessed using human dermal fibroblast (HDF) cells; which play a critical role in the formation of granulation tissue.[392,393] Briefly, HDF cells were seeded into a 96-well plate, 7 x 10^4 cells per well, and incubated for 24 hours. The media was then replaced by media with 10% PBS containing the IK8 or lipid-coated AuNRs to provide final concentrations between 8-125 μg ml^{-1}. The cells were agian left to incubate for 24 hours before the HDF viability was determined using a WST-1 assay.
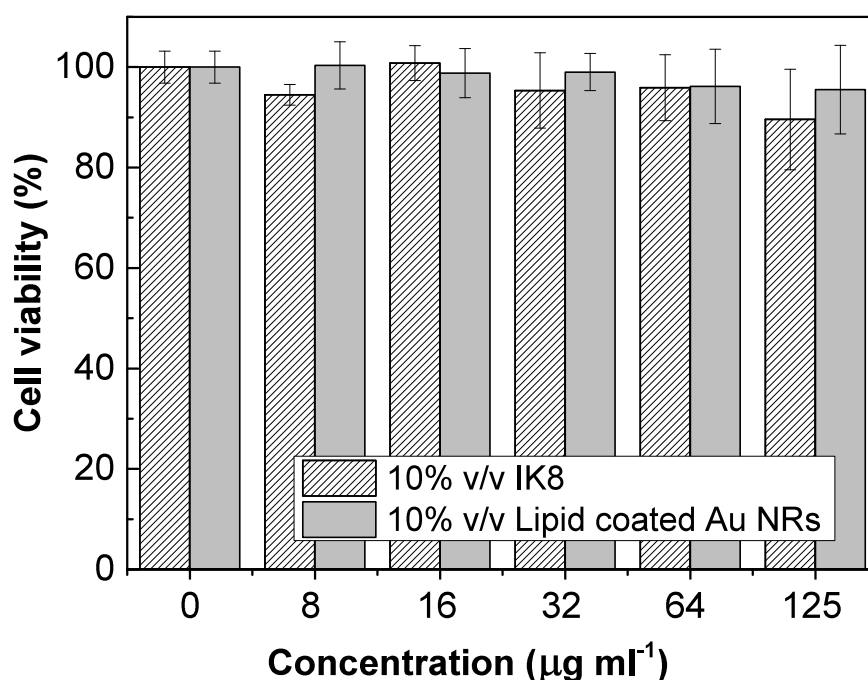
Figure 5.14: Human dermal fibroblast cell viability after incubation with increasing concentrations of IK8 and phospholipid stabilised AuNRs for 24 hours. Results are the average of 6 independent samples.

No cytotoxicity was observed upon incubation of the HDF cells with either the lipid coated AuNRs or free IK8 in media at concentrations four times greater than those required to completely inhibit the growth of both *S. aureus* and *P. aeruginosa*, Figure 5.14. Ong *et al.* have previously demonstrated that IK8 has very weak hemolytic properties requiring 2 g l^{-1} in order to induce ~10% hemolysis.[16] The lack of cytotoxicity and hemolytic activity of IK8 at concentrations several times the MIC against S. aureus potentially allows for the liposomal loading of high concentrations of peptide to provide multiple treatment events, with no risk of toxicity in the event of leakage. There are currently only two studies in the literature investigating the toxicity of phospholipid-coated AuNRs, both of which provide significantly higher toxicity values than we present. Early work by Takahasi *et al.* demonstrated a 20% reduction in HeLa cell viability at 2.4 μg ml^{-1} of PC-AuNRs, however it appears likely that residual amounts CTAB remained in solution.[394] A later study demonstrated a decrease in viability of MCF-7 breast cancer cells, 3T3 fibroblast cells and HMEC-1 dermal microvessel endothelial cells when incubated with 1,2-dimyristoyl-sn-glycero-3-phosphocholine (DMPC) coated AuNRs.[395] However, the maximum Au concentration used in this study was 20 μg ml^{-1} and all cell lines showed less than a 20% drop in viability. It is clear that considerably more research is required to gain a

better understanding of the toxicity profiles of phospholipid-stabilised AuNRs.

5.8   Light-stimulated delivery of IK8 to treat *S. aureus*

To determine the antimicrobial capabilities of the photothermal triggered release of liposome encapsualted IK8, different concentrations of liposomes, corresponding to IK8 concentrations between 0-4 times the MIC against *S. aureus*, were added to a bacteria suspension ($1x10^6$ CFU ml^{-1}) along with 48 μg ml^{-1} of lipid-coated AuNRs, allowed to incubate for 1 hour before being irradiated at 2.1 W cm^{-2}, 860 nm, for 10 mins, heating the sample to 55°C. After an 18 hour incubation the bacteria are diluted and spread on MHII agar plates, the number of viable CFUs was then counted the following day.
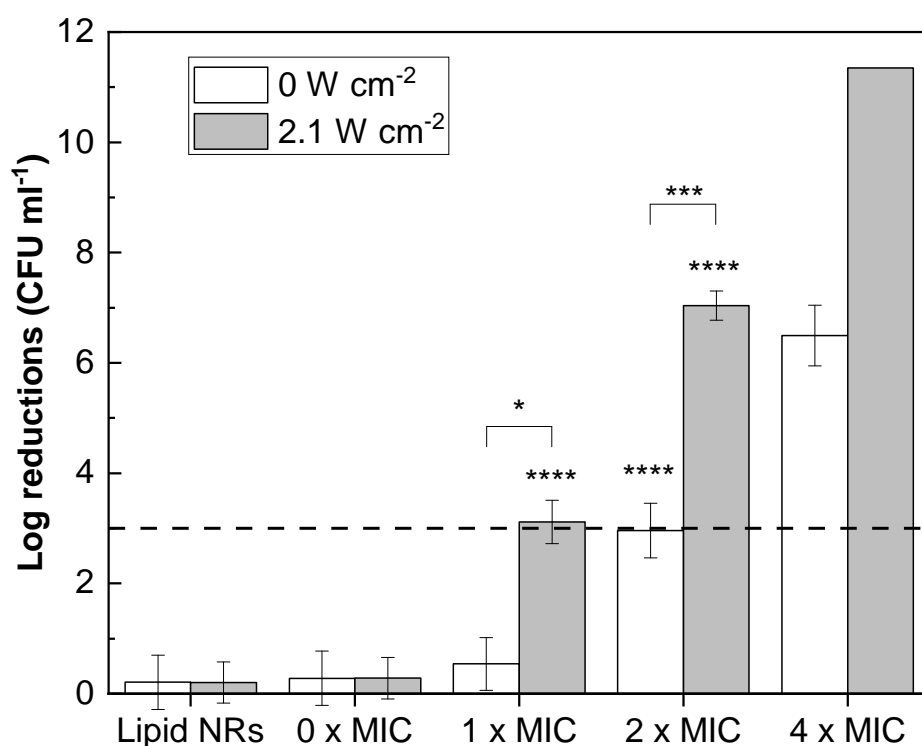
Figure 5.15: The effects upon *S. aureus* viability when treated with liposomes loaded with 0, 1, 2 and 4 times the MIC and 48μg ml^{-1} of phospholipid-coated AuNRs, when irradiated at 0 and 2.1 W cm^{-2} for 10 mins. Control samples containing just NRs are used to determine the toxicity of the NRs and the photothermal killing in the absence of liposomes. The threshold for bactericidal activity, a 3-log reduction in CFU ml^{-1}, is denoted as a dashed line. Results are the average of 2 independent experiments, each containing 6 replicates of treated bacteria and plated thrice. Two-tailed T-testing was performed against untreated *S. aureus* in broth unless otherwise stated with p-values indicating; $* < 0.05$, $*** < 0.001$, $**** < 0.0001$.

Several results may be drawn from Figure 5.15. Firstly, all samples containing IK8 demonstrate a significant increase in number of log reductions in CFU ml^{-1} when irradiated at 2.1 W cm^{-2}, compared to no irradiation. This clearly indicates that the photothermal heating has triggered the release of the encapsulated AMP causing the reduction in bacteria viability compared to the sample without irradiation. Secondly, bactericidal activity, a 3-log reduction in the number of viable bacteria, was achieved when using only 1 x the MIC of IK8 when irradiated. Thirdly, samples containing liposomes with 2 and 4 x the MIC both showed 3- and 7-log reductions in the CFU ml^{-1} without the application of the laser indicating that the bacteria induced leakage of IK8 from the liposomes has then produce bacteria killing effects itself. The bacteria treated with liposomes containing no IK8 showed no bacteria killing both with and without the laser irradiation, meaning that the liposomes themselves do not affect the bacteria viability and that the laser irradiation also does not cause any bacteria death. The bacteria treated with the lipid-coated AuNRs also showed no bacteria killing activity both with and without the laser irradiation. This demonstrates that not only are the lipid AuNRs non-toxic to the *S. aureus* but that the photothermal heating to 55°C for 10 minutes did not hinder the bacteria proliferation.

5.9 Photothermal enhancement of the IK8 antimicrobial efficacy

Preliminary experiments incubating *S. aureus* at 60°C for 10 mins demonstrated a decrease in viability. As such, it was investigated as to whether the photothermal heating can induce bacteria death by increasing the concentration of AuNRs which in turn increases the temperature attained during photothermal heating using a continuous wave laser at 2.1 W cm^{-2}. By increasing the AuNR concentration to 105 μg ml^{-1} a maximum temperature of 65°C could be reached. The *S. aureus* were treated with three different conditions; 1) liposomes containing 1 x MIC of IK8 alongside the AuNRs under irradiation, to show triggered release of IK8 and possible photothermal enhancement of the AMP killing, 2) AuNRs with irradiation, to demonstrate the potential antimicrobial effects of photothermal heating alone, 3) 1 x MIC IK8-loaded liposomes and AuNRs, to demonstrate whether the inclusion of higher concentrations of AuNRs can induce AMP leakage.
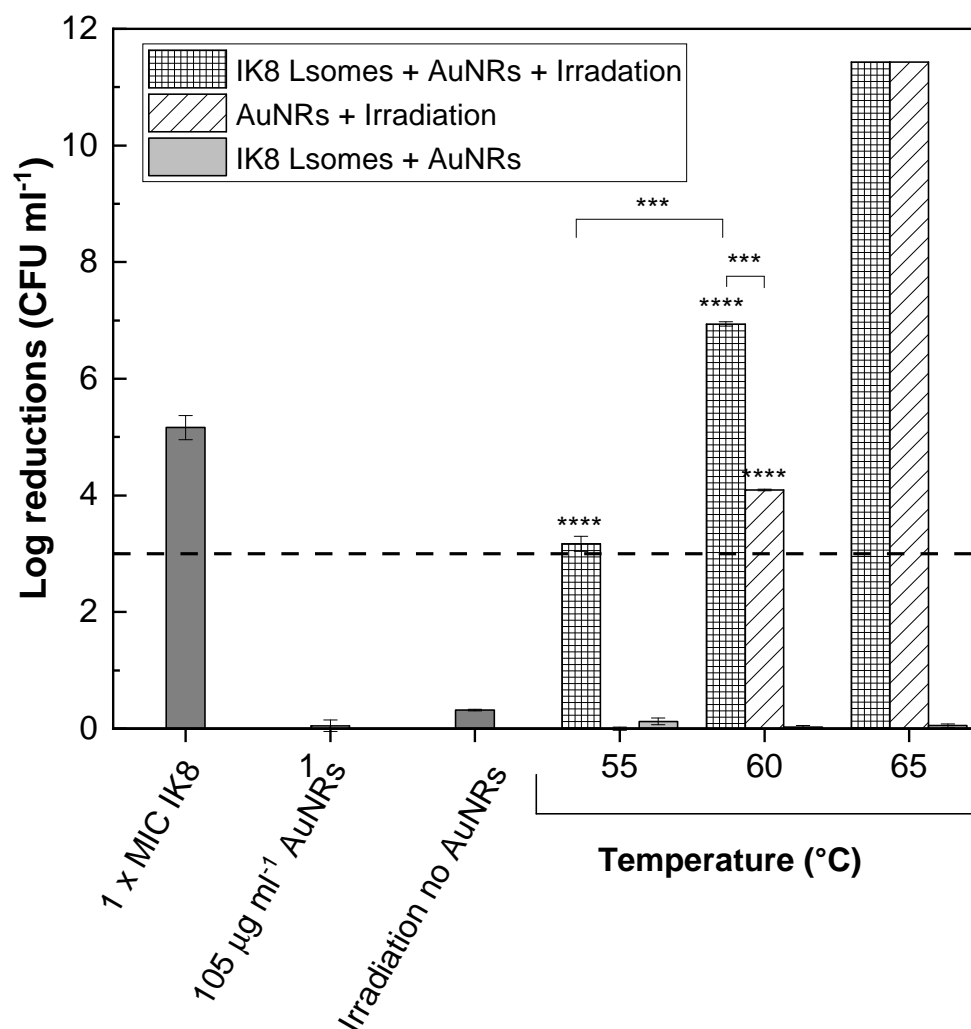
Figure 5.16: The log-reductions in *S. aureus* when treated with IK8-loaded liposomes and AuNRs (grey) without irradiation and AuNRs alone (diagonal slashed) and IK8-liposomes with AuNRs (hashed) both when irradiated at 2.1 W cm^{-2} for 10 mins. The *S. aureus* were treated with 50, 80 and 105 μg ml^{-1} of AuNRs to heat the samples to 55°C, 60°C and 65°C respectively. Results are the average of 2 independent experiments, each containing 6 replicates of treated bacteria and plated thrice. Two-tailed T-tests were performed against untreated *S. aureus* in broth unless otherwise stated with p-values indicating; *** < 0.001, **** < 0.0001.

There are three main conclusions that can be drawn from Figure 5.16. Firstly photothermal triggered release of IK8 is again demonstrated, resulting in a 3-log reduction in *S. aureus* CFU ml^{-1}, when IK8-loaded liposomes and AuNRs were heated to 55°C. Secondly, photothermal killing of *S. aureus* is observed at 60°C. In the absence of AMPs a 4-log reduction in CFU ml^{-1} was observed under irradiation, clearly indicating that the bacteria death can only be attributed to the temperature. Further increasing the temperature to 65°C resulted in complete bacteria eradication. Thirdly, the use of the AMP-loaded liposomes and the photothermal heating

provided additive antimicrobial effects. As demonstrated in Figure 5.6A, when heating 30 mol% cholesterol liposomes beyond their gel-fluid phase transition temperature there is little additional release of materials, meaning that the antimicrobial effects of the IK8-liposomes are likely to be very similar, independent of whether the sample is heated to 55°C or 60°C. The 7-log reduction in viable *S. aureus* is therefore due to the additive 3-log reduction from the release of IK8 and the 4-log reduction from the photothermal heating to 60°C. This figure also depicts that the antimicrobial activity of the irradiated IK8-liposome and AuNRs at 55°C is 2-log lower than when the AMP is in solution, implying that some of the peptide is retained within the liposomes. There was no decrease in the *S. aureus* viability when the IK8-liposomes and AuNRs were added to the bacteria without the laser application, meaning that the AuNRs do not destabilise the liposomes causing release. Again no bacteria decrease was observed when treated with the maximum concentration of AuNRs, 105 μg ml^{-1}, and when irradiated in the absence of AuNRs.

Conclusion

In this chapter the optimal lipid composition, DSPC/cholesterol/DSPE-mPEG2k (65/30/5 mol%), was determined to prevent premature leakage of encapsulated materials ($< 5\%$ at 37°C in all media), but provide release when heated above the gel-fluid lipid phase transition temperature, T$_m$=55°C, in the presence of pathogenic bacteria. The liposome fabrication procedure was also optimised to encapsulate 770 μg ml^{-1} of IK8, approximately 24 times the MIC against both *S. aureus* and *P. aeruginosa*. These liposomes are also suitable for storage at 4°C, demonstrating no leakage of encapsulated materials or change in diameter after 3 weeks. The liposomal encapsulation of AMPs also offers significant protection against proteases in solution with 80% of liposome encapsulated AMP remaining after incubation with trypsin, as opposed to 36% of free IK8 in solution remaining, potentially providing a viable route to toward clinical translation. Utilising the IK8-loaded liposomes in combination with phospholipid stabilised AuNRs the first instance of the triggered delivery of AMPs was demonstrated, enabling antibacterial treatment against *S. aureus*. Using liposomes containing the MIC of IK8 no antimicrobial effects were observed until the system was heated to 55°C, the gel-fluid phase transition temperature of the liposomes, at which point there was a 3.1-log reduction in CFU ml^{-1}. The bacteria killing effects of photothermal heating alone were also investigated; *S. aureus* viability was unaffected

until the sample was heated to 60°C leading to a 4.1-log reduction in CFU ml^{-1}. When used in combination with the IK8-liposomes the system produced a 6.9-log reduction in CFU ml^{-1}, depicting an additive antimicrobial effect from the AMP and photothermal treatments. This is the first demonstration of the photothermal enhancement of AMPS. Moving forward this thesis will be discussing the incorporation of this AuNR - IK8-liposome system into a hydrogel to form the basis of a therapeutic wound dressing.

Chapter 6

Nanoparticle loaded hydrogel for the light-activated release and photothermal enhancement of antimicrobial peptide activity

Some of the content within this chapter can be found within the following the following publications: S. C. T. Moorcroft *et al.* Nanoparticle-Loaded Hydrogel for the Light-Activated Release and Photothermal Enhancement of Antimicrobial Peptides. *ACS Appl. Mater. Interfaces* 2020, 12(22), 24544–24554.[350]

Motivation:

In this chapter we will be investigating the incorporation of the IK8-loaded liposome and phospholipid-stabilised AuNR system, described in Chapter 5, into a hydrogel to create a therapeutic wound dressing, see Figure 6.1. The incorporation of AMP-loaded liposomes and AuNRs into a hydrogel as a scaffold that could be placed in contact with a wound would provide a drug depot that releases the antimicrobial content only upon exposure to specific stimuli. Hydrogels are excellent materials to provide the structural basis for the dressing due their fundamental biocompatibility owed to their high levels of water content and high permeability for oxygen.[396,397]

The moist environment that hydrogels maintain aids the epidermal regeneration and reduces scarring by accelerating the angiogenesis process, preventing cell dehydration and increasing the rate at which dead cells and fibrin are broken down.[19,398] The wide range of materials from which to form a hydrogel provides an array of fabrication options and tunable mechanical properties.[399]

Here the fabrication of a 4-arm PEG-maleimide hydrogel (4APM) crosslinked with PEG dithiol was investigated, before studying how the properties of the gels are affected by the inclusion of AuNRs and liposomes. The photothermal properties of the nanoparticle loaded gel were characterised to determine whether antimicrobial triggered release and photothermal enhancement of antimicrobial activity are possible from within the gel dressing. Furthermore, this chapter discusses the possibility of finely tuning the AMP release properties such that an individual gel could provide multiple rounds of treatment.
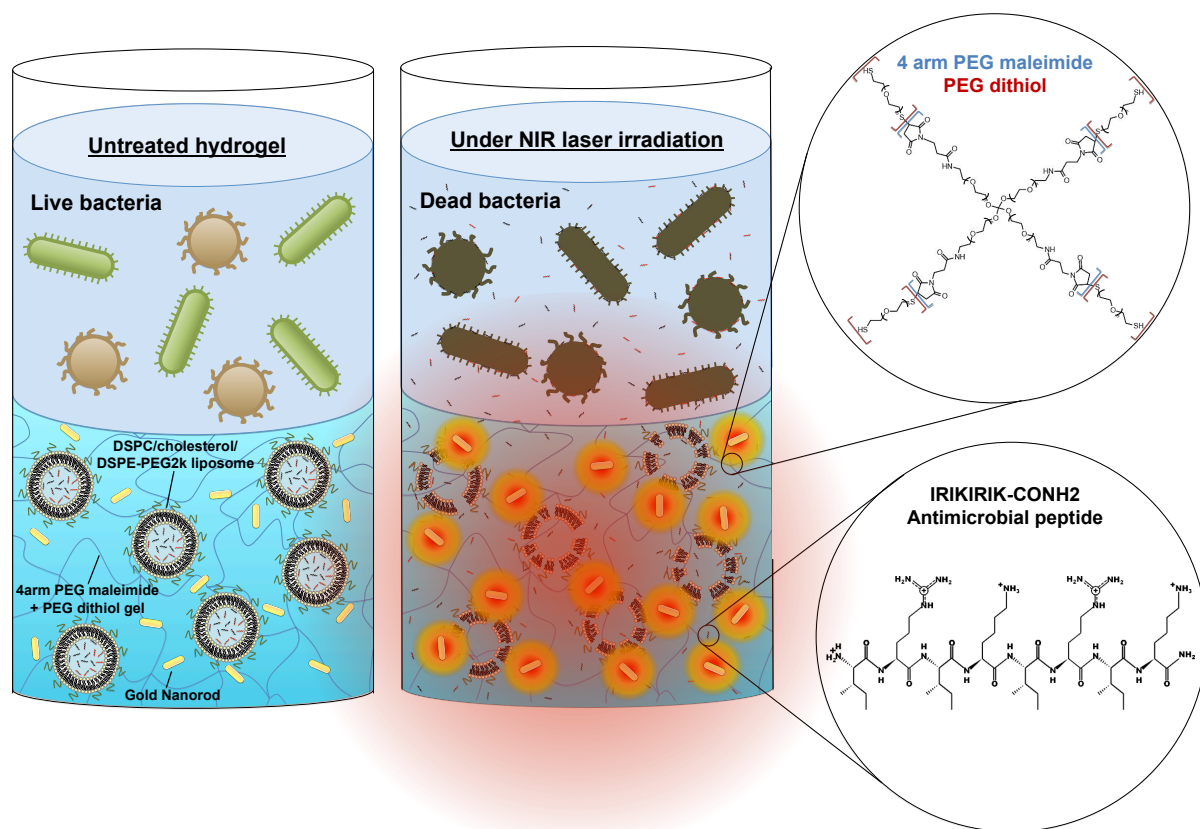
Figure 6.1: A schematic representation of the PEG-based hydrogel containing gold nanorods and antimicrobial peptide (IK8) loaded liposomes, demonstrating the mechanism for NIR light-triggered release of AMPs.

6.1   Hydrogel fabrication and characterisation

The properties of the IK8-liposome and AuNR system placed very stringent restrictions on the type of hydrogel that would be suitable for use. Commonly hydrogel gelation is initiated with heating, uv-irradiation or the use of toxic chemicals, however, these methods are unsuitable for the liposomal delivery of AMPS; heating could prematurely trigger the release of the encapsulated materials, peptide bonds absorb UV light meaning they are susceptible to UV irradiation that can alter the primary and secondary structures they form,[400] and it is highly preferential not to include any toxic components within a medical device.[401,402] As such, a hydrogel consisting of 4-arm poly(ethylene) glycol-maleimide (4APM) cross linked with PEG dithiol was deemed appropriate as the two components of the gel need only be mixed in the correct buffering environment to initiate and control the gelation time.[403] Both of the components have been confirmed as non-toxic and there is a large amount of literature describing the cytocompatibility of PEG-based hydrogels.[404–409] The PEG hydrogel was also chosen due to its high permeability by small hydrophilic molecules and largely neutral network, which means that the gel should provide minimal interference with the AMP release kinetics.[410]

6.1.1   Optimising the gel fabrication to control gelation time
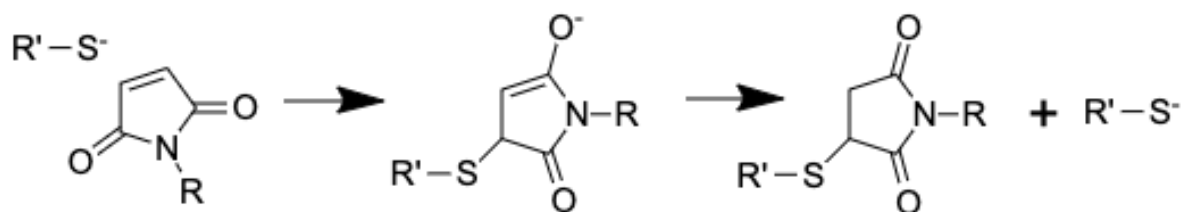
Figure 6.2: Thiol-maleimide michael addition reaction. Initially the thiolate anion will attack the π-bond within the maleimide group to form an enolate intermediate before the negatively charged oxygen deprotonates an additional thiol group, forming a thiolate anion that can react with another maleimide group.

The formation of the gel occurs through a thiol-michael addition 'click' reaction between the maleimide group of the 4APM (R) and the thiol groups of the PEG dithiol (R') as depicted by Figure 6.2. In this reaction the thiol-michael addition occurs through the deprotonation of the thiol to form a thiolate-anion, a strong nucleophile that can attack the π-bond within the maleimide group, binding the two PEG molecules together.[411] A basic enolate intermediate is formed which in turn deprotonates another thiol group causing a chain reaction. As demonstrated by Table 6.1, the weight percentage of the gel, the buffer, the buffering concentration

Section 6.1

Chapter 6. Nanoparticle loaded hydrogel for the light-activated release and photothermal
enhancement of antimicrobial peptide activity

and the pH all affect the rate of the thiol-maleimide reaction which in turn affects the gelation
time. In order to fabricate the gel a 40 μl droplet of the 4APM was placed onto a parafilm
coated glass slide and 10 μl of the PEG dithiol solution was injected directly into the droplet.
The solution was then retracted and expelled from a pipette until this was no longer possible,
the duration of this mixing was defined as the gelation time. The samples were also inverted in
order to ensure that the liquid does not flow.

Table 6.1: The effects of changing the gel wt%, the buffer, the buffering concentration and the
pH on the gelation time and the characteristics of the gel post gelation. Each bordered row
represents a different set of experimental results to compare, for ease of reading. The first bor-
dered row demonstrates the effects of fabricating gels of decreasing wt% and salt concentration
using PBS buffer, the second row to determine the effects of pH using sodium citrate buffer,
the third row was to observe how the salt concentration affects the gel formation and both the
fourth and fifth rows display the effects of the wt% on gels formed using different pH values.

Gel wt%	Buffer (conc.)	pH	Gelation time	Hydrogel description
10	PBS (1 X PBS)	7.4	0 s	Instant gelation
5	PBS (1 x PBS)	7.4	0 s	Instant gelation
2.5	PBS (1 X PBS)	7.4	0 s	Instant gelation
1	PBS (1 x PBS)	7.4	0 s	Instant gelation
5	PBS (0.1 X PBS)	7.4	0 s	Instant gelation
5	PBS (0.01 X PBS)	7.4	0 s	Instant gelation
5	Sod. cit. (10 μM)	4	> 30 mins	A gel was not formed in 30 mins
5	Sod. cit. (10 μM)	5	7.5 mins	A sticky and ductile gel
5	Sod. cit. (10 μM)	6	20 s	A solid, smooth and homogenous gel
5	Sod. cit. (10 μM)	7	0 s	Instant gelation
5	Sod. cit. (100 μM)	6	0 s	Instant gelation
5	Sod. cit. (1 μM)	6	90 s	A sticky and ductile gel
10	Sod. cit. (10 μM)	5	2 mins	A solid, smooth and homogenous gel
2.5	Sod. cit. (10 μM)	5	15 mins	A sticky and ductile gel
1	Sod. cit. (10 μM)	5	> 30 mins	A gel was not formed in 30 mins
10	Sod. cit. (10 μM)	6	0 s	Instant gelation
2.5	Sod. cit. (10 μM)	6	2.5 mins	A sticky and ductile gel
1	Sod. cit. (10 μM)	6	20 mins	A very sticky and ductile gel

When the two components of the gel were initially dissolved in PBS, regardless of the final weight
percentage of the gel and the PBS concentration, all gels exhibited instantaneous gelation, Table
6.1. The gelation occurred so rapidly that the pipette tip containing the PEG dithiol pierced
the 4APM droplet a gel formed in the pipette tip meaning the majority of the PEG dithiol
solution could not be injected. As such, in order to slow the reaction down it was decided to
move to a more acidic buffer.[403] Sodium citrate buffer (10 μM) was chosen as the pH could
be tuned between pH 2-8 and allowed simple control over the salt concentration. 5 wt% gels
were then fabricated using buffers ranging from pH 4-7. It was found that increasing the buffer
acidity increased the gelation time, such that a gel that formed instantly using the pH 7 buffer

took > 30 mins at pH 4. This is expected as a more basic the buffer can deprotonate the thiol groups faster causing a more rapid gelation, whereas at the most acidic condition (pH 4) no deprotonation occurs and as such no gel was formed. The effects of salt concentration were then observed by fabricating 5 wt% gels using pH 6 citrate buffers at 1 and 100 μM. The highest salt concentration (100 μM) resulted in instant gel formation, and the lowest salt concentration (1 μM) increased the gelation time. The effects of varying the wt% of the gel were then observed with gels fabricated from 1-10 wt% using 10 μM citrate buffers of pH 5 and 6. Gels made at both pH values demonstrated an a decrease in gelation time with an increasing wt%. This is due to the higher wt% gel having an increased concentration of reactive groups meaning that the first reactions will occur more rapidly. Using the pH 6 buffer to fabricate a 10 wt% gel resulted in an instantaneous gelation directly at the tip of the pipette leaving the majority of the 4APM solution as a liquid surrounding a solid sphere, demonstrating the heterogeneity that occurs when the reaction occurs too quickly. All of gels formed at pH 5 took longer to gelate than the gels of equal mass at pH 6, reiterating the effects of pH on the gelation process. The 5 wt% gel fabricated at pH 6 was deemed the most desirable, allowing for a reasonable degree of mixing before gelation at 20 seconds producing a stiff and smooth gel that was not drawn out by removing the pipette tip.

6.1.2   Hydrogel viscoelastic properties
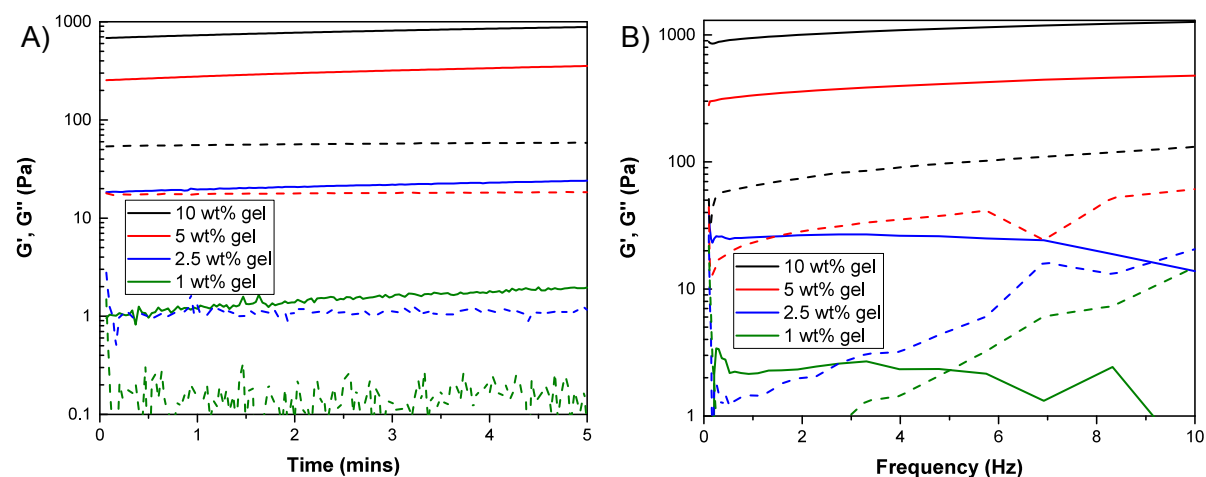
Figure 6.3: The storage moduli, G', (solid lines) and loss moduli, G", (dashed lines) of PEG gels of 10 wt% (black), 5 wt% (red), 2.5 wt% (blue) and 1 wt% (green), under A) a constant 1% strain for 5 minutes and B) under an oscillating strain of up to 1% of increasing frequency up to 10 Hz.

The mechanical properties of the gels are important, it is vital that the dressing will form a solid gel, not a fluid that could flow into a wound, and is flexible to withstand skin stretching. Rheometry was used to gain a better understanding of the viscoelastic properties. Gels were fabricated on the base plate of the rheometer, allowed to gelate and were then subjected to either a constant 1% strain force or to 1% strain from an oscillating top plate of increasing frequencies up to 10 Hz. This provided storage and loss moduli (G' and G" respectively), which describe the energy stored within the network and the energy lost when under strain. For the 5 and 10 wt% gels the concentrations of each component were sufficiently high to allow extensive chemical crosslinking that resulted in significantly higher storage moduli than loss moduli, indicating that the material is solid, Figure 6.3A.[412,413] The 2.5 and 1 wt% gels show very little difference between G' and G" indicating that they exhibit viscous properties. These results correlate with the gelation times and characteristics observed from the gels as displayed in Table 6.1. The frequency sweep data also shows the elastic properties of the 5 and 10 wt% gels, with substantially higher G' values than G" at all frequencies, Figure 6.3B. At 5.75 and 9.11 Hz the G' and G" values for the 1 and 2.5 wt% gels cross such that the loss modulus is dominant. This means that under these strain forces more energy is lost than is stored within the material, this behaviour is indicative of a fluid rather than a gel.[414] These rheological measurements show the ability to tune the mechanical properties of the gel by simply changing the concentration of the gel components, with fluidic properties at low concentrations ($\leq$ 2.5 wt%), and a solid of increasing stiffness (G' is increasingly larger than G"), at higher concentrations ($\geq$ 5 wt%). This demonstrates the potential for the gel to be applied in a variety of ways, for example a stiff high wt% gel that does not flow would be useful as a prefabricated dressing placed inside a sterilised packaging that could simply be opened and applied, whereas the viscous properties of the low wt% gels would allow the gel to be spread directly on the skin/wound.

6.1.3   Hydrogel swelling ratio

The swelling ratio of the hydrogel is defined as the fractional increase in the weight of the hydrogel due to the absorption of water. Hydrogel swelling occurs when a compatible solvent penetrates the dehydrated polymer network causing an increase in the volume within the gel and as such providing an outward osmotic force. The crosslinks between the polymers resist the deformation and as such provide an elastic force that opposed the outward osmotic pressure.[415] The solvent sorption ceases when the osmotic and elastic forces are equal. The maximum

hydrogel masses therefore correlate with the results of the rheology testing, the higher the elasticity of the gel the larger the volume of water that the gel can absorb.

To determine the swelling ratio, gels of 1-10 wt% were fabricated to 50 μl in eppendorfs and freeze-dried. The dehydrated gels were then weighed before 1 ml of Milli-Q was added and the gel was left to rehydrate. The Milli-Q was removed at 10, 30, 60, 120, 180 and 240 mins and the gels dabbed with lint free tissue paper, to remove all excess water, before reweighing the gels and adding 1 ml of fresh Milli-Q to the eppendorf.
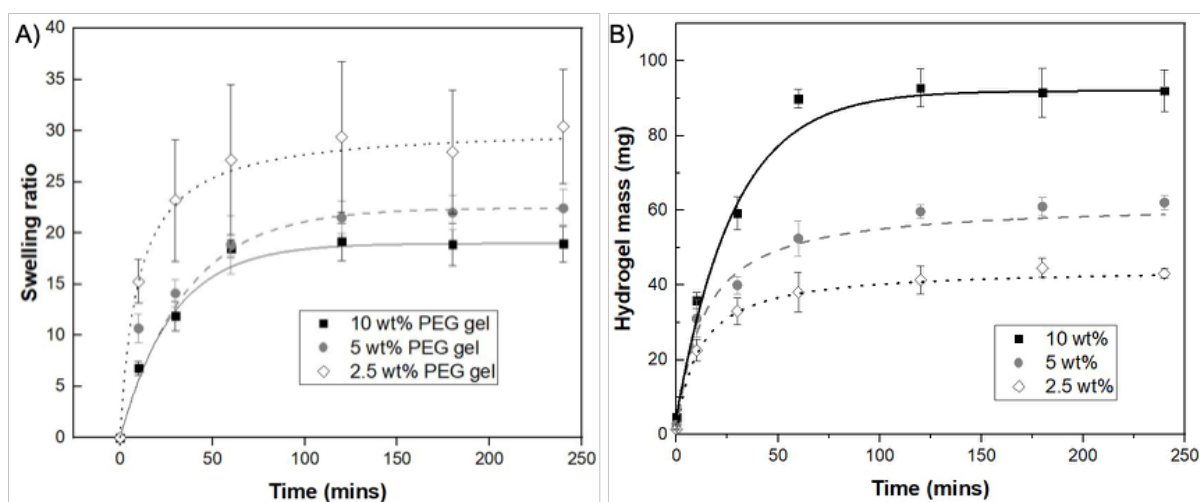
Figure 6.4: The A) swelling ratio and B) the hydrogel mass as freeze-dried gels of 10 wt% (black squares, solid line), 5 wt % (dark grey circles, dashed line) and 2.5 wt% (hollow diamonds, dotted line) were added to 1 ml of Milli-Q. Errors bars indicate the standard deviation (n=5).

The swelling ratio of the 1 wt% gel was unobtainable due to the complete solublisation of the gel components after 10 minutes of hydration, all other samples provided a defined gel. The swelling ratio of the gels was found to decrease as the wt% increased, after 4 hours the 2.5, 5 and 10 wt% gels displayed ratios of 30.4 $\pm$ 5.6 (absorbing 41 $\pm$ 1 mg of Milli-Q), 22.4 $\pm$ 1.8 (59 $\pm$ 2 mg of Milli-Q) and 19.0 $\pm$ 1.8 (87 $\pm$ 6 mg of Milli-Q) respectively, Figure 6.4A and B. A swelling decrease with the gel wt% has been identified in similar 4 arm PEG hydrogels with comparable swelling ratios.[416] All gels appeared to saturate after an hour in the hydrating medium. The hydrogel mass displays the opposite effect to the swelling ratio, an increase in the wt% increases the mass of water that can be absorbed. After rehydration the gels of 2.5, 5 and 10 wt% had final masses of 43 $\pm$ 1 mg, 62 $\pm$ 2 mg and 92 $\pm$ 6 mg respectively. In terms of the experimental procedures it is beneficial that the 5 wt% gel absorption saturation mass was 59 mg, or 59 μl of Milli-Q, as the gels used for experimentation were initially 50 μl meaning they

would only swell by 9 μl upon the addition of excess fluids.

6.2   AuNR-liposome loaded hydrogel characterisation

The loading of liposomes and Au nanoparticles was achieved by the addition of the particles to the 4APM dissolved in sodium citrate buffer, to a final volume of 40 μl. The inclusion of the liposomes/AuNPs appeared to have little affect on the gelation time. The 5 wt% gel remained solid upon inversion, Figure 6.5A, after 20 seconds of mixing and had a slight uniform brown coloration indicating a homogenous distribution of the NRs. The gel was however predominantly transparent, particularly when placed next to the skin, Figure 6.5B. A prototype dressing was comprised of a 5 mm thick layer of the PEG hydrogel loaded with AuNRs and IK8-liposomes and covered in a Tegaderm$^{\text{TM}}$transparent film dressing, Figure 6.5B. The details on the skin below are clearly visible, such as the freckle at the center of the gel, offering the additional benefit of being able visually assess the wound. The gel was formed in the bottom of a petri dish mould to provide the circular shape with a distinct edge. Such was the ease of fabrication, a wide variety of particles may be loaded into the gel simply through addition to the 4APM solution prior to gelation. This was demonstrated through the inclusion of gold nanoseaweed into the gel at varying concentrations, Figure 6.5C. This image also shows the different visual characteristics of gels of different wt% PEG, after being allowed to dry at room temperature for 30 mins. The left most and central gels, 10 and 5 wt% PEG respectively, can be identified as being solid due to the fact that they have dried from a droplet into amorphous shapes, if they had remained liquid they would have maintained their droplet shape due to presence of surface tension. The different colours are due to the concentrations of AuNSW, 240 and 24 μg ml^{-1} left and center gels respectively. The right hand gel, 2.5 wt%, is being drawn away from the slide using a pipette tip demonstrating the viscous and highly ductile properties of the gel when at low PEG concentrations.
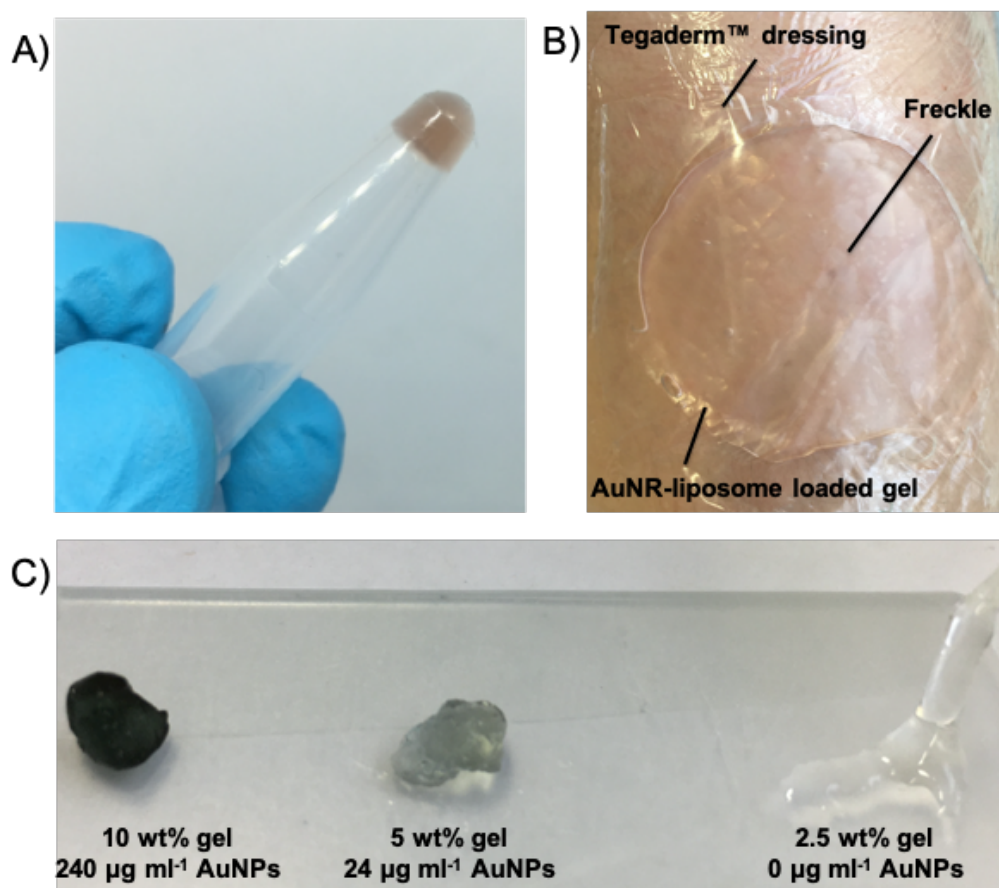
Figure 6.5: Images of the 5 wt% PEG hydrogels: A) loaded with liposomes and AuNRs, providing the brown colouration, B) as a prototype dressing loaded with AuNRs and IK8-liposomes, placed against the skin and covered with a Tegaderm^{TM}transparent film dressing, C) gels of 10, 5 and 2.5 wt % (left, centre, right) containing 240, 24 and 0 μg ml^{-1} of gold nanoseaweed,[417] after drying at room temperature for 30 mins.

6.2.1   Viscoelastic properties

To determine whether the inclusion of liposomes and AuNRs had any effect on the mechanical properties of the PEG-hydrogel, rheology was performed on separate gels containing 48 μg ml^{-1} of AuNRs, liposomes containing 1 x the MIC against *S. aureus* and both particles simultaneously, and compared against a 5 wt% with no particles.
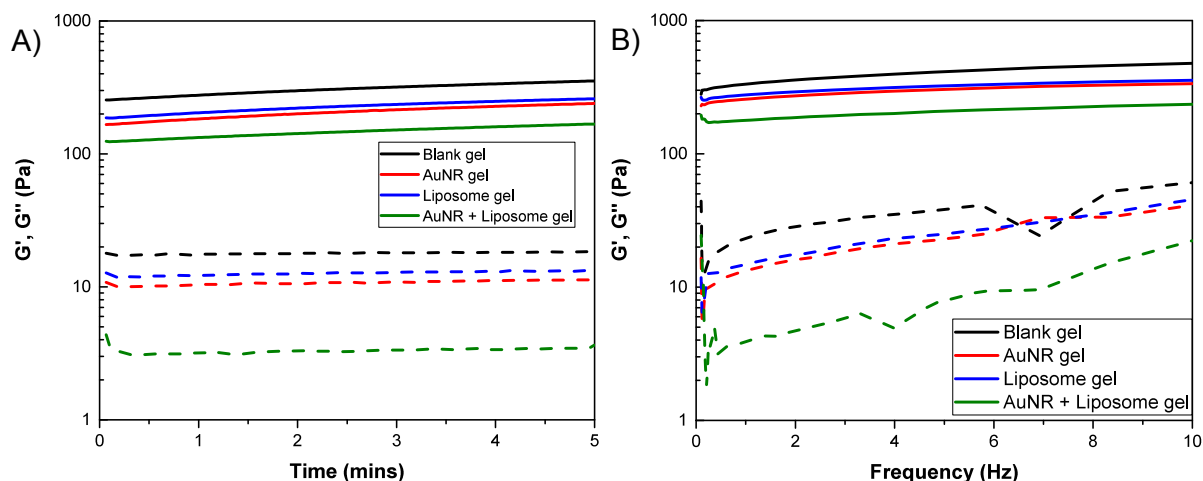
Figure 6.6: The storage moduli (solid lines) and loss moduli (dashed lines) of 5 wt% gel (black) and 5 wt% gels containing AuNRs (red), liposomes (blue) and AuNRs with liposomes (green).

The inclusion of both AuNRs and liposomes imparted a decrease in the storage modulus compared to the blank 5 wt% PEG gel, 114 and 94 Pa reductions respectively, Figure 6.6A. The addition of both particles to the gel offers a further reduction in G' of 186 Pa, almost an additive reduction from the AuNRs and liposomes independently. This is attributed to the inclusion of the particles producing a disruption in the hydrogel network, leaving a zone surrounding the particles with unbound 4APM and PEG dithiol molecules that affects the bulk mechanical properties.[418] The same decrease in elasticity was observed during the frequency sweep, with reductions in G' of 158 Pa, 178 Pa and 279 Pa upon including liposomes, AuNRs and both types of particle into the hydrogel, Figure 6.6B.

6.2.2 AuNR and liposome retention within the gel

The next step in the AuNR-liposome loaded gel characterisation was to determine the AuNR and liposome retention. High retention rates are vitally important, the leakage of substantial amounts of liposomes could lead to the premature leakage of non-lethal doses of AMP into a bacteria infected wound, thus promoting resistance, or it could leave the gel with an insufficient drug payload to kill bacteria upon triggered release. Similarly if the AuNRs show significant leakage, the photothermal heating profile may not be adequate to trigger the release of the AMPs. The gel retention was measured by including AuNRs and Texas-red labelled liposomes within a 50 μl gel along with 150 μl of sodium citrate buffer (pH6, 10mM). The maximum fluorescence (EX/EM, 596/615 nm) and the absorbance (860 nm) were obtained by measuring the gels directly, and each day the supernatant was moved to an empty well of a clear bottom

well plate before the fluorescence and absorbance were measured to determine the amount of liposomes and AuNRs that had leaked from the gel.
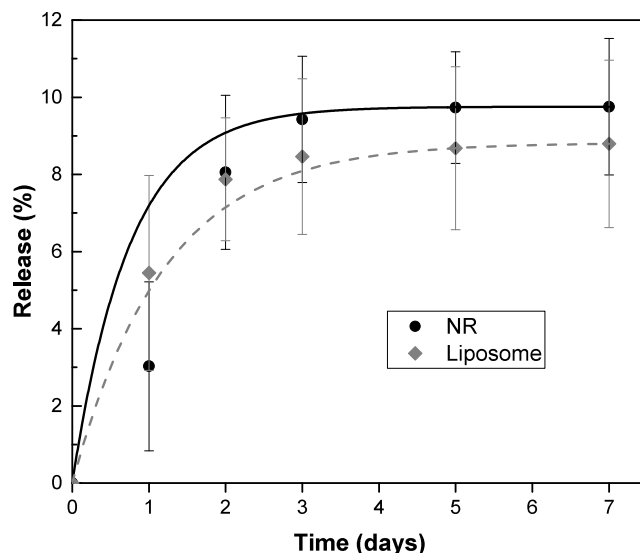
Figure 6.7: The release of lipid-coated AuNRs (black circles) and Texas-red labeled liposomes (grey diamonds) from a 50 μl 5 wt% PEG hydrogel into 150 μl of citrate buffer over a 7-day observation. Results are the average of four independent experiments.

The PEG gel demonstrated high retention of both particles with $10 \pm 2\%$ of AuNRs and $9 \pm 2\%$ liposomes released after 3 days, after which no further particles were lost, Figure 6.7. The high retention of the particles means that this system would be viable for use as a wound dressing that could be last for several days with little effect on the antimicrobial viability. These results also confirm the high liposome loading efficiency into the gel. Given the gel was fabricated *in situ* and only $\sim$5% of the liposomes were observed in the supernatant after 24 hours indicates that a minimum of $\sim$95% of the liposomes are within the gel immediately after fabrication.

6.2.3   Characterisation of AuNR-loaded gel photothermal properties

The photothermal response of the AuNR-loaded gels was characterized in order to control the thermally induced liposome release of AMPs. It is important that the inclusion of the AuNRs into the gel did not cause aggregation that could affect the photothermal heating profile. As such, 50 μl gels were fabricated in 96-well plates before the addition of 150 μl of MHB II and a thermocouple. The wells were then irradiated with a continuous wave laser, 860 nm, at $1.8 - 2.8$ W cm^{-2} for 10 min. This gave control of the maximum temperature achieved within the wells to

be between 50 and 65°C (±1°C), which was reached in 5 mins and maintained for a further 5 min, Figure 6.8A. The photothermal efficiency was maintained through repeated irradiation cycles, Figure 6.8B, demonstrating the ability to achieve dose-dependent temperature increases with the NR-loaded hydrogels and provide reproducible levels of heating (with the same temperature attained) over several irradiation cycles. The reproducibility of the heating profiles indicates that there is no change in optical properties and therefore no reshaping or aggregation of the AuNRs under irradiation, at these laser intensities. This is be beneficial within a wound dressing as it would allow a single gel to be provide multiple rounds of photothermal treatment that could achieve multi-stage delivery of antimicrobial agents.
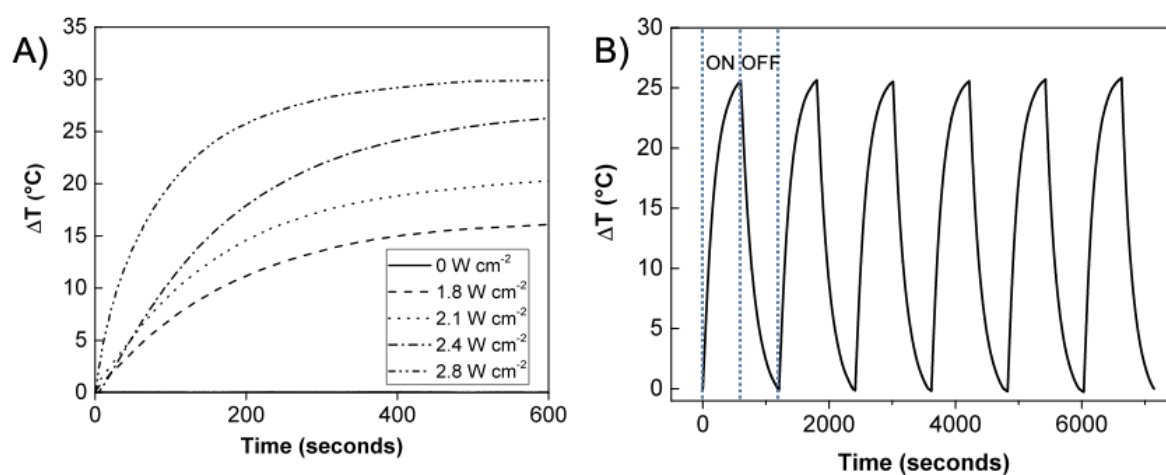
Figure 6.8: A) Photothermal heating profiles of the AuNR loaded 5 wt% hydrogel under varying laser intensities for 10 minutes, starting from a base temperature of 35°C. B) The photothermal heating profile of the NR loaded gel over repeated irradiation cycle at 2.4 W cm^{-2} laser intensity ($\lambda = 860$ nm) for 10 minutes.

6.2.4   Photothermal triggered released from liposome loaded hydrogels

The final step in the characterisation of the gel was to determine whether the photothermal release of liposome encapsulated materials was affected by the inclusion into the gel matrix. Gels of 2.5, 5 and 10 wt% were fabricated containing AuNRs and calcein-loaded liposomes, incubated with an *S. aureus* suspension for one hour before irradiation at 0 or 2.1 W cm^{-2} (λ = 860 nm) for 10 mins. A control sample without the gel was included for comparison.
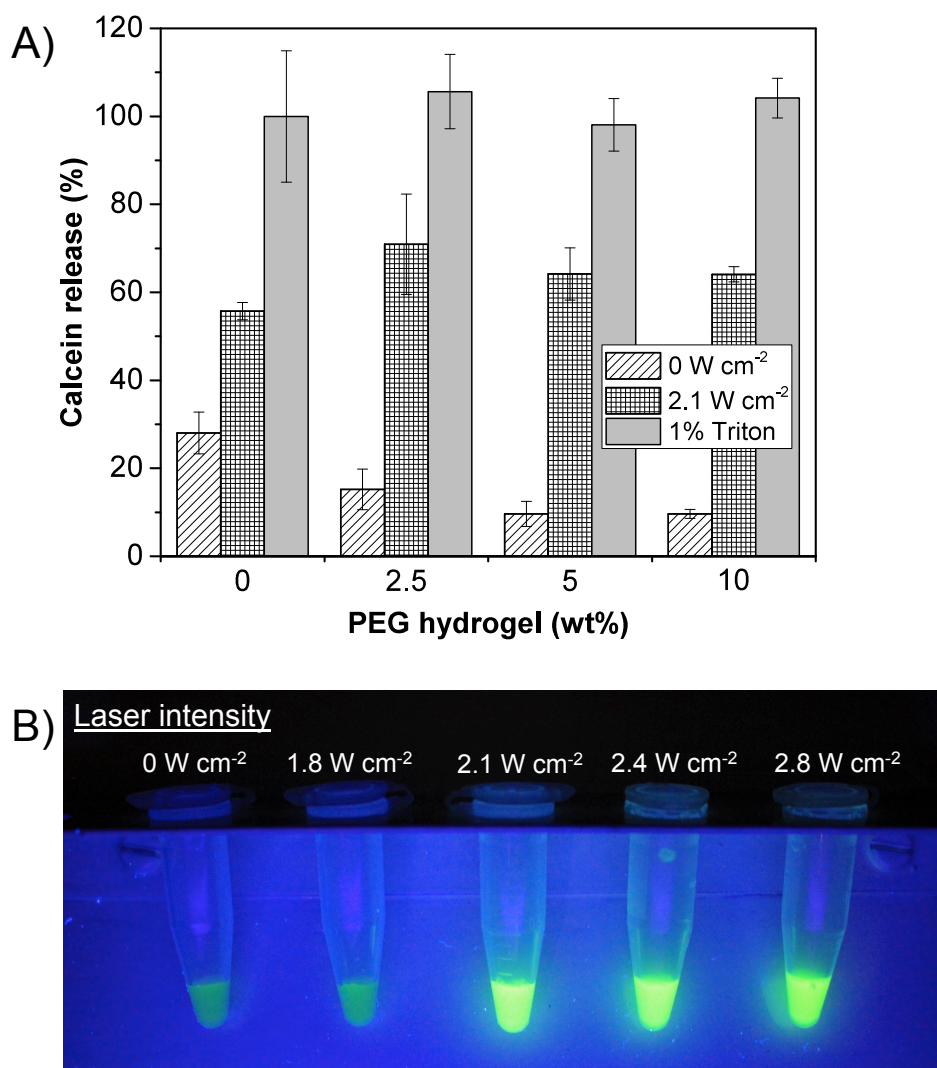
Figure 6.9: A) Bacterial and photothermal induced release of calcein (diagonal lines and hashed columns respectively) from liposomes in PEG gels of different wt% when incubated in a *S. aureus* suspension. All gels contained 48 μg ml^{-1} AuNRs and a laser power of 2.1 W cm^{-2} was used to irradiate the samples to heat them to 55°C for 5 mins. 1% Triton-X100 was added to samples (grey columns) to ensure that the maximum fluorescent response was the same across all gels. Results are the average from 6 replicates. B) AuNR and calcein liposomes loaded into the 5 wt% PEG hydrogel, irradiated for 10 mins with intensities between 0 - 2.8 W cm^{-2} ($\lambda = 860$ nm) and placed under a UV-lamp.

The incorporation of AuNRs and liposomes into the PEG matrix was found to increase the delivery profile from all of the gels with 71 ± 11%, 64 ± 6% and 64 ± 2% calcein release from gels of 2.5, 5 and 10 wt% respectively, compared to 56 ± 2% release from liposomes free in suspension, Figure 6.9A. This increase may be due to the confinement of the liposomes and AuNRs within the 50 μl volume of the gel, rather than when they are free in solution and are able to diffuse throughout the 200 μl total volume of liquid. This would increase the

Section 6.2

Chapter 6. Nanoparticle loaded hydrogel for the light-activated release and photothermal
enhancement of antimicrobial peptide activity

likelihood of the liposomes and thermally radiating AuNRs being in a close proximity to one another making the liposomes more susceptible to thermal destabilization. The inclusion of the liposomes within a gel also exhibited reduced bacteria induced release leakage. This may be due to the PEG matrix restricting access of the bacteria to the liposomes and hence limiting their direct interaction, meaning any induced leakage most likely arises due to the bacteria producing toxins that target the membrane.

The triggered release of calcein was also visually demonstrated by fabricating 5 wt% gels with AuNRs and calcein-loaded liposomes. The gels systems were incubated with *S. aureus* for an hour and then irradiating between 0 - 2.8 W cm^{-2} for 10 mins, before the supernatant containing the planktonic bacteria was removed. Under a UV-lamp an obvious fluorescent response can be observed upon irradiation at 2.1 W cmcm^{-2} and above (heating to 55°C and and above), Figure 6.9B.

6.2.5   Hydrogel toxicity to fibroblast cells

The cytotoxicity of the 5 wt% hydrogel and the gel containing both IK8-liposomes and lipid-coated AuNRs was assessed against human dermal fibroblasts (HDFs), cells that are integral to the reepithelialisation process. 10 μl gels were fabricated within the sterile biohood on top of a glass slide coated in parafilm. The hydrophobicity of the parafilm allowed the hydrogels to slide across the surface of the slide, and easily be placed into wells containing seeded HDFs and 90μl of fibroblast growth media. The cells were then incubated for 24 hours utilising the WST-1 assay to obtain the cell viability.
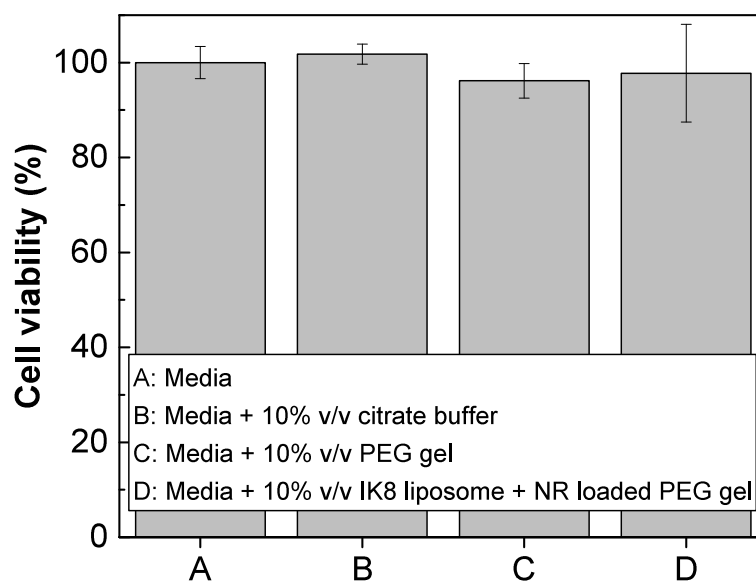
Figure 6.10: Cytotoxicity of the PEG hydrogel and the therapeutic IK8 liposomes-NR loaded PEG hydrogel when incubated with HDFs for 24 h. Results are the average from two independent experiments, each with 4 replicates.

Figure 6.10 demonstrates that the incubation of the HDF cells with the AuNR and IK8-liposome loaded 5 wt% PEG gel showed no detrimental effects on cell viability; with > 97% cell viability observed in the formulation used. Taken together with the results from 5.14, each component within the therapeutic gel demonstrates excellent biocompatibility indicating that the gel would be suitable for treatment of infections in a vulnerable wound environment. The lack of cyto-toxicity of IK8 at concentrations several times the MIC against *S. aureus* potentially allows for the liposomal loading of high concentrations of peptide to provide multiple treatment events, with no risk of toxicity in the event of premature leakage.

6.3   Treatment of pathogenic bacteria

The antimicrobial efficacy of the dressing was assessed against both *S. aureus* and *P. aeruginosa.* Both bacteria are part of the ESKAPE pathogens, a list of bacteria that are the leading cause of nosocomial infections due to multidrug resistance,[419] and have been highlighted by the world health organisation as part of the 'priority pathogens' that pose the greatest threat to human health.[420] *S. aureus* and *P. aeruginosa* were chosen in particular to analyse the therapeutic loaded gel and photothermal antimicrobial effects against a Gram-positive and Gram-negative

bacterium, respectively. To demonstrate the antibacterial capabilities of the AuNR and IK8-liposome loaded PEG gel system, planktonic bacteria were treated with one of three variations on the gel; the IK8-liposome and AuNR loaded gel to demonstrate potential triggered release of AMPs, an AuNR loaded gel to determine the photothermal induced antimicrobial activity, and a gel containing free IK8 and AuNRs to demonstrate the photothermal enhancement of the AMP.

The antimicrobial properties of the AuNR and IK8-liposome loaded gel were assessed through the treatment of Gram-positive *S. aureus* and Gram-negative *P. aeruginosa*. By controlling the applied laser irradiation intensity between 1.8 and 2.8 W cm^{-2}, we were able to provide photothermal heating profiles between 50°C and 65°C and demonstrate the first instance of triggered release of AMPs from liposomes. The triggered release of IK8 was observed to occur for an irradiation of 2.1 W cm^{-2} for 10 minutes and heating the sample to 55°C. This produced 6- and 7-log reductions in the number of CFU ml^{-1} when treating *S. aureus* and *P. aeruginosa* respectively, Figure 6.11. No decrease in bacteria viability was observed when treating either bacteria with a laser intensity of 1.8 W cm^{-2}, 50°C. This clearly indicates that the sample must be heated to the lipid gel-fluid phase transition temperature of DSPC (55°C) in order to trigger release of encapsulated materials.[235,236,383,421–423] The thermally induced release is highest close to the phase transition temperature, T$_m$, due to the coexistence of both gel and fluid domains, producing grain boundaries that have an increased permeability of hydrophilic molecules.[424–427] The liposomal release of the MIC of IK8 showed a similar level of bactericidal activity as the gel containing the MIC of free IK8 against both bacterial types, 5.5- and 6.7-log reductions in CFU ml^{-1} against *S. aureus* and *P. aeruginosa* respectively. This indicates that the liposomal encapsulation and subsequent triggered release did not affect the peptide's antimicrobial efficacy. When taken together with the liposomal protease protection, these results indicate that this therapeutic gel offers a potential means of maintaining AMPs in a protease rich wound environment until required, with no decrease in bactericidal efficacy upon triggered release. By utilizing a photothermal trigger, we are also able to enhance the bactericidal activity of the therapeutic gel by heating the bacteria to higher temperatures. Enhanced bacterial kill was observed when treating both bacteria with IK8 and laser irradiation at 2.4 W cm^{-2} (60°C) for 10 min, leading to a 7.8-log reduction in CFU ml^{-1} of *S. aureus* and complete bacteria killing of *P. aeruginosa*. This is similar to previous observations demonstrating thermal enhancement of antibiotics against planktonic *S. aureus* and *P. aeruginosa*.[249,265,428] Furthermore, there have

been several *in vivo* studies investigating the antibacterial properties of photothermal heating from nanoparticle loaded-hydrogels, that heat infected wounds up to 50-60°C for up to 10 minutes.[6–9,261,267,297,428] In all cases the heating demonstrated no thermally induced damage to peripheral tissues or detrimental effects upon reepithelialization. Through the fabrication of gels containing AuNRs only, we also evaluated the antimicrobial effects of photothermal heating alone. Neither bacterial species displayed any decrease in bacteria viability until irradiation at 2.4 W cm^{-2} (heating to 60°C), at which point there was a 2.6-log decrease in *S. aureus* and a 4.4-log decrease in *P. aeruginosa*. This correlates with previous studies that have demonstrated that Gram-negative bacteria are more susceptible to thermal killing than Gram-positive.[297] Further increasing the laser intensity to 2.8 W cm^{-2} (heating to 65°C) showed complete antimicrobial killing of both bacterial species in all samples containing the NRs. All bactericidal activity was attributed to the photothermal heating, with no bacteria death observed under irradiation at 2.8 W cm^{-2} in the absence of AuNRs. These results show that the IK8 liposome and AuNR loaded hydrogel has the potential for use as a broad-spectrum antimicrobial treatment that, through the regulation of the applied laser intensity, can not only trigger the release of AMPs, but amplify their antimicrobial effects. By harnessing the photothermal enhancement, the chances of providing non-lethal treatment are reduced, as such this treatment should provide a decreased likelihood of bacterial AMP resistance.
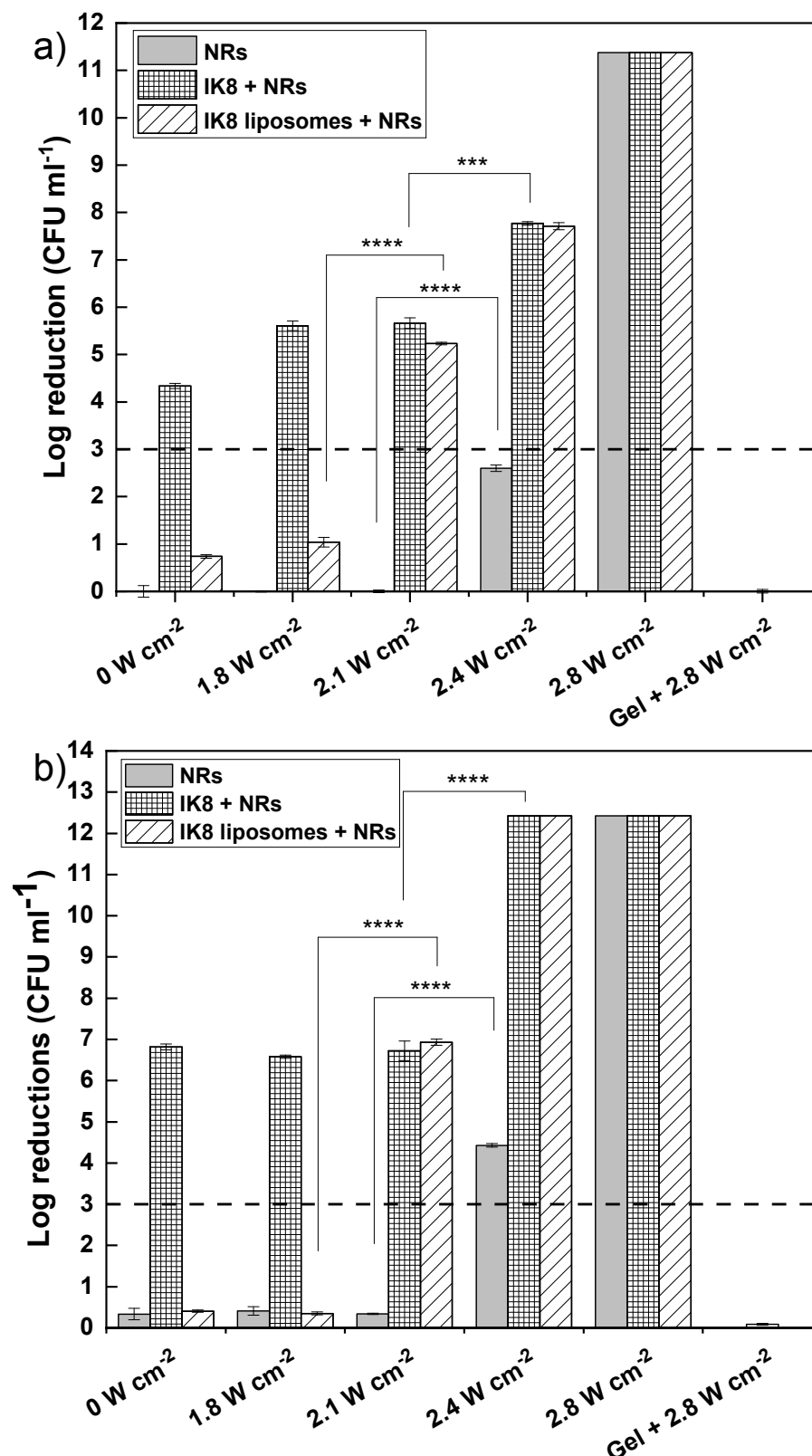
Figure 6.11: The reduction in the number of viable A) *S. aureus* and B) *P. aeruginosa*, CFU following treatment with gels containing AuNRs, AuNRs and free IK8, and AuNRs with IK8-loaded liposomes, irradiated with an 860 nm laser, at intensities between 1.8 - 2.8 W cm^{-2} for 10 mins. The bactericidal threshold is noted with a dashed line. Results are the average over three independent experiments. Two-tailed T-tests were were used to obtain statistical significance, p-values indicate; *** < 0.001, **** < 0.0001.

6.4   Repeated treatment of *S. aureus* from the hydrogel formation

The ability to utilize the hydrogel as a drug depot to provide repeated triggered release of antimicrobial agents at lethal dosages, and in combination with photothermal ablation of bacteria would provide significant advantages in wound management. Whenever a wound is exposed to the environment there is a chance of infection occurring.[429] As such, it would be beneficial for a single dressing to be able to provide multiple rounds of treatment, thus decreasing the frequency with which the dressing needs to be replaced. Being able to use a single dressing for repeated treatments also makes the dressing financially more viable, as a new gel would not need to be purchased each time treatment is required, potentially increasing the chances of use in clinic. In order to determine whether multiple rounds of triggered delivery of AMPs is possible from the IK8-liposome/AuNR loaded gel, the number of liposomes must be increased such that they contain enough AMP to provide multiple rounds of bactericidal activity. As such, gels were fabricated containing different numbers of IK8-liposomes correlating to 0-4 times the MIC and incubated with a suspension of *S. aureus* for 18 hours to determine the antimicrobial activity of IK8 that has been released through the bacteria induced liposome disruption.
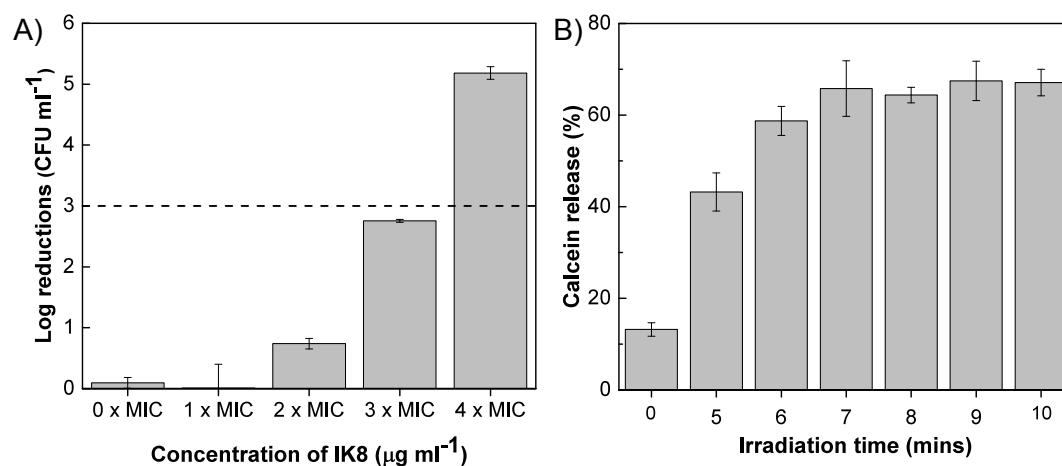
Figure 6.12: A) The reduction in *S. aureus* viability when different numbers of IK8-liposomes
are incorporated into a 5 wt% gel and incubated with the bacteria suspension for 18 hours.
The dashed line indicates the bactericidal threshold. The CFU ml^{-1} values are the average
across six replicates of bacteria that are combined before being spread onto three agar plates.
B) Triggered release of calcein from liposomes loaded into 5 wt% gels after incubation in a *S.
aureus* suspension for 1 h before laser irradiation at 860 nm for 5-10 min, with a laser intensity
of 2.1 W cm^{-2}. Fluorescence measurements (EX/EM, 496/515 nm) were taken immediately
after addition to the bacteria suspension and after an 18 h incubation at 37°C. 1% Triton-X100
was added to the control wells to find the maximum fluorescence. Results are the average of six
replicates.

Figure 6.12A shows that there was no affect on the bacteria viability until liposomes containing

2 x the MIC of IK8 were incorporated into the gel at which point there was a 0.7-log reduction

in bacteria. Increasing the concentration of IK8 to 3 and 4 x the MIC showed significantly more

bacterial activity with 2.8- and 5.2-log reductions respectively. These values are substantially

lower than the bacteria death observed when performing the equivalent experiment without the

gel (Figure 5.12), liposomes containing 2 and 4 x the MIC showed 3- and 6.5-log reductions.

This decrease in bacteria killing from IK8-liposomes loaded into a gel indicates that the gel

offers a protective effect against direct interaction with bacteria.

The liposome release with laser irradiation time was then investigated to determine whether

the amount of AMP released could be reduced to ensure that a lethal dose of the drug can

be maintained within the liposome reservoirs after the first stimulated release event. Calcein-

loaded liposomes were incorporated into gels, incubated with a 1x10^6 suspension of *S. aureus*

for an hour before being irradiated at 2.1 W cm^{-2} for 5 to 10 mins. As shown in Figure 6.12B,

irradiating the samples for 5 mins resulted in 44 ± 4% release, which increased with irradiation

time up to 7 mins, 66 ± 6%, after which there was no change in the release profile up to the

143

maximum irradiation time of 10 mins, $67 \pm 3\%$. This means that using an irradiation time of 5 mins as opposed to 10 mins, would allow the retention of 23% more drug for use in the second round of treatment. This also means that by increasing the irradiation time to 7 mins or above in the second round of treatment we would be able to provide a release of a larger proportion of the IK8 that remained encapsulated.
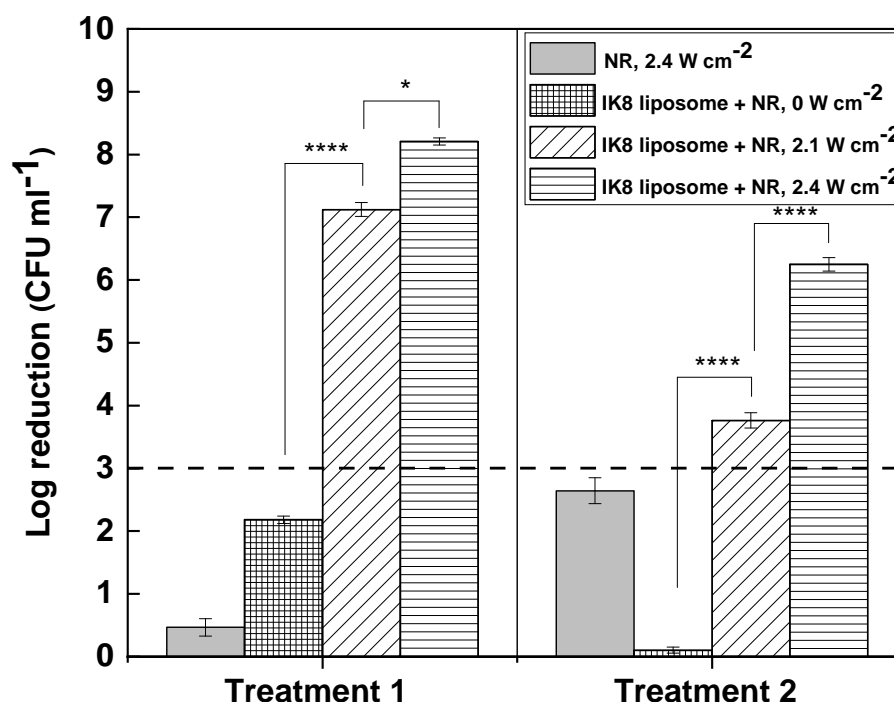
Figure 6.13: The log reductions in *S. aureus* CFUs over two treatment cycles when treated with the the PEG hydrogel containing 48 μg mL^{-1} of AuNRs irradiated with a laser intensity of 2.4 W cm^{-2} (grey), and gels containing AuNRs and liposomes encapsulating 2.5 times the MIC of IK8 irradiated at 0 W cm^{-2} (hashed), 2.1 W cm^{-2} (diagonal slashed) and 2.4 W cm^{-2} (horizontal lined). Gels were irradiated for a period of 5 mins during the first treatment event and left to incubate for 18 h before being replaced with fresh bacteria and irradiated for 10 mins during the second treatment. Results are averaged across four replicates of bacteria combined and spread onto three agar plates. Two-tailed T-tests were were used to obtain statistical significance p-values indicate: * < 0.05, **** < 0.0001.

To demonstrate the antimicrobial capabilities of the AuNR and IK8-liposome loaded gel over multiple rounds of treatment, gels were fabricated with AuNRs and an increased number of liposomes such that they contained 2.5 times the MIC of IK8. The gels were inoculated with the first round of *S. aureus* before irradiation at 2.1 or 2.4 W cm^{-2} for 5 mins. The bacteria were then incubated with the gel for 18 h, before removal and quantification of CFU ml^{-1}. The gel was then inoculated with a fresh *S. aureus* suspension and subjected to irradiation at 2.1

Section 6.4

Chapter 6. Nanoparticle loaded hydrogel for the light-activated release and photothermal enhancement of antimicrobial peptide activity

or 2.4 W cm^{-2} for 10 minutes, before incubation for 18 h. The second round of bacteria was then removed for CFU quantification. Under irradiation at 2.1 W cm^{-2} (heating to 55°C), the triggered release of IK8 resulted in bactericidal activity over both treatment cycles, with 7.1- and 3.8-log reductions in *S. aureus* after the first and second cycles respectively, Figure 6.13. The decrease in antimicrobial efficacy is attributed to the diminishing number of intact IK8-liposomes remaining after each release event. The photothermal enhancement of IK8 can also be observed over both treatments, under irradiation at 2.4 W cm^{-2} (60°C). The photothermal heating produced further 1.1- and 2.5-log reductions in CFUs, in the first and second cycles respectively, compared to systems providing bacteria killing through only AMP delivery. Using a gel containing only AuNRs the difference in photothermal killing was confirmed to be due to the alterations in irradiation time, with the 5 min irradiation in treatment one resulting in a 0.5-log decrease in CFU ml^{-1} and the 10 min irradiation during treatment two producing a 2.6-log reduction in CFU ml^{-1}. The bactericidal activity of the gel, both with and without the photothermal enhancement, demonstrates the potential for multiple therapeutic events and can be optimized for a variety of treatments. Furthermore, this indicates that the main limitation in the number of treatments that can be performed is the concentration of antimicrobial agents encapsulated within the system.

Conclusion

This chapter has demonstrated the fabrication of an AuNR and IK8-liposome loaded hydrogel, that can effectively treat pathogenic bacteria through the photothermal stimulated release of AMPs, which is the first example of an exogenous stimuli-responsive release of AMPs. The chapter started with the optimisation of the PEG hydrogel formulation protocol. It was demonstrated that the wt% of the gel, the buffer pH, and the salt concentration of the gel can be used to control the gelation time and mechanical properties of the gel. A 5 wt% gel fabricated using a 10 mM citrate buffer at pH 6 was desirable due to the reasonable gelation time, 20 seconds, and the production of a smooth and homogeneous gel. The incorporation of AuNRs and IK8-loaded liposomes did not affect the liposome integrity nor did it cause any AuNR aggregation. Through irradiation of the AuNR loaded gel between 1.8-2.8 W cm^{-2} the photothermal heating could be regulated to control the temperature of a bulk 200 μl solution between 50-65°C to within 1°C of a target temperature. As such, the photothermal triggered release of calcein from liposomes

within the gel was demonstrated, and subsequently the incorporation of the AuNR-liposome system into a 5 wt% PEG matrix increased the release efficiency by 8%.

The antimicrobial properties of the AuNR and IK8-loaded gel system were then investigated. Irradiation at 2.1 W cm^{-2} for a period of 10 min heated the sample to 55°C, triggered the release of IK8, and resulting in ∼6- and ∼7-log reductions in the number of Gram-positive *S. aureus* and Gram-negative *P. aeruginosa* CFU ml^{-1} respectively. Increasing the laser intensity to 2.4 W cm^{-2}, heating to 60°C, enhanced the antimicrobial activity of the system with additional 2- and 5-log reductions in viable *S. aureus* and *P. aeruginosa* respectively. Through the optimization of the irradiation time and increasing the number of AMP-loaded liposomes, such that the final concentration of IK8 was 2.5 times the MIC against S. aureus, the gel was shown to release bactericidal dosages of IK8 to treat two sequential bacterial suspensions, resulting in 7- and 4-log reductions in CFU ml^{-1} from the first and second treatment cycles respectively. Furthermore, irradiation at 2.4 W cm^{-2} demonstrated enhanced antimicrobial activity over both treatment cycles. This study demonstrates the capability to perform multiple treatment events using an individual gel, offering a reduced cost per treatment. Other studies have also demonstrated the photothermal destruction of biofilms using nanorod loaded hydrogels,[10,298] and given the innate antibiofilm properties of IK8[15] results from this chapter indicate that the photothermal enhancement of these properties will be able to continue into the treatment of mature biofilms, which are more representative of infections than treating planktonic bacteria. These results indicate that the facile integration of AMP-loaded liposomes and AuNRs into a PEG hydrogel network offers protection of encapsulated materials and tunable release profiles showing potential for the treatment of infections.

Chapter 7

Pulsed laser triggered release of AMPs without bulk heating

Motivation:

Chapters 5 and 6 of this thesis describe the development of a wound dressing that offers triggered release of AMPs in response to bulk heating mediated by AuNR photothermal agents dispersed through a gel. Whilst there are many advantages to this, it is hypothesised that the conjugation of gold nanoparticles to AMP-loaded liposomes would provide a higher release efficiency, when using a pulsed laser system. The application of a pulsed laser system allows the deposition of large quantities of energy over timescales equivalent to the thermalisation time of the particle with the surrounding media; meaning the particle is able to generate large thermal gradients without providing a bulk heating effect. The high temperature in the immediate vicinity to the particle is able to cause membrane disintegration, whilst the thermal gradients are capable of vapourising the surrounding liquid creating cavitation bubbles that produce intense pressure waves that can also disrupt a lipid membrane.[180,181] Wu *et al.*, demonstrated as such by tethering hollow gold nanoshells (HGNs) to lipid vesicles (1,2-dipalmitoyl-*sn*-glycero-3-phosphocholine, DPPC); the HGN-liposome complex provided substantially higher release of encapsulated calcein (93%) than HGNs mixed freely in suspension (35%), when irradiated at 16.1 W cm^{-2} at 800nm with a pulse width of 130 fs and a repetition rate of 1 kHz.[180] Not only would the liposome-AuNP conjugation increase the release efficiency but would remove the reliance upon the bacterial toxins for AMP delivery. Furthermore, triggering release without bulk

heating would minimise any toxicities that could arise from heating of tissues.

In recent years several studies describe the use of liposomes as a soft template for AuNP synthesis, utilising the lipid bilayer as a nucleation site onto which Au is deposited and at high enough concentrations a coating of AuNPs can be formed. This was first observed by Troutman *et al.* using 63 nm DPPC liposomes as a soft template for the adsorption of gold clusters to form a shell-shaped array.[223] They demonstrated that the absorption peak of the particles could be tuned by altering the quantity of gold used during the synthesis, with higher concentrations of Au resulting in a higher density of liposome coverage causing the extinction spectra to be red-shifted displaying shell-like optical properties. Au-coated liposomes were first applied to medicine by Rengan *et al.* using the particles to demonstrate phothotermal ablation of MDA MB 231 cancer cells.[213] This study identified that increasing the ratio of ascorbic acid (AA) to Au ions caused a red shift in the absorption peak, allowing finer control of the peak position between 550-900 nm. Since this study the AuNP coated liposomes have been used *in vivo* to demonstrate the photothermal treatment of HT1080-*fluc2-tuboFP* tumour xenografts in murine models leading to an 80% survival rate after 60 days with treatment and 0% survival after 35 days without. Interestingly, this study also demonstrated that the laser induced degradation of the Au complex to particles ≤ 5-8 nm enables removal through the renal system. The anticancerous capabilities of the Au-nanocontainers have also been enhanced through loading with chemotherapeutics that are release upon laser induced degradation.[430] The triggered release of curcumin loaded into the liposome lumen resulted in an additional 2-fold decrease in B16F10 cells, on top of the initial photothermal ablative effects. Despite the advantages of using Au coated liposomes these systems have not been applied to the field of infectious therapies. As such, it is hypothesised that the synthesis of AuNP-coated AMP-loaded liposomes will provide pulse laser triggered release of peptides to treat pathogenic bacteria, Figure 7.1.
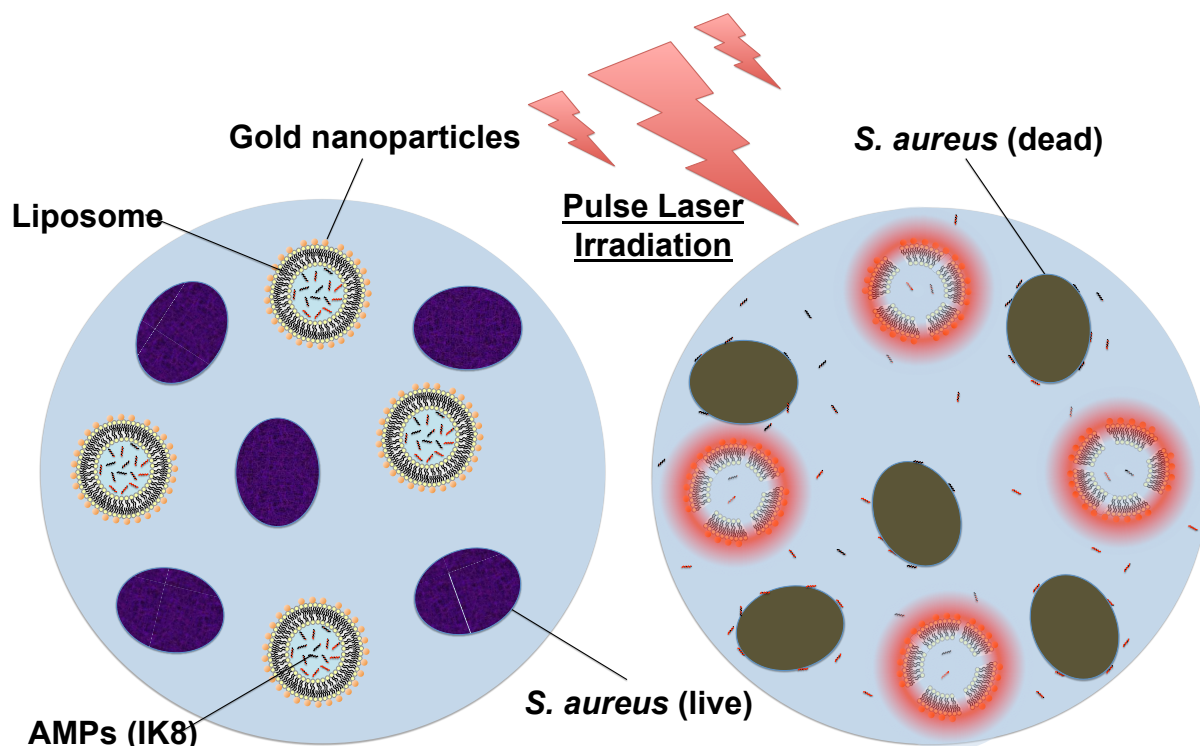
Figure 7.1: Schematic representation of gold nanoparticles adsorbed to AMP-loaded liposomes to provide pulse laser irradiation triggered release of peptides to incite bactericidal activity against *S. aureus*. Liposomes and gold nanoparticles have been scaled up for ease of viewing.

7.1   Synthesis of gold nanoparticles in the presence of IK8-loaded liposomes

This section will cover the attempted gold coating of liposomes by synthesising AuNPs in the presence of the vesicles. This will involve exploring the ratios between the gold precursor (chloroauric acid, $HAuCl_4$), the reducing agent (AA) and the liposome concentrations, as well as identifying the effects of using PEGylated and thiolated lipids.

In the absence of a template, mixing a gold salt with a reducing agent synthesises isotropic spherical colloidal AuNPs, with a transverse plasmon peak at 550 nm. However, in the presence of liposomes gold ions can be adsorbed onto the lipid bilayer creating nucleation points for crystal growth, Figure 7.2A. Upon addition of a reducing agent the charge on the Au ions is lost causing aggregation onto the nucleation sites on the liposome surface, Figure 7.2B, leading to the formation of AuNPs, Figure 7.2C. At low AuNP densities on the liposome surface the plasmonic properties of the AuNPs remain the same as those free in suspension with a transverse absorption peak at 550 nm. As the density of AuNPs on the liposome surface increases the

coating can be modelled as a continuous gold shell, and the plasmonic resonance wavelength is red shifted with increasing packing density, Figure 7.2D.
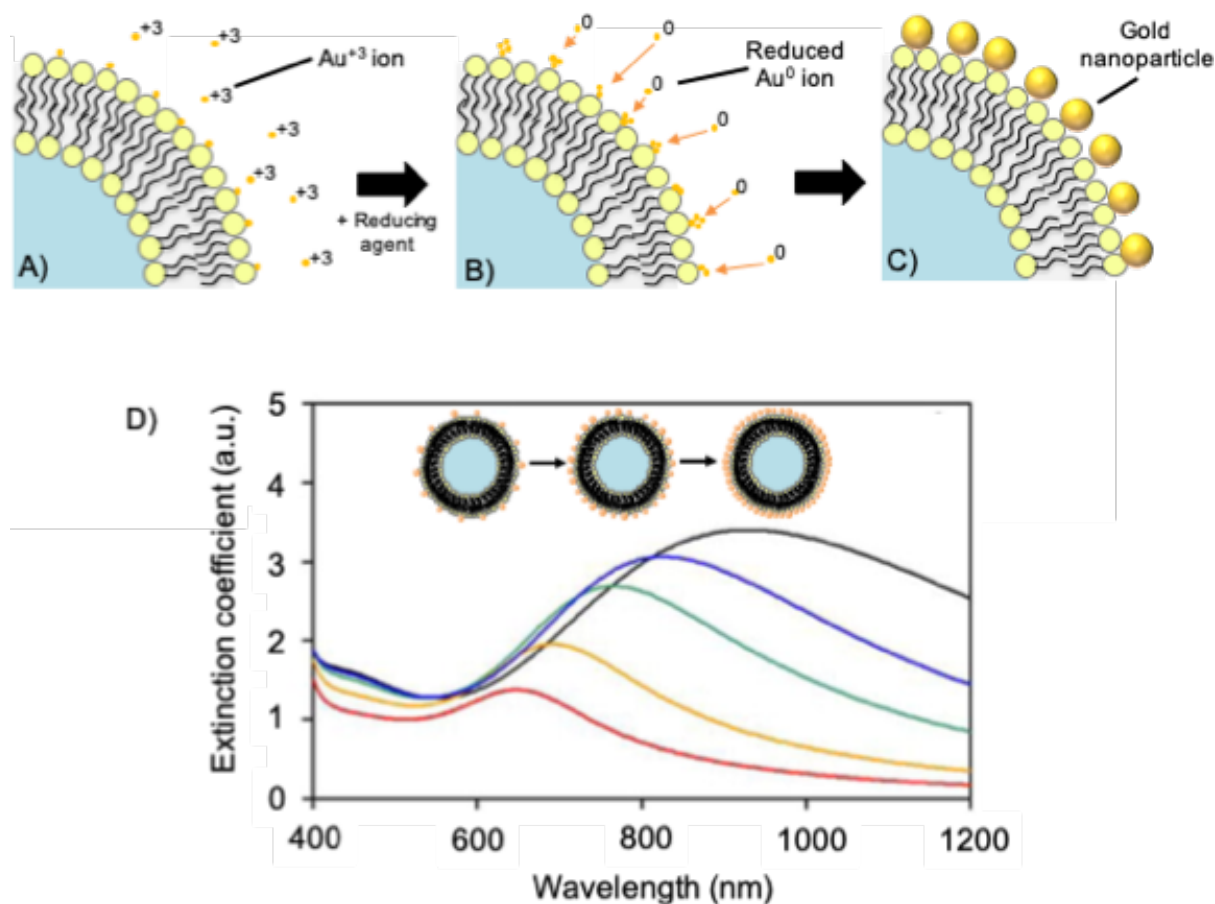
Figure 7.2: Schematic representation of the gold nanoparticle synthesis on the surface of a phospholipid liposome. A) Au^{+3} ions in solution adsorb onto the surface of the liposome, B) addition of a reducing agent causes the reduced ions to aggregate on the nucleation points on the liposome surface, C) gold nanoparticles on the liposome surface continue to grow until the gold is expended. D) As the surface density (Φ) of gold nanoparticles increases the plasmonic absorbance peak increases in amplitude and is shifted to longer wavelengths. $\Phi = 0.7$ (red), 0.8 (yellow), 0.9 (green), 0.95 (blue), and 1 (black). Edited with permission.[223] Copyright 2008, Wiley.

The liposome gold coating was synthesised through the reduction of $HAuCl_4$ using AA in the presence of liposomes. Briefly, AMP-loaded liposomes, cleaned using dialysis for 48 hours, were diluted to 2 mg ml^{-1} in PBS. 200 μl of the liposomes was then mixed with 100 μl of $HAuCl_4$ before the rapid injection of 400 μl of AA (AA:Au ratios of 1-4:1).

7.1.1   Liposomes containing PEGylated lipids

The Au coating of PEGylated liposomes has been demonstrated by Orsinger *et al.* to provide triggered release of carboxyfluorescein.[431] As such, during this study initial attempts at Au

coating were performed on the PEGylated liposomes developed in Chapter 5. These liposomes were thoroughly characterised and produced efficient encapsulation of IK8 with low sample-to-sample variability. The Au coating of these liposomes was performed by varying the ratio of AA to Au ions (1:1 to 4:1) added to the peptide loaded vesicles. The UV-vis spectra of the particles was initially used to determine the nanoparticle coating, increasing the AA:Au ratio should cause a red shift in the plamonic peak position if the AuNPs are adsorbed onto the liposome surface, if the AuNPs are not on adsorbed onto the liposome the plasmonic peak should remain around 550-600 nm, independent of the AA:Au ratio.[213,214]

The UV-vis spectra for the attempted Au coating using 2.5 mM and 5 mM $HAuCl_4$ predominantly displayed absorbance peaks at 600 nm, with little change upon varying the AA:Au ratio, Figure 7.3A. However, upon increasing the Au concentration to 7.5 and 10 mM $HAuCl_4$ the liposome-AuNP complexes exhibited absorption peaks that can be red-shift from 600 nm to 850 nm by increasing the AA:Au from 1:1 to 4:1, Figures 7.3B and C. At 10 mM $HAuCl_4$ the absorption peaks were more defined with a heightened extinction coefficient as the AA:Au ratio was increased. TEM Images of samples containing AuNPs synthesised using 10 mM $HAuCl_4$ with 10 and 40 mM AA, Figures 7.3E and F respectively, showed that the liposomes are not being coated in AuNPs. Figure 7.3E, displays the synthesis of a large number of small (< 50 nm) spherical particles, that are not adhered to the liposomes. The particles shown in Figure 7.3E, are much larger, mostly between 100-200 nm, and the surfaces appear rough with many protrusions. Rather than the Au coating causing the red-shift as the AA:Au ratio is increased, it appears that the increase in the peak absorbance wavelength is caused by the synthesis of larger and more anisotropic particles, both factors have been shown to provide a red shift in the optical absorbance.[432–434]
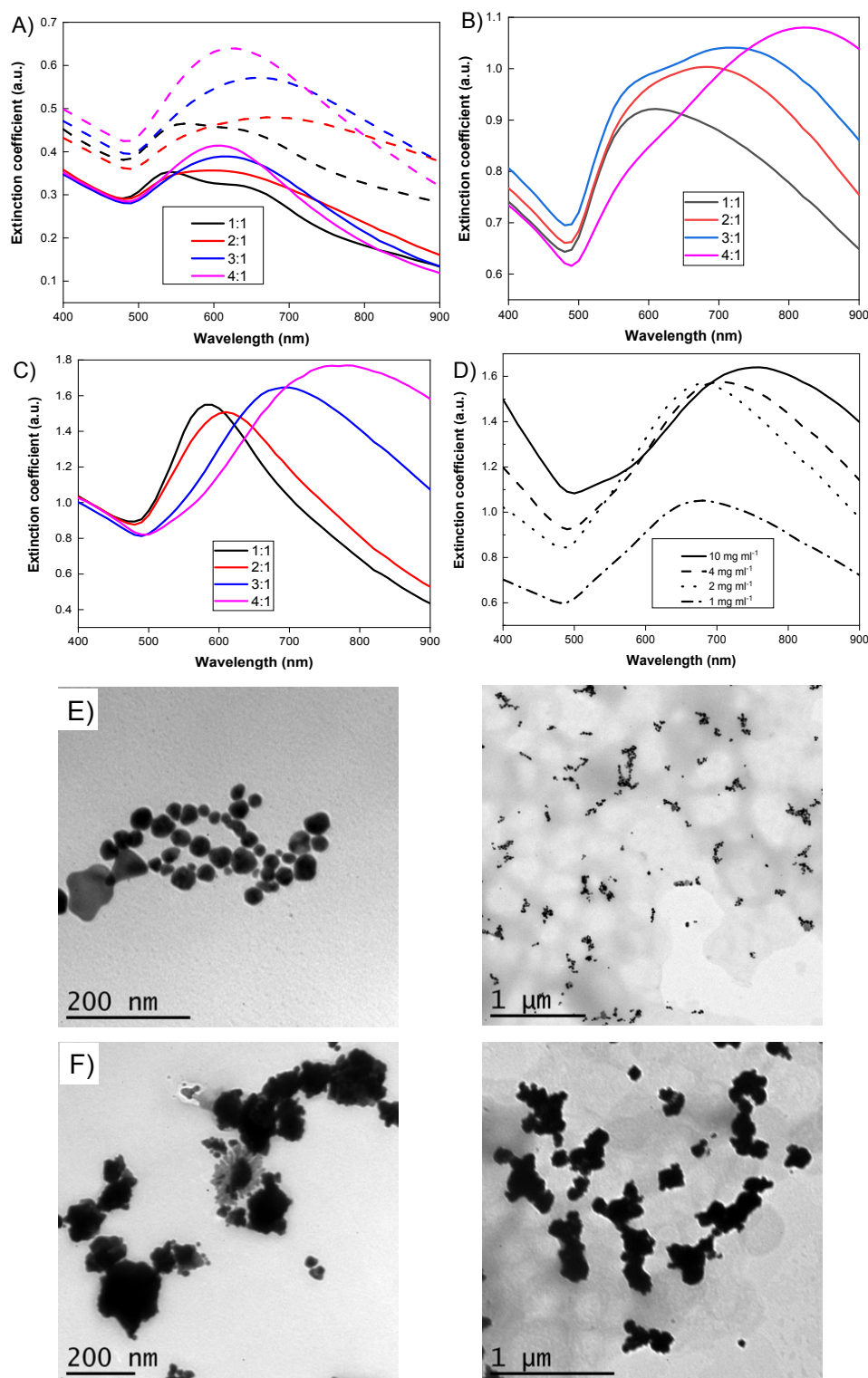
Figure 7.3: The UV-vis spectra of gold nanoparticles synthesised in the presence of PEGylated liposomes using A) 2.5 mM and 5 mM HAuCl$_4$, B) 7.5 mM HAuCl$_4$ and C) 10 mM HAuCl$_4$, with 1:1 (solid), 2:1 (dashed), 3:1 (dotted) and 4:1 (dashed and dotted) ratio of AA:Au ions. D) The absorbance spectra of 10 mM HAuCl$_4$ and 30 mM AA synthesised in the presence of different concentrations of liposomes. E) TEM images of AuNPs synthesised with liposomes, using 10 mM HAuCl$_4$ and 10 mM AA. F) TEM images of AuNPs synthesised with liposomes, using 10 mM HAuCl$_4$ and 40 mM AA.

Both the TEM and absorbance results indicate that instead of coating the liposomes the gold was forming branched gold nanoparticles, often termed as nanostar (AuNS)[435–439], nanourchin[440–443] or nanoflower[444,445] structures. Gold branched AuNPs have a solid metallic core that provides an absorbance peak similar to that of a nanosphere, between 500-600 nm, and protrusions from the particle surface that absorb light at longer wavelengths. Barbosa *et. al* demonstrated that using a seeded synthesis of AuNSs the peak position and amplitude may be controlled by varying the size of the Au seed and the ratio of Au seeds to the concentration of HAuCl$_4$ used during the synthesis.[435] Figure 7.3B, depicts that the protruding tips produce a shoulder at higher wavelengths than the absorption peak defined by the particle core (550-600 nm), however as the protrusions increase in length and the particles become more anistropic, the absorption at higher wavelengths becomes dominant resulting in the core absorbance becoming a shoulder at 500-600 nm. At the lowest AA:Au ratio (1:1) the peak at 600 nm had a broad slope at longer wavelengths, however upon increasing the AA:Au ratio to 3:1 the peak at 710 nm is the larger than that at 600 nm. Further increasing the ratio to 4:1, the 600 nm peak is almost completely enveloped by the larger peak at 800 nm and syntheses performed using 10 mM HAuCl$_4$ at 3:1 and 4:1 AA:Au ratios show no visible peak at 600 nm (Figure 7.3C).

In the absence of liposomes, the synthesis produces spherical particles with an absorbance at 500-600 nm, at all AA:Au ratios and independent of the HAuCl$_4$ concentration. It is therefore evident that the synthesis is affected by the presence of the liposomes that induce the anisotropic growth. This effect has been utilised to synthesise AuNS particles through the deposition of gold onto liposomes (DPPC/1-palmitoyl-2-hydroxy-*sn*-glycero-3 phosphocholine (MPPC)/1,2-distearoyl-*sn*-glycero-3-phosphoethanolamine-N-[methoxy(polyethylene glycol)-2000] (DSPE-mPEG2k)), producing particles with an absorbance peak at 700 nm and a shoulder at 500 nm.[446] Sivasubramanian *et al.* did not demonstrate control over the absorbance properties, nor did they clarify the synthesis mechanisms beyond stating that the addition of zero valence metal atoms to a liposome solution has been shown to produce deposition onto the vesicle bilayer.[447] This reinforces that the gold deposited onto the bilayer acts as a nucleation point, or seed, onto which further gold is adsorbed to form the AuNS structure.

The effects of the liposome concentration on particle synthesis were also investigated. The lipid concentration was varied between 10 and 0.7 mg ml^{-1} and particles were synthesised using 10 mM HAuCl$_4$ and 30 mM AA. Increasing the liposome concentration above 2 mg ml^{-1} caused

a slight red-shift in the absorbance peak position, $\sim$80 nm from 2 to 10 mg ml^{-1}, but had little effect on the peak extinction coefficient, Figure 7.3D. However, upon decreasing the lipid concentration to 1 mg ml^{-1} there was a significant decrease in the peak extinction coefficient.

7.1.1.1   Laser irradiation of gold nanostars
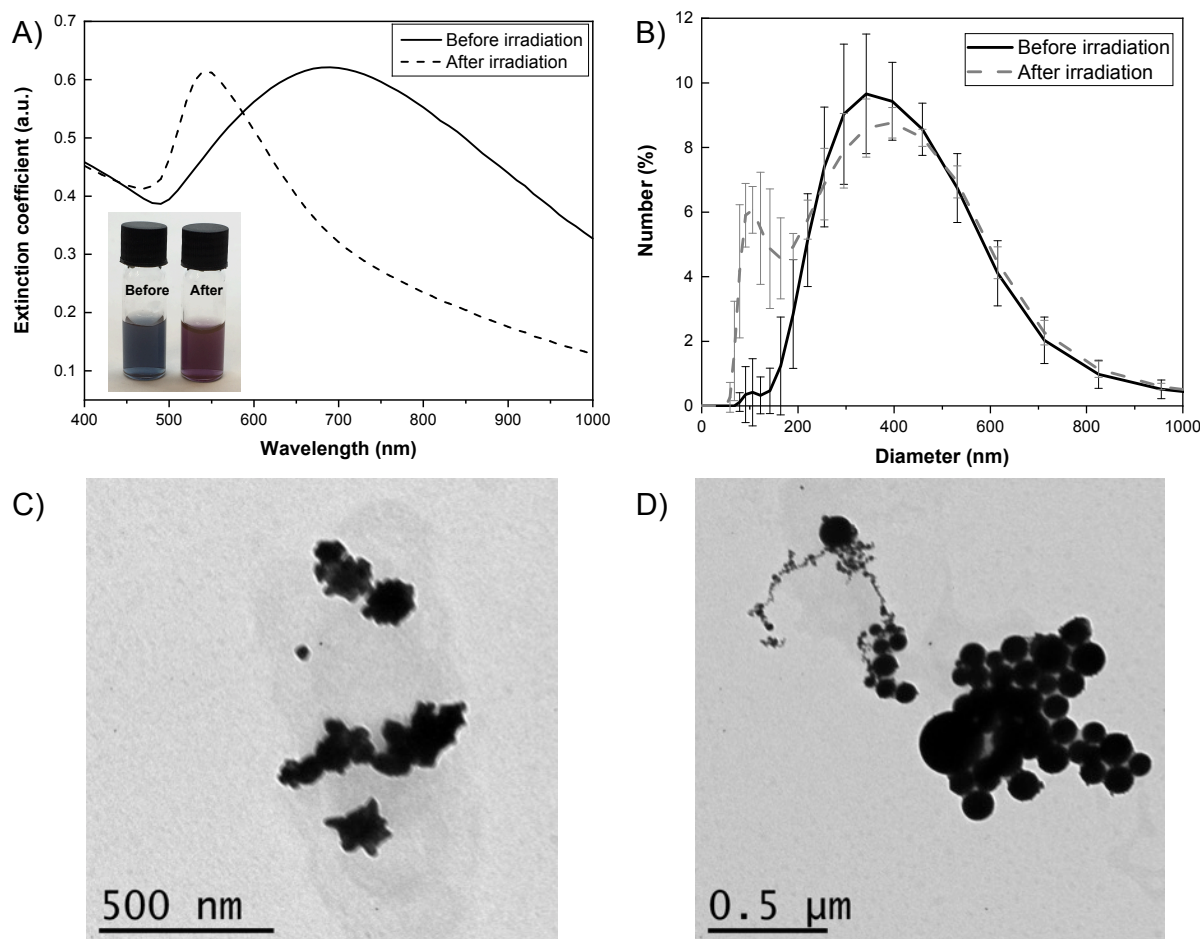
Figure 7.4: A) The UV-vis spectra and B) DLS sizing data of AuNPs synthesised in the presence of PEGylated liposomes before and after irradiation at 4,500 μJ cm^{-2} (10 Hz) at 700 nm for 1 min. Inset is an image of the solutions before and after irradiation. TEM images of the AuNP-liposome complex C) with and D) without laser irradiation.

The study by Sivasubramanian *et al.* demonstrated that the AuNSs synthesised using calcein-loaded liposomes could be used to trigger release under pulse laser irradiation, fluence of 10 mJ cm^{-2} at 690 nm and a frequency of 10 Hz.[446] As such, the laser irradiation of AuNSs synthesised with the IK8-loaded PEGylated liposomes was investigated. The IK8 release from the liposome-AuNS (3:1 AA:Au, 10 mM HAuCl$_4$) system under pulse laser irradiation at 4,500 μJ cm^{-2}, frequency 10 Hz at 700 nm for 1 minute, was assessed. This resulted in rapid melting and reshaping of the of the AuNSs into AuNPs, causing a visible colour change from a deep

blue to the distinctive red of AuNPs, and can be clearly seen in the blue shift in the absorbance spectrum, Figure 7.4A. TEM images of the AuNSs before and after irradiation, Figures 7.4C and D respectively, show the morphological change from anisotropic spiky to smooth spherical particles that produced the change in the absorbance spectrum. Despite the AuNS melting, no liposome destruction was observed using dynamic light scattering (DLS), Figure 7.4B. After irradiation there was a prominent peak at 100 nm attributed to the AuNS melting, however there was little change in the liposome distribution at 350-400 nm. Samples containing calcein-loaded liposomes were also irradiated however there was no change in fluorescence, indicating that there was no release of encapsulated materials.

7.1.2 Non-PEGylated liposomes

The presence of a PEG periliposomal layer may have sterically or electrostatically hindered the gold ion adsorption onto the lipid membrane. As such, the AuNP synthesis was repeated using non-PEGylated liposomes containing only 1,2-distearoyl-sn-glycero-3-phosphocholine (DSPC) and cholesterol (70/30 mol%).

Using 2.5 mM HAuCl$_4$ the UV-vis spectra of the synthesised AuNPs show a very broad peak at 680 nm with a 1:1 AA:Au ratio, Figure 7.5A. At AA:Au ratios of 2:1 and higher the peak increases and is red-shifted to 900 nm. At 5 mM HAuCl$_4$ all samples exhibit similar absorbance profiles with a peak at 850-900 nm, however as the AA:Au is increased a shoulder at 670 nm starts to form, Figure 7.5B. This shoulder becomes more prominent upon increasing the HAuCl$_4$ concentration to 10 mM, Figure 7.5C. TEM images were taken of samples containing 2.5 and 5 mM HAuCl$_4$ at 4:1 ratios of AA:Au. Both samples display the formation of fractal like gold nanoparticles that resemble snowflakes, with a dense centre and seemingly thin fractal growths forming a flake like structure. It is also apparent that the particles are free in solution, not adhered to liposomes; meaning such a system would be unable to provide triggered release in response to the pulsed laser irradiation. In order to increase the chances of AuNP synthesis occurring directly on the liposome surface the thiolated lipid 1,2-dipalmitoyl-sn-Glycero-3-Phosphothioethanol (DPPE-Ptd) was added to the vesicle composition. Thiols contain sulphur ions that have a high affinity to Au, meaning that the Au ions should bind to the thiol groups providing initial nucleation sites onto which the reduced Au$^+$ ions will adhere.
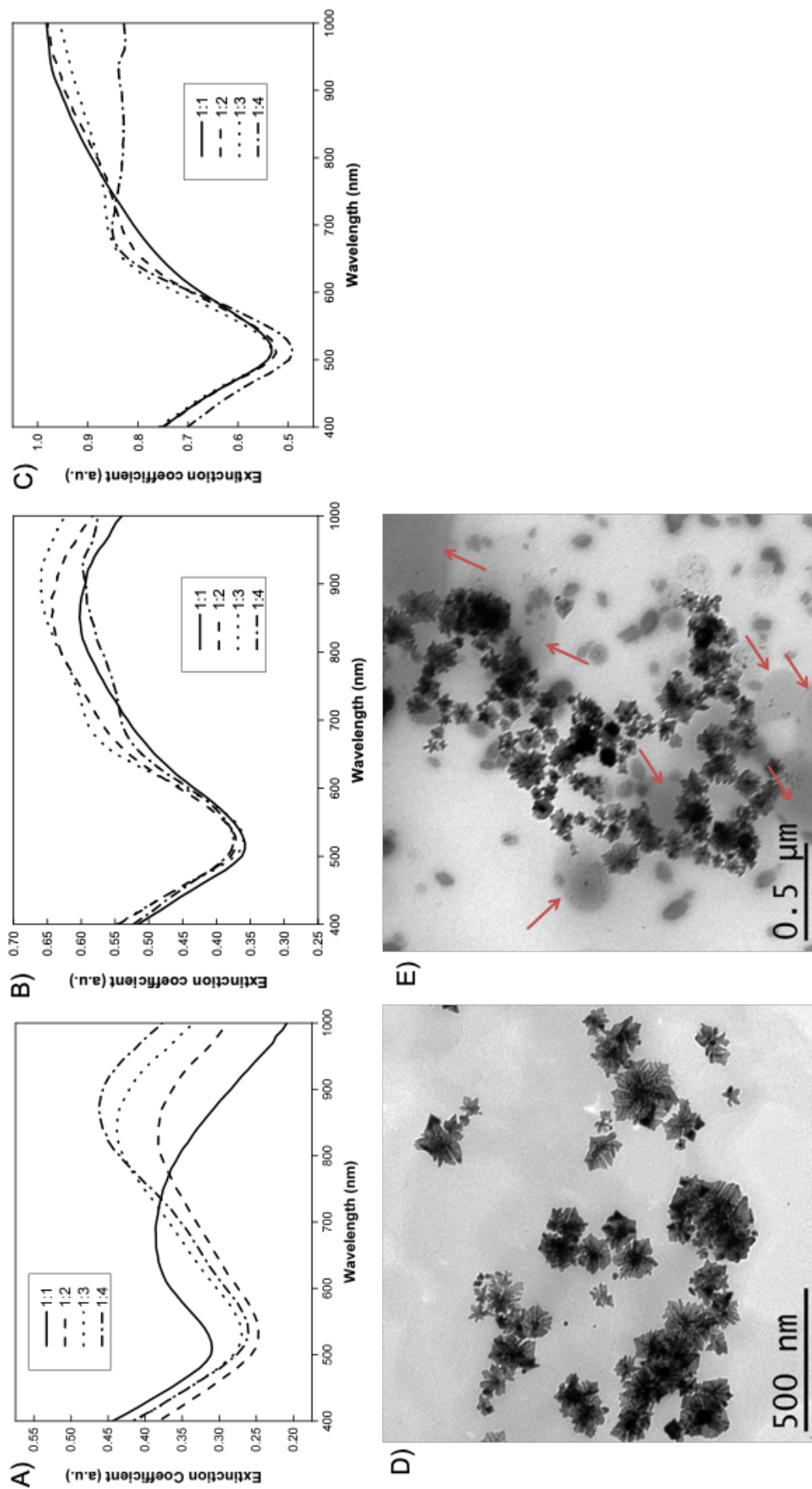
Figure 7.5: UV-vis spectra of AuNP synthesis in the presence of DSPC/cholesterol liposomes (70/30 mol%) by varying the ascorbic acid to gold ratio using A) 2.5 mM, B) 5 mM and C) 10 mM of HAuCl$_4$. D,E) transmission electron micrographs of AuNPs synthesised in the presence of DSPC/cholesterol liposomes using 5 mM HAuCl$_4$ at a 4:1 AA:Au ratio. Liposomes are indicated with red arrows.

7.1.3   Liposomes containing thiol-functionalised lipids

DPPE-Ptd thioethanol was introduced into the liposome composition with the idea that the reduced gold ions will bind to the thiol group creating a nucleation site for further gold deposition, thus increasing the likelihood of AuNPs being bound to the liposome surface. Functionalising the liposome surface to facilitate Au adhesion has been demonstrated by Jin *et al.*, who utilised liposomes containing poly-L-histidine, a polymer capable of chelating metal ions, to initiate and control the growth of a gold shell around the lipid vesicle.[222]. As such, the initial step was to optimise the fabrication of the thiolated liposomes. Experiments were performed using liposomes of DSPC/cholesterol/DPPE-Ptd (69/30/1 mol%), however all samples exhibited rapid vesicle aggregation. As such, 2% DSPE-mPEG2K was introduced into the liposome structure to improve the colloidal stability. After 48 hours of dialysis the IK8-loaded PEGylated and thiolated liposomes (DSPC/chol/DSPE-mPEG2K/DPPE-Ptd, 67/30/2/1 mol%) were 330 $\pm$ 96 nm in diameter (Figure 7.6A), demonstrating that the inclusion of DPPE-Ptd did not affect the liposome formation and that the introduction of the PEG prevented aggregation. These liposomes also exhibited the encapsulation of 681 $\pm$ 60 μg ml^{-1}, over 20 times the MIC of IK8 against *S. aureus*, when using a 10 mg lipid film and a 5 mg ml^{-1} IK8 solution in PBS.

The AuNP synthesis was performed using liposomes containing 5%, 3% and 1% DPPE-Pdt, the UV-vis spectra can be seen in Figures 7.6 B, C and D respectively. The absorption spectra of the samples using 5% and 3% DPPE-Pdt liposomes depict AuNP formation using 2.5 mM of HAuCl$_4$ at a 1:1 AA:Au ratio, but using a higher AA:Au ratios and higher HAuCl$_4$ concentrations, the particles either aggregated or had very broad spectra that peaked above 900 nm. Using liposomes containing 1% DPPE-Ptd more control was afforded using 5 mM HAuCl$_4$. At an AA:Au ratio of 1:1 the AuNPs produced a broad spectrum with a peak at 780 nm. The TEM images of this sample (Figure 7.6E) show that the AuNPs were anisotropic structures, providing the red-shift in the absorbance peak. The TEM images also show that the AuNPs have a high affinity to the thiolated liposomes, over 99% of the particles are adjacent to liposomes. This indicates that the thiol group can be used to adhere AuNPs to the liposome structure, even if it does not encourage the synthesis of a Au coating. As such, it was decided that it would be preferential to bind thoroughly characterised and monodispersed AuNPs to the liposomes, rather than the amorphous structures displayed in Figure 7.6E.
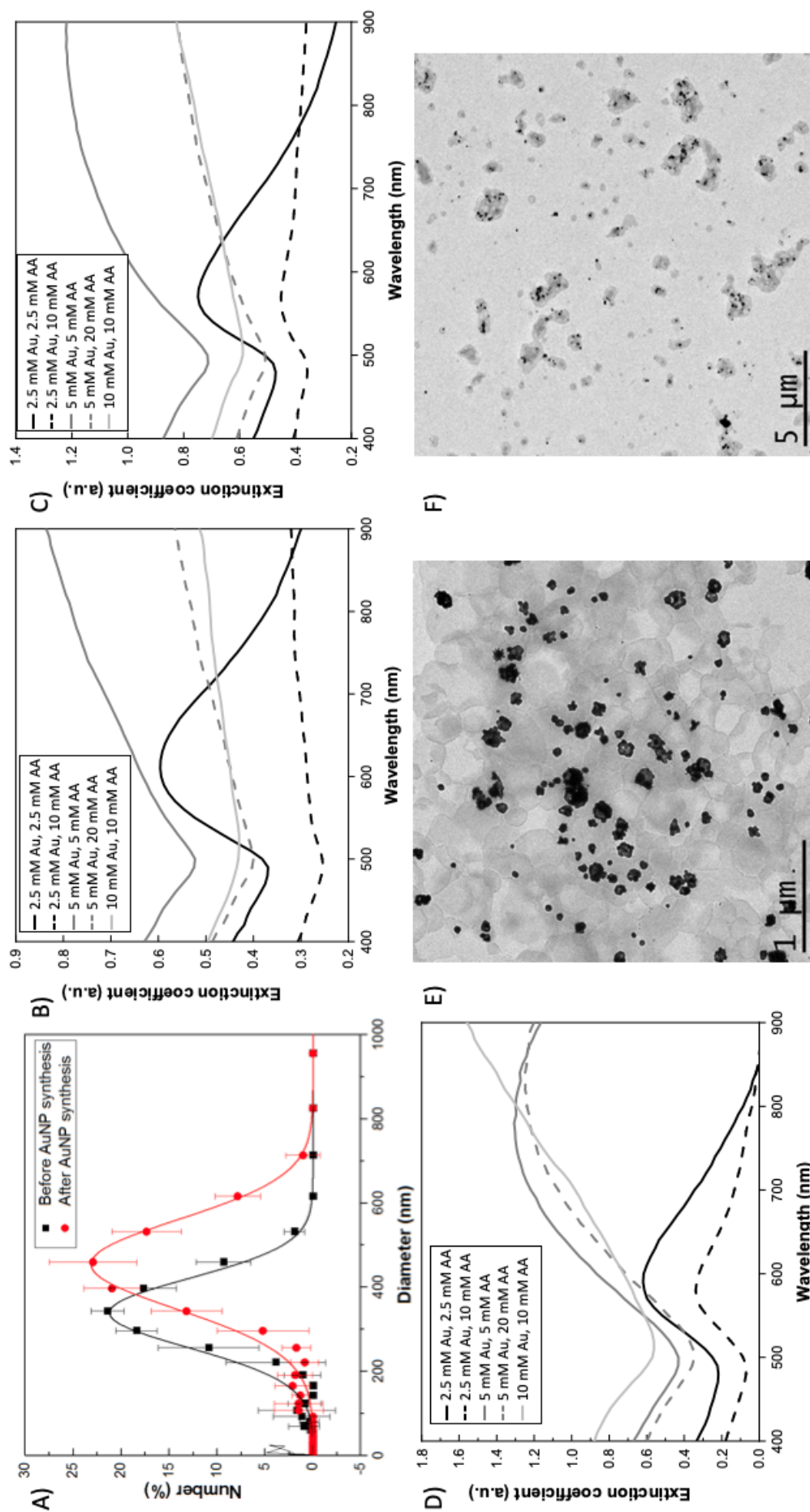
Figure 7.6: The UV-vis spectra of gold nanoparticles synthesised in the presence of liposomes (DSPC/cholesterol/DSPE-mPEG2k, 68/30/2 mol%) replacing A) 5% and B) 3% and C) 1% of DSPC with DPPE-Ptd. Numbers in the legend refer to the concentrations of AA and $HAuCl_4$ in mM. D) DLS data of liposomes (DSPC/cholesterol/DSPE-mPEG2k/DPPE-Ptd, 67/30/2/1 mol%) before (black) and after (red) AuNPs are synthesised (5 mM $HAuCl_4$ + 5mM AA). E) TEM images of 1% DPPE-Ptd liposomes and AuNPs synthesised with liposomes, using 5 mM $HAuCl_4$ and 5 mM AA.

7.2   Gold nanoparticle conjugation to thiolated-liposomes

The facile conjugation of AuNPs to thiolated liposomes indicated that rather than synthesise an Au coating for the liposomes, simply binding particles to the bilayer may prove an equally viable means of providing pulsed laser triggered AMP delivery. Given their exceptionally high absorption cross-section and simplicity of functionalisation, AuNRs were chosen as the ideal photothermal agent to bind to the liposome surface, see Figure 7.7.
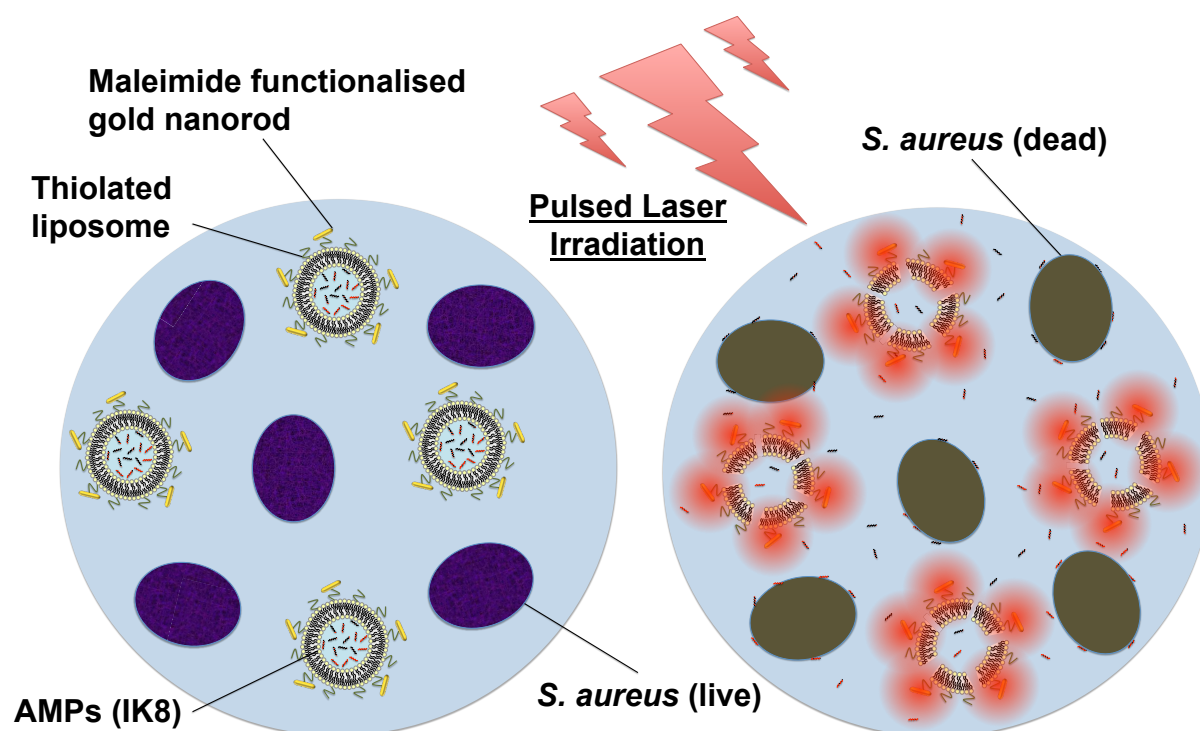
Figure 7.7: Schematic representation of AuNR-conjugated IK8-loaded liposomes providing pulsed laser stimulated release of IK8 to treat a *S. aureus* suspension.

7.2.1   Citrate capped gold nanospheres

Initially to test whether prefabricated gold nanoparticles can be conjugated to the liposomes, AA-stabilised AuNPs were mixed with liposomes both with and without 1% DPPE-Ptd. The AuNPs were synthesised by mixing 5 mM HAuCl$_4$ with 5 mM AA, turning the solution a deep red. Equal volumes of the AuNP solution and liposome suspensions were allowed to mix overnight. The sample containing liposomes without DPPE-Ptd displayed large amounts of precipitation on the surfaces of the vial, whereas the sample with thiolated-liposomes remained a deep red coloration. The 5 μl sample for TEM imaging was extracted from the centre of the vial without mixing.
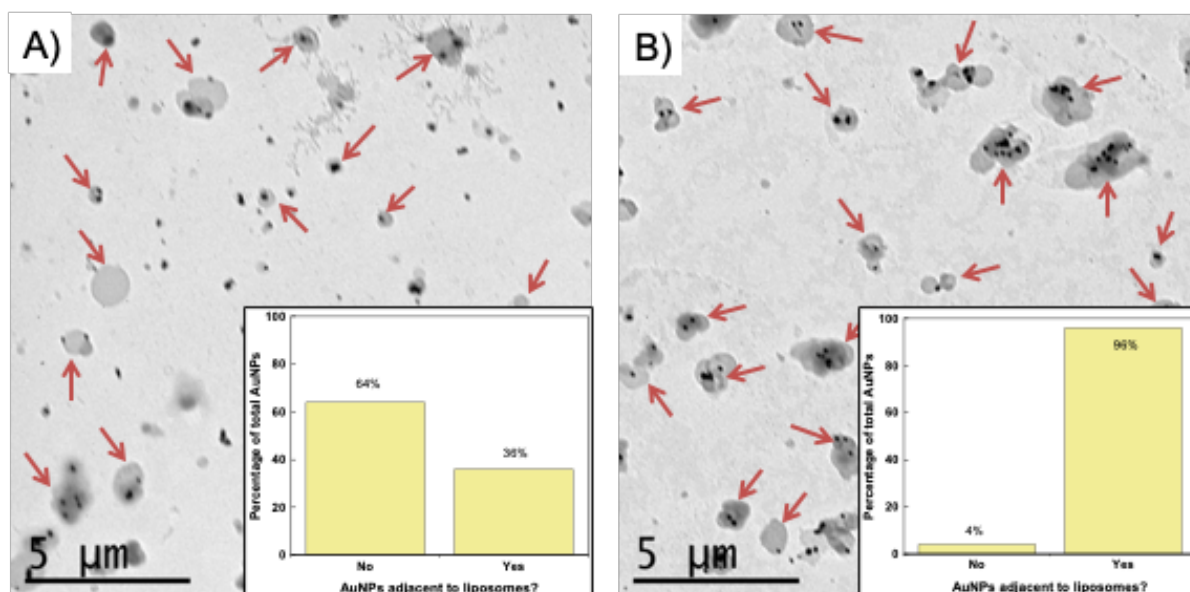
Figure 7.8: TEM images of citrate-stabilised AuNPs mixed with liposomes A) without and B) with thiolated lipids. AuNPs can be seen as small dark spots, liposomes are indicated with red arrows. Inset bar charts display the percentage of the total AuNPs than are immediately adjacent to a liposome. n = 2961 & 1616 for liposomes without and with thiolated lipids respectively.

TEM images of the samples displayed a significant difference in the AuNP distribution. The sample containing liposomes without the thiolated lipids displayed a random distribution of AuNPs, with 64% not adjacent to a liposome (n=2961), Figure 7.8A. Images of the equivalent sample with liposomes containing DPPE-Ptd showed 96% of AuNPs associated with liposomes (n=1616), Figure 7.8B. The significant difference in the particle positioning indicates that the DPPE-Ptd does provide AuNP-liposome adhesion.

7.2.2 PEG-maleimide functionalised phospholipid stabilised AuNRs

Conjugation of thiolated molecules to AuNP can be performed by simply mixing the two components and utilising the high affinity of sulphur ions to gold to replace the original coating. This procedure however relies on the thiol gaining direct access to the AuNP surface, meaning the steric stabilisation afforded to PEGylated AuNPs can obstruct the binding process. As such, binding between the thiolated liposomes and the PEGylated phospholipid coated AuNRs, as described in chapter 4, was hindered. Given the significant reduction in toxicity of the phospholipid stabilised AuNRs against *S. aureus* compared to alternate coatings (Figure 4.5), functionalising the phospholipid coating to enable binding to the thiolated liposomes was deemed the best way forward. As such, a portion of the DSPE-mPEG2k in the phospholipid bilayer coating

the AuNR, was substituted with DSPE-mPEG2k-maleimide to enable a maleimide-thiol "click" reaction (as described in Section 6.1.1) to conjugate the AuNR to the liposome surface. The inclusion of the maleimide functionalised phospholipids was achieved through the lipid coating procedure as described in section 4.2, however the final batch of liposomes to be sonicated with the AuNRs, was fabricated using DSPC/DSPE-mPEG/DSPE-mPEG-maleimide (95/4/1 mol%). Maleimide-functionalised lipids were only included in the final round of the CTAB + NaOL replacement as inclusion in earlier stages made the dispersion of the pellet significantly more difficult.
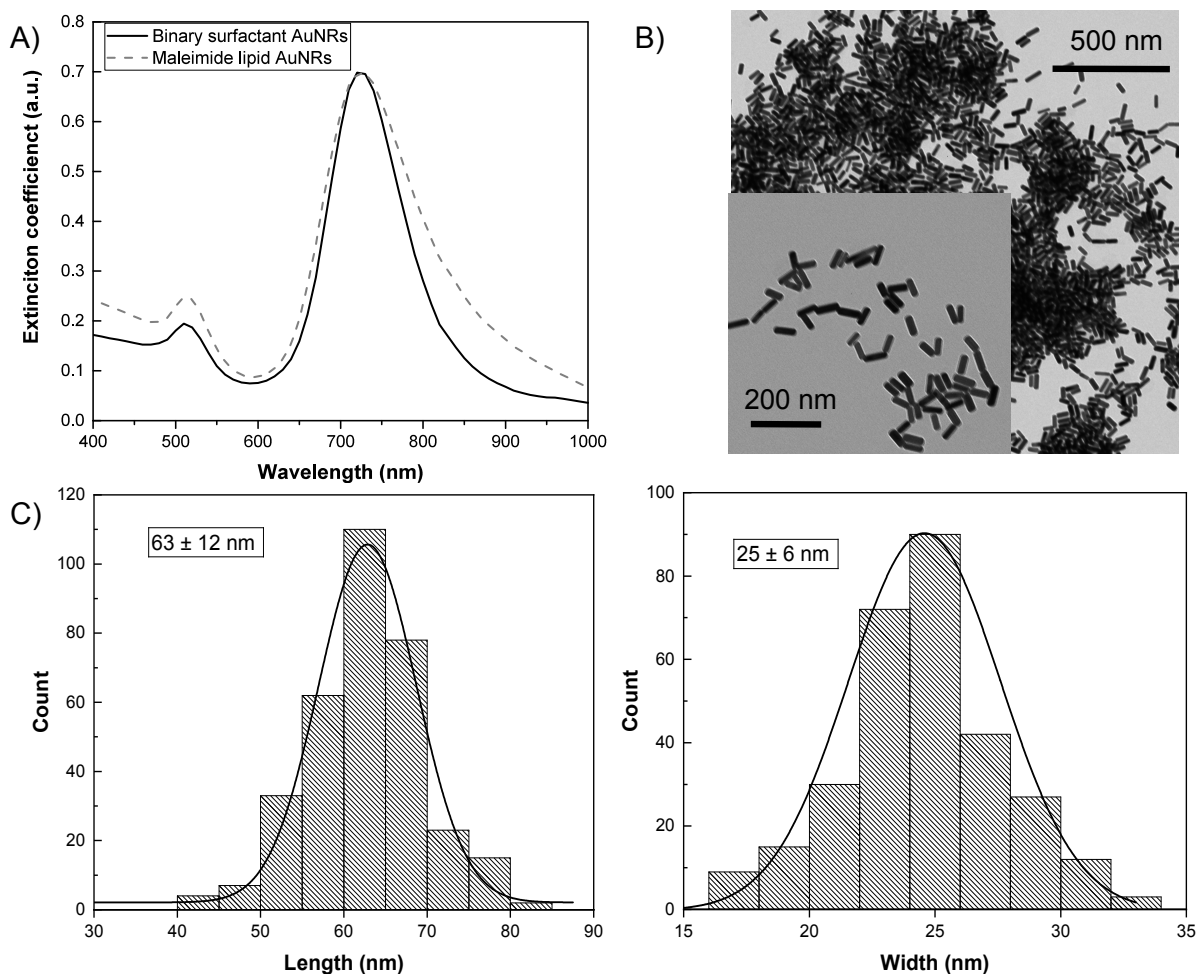
Figure 7.9: A) The absorbance spectra of binary surfactant (solid black line) and maleimide-functinalised phospholipid stabilised (grey dashed line) AuNRs. B) TEM images of maleimide-functionalised phospholipid stabilised AuNRs. C) The length (left) and width (right) distributions of the maleimide-functionalised phospholipid stabilised AuNRs (n=311).

Initially liposomes containing 1, 3 and 5% DPSE-mPEG2k-maleimide (DSPC/DPSE-mPEG2k /DPSE-mPEG2k-maleimide molar ratios of 95/4/1, 95/2/3 and 95/0/5 respectively), were sonicated with AuNRs, however after the lipid replacement with 3 and 5% maleimide-functionalised

lipids the resultant AuNR pellets could not be dispersed. AuNRs coated with 1% DSPE-mPEG2k-maleimide were easily dispersed and the lipid coating process had little effect on the AuNR optical properties, Figure 7.9A. The TEM images show a tight size distribution of AuNRs (63 x 25 nm, Figure 7.9C) and a high shape yield (>99%, Figure 7.9B).

7.2.3 Maleimide-functionalised phospholipid coated AuNR conjugation to thiolated liposomes
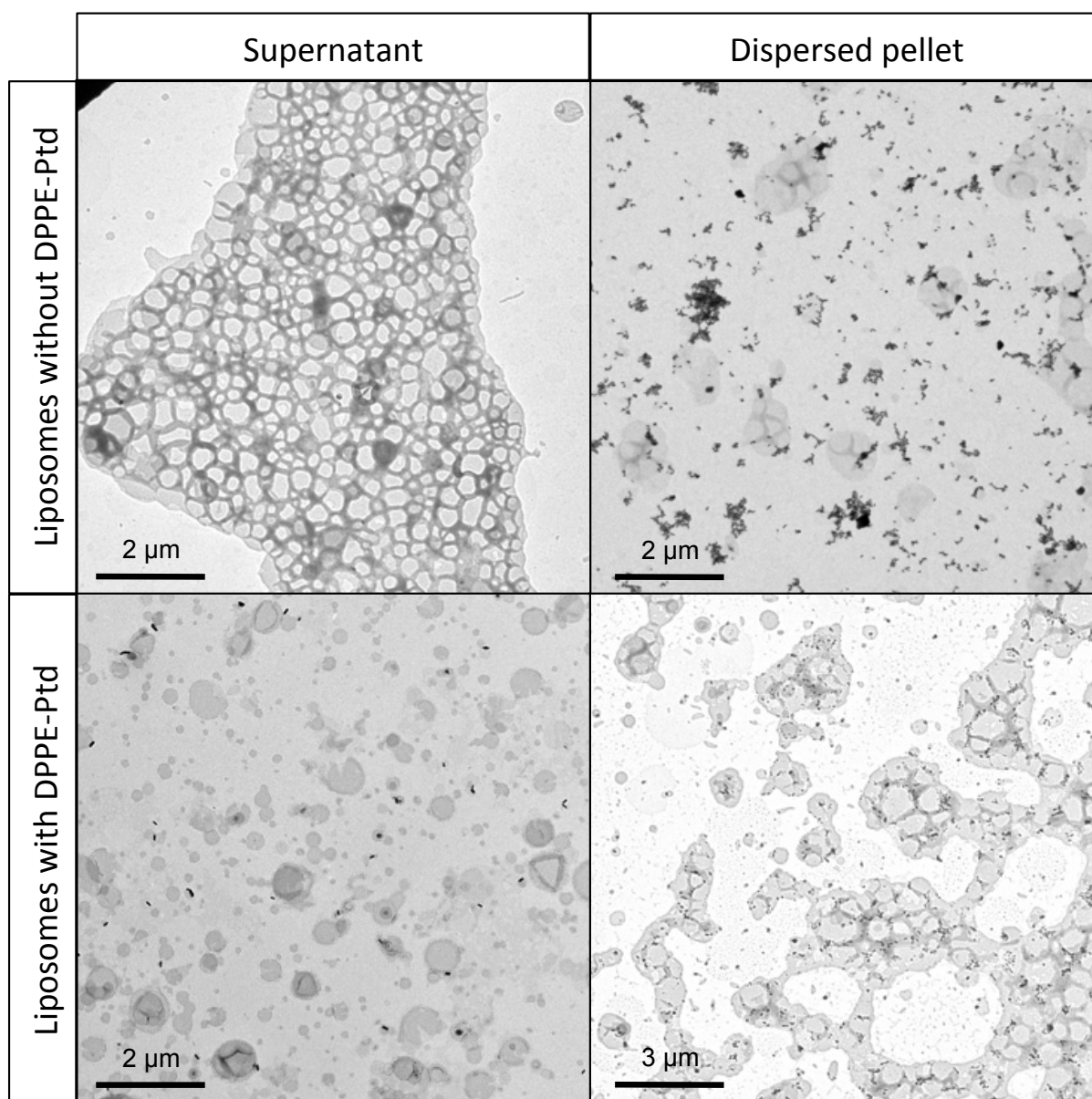
Figure 7.10: TEM images of the supernatant and dispersed pellets of maleimide-functionalised AuNRs mixed with liposomes both with and without DPPE-Ptd. These effects were observed in two independent samples.

To determine whether the maleimide-thiol "click" reaction was possible, equal volumes of maleimide-functionalised AuNRs (200 μg ml^{-1} of Au) were mixed with liposomes both with and without DPPE-Ptd (10 mg ml^{-1} lipid) and left overnight. The following morning the samples were centrifuged (9,000 x g, 30 mins), the supernatant was removed and the pellet was dispersed in Milli-Q. The supernatant and dispersed particles of both samples were then imaged using TEM.

Figure 7.10 displays clear differences in the AuNR and liposome distribution between the two samples. The supernatant of the sample containing liposomes without DPPE-Ptd was found to contain the majority of the liposomes, as they do not have the density to be pelleted at 9,000 x g, with no AuNRs. Conversely, the dispersed pellet displays predominantly the dense AuNRs, with very few liposomes. The distinct separation between the liposomes in the supernatant and the AuNRs within the pellet, clearly indicating that there was no binding between the liposomes and the AuNRs. The sample containing the thiolated liposomes however, displayed a larger proportion of the liposomes within the pellet than in the supernatant. These liposomes also all have AuNRs adjacent to them, indicating that the AuNRs had bound to the vesicles making complexes dense enough to be pelleted at 9,000 g. The liposomes in the supernatant do not have associated AuNRs, meaning they would not be pelleted. These results demonstrate the successful conjugation of phospholipid AuNRs to thiolated liposomes using "click" chemistry.

7.3　Pulse laser irradiation of maleimide-functionalised phopholipid stabilised AuNRs and triggered liposomal release

The photothermal response of the AuNRs under pulsed laser irradiation was next investigated. AuNRs were added to a quartz curvette and placed directly in the beam path, the power was regulated by inserting filters of neutral density (ND) 1 and 2, reducing the pulse power by 90 and 99% respectively. The AuNRs were then irradiated with a fluence of 4,500 μJ cm^{-2}, with a pulsewidth of 5 ns and a repetition rate of 10 Hz at 738 nm, before the optical properties of the AuNRs were then analysed using the UV-vis to identify any morphological changes.
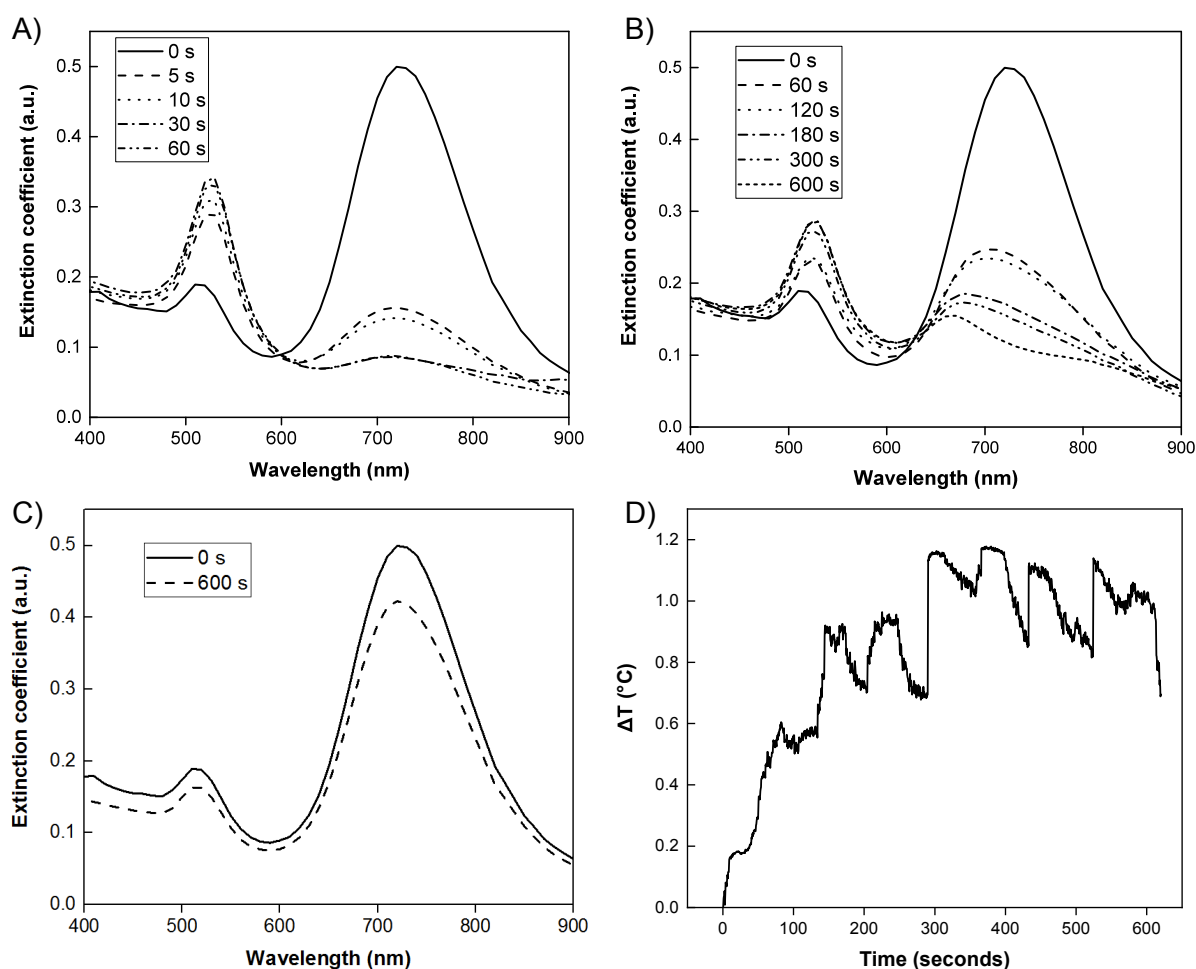
Figure 7.11: The AuNR absorbance spectra when irradiated for up to 10 mins at 738 nm using a 10 Hz pulse laser at A) 4,500 μJ cm^{-2}, B) 450 μJ cm^{-2} and C) 45 μJ cm^{-2}. D) The change in bulk temperature within a quartz curvette containing 200 μl of 200 μg ml^{-1} AuNRs in Milli-Q, starting from a base temperature of 22°C, upon irradiation for 10 mins with a fluence of 450 μJ cm^{-2} at 10 HZ at 738 nm.

Significant changes in the AuNR absorbance properties can be observed within 5 seconds of irradiation with a 4,500 μJ cm^{-2} fluence. The AuNRs exhibited an almost complete reduction in the longitudinal plasmonic peak at 738 nm and a substantial increase in the transverse plasmonic peak at 520 nm, Figure 7.11A. The change in the absorbance is attributed to the plasmonic absorbance of the light causing electron-phonon relaxation within the gold matrix providing enough kinetic energy to allow gold atom migration.[182] The AuNR surface atoms at the highest energy move from the areas of highest curvature, at the ends of AuNR, to the lower energy edges, and has been confirmed in the literature.[159,182–187] As such, this migration causes a reduction in the aspect ratio until a sphere is formed. The same transformational effects are observed upon irradiation at a fluence of 450 μJ cm^{-2}, however the change in the morphology

164

takes significantly longer, Figure 7.11B, with the peak absorbance value decreasing exponentially over time. The 10-fold decrease in the laser fluence decreases the energy available to be absorbed by the electrons, which in turn reduces the temperature achieved through electron-phonon scattering and kinetic energy of the surface atoms, ultimately slowing the migration process.[189] It is apparent however that from this slower process there is a red shift in the longitudinal absorption peak. Over the course of the 10 minute irradiation the longitudinal peak position decreases by ∼70 nm, in agreement with the literature that the irradiation does cause a decrease in the aspect ratio as the atoms migrate toward the formation of a sphere. This also affects the rate of transformation. As the absorbance efficiency at 738 nm decreases, less energy is transferred to the gold lattice meaning that the migration process slows with the irradiation time. The ∼1°C increase after 10 mins of irradiation at 450 μJ cm^{-2} also demonstrates low bulk heating that is desired from this AMP delivery system, Figure 7.11D. Upon further reducing the laser fluence to 45 μJ cm^{-2}, after a 10 minute irradiation only 16% reduction in the AuNR longitudinal peak was observed, Figure 7.11C.

7.3.1 Photothermal triggered release from AuNR adsorbed liposome complexes

The next stage of development was to ascertain whether the liposome-AuNR system can provide triggered release under pulsed laser irradiation. IK8-loaded liposomes were fabricated both with and without thiolated lipids and mixed with an equal volume of maleimide-functionalised phospholipid coated AuNRs (200 μg ml^{-1}). The following day the samples were irradiated for 10 mins with a fluence of 45 or 45 μJ cm^{-2} (10 Hz at 738 nm), before centrifuging at 17,000 x g for 30 mins to pellet the AuNRs and liposomes. The particle-free supernatant was then added to the colorimetric Bicinchoninic acid (BCA) assay that utilises the absorbance at 562 nm to quantify the peptide concentration.
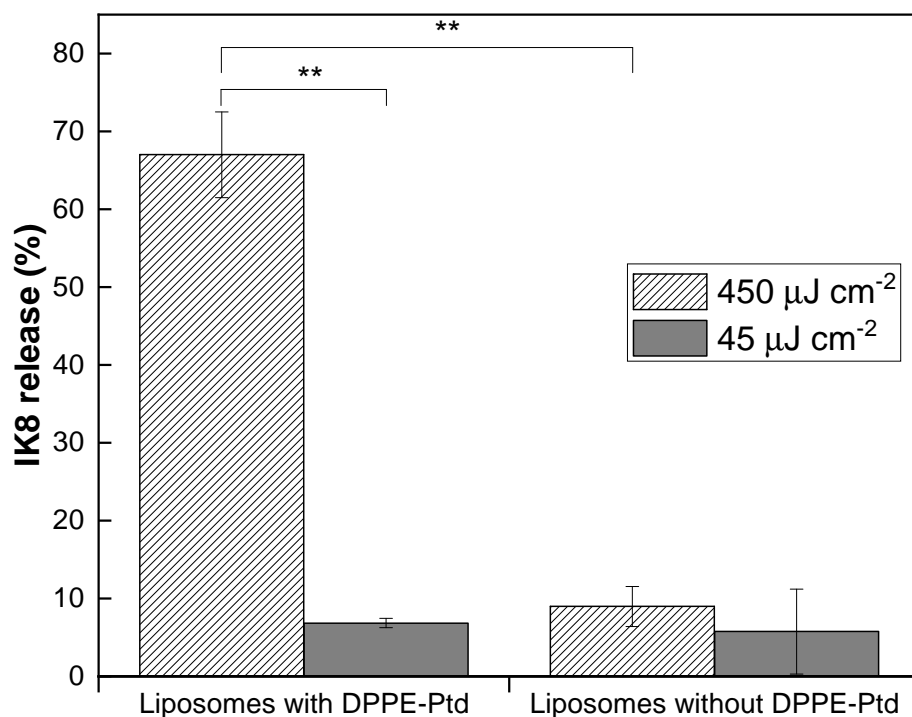
Figure 7.12: The IK8 release profile from liposomes with and without DPPE-Ptd, when mixed with maleimide-functionalised AuNRs and irradiated with a fluence of 45 (dark grey column) or 450 (diagonal slashed column) μJ cm^{-2} for 10 mins. Error bars indicate the standard deviation (n=4) and Two-tailed T-testing was performed to identify statistical significance, p-values indicate: ** < 0.01.

The main conclusion that can be drawn from Figure 7.12 is that triggered delivery of IK8 was only achieved when utilising the maleimide-AuNRs in combination with thiolated liposomes and irradiated at a fluence of 450 μJ cm^{-2}, releasing $67 \pm 5\%$ of encapsulated AMP. The same system using a fluence of 45 μJ cm^{-2} resulted in release of $7 \pm 1\%$, a statistically significant decrease, indicating that a higher laser energy is required to cause liposome disruption. In both circumstances where the liposomes did not contain DPPE-Ptd there was little release under laser irradiation, $< 10\%$ in both samples. In this system the maleimide-functionalised AuNRs cannot bind to the liposomes meaning they are free in suspension, and as such upon irradiation at 450 μJ cm^{-2} displayed a 58% reduction in AMP release compared to their counterpart with AuNR-liposome binding. The importance of the proximity of a photothermal source to the liposome is dependent on the means of liposome disruption. As opposed to the use

of a CW laser, the liposome disruption from a pulse laser does not utilise the photothermal heating directly but instead exploits mechanical disruption of drug carriers through micro- or nano-bubble cavitation.[194,222,241] Wu *et al.* (2008) suggested that the high thermal gradients produced AuNPs upon pulsed laser irradiation, are capable of vaporising water molecules in the immediate vicinity to the particle.[180] This vaporised pocket of water expands rapidly before imploding and releasing a shock wave that can disrupt a lipid bilayer. These effects are so highly localised that tethering HGNs to the liposome surface increased the cargo release profile by 58% compared to HGNs free in suspension.
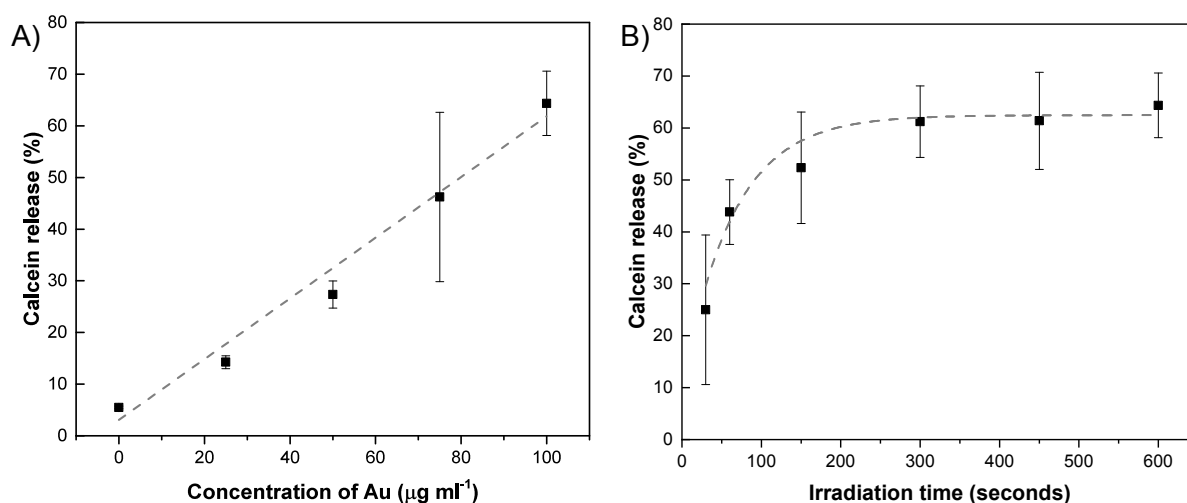
Figure 7.13: The calcein release profiles from maleimide-functionalised AuNRs bound to thiolated liposomes when A) varying AuNR concentration between 0 - 100 μg ml^{-1} under irradiation for 10 mins, and B) varying the irradiation time, 1 - 10 mins, using 100 μg ml^{-1} of AuNRs. All samples were irradiated at 738 nm with a fluence of 450 μJ cm^{-2} at 10 Hz.

The effects of the AuNR concentration and the irradiation time were next investigated to optimise the release profiles from the AuNR-liposome complex. As the AuNRs free in suspension produced a 58% reduction in release compared to AuNRs conjugated to the liposomes, there no further optimisation of the free AuNR system. A linear relationship was displayed when increasing the concentration of AuNR bound to the liposome, with a maximum release of 64 $\pm$ 6% with 100 μg ml^{-1} of Au, Figure 7.13A. The rate of increase of calcein release was found to exponentially decrease with time. After 1 minute 44 $\pm$ 6% of the calcein was released, after which there was a rapid decrease in release rate resulting in 61 $\pm$ 7% after 5 mins and 64 $\pm$ 6% after 10 mins. This exponential decrease in release correlates with the exponential decrease in absorbance at 738 nm as the AuNRs reshape with irradiation time, Figure 7.11B. This indicates that if the AuNR were able to retain its absorbance at 738 nm it would be possible to enhance

the liposome release profile.

7.3.2   Photothermal triggered AMP delivery to treat *S. aureus*
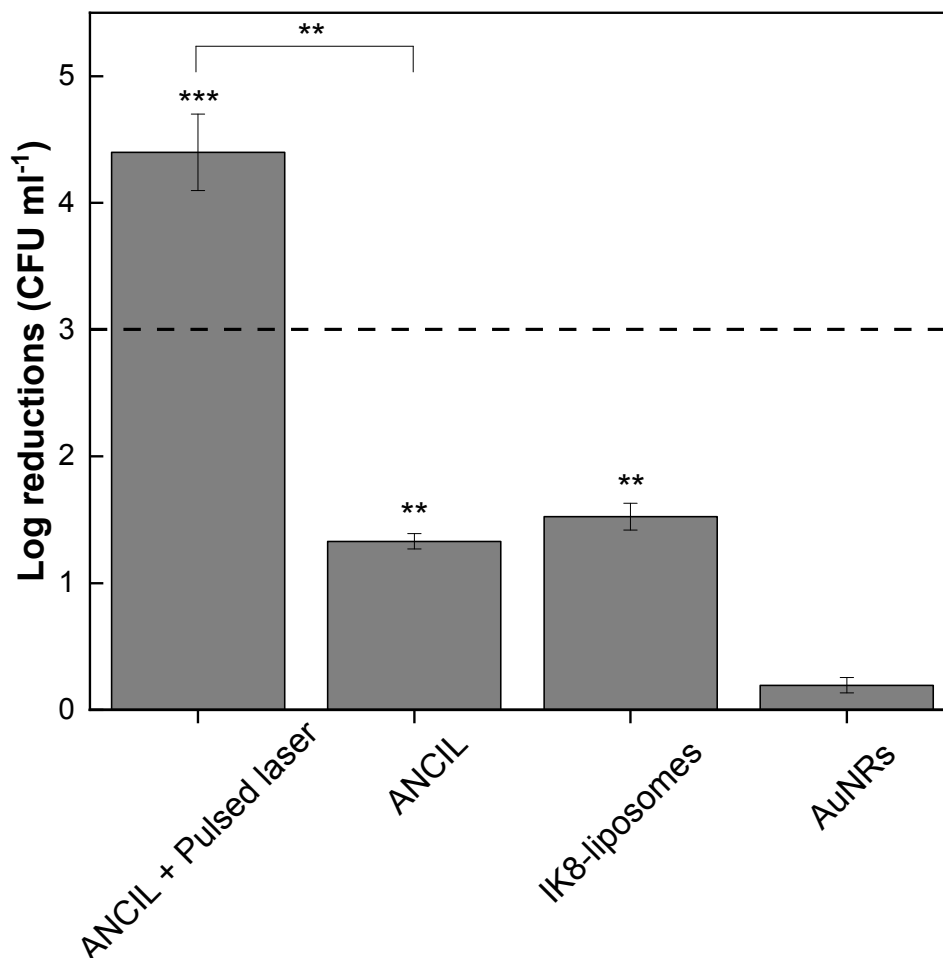
Figure 7.14: The reductions in *S. aureus* when treated with AuNR conjugated IK8-liposomes (ANCIL) with and without pulse laser irradiation at 450 μJ cm^{-2} at 738 nm for 5 mins, as well as CFU reductions from IK8-liposomes and AuNRs independently. The ANCIL complex was formed between liposomes functionalised with thiolated lipid DPPE-PtD, encapsulating the MIC of IK8, and 100 μg ml^{-1} of maleimide-functionalised phospholipid stabilised AuNRs. Results are the average of six replicates. Two-tailed T-testing was used to determine statistical significance, against *S. aureus* samples grown in MHB II, unless otherwise indicated. p-values indicate: ** < 0.01 and *** < 0.001.

The antimicrobial capabilities of this system were next assessed. Briefly, equal volumes of IK8 loaded thiolated-liposomes (10 mg ml^{-1} of lipid) and maleimide-functionalised AuNRs (200 μg ml^{-1} of Au) were mixed overnight. The following day the AuNR-liposome complexes were irradiated at 450 μJ cm^{-2}, at 738 nm for 5 minutes. The sample was then diluted in MHB II to 2 x the MIC before 100 μl was combined with 100 μl of *S. aureus* (1 x 10^5 CFU ml^{-1}).

The suspension was then incubated for 18 hours before microdilution and spreading onto agar plates. IK8-liposomes containing DPPE-Ptd (encapsulating 1 x the MIC of IK8) and maleimide-functionalised phospholipid coated AuNRs (100 μg ml^{-1}) were incubated with the bacteria as controls.

Upon irradiation, the AuNR conjugated IK8-liposome (ANCIL) complexes exhibited triggered release of IK8 resulting in bactericidal activity with a 4.4-log reduction in CFU ml^{-1}, Figure 7.14. This represents an additional 3.1-log reduction increase in antimicrobial activity compared to the equivalent system without laser irradiation. To our knowledge, this is the first instance of pulsed laser induced phothermally triggered delivery of AMPs to treat pathogenic bacteria. The second conclusion that can be drawn is that the IK8-loaded liposomes exhibited leakage that resulted in a 1.5-log reduction in CFU ml^{-1}. This decrease in *S. aureus* viability is greater than that exhibited by the DSPC/cholesterol/DSPE-mPEG2k (65/30/5 mol%) liposomes used in previous chapters (Figure 5.16). The increase in bacteria induced leakage may be due to the decrease in DSPE-mPEG2k in the liposomes containing DPPE-Ptd, in order to allow access of the maleimide groups of the AuNRs. DSPE-mPEG2k has been shown to provide steric hinderance between liposomes and bacteria[448], as such reducing the concentration of DSPE-mPEG2k may have increased the bacterial interactions, inducing a greater degree of IK8 leakage that produced more prominent antimicrobial effects. Finally the maleimide functionalised AuNRs had little affect on the *S. aureus* viability, but appeared to slightly decrease the degree of leakage from bound IK8-liposomes, however this difference is not statistically significant.

Conclusion:

This chapter has demonstrated the fabrication of a liposome-AuNR conjugate to provide bactericidal activity, using the first instance of pulsed laser induced photothermal triggered release of AMPs from liposomes. Initial attempts to conjugate AuNPs onto the liposome surface were performed by synthesising the particles in the presence of the AMP-loaded liposomes characterised in Chapter 5. However, these syntheses were unsuccessful in producing an AuNP coating instead producing a controllable growth of gold nanostars using the liposomes as a soft template. Through the regulation of the concentration of HAuCl$_4$, the AA to Au ion ratio and the liposome concentration the AuNS size and morphology could be altered such that the absorption peak could be tuned between between 550-800 nm. The system was then irradiated

for 1 minute using a nanosecond pulse laser with a fluence of 4,500 μJ cm^{-2} at 700 nm with a pules rate of 10 Hz, to determine the effects on the AuNS-liposome system and to see whether this triggered release from the liposomes. The irradiation caused rapid melting of the nanostars resulting in the transformation into nanospheres, with a characterisitic peak at 550 nm and caused a colour change from blue to red. This failed to induce liposome disruption or release of encapsualted materials, as such the Au coating was attempted on non-PEGylated liposomes to allow increased access of Au ions onto the lipid bilayer. This resulted in the formation of anisotropic gold fractal structures that were free in suspension alongside the liposomes. In an attempt to conjugate the AuNPs to the liposome, 1 mol% of the thiolated lipid DPPE-Ptd was included in the lipid composition. Synthesis of the AuNPs in the presence of the thiolated liposomes resulted in the fabrication of amorphous AuNPs, that exhibited highly efficient binding to the liposomes, $> 99\%$ of particles had formed complexes with liposomes. It was then decided to conjugate AuNRs to the thiolated liposomes through the functionalisation of the AuNR phospholipid bilayer with maleimide groups that enable "click" reactions with the thiols groups. Through simply mixing the two components overnight $> 99\%$ of the AuNRs were tethered to liposomes. The resultant AuNR-liposome complex provided triggered release of 67% of encapsualted AMP under irradiation at 450 μJ cm^{-2} (10 Hz, 738 nm) for 10 mins, a substantial increase in the 9% released using AuNRs free in the liposome suspension. This system was then used to demonstrate the triggered release of AMPs in order to treat planktonic *S. aureus*, resulting in a 4.4-log reduction in CFU ml^{-1}. Further characterisation of the AuNR-liposome systems is required in order to ensure long-term stability, biocompatibility and increased release efficacy, however this proof of concept study demonstrates pulsed laser triggered release, with no bulk heating effects, exhibiting huge potential for the stimuli-responsive delivery of antimicrobial agents.

Chapter 8

Conclusions and Future Work

The aim of this work was to develop drug delivery systems that provide light-responsive release of AMPs. Despite the high antimicrobial efficacy and reduced chances of resistance development AMP clinical translation has been hindered by low biostability, potential systemic toxicity, and susceptibility to protease degradation. As such, the delivery systems aim to address these issues to forward the implementation of AMPs as a part of the antimicrobial arsenal.

The development of the AMP delivery system started with the synthesis and characterisation of AuNRs that provided the light-responsive capabilities of the systems. Chapter 4 described how varying the centrimmonium bromide (CTAB) and sodium oleate (NaOL) ratios controlled the synthesis of AuNRs. Further we also showed that phospholipid replacement of the binary surfactants stabilising the AuNR provided both improved colloidal stability and cytocompatibility.

Through varying the concentrations of CTAB and NaOL in the AuNR growth solution, the longitudinal plasmonic absorption peak was be tuned between 650-1,000 nm, producing a high AuNR yield (>98%), reproducibility and scalable up to 5 litres.[208] The binary surfactant stabilised AuNRs demonstrated an innate colloidal instability, requiring a critical concentration of CTAB in solution to inhibit aggregation. In order to avoid potential toxicity effects associated with high CTAB concentrations, a surface replacement was performed coating the AuNRs with a phospholipid bilayer (DSPC/DSPE-mPEG2k, 95/1 mol%) containing PEG-functionalised lipids to provide steric stability. The replacement procedure had little effect on the AuNR optical properties, with the rods displaying no aggregation from UV-vis spectroscopy and TEM imaging.

The phospholipid stabilised AuNRs demonstrated colloidal stability in Mueller-Hinton broth II for 24 hours with little change in optical properties, as opposed to the binary surfactant coated AuNRs, which show significant aggregation nearly eliminating the longitudinal absorption peak. Furthermore, the phospholipid stabilised AuNRs exhibit increased cytocompatibility against *S. aureus*, with no significant decrease in viability upon inoculation at 250 μg ml^{-1} of Au, as opposed to the binary surfactant AuNRs which completely inhibited *S. aureus* proliferation at 63 μg ml^{-1}. The photothermal capabilities of the phospholipid stabilised AuNRs was next assessed, attaining heating up to 70°C using a 2.1 W cm^{-2} continuous wave laser at 860 nm for 10 mins.

In chapter 5 the viability of an AMP-loaded liposome and AuNR delivery system was investigated. The system development started by optimising the liposome composition and encapsulation efficiency. Depending on the concentration cholesterol can provide a stiffening effect within a lipid bilayer influencing the small-molecule permeability and lipid phase transition properties, as such its effect on the liposome leakage and thermo-responsive release were first assessed. Vesicles composed of DSPC/DSPE-mPEG2k with varying cholesterol content (0-30 mol%) encapsulating calcein at self-quenching concentrations (0.1 M) incubated at 37°C, showed that increasing cholesterol concentrations decreased calcein leakage such that at 30 mol% cholesterol negligible leakage was observed 4 days post fabrication. Increasing the cholesterol content also decreased both the bacteria induced leakage and the liposomal thermo-responsive release at the lipid gel-fluid phase transition temperature (T$_m$). However, incubating the liposomes with a bacterial suspension for one hour before heating to the T$_m$ released 55 $\pm$ 6% of encapsulated dye. Using the conventional thin lipid film hydration liposome fabrication technique, with 10 mg lipid films hydrated with 5 mg ml^{-1} IK8 solutions, the vesicles encapsulated approximately 24 times the MIC of IK8 against both *S. aureus* and *P. aeruginosa*, 32 μg ml^{-1}. Liposomal encapsulation provided a protective effect against proteases, with over double the amount of liposome encapsulated IK8 remaining compared with free IK8 in solution, when incubated in a trypsin solution for 5 hours. As such, these liposomes demonstrate negligible premature leakage, an adequate thermal release profile, encapsulation of bactericidal concentrations of AMP and a protection of cargo from protease degradation.

To demonstrate the antimicrobial capabilities of IK8-loaded liposomes a mixture of vesicles and phospholipid stabilised AuNRs, described in Chapter 4, was used to inoculate a *S. aureus*

suspension before continuous wave laser irradiation at 860 nm. *S. aureus* suspensions treated with AuNRs and liposomes containing 1, 2 and 4 times the MIC of IK8 resulted in additional 3-, 4- and 5-log reductions in CFU ml^{-1} respectively, when irradiated at 2.1 W cm^{-2} (860 nm, for 10 mins) compared to non-irradiated controls. This clearly demonstrated the first instance of light stimulated release of AMPs. Furthermore, irradiating samples at 2.4 W cm^{-2} (heating to 60°C) demonstrated a photothermal induced killing effect, that enhanced the IK8 efficacy with an additional 4-log reduction in viable bacteria.

Chapter 6 built upon the AuNR and IK8-loaded liposome system developed in chapter 5, by incorporating the particles into a PEG-based hydrogel wound dressing. The hydrogel network was formed by mixing 4-arm PEG maleimide (4APM) with PEG dithiol at a 1:1 thiol to maleimide ratio. A 5 wt% gel fabricated using citrate buffer (pH 6) formed a homogeneous and stiff gel in 20 s. Rheological analysis of the gels using both constant strain (1%) and frequency sweep techniques demonstrated that at 5 wt% the network formed an elastic gel that did not break even at the highest frequencies, meaning it is an ideal material for topical use where it would be frequently be under strain due to the stretching of the skin. AuNR and liposome loading into the hydrogel network was achieved by adding the particles to the 4APM solution prior to gelation, offering a facile means of integration at ∼100% loading efficiency. The resultant gel displayed a slight decrease in elasticity, and was able to retain over 90% of AuNRs and liposomes after incubation in buffer for a week. Additionally, a 5 mm thick prototype dressing allowed clear visibility of underlying features when placed next to the skin, meaning a visible assessment of a wound would not require the removal of the dressing.

Loading the AuNRs into the PEG matrix did not affect the gel optical properties, allowing controlled heating up to 65°C and demonstrating no decrease in photothermal efficiency after several irradiation cycles. The incorporation of the AuNR-liposome system into the gel did not decrease the photothermal release efficiency, providing 64% release under irradiation at 2.1 W cm^{-2} for 10 mins. The light-stimulated release of the MIC of IK8 from the gel dressing provided 5- and 7-log reductions in the CFU ml^{-1} against *S. aureus* and *P. aeruginosa* respectively, whilst the photothermal enhancement of the AMP efficacy was maintained when the gel was irradiated at 2.4 W cm^{-2} (60°C) for 10 mins, killing an additional 3-log CFU ml^{-1} of *S. aureus* and eradicating *P. aeruginosa*. Individual gels then demonstrated the potential for multiple treatment rounds. Loading gels with 2.5 times the MIC of liposomal IK8 and decreasing

the irradiation time of the first treatment cycle to 6 mins enabled the delivery of bactericidal concentrations of IK8 more than once. The dressing displayed 7- and 4-log reductions in *S. aureus* after the first and second irradiation cycles at 2.1 W cm^{-2} respectively. The photothermal antibacterial effects were also displayed over both cycles producing further 1.1- and 2.5-log reductions in the first and second treatments.

Taken together, the results from chapters 5 and 6 describe the development of a AuNR and AMP-loaded wound dressing that provides the first examples of both light stimulated delivery of AMPs and the photothermal enhancement of AMPs.[350] The liposome encapsulation of AMPs demonstrated a protective effect against protease degradation, whilst the light sensitivity allowed spatial and temporal delivery of the AMPs. The delivery of AMPs transdermally from a wound dressing directly to an infection site increases the pharmacodynamic profile and in turn decreases the required drug dose compared to alternative routes of administration; reducing both the chances of systemic toxicity and the cost of treatment.[449] As such, this wound dressing addressed some of the main factors hindering AMP clinical translation; proteolytic degradation, low toxicity, and cost-efficient treatment. The IK8-liposome fabrication using the traditional thin-lipid film technique allows the facile encapsulation of most hydrophilic molecules, as demonstrated by the loading of both calcein and IK8, meaning this system could be adapted for delivery of a range of therapeutics.

Chapter 7 described the development of an alternative AMP delivery system that is responsive to pulsed laser irradiation, providing AMP release without bulk heating effects. Initially, attempts were made to coat IK8-loaded liposomes with AuNPs by utilising the vesicles as a soft template when performing the particle synthesis. The synthesis using PEGylated liposomes produced anisotropic gold nanostars (AuNSs) with a tunable plamonic absorption peak, however the AuNSs did not induce liposomal release of encapsualted cargoes under the pulsed laser irradiation (4.5 mJ cm^{-2} for 10 mins at 738 nm). Using TEM imaging the AuNSs did not appear to be conjugated to the liposome templates, hypothesising that this was due to the PEG steric hinderance of Au atoms reaching the liposome surface the Au coating was attempted using non-PEGylated liposomes. This produced fractal snowflake-like gold nanoparticles that again did not appear conjugated to the liposome template. As such, the thiol containing lipid DPPE-Ptd (DSPC/cholesterol/DSPE-mPEG2k/DPPE-Ptd, 67/30/2/1 mol%) was included in the liposome composition to provide initial binding sites for the Au ions. The synthesis in

the presence of the thiolated liposomes resulted in particles with poor absorbance efficiency and little control over the peak position, however 96% of the AuNPs were conjugated to the liposomes. Instead of binding AuNPs to the liposome template during synthesis it was deemed preferential to conjugate AuNRs to the lipid bilayer due to their monodisperse structures, high photothermal efficiency and tunable plasmonic absorption wavelength. DPSE-mPEG2k-maleimide was included into the phospholipid bilayer (DSPC/DSPE-mPEG2k/DSPE-mPEG2k-maleimide, 95/4/1 mol%) stabilising the AuNRs and provided conjugation to the liposome bilayer using a "click" reaction with the DPPE-Ptd. After mixing the particles overnight AuNR conjugated IK8-liposomes (ANCIL) complexes were formed, demonstrating release of 67% of encapsulated IK8 when irradiated at 450 μJ cm^{-2} for 10 mins at 738 nm. Mixing maleimide-functionalised AuNRs with liposomes without DPPE-Ptd (DSPC/cholesterol/DSPE-mPEG2k, 69/30/1 mol%), showed no binding and released only 9% of encapsulated IK8, demonstrating the necessity of the conjugation between the photothermal agent and the liposome when using a pulsed laser source. The laser irradiation of the ANCIL complexes containing the MIC of IK8 displayed a 4.4-log reduction in *S. aureus* CFUs ml^{-1}, a 3.1-log increase in bactericidal activity compared to *S. aureus* inoculation with non-irradiated ANCILs. This provided proof-of-concept that AuNP conjugated liposome complexes can be utilised to provide light-stimulated delivery of therapeutics with only a 1°C increase in sample temperature.

8.1   Future work

8.1.1   Further testing of the AuNR and IK8-liposome hydrogel dressing

The next step in the testing of the AuNR and IK8-liposome loaded wound dressing would be *in vivo* testing on a murine model. Based off the study by Tao *et al.* who treated infected wounds *in vivo* using a copper nanoparticle loaded hydrogel[6], this would involve using a skin biopsy punch to remove a 5 mm radius circle of dermal tissue from the back of a Sprague Dawley rat and inoculation with 10 μl of *S. aureus* or *P. aeruginosa* at 1 x 10^7 CFU ml^{-1}. A prefabricated gel would then be administered and irradiation of the the wound dressing for 10 mins, heating the dressing and wound to induce delivery of the AMP and to provide photothermal bacteria killing. The wound would then be imaged daily to determine whether the therapeutic dressing can increase the healing rate compared to models with control dressings and no dressings. The

wound coalescence is calculated using

$$WC(\%) = \frac{A_0 - A_t}{A_0} \times 100 \qquad (8.1)$$

where A_0 and A_t are the initial area and area after time t. Quantification of the viable bacteria would be obtained by removing the wounded tissue, post euthanisation of the model, and homogenising the sample in PBS before spreading onto agar plates for bacteria counting the following day. This would not only test the efficacy of treatment but would determine whether the photothermal enhancement of the AMP efficacy is also maintained *in vivo*. Histological analysis of the infected tissue could also be performed to determine the whether the dressing and the heat affect the inflammatory response and angiogenesis. Furthermore, the major organs could be harvested to determine the toxicity of the AMP.

The IK8-liposome and AuNR loaded wound dressing could also be tested against biofilms, both IK8 and photothermal heating have both demonstrated antibiofilm effects, but never in conjunction with one another. Initial testing would be performed on mature biofilms grown in well plates, before the fabrication of the gel *in situ*. The samples would then be irradiated and left to incubate for 18 hours before using a live/dead assay to determine the bacteria viability. If the wound dressing effectively kills the biofilm bacteria then the treatment would be assessed on mature biofilms grown on murine models.

8.1.2 Decreased AMP resistance when used in conjunction with thermal killing

Despite the reduced chances of bacteria developing resistance to AMPs, resistance still a concern.[450] Given that in chapters 5 and 6 the AMP efficacy has been shown to increase when used in conjunction with heating it would be worthwhile investigating whether using both effects simultaneously can reduce the acquired AMP resistance. This could be ascertained by inoculating bacteria with an AMP and heating the sample to 60°C for 10 mins, the bacteria that survive the treatment would then be quantified and cultured. This process would be repeated until the treatment becomes ineffective. This would then be compared to bacteria treated with equal amounts of AMP without the additional heating. If the bacteria treated with the heating as well as the AMP took more treatment rounds to becoming ineffective then the heating can be stated to decrease the chances of resistance acquisition. If this were to be proven the impli-

cations could be incredibly significant, given that heating a wound to bactericidal temperatures for short periods of time has been demonstrated not to affect wound healing, this could become an integral part of future infection treatments to decrease likelihood of resistance.

8.1.3   Further characterisation of the ANCIL system

Chapter 7 provides proof-of-concept for the ANCIL system treating Gram-positive *S. aureus*, however more characterisation is required before the complex could be taken forward as a medical device. Firstly, the cytotoxicity of the liposomes containing DPPE-Ptd, the maleimide-funcationalised phospholipid stabilised AuNRs and the ANCIL complex, needs to be assessed against a cell type associated with wound healing, such as the dermal fibroblast. The leakage from the ANCIL complex must also be assessed to ensure that the inclusion of DPPE-Ptd or the AuNR conjugation does not affect the membrane integrity promoting premature drug leakage. Finally, the ANCIL system should be use to demonstrate efficacy against a Gram-negative bacteria to show broad-spectrum activity.

8.1.4   Further investigation of AuNP synthesis using liposomal soft templates

Nanoparticle synthesis is a burgeoning field, with particular focus on the discovery of novel surfactants that control the particle morphology. Many surfactants have an inherent cytotoxicity, meaning they have to be replaced by biocompatible stabilising molecules post fabrication, increasing the time and cost of manufacture. The unique nanostar and fractal flake-like morphologies of the AuNPs synthesised in the presence of biocompatible liposomes, as described in chapter 7, offer tunable plasmonic properties that are desirable in photothermal agents. The AuNS and flake-like particle morphologies are completely different however the only difference between the syntheses was the inclusion of DSPE-mPEG2k in the liposome, as such it would be a good idea to expand this parameter space using alternative lipids to determine what effects they have on the crystal growth. Furthermore, the liposomes appeared to increase the gold nanoparticle colloidal stability demonstrating no precipitation even after several weeks. As such, the AuNP synthesis utilising liposomes as soft templates requires further investigation offering a facile means of production, without the requirement of costly materials and ensures biocompatibility.

Bibliography

[1] P. Ehrlich. On experimental researches on specific therapy. On immunity with special relationship between distribution and action of antigens. *The Lancet*, 170(4380):351–353, 1907.

[2] World Health Organisation. www.www.who.int/en/news-room/fact- sheets/detail/anti biotic-resistance (accessed: April 2020).

[3] E. Geisinger and R. R. Isberg. Interplay Between Antibiotic Resistance and Virulence During Disease Promoted by Multidrug-Resistant Bacteria. *The Journal of Infectious Diseases*, 215(suppl_1):S9–S17, Mar. 2017.

[4] E. Tacconelli et al. Discovery, research, and development of new antibiotics: the WHO priority list of antibiotic-resistant bacteria and tuberculosis. *The Lancet Infectious Diseases*, 18(3):318–327, 2018.

[5] S. Basak, P. Singh, and M. Rajurkar. Multidrug Resistant and Extensively Drug Resistant Bacteria: A Study. eng. *Journal of pathogens*, 2016:4065603, 2016.

[6] B. Tao, C. Lin, Y. Deng, Z. Yuan, X. Shen, M. Chen, Y. He, Z. Peng, Y. Hu, and K. Cai. Copper-nanoparticle-embedded hydrogel for killing bacteria and promoting wound healing with photothermal therapy. *Journal of Materials Chemistry B*, 7(15):2534–2548, 2019.

[7] C. W. Hsiao, H. L. Chen, Z. X. Liao, R. Sureshbabu, H. C. Hsiao, S. J. Lin, Y. Chang, and H. W. Sung. Effective photothermal killing of pathogenic bacteria by using spatially tunable colloidal gels with nano-localized heating sources. *Advanced Functional Materials*, 25(5):721–728, 2015.

[8] D. Hu, H. Li, B. Wang, Z. Ye, W. Lei, F. Jia, Q. Jin, K. F. Ren, and J. Ji. Surface-Adaptive Gold Nanoparticles with Effective Adherence and Enhanced Photothermal Ablation of Methicillin-Resistant Staphylococcus aureus Biofilm. *ACS Nano*, 11(9):9330–9339, 2017.

[9] L. X. Yan, L. J. Chen, X. Zhao, and X. P. Yan. pH Switchable Nanoplatform for In Vivo Persistent Luminescence Imaging and Precise Photothermal Therapy of Bacterial Infection. *Advanced Functional Materials*, 1909042:1–12, 2020.

[10] A. G. Al-Bakri and N. N. Mahmoud. Photothermal-induced antibacterial activity of gold nanorods loaded into polymeric hydrogel against pseudomonas aeruginosa biofilm. *Molecules*, 24(14), July 2019.

[11] A. Espinosa, R. Di Corato, J. Kolosnjaj-Tabi, P. Flaud, T. Pellegrino, and C. Wilhelm. Duality of Iron Oxide Nanoparticles in Cancer Therapy: Amplification of Heating Efficiency by Magnetic Hyperthermia and Photothermal Bimodal Treatment. *ACS Nano*, 10(2):2436–2446, Feb. 2016.

[12] J. Liu, X. Guo, Z. Zhao, B. Li, J. Qin, Z. Peng, G. He, D. J. L. Brett, R. Wang, and X. Lu. Fe3S4 nanoparticles for arterial inflammation therapy: Integration of magnetic hyperthermia and photothermal treatment. *Applied Materials Today*, 18:100457, 2020.

[13] A.-C. Groo, N. Matougui, A. Umerska, and P. Saulnier. Reverse micelle-lipid nanocapsules: a novel strategy for drug delivery of the plectasin derivate AP138 antimicrobial peptide. eng. *International journal of nanomedicine*, 13:7565–7574, 2018.

[14] G. M. F. Calixto, M. H. Garcia, E. M. Cilli, L. A. Chiavacci, and M. Chorilli. Design and Characterization of a Novel p1025 Peptide-Loaded Liquid Crystalline System for the Treatment of Dental Caries. *Molecules*, 21(2):158–168, 2016.

[15] Z. Y. Ong, S. J. Gao, and Y. Y. Yang. Short synthetic β-sheet forming peptide amphiphiles as broad spectrum antimicrobials with antibiofilm and endotoxin neutralizing capabilities. *Advanced Functional Materials*, 23(29):3682–3692, 2013.

[16] Z. Y. Ong, J. Cheng, Y. Huang, K. Xu, Z. Ji, W. Fan, and Y. Y. Yang. Effect of stereochemistry, chain length and sequence pattern on antimicrobial properties of short synthetic β-sheet forming peptide amphiphiles. *Biomaterials*, 35(4):1315–1325, Jan. 2014.

[17] M. Comotto, S. Saghazadeh, S. Bagherifard, B. Aliakbarian, M. Kazemzadeh-Narbat, F. Sharifi, S. A. Mousavi Shaegh, E. Arab-Tehrany, N. Annabi, P. Perego, A. Khademhosseini, and A. Tamayol. Breathable hydrogel dressings containing natural antioxidants for management of skin disorders. *Journal of Biomaterials Applications*, 33(9):1265–1276, 2019.

[18] R. Z. Murray, Z. E. West, A. J. Cowin, and B. L. Farrugia. Development and use of biomaterials as wound healing therapies. eng. *Burns & trauma*, 7:2, 2019.

[19] C. K. Field and M. D. Kerstein. Overview of wound healing in a moist environment. *The American Journal of Surgery*, 167(1):S2–S6, 1994.

[20] I. P. Harrison and F. Spada. Hydrogels for Atopic Dermatitis and Wound Management: A Superior Drug Delivery Vehicle. eng. *Pharmaceutics*, 10(2):71, 2018.

[21] C. Sohlenkamp and O. Geiger. Bacterial membrane lipids: diversity in structures and pathways. *FEMS Microbiology Reviews*, 40(1):133–159, 2015.

[22] Y.-J. Zhang, S. Li, R.-Y. Gan, T. Zhou, D.-P. Xu, and H.-B. Li. Impacts of gut bacteria on human health and diseases. eng. *International journal of molecular sciences*, 16(4):7493–7519, 2015.

[23] M. C. Robson. WOUND INFECTION: A Failure of Wound Healing Caused by an Imbalance of Bacteria. *Surgical Clinics of North America*, 77(3):637–650, 1997.

[24] J. W. Peterson. Bacterial Pathogenesis. In S. Baron, editor, *Medical Microbiology*, chapter 7. University of Texas Medical Branch at Galveston, Galveston, 4th edition, 1996.

[25] D. H. Walker. Rickettsiae. In S. Baron, editor, *Medical Microbiology.* Chapter 38. University of Texas Medical Branch at Galveston, Galveston, 4th edition, 1996.

[26] C. Galanos and M. A. Freudenberg. Bacterial endotoxins: biological properties and mechanisms of action. eng. *Mediators of inflammation*, 2(7):S11–S16, 1993.

[27] N. Høiby, T. Bjarnsholt, M. Givskov, S. Molin, and O. Ciofu. Antibiotic resistance of bacterial biofilms. *International Journal of Antimicrobial Agents*, 35(4):322–332, 2010.

[28] A. M. Sousa, I. Machado, and M. Pereira. Phenotypic switching: An opportunity to bacteria thrive. *Science against Microbial Pathogens: Communicating Current Research and Technological Advances*, 1, 2012.

[29] E. Drenkard. Antimicrobial resistance of Pseudomonas aeruginosa biofilms. *Microbes and Infection*, 5(13):1213–1219, 2003.

[30] T.-F. C. Mah and G. A. O'Toole. Mechanisms of biofilm resistance to antimicrobial agents. *Trends in Microbiology*, 9(1):34–39, 2001.

[31] K Lewis. Riddle of biofilm resistance. eng. *Antimicrobial agents and chemotherapy*, 45(4):999–1007, 2001.

[32] A. L. Spoering and K Lewis. Biofilms and planktonic cells of Pseudomonas aeruginosa have similar resistance to killing by antimicrobials. eng. *Journal of bacteriology*, 183(23):6746–6751, 2001.

[33] C. Potera. Forging a Link Between Biofilms and Disease. *Science*, 283(5409):1837, 1999.

[34] NIH Research on microbial biofilms. 2002. Available online:http://grants.nih .gov/grants /guide/pa-files/PA-03–047.html. 2002.

[35] G. A. James, E. Swogger, R. Wolcott, E. d. Pulcini, P. Secor, J. Sestrich, J. W. Costerton, and P. S. Stewart. Biofilms in chronic wounds. *Wound Repair and Regeneration*, 16(1):37–44, 2008.

[36] A. Parnham and C. Bousfield. The influence of matrix metalloproteases and biofilm on chronic wound healing: a discussion. *British Journal of Community Nursing*, 23(Sup3):S22–S29, 2018.

[37] T. Bjarnsholt. The role of bacterial biofilms in chronic infections. *APMIS*, 121(s136):1–58, 2013.

[38] J. S. VanEpps and J. G. Younger. Implantable Device-Related Infection. eng. *Shock (Augusta, Ga.)*, 46(6):597–608, 2016.

[39] M. Hadla and M. A. Halabi. Effect of Quorum Sensing. *Comprehensive Analytical Chemistry*, 81:95–116, 2018.

[40] M. A.-S. Vigeant, R. M. Ford, M. Wagner, and L. K. Tamm. Reversible and irreversible adhesion of motile Escherichia coli cells analyzed by total internal reflection aqueous fluorescence microscopy. eng. *Applied and environmental microbiology*, 68(6):2794–2801, June 2002.

[41] H. H. Tuson and D. B. Weibel. Bacteria-surface interactions. eng. *Soft matter*, 9(18):4368–4380, 2013.

[42] S. T. Rutherford and B. L. Bassler. Bacterial quorum sensing: its role in virulence and possibilities for its control. eng. *Cold Spring Harbor perspectives in medicine*, 2(11):a012427, 2012.

[43] Y.-H. Li and X. Tian. Quorum sensing and bacterial social interactions in biofilms. eng. *Sensors*, 12(3):2519–2538, 2012.

[44] B. Vu, M. Chen, R. J. Crawford, and E. P. Ivanova. Bacterial extracellular polysaccharides involved in biofilm formation. eng. *Molecules (Basel, Switzerland)*, 14(7):2535–2554, 2009.

[45] G. Kapoor, S. Saigal, and A. Elongavan. Action and resistance mechanisms of antibiotics: A guide for clinicians. eng. *Journal of anaesthesiology, clinical pharmacology*, 33(3):300–305, 2017.

[46] N Nanninga. Cell Structure, Organization, Bacteria and Archaea. In *Biomedical Sciences*. Elsevier, 2014.

[47] K.-F. Kong, L. Schneper, and K. Mathee. Beta-lactam antibiotics: from antibiosis to resistance and bacteriology. *APMIS*, 118(1):1–36, Jan. 2010.

[48] E. Binda, F. Marinelli, and G. L. Marcone. Old and New Glycopeptide Antibiotics: Action and Resistance. eng. *Antibiotics*, 3(4):572–594, Nov. 2014.

[49] Fluoroquinolones. In *LiverTox: Clinical and Research Information on Drug-Induced Liver Injury*, chapter Fluoroquinolones, pages 1–11. National Institute of Diabetes, Digestive, and Kidney Diseases, Bethesda (USA), 2012.

[50] R. J. Reece and A Maxwell. DNA Gyrase: Structure and Function. *Crit Rev Biochem Mol Biol*, 26(3):335–375, 1991.

[51] J. M. Berg, J. L. Tymoczko, and L. Stryer. A Ribosome Is a Ribonucleoprotein Particle (70S) Made of a Small (30S) and a Large (50S) Subunit. In *Biochemistry*, chapter 29. W H Freeman, New York, 5th edition, 2002.

[52] K. M. Krause, A. W. Serio, T. R. Kane, and L. E. Connolly. Aminoglycosides: An Overview. eng. *Cold Spring Harbor perspectives in medicine*, 6(6):a027029, June 2016.

[53] I. Chopra and M. Roberts. Tetracycline antibiotics: mode of action, applications, molecular biology, and epidemiology of bacterial resistance. eng. *Microbiology and molecular biology reviews*, 65(2):232–260, June 2001.

[54] H. Yoneyama and R. Katsumata. Antibiotic resistance in bacteria and its future for novel antibiotic development. *Bioscience Biotechnology Biochemistry*, 70(5):1060–1075, 2006.

[55] B. Bozdogan and P. C. Appelbaum. Oxazolidinones: activity, mode of action, and mechanism of resistance. *International Journal of Antimicrob Agents.*, 23(2):113–119, 2004.

[56] F. van Bambeke, M.-P. Mingeot-Leclercq, Y. Glupczynski, and P. M. Tulkens. Mechanisms of Action. In J. Cohen, W. G. Powderly, and S. M. Opal, editors, *Infectious Diseases (Fourth Edition)*, chapter 137, pages 1162–1180. Elsevier, Amsterdam, 1st edition, 2017.

[57] M. R. Mulvey and A. E. Simor. Antimicrobial resistance in hospitals: How concerned should we be? *Canadian Medical Association Journal*, 180(4):408, 2009.

[58] R. J. Worthington and C. Melander. Overcoming resistance to β-lactam antibiotics. eng. *The Journal of organic chemistry*, 78(9):4207–4213, May 2013.

[59] L. B. Rice. Mechanisms of resistance and clinical relevance of resistance to β-lactams, glycopeptides, and fluoroquinolones. eng. *Mayo Clinic proceedings*, 87(2):198–208, Feb. 2012.

[60] Y. Katayama, T. Ito, and K Hiramatsu. A New Class of Genetic Element, Staphylococcus Cassette Chromosome mec, Encodes Methicillin Resistance in Staphylococcus aureus. *Antimicrobial Agents and Chemotherapy*, 44(6):1549, 2000.

[61] J Garcia-Bustos and A Tomasz. A biological price of antibiotic resistance: major changes in the peptidoglycan structure of penicillin-resistant pneumococci. eng. *Proceedings of the National Academy of Sciences of the United States of America*, 87(14):5415–5419, 1990.

[62] A. Tomasz and R. Munoz. β-Lactam Antibiotic Resistance in Gram-Positive Bacterial Pathogens of the Upper Respiratory Tract: A Brief Overview of Mechanisms. *Microbial Drug Resistance*, 1(2):103–109, 1995.

[63] F. Van Bambeke, E. Balzi, and P. M. Tulkens. Antibiotic efflux pumps. *Biochemical Pharmacology*, 60(4):457–470, 2000.

[64] G. P. Tegos, M. Haynes, J. J. Strouse, M. M. T. Khan, C. G. Bologa, T. I. Oprea, and L. A. Sklar. Microbial efflux pump inhibition: tactics and strategies. eng. *Current pharmaceutical design*, 17(13):1291–1302, 2011.

[65] M. A. Webber and L. J. V. Piddock. The importance of efflux pumps in bacterial antibiotic resistance. *Journal of Antimicrobial Chemotherapy*, 51(1):9–11, 2003.

[66] K. Housseini B Issa, G. Phan, and I. Broutin. Functional Mechanism of the Efflux Pumps Transcription Regulators From Pseudomonas aeruginosa Based on 3D Structures. *Frontiers in Molecular Biosciences*, 5:57, 2018.

[67] J.-M. Pagès, C. E. James, and M. Winterhalter. The porin and the permeating antibiotic: a selective diffusion barrier in Gram-negative bacteria. *Nature Reviews Microbiology*, 6(12):893–903, 2008.

[68] A. H. Delcour. Outer membrane permeability and antibiotic resistance. *Biochimica et Biophysica Acta - Proteins and Proteomics*, 1794(5):808–816, 2009.

[69] H. Nikaido. Molecular basis of bacterial outer membrane permeability revisited. eng. *Microbiology and molecular biology reviews : MMBR*, 67(4):593–656, 2003.

[70] I. Ghai and S. Ghai. Understanding antibiotic resistance via outer membrane permeability. eng. *Infection and drug resistance*, 11:523–530, 2018.

[71] N. A. Lerminiaux and A. D. S. Cameron. Horizontal transfer of antibiotic resistance genes in clinical environments. *Canadian Journal of Microbiology*, 65(1):34–44, 2018.

[72] K. B. Low. Conjugation. In S. Brenner and J. H. Miller, editors, *Encyclopedia of Genetics*, pages 449–453. Academic Press, New York, 2001.

[73] D. Sun. Pull in and Push Out: Mechanisms of Horizontal Gene Transfer in Bacteria. *Frontiers in Microbiology*, 9:2154, 2018.

[74] N. Principi, E. Silvestri, and S. Esposito. Advantages and Limitations of Bacteriophages for the Treatment of Bacterial Infections. *Frontiers in Pharmacology*, 10:513, 2019.

[75] C. Torres-Barceló. The disparate effects of bacteriophages on antibiotic-resistant bacteria. eng. *Emerging microbes & infections*, 7(1):168, 2018.

[76] E. F. Haney, S. K. Straus, and R. E. W. Hancock. Reassessing the Host Defense Peptide Landscape. *Frontiers in Chemistry*, 7:43, 2019.

[77] N. Mookherjee, M. A. Anderson, H. P. Haagsman, and D. J. Davidson. Antimicrobial host defence peptides: functions and clinical potential. *Nature Reviews Drug Discovery*, 2020.

[78]   M. Hemshekhar, V. Anaparti, and N. Mookherjee. Functions of Cationic Host Defense Peptides in Immunity. eng. *Pharmaceuticals*, 9(3):40, 2016.

[79]   Z. Y. Ong, J. Cheng, Y. Huang, K. Xu, Z. Ji, W. Fan, and Y. Y. Yang. Effect of stereochemistry, chain length and sequence pattern on antimicrobial properties of short synthetic β-sheet forming peptide amphiphiles. *Biomaterials*, 35(4):1315–1325, 2014.

[80]   P. M. López-Pérez, E. Grimsey, L. Bourne, R. Mikut, and K. Hilpert. Screening and Optimizing Antimicrobial Peptides by Using SPOT-Synthesis. *Frontiers in Chemistry*, 5:25, 2017.

[81]   Z. Amso and Z. Hayouka. Antimicrobial random peptide cocktails: a new approach to fight pathogenic bacteria. *Chemical Communications*, 55(14):2007–2014, 2019.

[82]   M. Zasloff. Antimicrobial peptides of multicellular organisms. *Nature*, 415(6870):389–395, 2002.

[83]   S. Dzidic and V. Bedekovic. Horizontal gene transfer-emerging multidrug resistance in hospital bacteria. *Acta Pharmaco.*, 24(6):519–526, 2003.

[84]   J. M. Munita and C. A. Arias. Mechanisms of Antibiotic Resistance. *Microbiology Spectrum*, 4(2), 2016.

[85]   M. E. Bauer and W. M. Shafer. On the in vivo significance of bacterial resistance to antimicrobial peptides. *Biochimica et Biophysica Acta (BBA) - Biomembranes*, 1848(11):3101–3111, 2015.

[86]   V. I. Band and D. S. Weiss. Mechanisms of Antimicrobial Peptide Resistance in Gram-Negative Bacteria. eng. *Antibiotics*, (1):18–41, 2015.

[87]   J. Z. Kubicek-Sutherland, H. Lofton, M. Vestergaard, K. Hjort, H. Ingmer, and D. I. Andersson. Antimicrobial peptide exposure selects for Staphylococcus aureus resistance to human defence peptides. *Journal of Antimicrobial Chemotherapy*, 72(1):115–127, 2016.

[88]   A. Nijnik and R. E. W. Hancock. Host defence peptides: antimicrobial and immunomodulatory activity and potential applications for tackling antibiotic-resistant infections. *Emerging Health Threats Journal*, 2(1):7078, 2009.

[89]   N. Raheem and S. K. Straus. Mechanisms of Action for Antimicrobial Peptides With Antibacterial and Antibiofilm Functions. *Frontiers in Microbiology*, 10:2866, 2019.

[90] E. Breukink and B. de Kruijff. The lantibiotic nisin, a special case or not? *Biochimica et Biophysica Acta (BBA) - Biomembranes*, 1462(1-2):223–234, 1999.

[91] K. A. Brogden. Antimicrobial peptides: pore formers or metabolic inhibitors in bacteria? *Nature Reviews Microbiology*, 3(3):238–250, 2005.

[92] D. Sengupta, H. Leontiadou, A. E. Mark, and S.-J. Marrink. Toroidal pores formed by antimicrobial peptides show significant disorder. *Biochimica et Biophysica Acta (BBA) - Biomembranes*, 1778(10):2308–2317, 2008.

[93] P. Kumar, J. N. Kizhakkedathu, and S. K. Straus. Antimicrobial Peptides: Diversity, Mechanism of Action and Strategies to Improve the Activity and Biocompatibility In Vivo. *Biomolecules*, 8(1):4, 2018.

[94] M. R. Yeaman and N. Y. Yount. Mechanisms of Antimicrobial Peptide Action and Resistance. *Pharmacological Reviews*, 55(1):27, 2003.

[95] Y. Shai. Mode of action of membrane active antimicrobial peptides. *Peptide Science*, 66(4):236–248, 2002.

[96] B Bechinger and S.-U. Gorr. Antimicrobial Peptides: Mechanisms of Action and Resistance. eng. *Journal of dental research*, 96(3):254–260, 2017.

[97] S. Baltzer and M. Brown. Antimicrobial Peptides – Promising Alternatives to Conventional Antibiotics. *Journal of molecular microbiology and biotechnology*, 20:228–235, 2011.

[98] H. Zhang. Challenges and future prospects. In N. Cioffi and M. Rai, editors, *Nano-Antimicrobials: Progress and Prospects*, chapter 1.5, pages 27–45. Springer science & business media, Berlin, Heidelberg, 1st edition, 2012.

[99] K. M. Scherer, J.-H. Spille, H.-G. Sahl, F. Grein, and U. Kubitscheck. The lantibiotic nisin induces lipid II aggregation, causing membrane instability and vesicle budding. eng. *Biophysical journal*, 108(5):1114–1124, 2015.

[100] F. Grein, T. Schneider, and H.-G. Sahl. Docking on Lipid II—A Widespread Mechanism for Potent Bactericidal Activities of Antibiotic Peptides. *Journal of Molecular Biology*, 431(18):3520–3530, 2019.

[101] N. Ishaq, M. Bilal, and H. M. N. Iqbal. Medicinal Potentialities of Plant Defensins: A Review with Applied Perspectives. eng. *Medicines*, 6(1):29, Feb. 2019.

[102] F. Costa, C. Teixeira, P. Gomes, and M. C. L. Martins. Clinical Application of AMPs. In K. Matsuzaki, editor, *Antimicrobial Peptides. Advances in Experimental Medicine and Biology*, chapter 4, pages 281–298. Springer, Singapore, 1117th edition, 2019.

[103] M. Mahlapuu, J. Håkansson, L. Ringstad, and C. Björn. Antimicrobial Peptides: An Emerging Category of Therapeutic Agents. eng. *Frontiers in cellular and infection microbiology*, 6:194, 2016.

[104] M. Divyashree, M. K. Mani, D. Reddy, R. Kumavath, P. Ghosh, V. Azevedo, and D. Barh. Clinical Applications of Antimicrobial Peptides (AMPs): Where do we Stand Now? *Protein Pept. Lett.*, 27(2):120–134, 2019.

[105] L. S. Biswaro, M. G. da Costa Sousa, T. M. B. Rezende, S. C. Dias, and O. L. Franco. Antimicrobial Peptides and Nanotechnology, Recent Advances and Challenges. eng. *Frontiers in microbiology*, 9:855, 2018.

[106] L. Gentilucci, R. De Marco, and L. Cerisoli. Chemical Modifications Designed to Improve Peptide Stability: Incorporation of Non-Natural Amino Acids, Pseudo-Peptide Bonds, and Cyclization. *Current Pharmaceutical Design*, 16(28):3185 –3203, 2010.

[107] A. Reinhardt and I. Neundorf. Design and Application of Antimicrobial Peptide Conjugates. eng. *International journal of molecular sciences*, 17(5):701, 2016.

[108] C. J. Morris, K. Beck, M. A. Fox, D. Ulaeto, G. C. Clark, and M. Gumbleton. Pegylation of antimicrobial peptides maintains the active peptide conformation, model membrane interactions, and antimicrobial activity while improving lung tissue biocompatibility following airway delivery. eng. *Antimicrobial agents and chemotherapy*, 56(6):3298–3308, 2012.

[109] J. Lei, L. Sun, S. Huang, C. Zhu, P. Li, J. He, V. Mackey, D. H. Coy, and Q. He. The antimicrobial peptides and their potential clinical applications. eng. *American journal of translational research*, 11(7):3919–3931, 2019.

[110] C. G. Starr, J. L. Maderdrut, J. He, D. H. Coy, and W. C. Wimley. Pituitary adenylate cyclase-activating polypeptide is a potent broad-spectrum antimicrobial peptide: Structure-activity relationships. *Peptides*, 104:35–40, 2018.

[111] C Subbalakshmi, R Nagaraj, and N Sitaram. Biological activities of C-terminal 15-residue synthetic fragment of melittin: design of an analog with improved antibacterial activity. *FEBS Letters*, 448(1):62–66, 1999.

[112] Y. Park, S.-C. Park, H.-K. Park, S. Y. Shin, Y. Kim, and K.-S. Hahm. Structure-activity relationship of HP (2–20) analog peptide: Enhanced antimicrobial activity by N-terminal random coil region deletion. *Peptide Science*, 88(2):199–207, 2007.

[113] R. Mourtada, H. D. Herce, D. J. Yin, J. A. Moroco, T. E. Wales, J. R. Engen, and L. D. Walensky. Design of stapled antimicrobial peptides that are stable, nontoxic and kill antibiotic-resistant bacteria in mice. *Nature Biotechnology*, 37(10):1186–1197, 2019.

[114] K. Hilpert, M. R. Elliott, R. Volkmer-Engert, P. Henklein, O. Donini, Q. Zhou, D. F. Winkler, and R. E. Hancock. Sequence Requirements and an Optimization Strategy for Short Antimicrobial Peptides. *Chemistry & Biology*, 13(10):1101–1107, 2006.

[115] P. Basnet and N. Skalko-Basnet. Nanodelivery Systems for Improved Topical Antimicrobial Therapy. *Curr. Pharm. Des.*, 19(41):7237–7243, 2013.

[116] Z. Rukavina and Vanić. Current Trends in Development of Liposomes for Targeting Bacterial Biofilms. *Pharmaceutics*, 8(2):18, 2016.

[117] Z. Drulis-Kawa and A. Dorotkiewicz-Jach. Liposomes as delivery systems for antibiotics. *International Journal of Pharmaceutics*, 387(1):187–198, 2010.

[118] Z. Vanic, A. Holsaeter, and N. Skalko-Basnet. (Phospho)lipid-based Nanosystems for Skin Administration. *Curr. Pharm. Des.*, 21(29):4174–4192, 2015.

[119] S. Ron-Doitch, B. Sawodny, A. Kühbacher, M. M. David, A. Samanta, J. Phopase, A. Burger-Kentischer, M. Griffith, G. Golomb, and S. Rupp. Reduced cytotoxicity and enhanced bioactivity of cationic antimicrobial peptides liposomes in cell cultures and 3D epidermis model against HSV. *Journal of Controlled Release*, 229:163–171, May 2016.

[120] C. Pu and W. Tang. A chitosan-coated liposome encapsulating antibacterial peptide, Apep10: characterisation, triggered-release effects and antilisterial activity in thaw water of frozen chicken. *Food & Function*, 7(10):4310–4322, 2016.

[121] C. Li, X. Zhang, X. Huang, X. Wang, G. Liao, and Z. Chen. Preparation and characterization of flexible nanoliposomes loaded with daptomycin, a novel antibiotic, for topical skin therapy. eng. *International journal of nanomedicine*, 8:1285–1292, 2013.

[122] M. Imran, A.-M. Revol-Junelles, G. Francius, and S. Desobry. Diffusion of Fluorescently Labeled Bacteriocin from Edible Nanomaterials and Embedded Nano-Bioactive Coatings. *ACS Applied Materials & Interfaces*, 8(33):21618–21631, Aug. 2016.

[123] K. Yamakami, H. Tsumori, Y. Sakurai, Y. Shimizu, K. Nagatoshi, and K. Sonomoto. Sustainable inhibition efficacy of liposome-encapsulated nisin on insoluble glucan-biofilm synthesis by Streptococcus mutans. *Pharmaceutical Biology*, 51(2):267–270, 2013.

[124] J. He, K. Abdelraouf, K. R. Ledesma, D. S.-L. Chow, and V. H. Tam. Pharmacokinetics and efficacy of liposomal polymyxin B in a murine pneumonia model. *International Journal of Antimicrobial Agents*, 42(6):559–564, 2013.

[125] E. Sans-Serramitjana, E. Fusté, B. Martínez-Garriga, A. Merlos, M. Pastor, J. Pedraz, A. Esquisabel, D. Bachiller, T. Vinuesa, and M. Viñas. Killing effect of nanoencapsulated colistin sulfate on Pseudomonas aeruginosa from cystic fibrosis patients. *Journal of Cystic Fibrosis*, 15(5):611–618, 2016.

[126] A. Lewies, J. F. Wentzel, A. Jordaan, C. Bezuidenhout, and L. H. Du Plessis. Interactions of the antimicrobial peptide nisin Z with conventional antibiotics and the use of nanostructured lipid carriers to enhance antimicrobial activity. *International Journal of Pharmaceutics*, 526(1-2):244–253, 2017.

[127] M. Moreno-Sastre, M. Pastor, A. Esquisabel, E. Sans, M. Vinas, D. Bachiller, and D. L. Pedraz. Stability Study of Sodium Colistimethate-Loaded Lipid Nanoparticles. *Journal of Microencapsulation*, 33(7):636–645, 2016.

[128] L. Boge, A. Umerska, N. Matougui, H. Bysell, L. Ringstad, M. Davoudi, J. Eriksson, K. Edwards, and M. Andersson. Cubosomes post-loaded with antimicrobial peptides: characterization, bactericidal effect and proteolytic stability. *International Journal of Pharmaceutics*, 526(1-2):400–412, 2017.

[129] L. Boge, H. Bysell, L. Ringstad, D. Wennman, A. Umerska, V. Cassisa, J. Eriksson, M.-L. Joly-Guillou, K. Edwards, and M. Andersson. Lipid-Based Liquid Crystals As Carriers for Antimicrobial Peptides: Phase Behavior and Antimicrobial Effect. *Langmuir*, 32(17):4217–4228, 2016.

[130] L. Boge, K. Hallstensson, L. Ringstad, J. Johansson, T. Andersson, M. Davoudi, P. T. Larsson, M. Mahlapuu, J. Håkansson, and M. Andersson. Cubosomes for topical delivery

of the antimicrobial peptide LL-37. *European Journal of Pharmaceutics and Biopharmaceutics*, 134:60–67, 2019.

[131] D. A. Gyles, L. D. Castro, J. O. C. Silva, and R. M. Ribeiro-Costa. A review of the designs and prominent biomedical advances of natural and synthetic hydrogel formulations. *European Polymer Journal*, 88:373–392, 2017.

[132] B. Amsden. Solute Diffusion within Hydrogels. Mechanisms and Models. *Macromolecules*, 31(23):8382–8395, 1998.

[133] Y. Fu and W. J. Kao. Drug release kinetics and transport mechanisms of non-degradable and degradable polymeric delivery systems. eng. *Expert opinion on drug delivery*, 7(4):429–444, 2010.

[134] S. S. Rajan, V. L. Cavera, X. Zhang, Y. Singh, M. L. Chikindas, and P. J. Sinko. Polyethylene glycol-based hydrogels for controlled release of the antimicrobial subtilosin for prophylaxis of bacterial vaginosis. eng. *Antimicrobial Agents and Chemotherapy*, 58(5):2747–2753, 2014.

[135] R. Nordström, L. Nyström, O. C. Andrén, M. Malkoch, A. Umerska, M. Davoudi, A. Schmidtchen, and M. Malmsten. Membrane interactions of microgels as carriers of antimicrobial peptides. *Journal of Colloid and Interface Science*, 513:141–150, Mar. 2018.

[136] R. T. C. Cleophas, M. Riool, H. L. C. Quarles van Ufford, S. A. J. Zaat, J. A. W. Kruijtzer, and R. M. J. Liskamp. Convenient Preparation of Bactericidal Hydrogels by Covalent Attachment of Stabilized Antimicrobial Peptides Using Thiol–ene Click Chemistry. *ACS Macro Letters*, 3(5):477–480, 2014.

[137] M. A. Cole, T. F. Scott, and C. M. Mello. Bactericidal Hydrogels via Surface Functionalization with Cecropin A. *ACS Biomaterials Science & Engineering*, 2(11):1894–1904, 2016.

[138] H. Sun, Y. Hong, Y. Xi, Y. Zou, J. Gao, and J. Du. Synthesis, Self-Assembly, and Biomedical Applications of Antimicrobial Peptide–Polymer Conjugates. *ACS Biomacromolecules*, 19(6):1701–1720, 2018.

[139] K. Klein, R. B. Grønnemose, M. Alm, K. S. Brinch, H. J. Kolmos, and T. E. Andersen. Controlled Release of Plectasin NZ2114 from a Hybrid Silicone-Hydrogel Material for

Inhibition of Staphylococcus aureus Biofilm. *Antimicrobial Agents and Chemotherapy*, 61(7):00604–17, 2017.

[140] J. Cruz, J. Flórez, R. Torres, M. Urquiza, J. A. Gutiérrez, F. Guzmán, and C. C. Ortiz. Antimicrobial activity of a new synthetic peptide loaded in polylactic acid or poly(lactic-co-glycolic) acid nanoparticles against Pseudomonas aeruginosa, Escherichia coli O157:H7 and methicillin resistant Staphylococcus aureus (MRSA). *Nanotechnology*, 28(13):135102, 2017.

[141] A. Almaaytah, G. K. Mohammed, A. Abualhaijaa, and Q. Al-Balas. Development of novel ultrashort antimicrobial peptide nanoparticles with potent antimicrobial and antibiofilm activities against multidrug-resistant bacteria. eng. *Drug design, development and therapy*, 11:3159–3170, Nov. 2017.

[142] A. Vijayan, P. P. James, C. K. Nanditha, and G. S. V. Kumar. Multiple cargo deliveries of growth factors and antimicrobial peptide using biodegradable nanopolymer as a potential wound healing system. eng. *International journal of nanomedicine*, 14:2253–2263, Mar. 2019.

[143] B. Casciaro, I. d'Angelo, X. Zhang, M. R. Loffredo, G. Conte, F. Cappiello, F. Quaglia, Y.-P. P. Di, F. Ungaro, and M. L. Mangoni. Poly(lactide-co-glycolide) Nanoparticles for Prolonged Therapeutic Efficacy of Esculentin-1a-Derived Antimicrobial Peptides against Pseudomonas aeruginosa Lung Infection: in Vitro and in Vivo Studies. *Biomacromolecules*, 20(5):1876–1888, May 2019.

[144] S. Ramakrishna, K. Fujihara, W.-E. Teo, T. Yong, Z. Ma, and R. Ramaseshan. Electrospun nanofibers: solving global issues. *Materials Today*, 9(3):40–50, 2006.

[145] G. Amariei, V. Kokol, V. Vivod, K. Boltes, P. Letón, and R. Rosal. Biocompatible antimicrobial electrospun nanofibers functionalized with ϵ-poly-l-lysine. *International Journal of Pharmaceutics*, 553(1-2):141–148, 2018.

[146] K. M. Soto, M. Hernández-Iturriaga, G. Loarca-Piña, G. Luna-Bárcenas, and S. Mendoza. Antimicrobial effect of nisin electrospun amaranth: pullulan nanofibers in apple juice and fresh cheese. *International Journal of Food Microbiology*, 295:25–32, 2019.

[147] S. A. Maier. Electromagnetic so metals. In S. A. Maier, editor, *Plasmonics: Fundamentals and Applications*, chapter 1, pages 5–18. Springer US, Verlag, 1st edition, 2007.

[148]   L. Chang, L. V. Besteiro, J. Sun, E. Y. Santiago, S. K. Gray, Z. Wang, and A. O. Govorov. Electronic Structure of the Plasmons in Metal Nanocrystals: Fundamental Limitations for the Energy Efficiency of Hot Electron Generation. *ACS Energy Letters*, 4(10):2552–2568, 2019.

[149]   P. Drude. Zur Elektronentheorie der Metalle [German] (On the electronic theory of metals). *Ann. Phys.*, 306:566, 1900.

[150]   H. A. Lorentz. Zur Elektronentheorie der Metalle [Dutch] (Concerning the relation between the velocity of light propagation and the composition of media). *Verh. Kon. Akad. Wet. Amsterdam, Ads. Natuurkd*, 18:39, 1878.

[151]   D. F. Swinehart. The Beer-Lambert Law. *J. Chem. Educ.*, 39(7):333–335, 1962.

[152]   A. V. Zayats and I. I. Smolyaninov. Near-field photonics: surface plasmon polaritons and localized surface plasmons. *Journal of Optics A: Pure and Applied Optics*, 5(4):S16–S50, 2003.

[153]   E. Yasun, H. Kang, H. Erdal, S. Cansiz, I. Ocsoy, Y.-F. Huang, and W. Tan. Cancer cell sensing and therapy using affinity tag-conjugated gold nanorods. *Interface Focus*, 3(3), 2013.

[154]   G. Mie. Beiträge zur Optik trüber Medien, speziell kolloidaler Metallösungen [German] (Contributions to the optics of turbid media: Colloidal metal solutions. *Ann. Phys.*, 330(3):377–445, Jan. 1908.

[155]   R. Gans. Über die Form ultramikroskopischer Goldteilchen [German] (On the form of ultramicroscopic gold particles). *Ann. Phys.*, 342:881, 1912.

[156]   J. Pérez-Juste, I. Pastoriza-Santos, L. M. Liz-Marzán, and P. Mulvaney. Gold nanorods: Synthesis, characterization and applications. *Coordination Chemistry Reviews*, 249(17-18):1870–1901, 2005.

[157]   S. Eustis and M. A. El-Sayed. Determination of the aspect ratio statistical distribution of gold nanorods in solution from a theoretical fit of the observed inhomogeneously broadened longitudinal plasmon resonance absorption spectrum. *Journal of Applied Physics*, 100(4):044324, Aug. 2006.

[158]   Y. Hong, Y.-M. Huh, D. S. Yoon, and J. Yang. Nanobiosensors Based on Localized Surface Plasmon Resonance for Biomarker Detection. *Journal of Nanomaterials*, 2012:759830, 2012. M. A. Correa-Duarte, editor.

[159]   O. Ekici, R. K. Harrison, N. J. Durr, D. S. Eversole, M. Lee, and A. Ben-Yakar. Thermal analysis of gold nanorods heated with femtosecond laser pulses. *Journal of Physics D: Applied Physics*, 41(18), 2008.

[160]   X. Liu, G. Shan, J. Yu, W. Yang, Z. Ren, X. Wang, X. Xie, H.-j. Chen, and X. Chen. Laser heating of metallic nanoparticles for photothermal ablation applications. *AIP Advances*, (2):025308, 2017.

[161]   D. Wen. Intracellular hyperthermia: Nanobubbles and their biomedical applications. *International Journal of Hyperthermia*, 25(7):533–541, 2009.

[162]   V. K. Pustovalov and D. S. Bobuchenko. Heating, evaporation and combustion of a solid aerosol particle in a gas exposed to optical radiation. *International Journal of Heat Mass Transfer*, 32(1):3–17, 1989.

[163]   Z. Qin and J. C. Bischof. Thermophysical and biological responses of gold nanoparticle laser heating. *Chemical Society Reviews*, 41(3):1191–1217, Feb. 2012.

[164]   K. H. Luk, R. M. Hulse, and T. L. Phillips. Hyperthermia in cancer therapy. eng. *The Western journal of medicine*, 132(3):179–185, 1980.

[165]   Y. Chen, X. Bian, M. Aliru, A. A. Deorukhkar, O. Ekpenyong, S. Liang, J. John, J. Ma, X. Gao, J. Schwartz, P. Singh, Y. Ye, S. Krishnan, and H. Xie. Hypoxia-targeted gold nanorods for cancer photothermal therapy. eng. *Oncotarget*, 9(41):26556–26571, May 2018.

[166]   G. P. Goodrich, L. Bao, K. L. Gill-Sharp, K. L. Sang, J. C. Wang, and J. D. Payne. Photothermal therapy in a murine colon cancer model using near-infrared absorbing gold nanorods. *Journal of Biomedical Optics*, 15(1):1–8, 2010.

[167]   W. I. Choi, J.-Y. Kim, C. Kang, C. C. Byeon, Y. H. Kim, and G. Tae. Tumor Regression In Vivo by Photothermal Therapy Based on Gold-Nanorod-Loaded, Functional Nanocarriers. *ACS Nano*, 5(3):1995–2003, Mar. 2011.

[168] X. Li, J. Zhou, X. Dong, W.-Y. Cheng, H. Duan, and P. C. K. Cheung. In Vitro and In Vivo Photothermal Cancer Therapeutic Effects of Gold Nanorods Modified with Mushroom β-Glucan. *Journal of Agricultural and Food Chemistry*, 66(16):4091–4098, Apr. 2018.

[169] X. Kang, X. Guo, X. Niu, W. An, S. Li, Z. Liu, Y. Yang, N. Wang, Q. Jiang, C. Yan, H. Wang, and Q. Zhang. Photothermal therapeutic application of gold nanorods-porphyrin-trastuzumab complexes in HER2-positive breast cancer. *Scientific Reports*, 7(1):42069, 2017.

[170] M. R. K. Ali, M. A. Rahman, Y. Wu, T. Han, X. Peng, M. A. Mackey, D. Wang, H. J. Shin, Z. G. Chen, H. Xiao, R. Wu, Y. Tang, D. M. Shin, and M. A. El-Sayed. Efficacy, long-term toxicity, and mechanistic studies of gold nanorods photothermal therapy of cancer in xenograft mice. *Proceedings of the National Academy of Sciences*, 114(15):E3110, Apr. 2017.

[171] M. S. Brown and C. B. Arnold. Fundamentals of Laser-Material Interaction and Application to Multiscale Surface Modification. In K. Sugioka, editor, *Laser Precision Microfabrication*, chapter 4, pages 91–120. Springer, Berlin, Heidelberg, 135th edition, 2010.

[172] S. Kiwan and A. Al-Nimr. Thermalization time of thin metal lm heated by short pulse laser. *Chinese Physical Society*, 13(10):1758–1765, 2004.

[173] A. G. Bell. Upon the production and reproduction of sound by light. *American Journal of Science*, 9:404, 1880.

[174] W. Li and X. Chen. Gold nanoparticles for photoacoustic imaging. eng. *Nanomedicine*, 10(2):299–320, Jan. 2015.

[175] S. Kiselev. Kinetic boundary of metastable states in superheated and stretched liquids. *Physica A: Statistical Mechanics and its Applications*, 269(2-4):252–268, 1999.

[176] D. Lapotko. Plasmonic nanoparticle-generated photothermal bubbles and their biomedical applications. eng. *Nanomedicine (London, England)*, 4(7):813–845, Oct. 2009.

[177] C. H. Farny, T. Wu, R. G. Holt, T. W. Murray, and R. A. Roy. Nucleating cavitation from laser-illuminated nano-particles. *Acoustics Research Letters Online*, (3):138–143, 2005.

[178] A. Vogel, N. Linz, S. Freidank, and G. Paltauf. Femtosecond-Laser-Induced Nanocavitation in Water: Implications for Optical Breakdown Threshold and Cell Surgery. *Physical Review Letters*, 100(3):038102, 2008.

[179] V. Kotaidis, C. Dahmen, G. von Plessen, F. Springer, and A. Plech. Excitation of nanoscale vapor bubbles at the surface of gold nanoparticles in water. *The Journal of Chemical Physics*, 124(18):184702, 2006.

[180] G. Wu, A. Mikhailovsky, H. A. Khant, C. Fu, W. Chiu, and J. A. Zasadzinski. Remotely Triggered Liposome Release by Near-Infrared Light Absorption via Hollow Gold Nanoshells. *Journal of the American Chemical Society*, 130(26):8175–8177, July 2008.

[181] C. Yao, R. Rahmanzadeh, E. Endl, Z. Zhang, J. Gerdes, and G. Hüttmann. Elevation of plasma membrane permeability by laser irradiation of selectively bound nanoparticles. *Journal of Biomedical Optics*, 10(6):064012, 2005.

[182] S. Link, C. Burda, M. B. Mohamed, B. Nikoobakht, and M. A. El-Sayed. Laser Photothermal Melting and Fragmentation of Gold Nanorods: Energy and Laser Pulse-Width Dependence. *Journal of Physical Chemistry A*, 103(9):1165–1170, 1999.

[183] A. B. Taylor, A. M. Siddiquee, and J. W. M. Chon. Below Melting Point Photothermal Reshaping of Single Gold Nanorods Driven by Surface Diffusion. *ACS Nano*, 8(12):12071–12079, Dec. 2014.

[184] S. Link, Z. L. Wang, and M. A. El-Sayed. How Does a Gold Nanorod Melt? *The Journal of Physical Chemistry B*, 104(33):7867–7870, 2000.

[185] H. Petrova, J. P. Juste, I. Pastoriza-Santos, G. V. Hartland, L. M. Liz-Marzán, and P. Mulvaney. On the temperature stability of gold nanorods: comparison between thermal and ultrafast laser-induced heating. *Physical Chemistry Chemical Physics*, 8:814–821, 2006.

[186] Z. L. Wang, J. M. Petroski, T. C. Green, and M. A. El-Sayed. Shape Transformation and Surface Melting of Cubic and Tetrahedral Platinum Nanocrystals. *Journal of Physical Chemistry B*, 102(32):6145–6151, 1998.

[187] R. Kofman, P. Cheyssac, A. Aouaj, Y. Lereah, G. Deutscher, T. Ben-David, J. M. Penisson, and A. Bourret. Surface melting enhanced by curvature effects. *Surface Science*, 1994.

[188] K. C. Ng and W. Cheng. Fine-tuning longitudinal plasmon resonances of nanorods by thermal reshaping in aqueous media. *Nanotechnology*, 23(10):105602, 2012.

[189] W. J. Kennedy, S. Izor, B. D. Anderson, G. Frank, V. Varshney, and G. J. Ehlert. Thermal Reshaping Dynamics of Gold Nanorods: Influence of Size, Shape, and Local Environment. *ACS Applied Materials and Interfaces*, 10(50):43865–43873, 2018.

[190] Y. Horiguchi, K. Honda, Y. Kato, N. Nakashima, and Y. Niidome. Photothermal Reshaping of Gold Nanorods Depends on the Passivating Layers of the Nanorod Surfaces. *Langmuir*, 24(20):12026–12031, Oct. 2008.

[191] L. Cavigli, M. de Angelis, F. Ratto, P. Matteini, F. Rossi, S. Centi, F. Fusi, and R. Pini. Size Affects the Stability of the Photoacoustic Conversion of Gold Nanorods. *The Journal of Physical Chemistry C*, 118(29):16140–16146, July 2014.

[192] K. Jaskiewicz, A. Larsen, D. Schaeffel, K. Koynov, I. Lieberwirth, G. Fytas, K. Landfester, and A. Kroeger. Incorporation of Nanoparticles into Polymersomes: Size and Concentration Effects. *ACS Nano*, 6(8):7254–7262, 2012.

[193] B. M. Geilich, A. L. van de Ven, G. L. Singleton, L. J. Sepúlveda, S. Sridhar, and T. J. Webster. Silver nanoparticle-embedded polymersome nanocarriers for the treatment of antibiotic-resistant infections. *Nanoscale*, 7(8):3511–3519, 2015.

[194] E. Amstad, S. H. Kim, and D. A. Weitz. Photo- and thermoresponsive polymersomes for triggered release. *Angewandte Chemie - International Edition*, 51(50):12499–12503, 2012.

[195] R. J. Hickey, J. Koski, X. Meng, R. A. Riggleman, P. Zhang, and S. J. Park. Size-controlled self-assembly of superparamagnetic polymersomes. *ACS Nano*, 8(1):495–502, 2014.

[196] M. Kolasinska-Sojka, M. Wlodek, M. Szuwarzynski, S. Kereiche, L. Kovacik, and P. Warszynski. Properties of POPC/POPE supported lipid bilayers modified with hydrophobic quantum dots on polyelectrolyte cushions. *Colloids and Surfaces B: Biointerfaces*, 158:667–674, 2017.

[197] R. Martínez-González, J. Estelrich, and M. A. Busquets. Liposomes loaded with hydrophobic iron oxide nanoparticles: Suitable T2 contrast agents for MRI. *International Journal of Molecular Sciences*, 17(8), 2016.

[198]   F. Maestrelli, M. L. Gonzalez-Rodriguez, A. M. Rabasco, and P. Mura. Effect of prepara-
        tion technique on the properties of liposomes encapsulating ketoprofen-cyclodextrin com-
        plexes aimed for transdermal delivery. *International Journal of Pharmaceutics*, 312(2):53–
        60, 2006.

[199]   Z. Huang, X. Li, T. Zhang, Y. Song, Z. She, J. Li, and Y. Deng. Progress involving
        new techniques for liposome preparation. *Asian Journal of Pharmaceutical Sciences*,
        9(4):176–182, 2014.

[200]   S. H. Park, S. G. Oh, J. Y. Mun, and S. S. Han. Effects of silver nanoparticles on
        the fluidity of bilayer in phospholipid liposome. *Colloids and Surfaces B: Biointerfaces*,
        44(2-3):117–122, 2005.

[201]   S. H. Park, S. G. Oh, J. Y. Mun, and S. S. Han. Loading of gold nanoparticles inside
        the DPPC bilayers of liposome and their effects on membrane fluidities. *Colloids and
        Surfaces B: Biointerfaces*, 48(2):112–118, 2006.

[202]   M. R. Preiss, A. Hart, C. Kitchens, and G. D. Bothun. Hydrophobic Nanoparticles
        Modify the Thermal Release Behavior of Liposomes. *Journal of Physical Chemistry B*,
        121(19):5040–5047, 2017.

[203]   A. Wijaya and K. Hamad-Schifferli. High-density encapsulation of Fe3O4 nanoparticles
        in lipid vesicles. *Langmuir*, 23(19):9546–9550, 2007.

[204]   G. Béalle, R. Di Corato, J. Kolosnjaj-Tabi, V. Dupuis, O. Clément, F. Gazeau, C. Wil-
        helm, and C. Ménager. Ultra magnetic liposomes for MR imaging, targeting, and hyper-
        thermia. *Langmuir*, 28(32):11834–11842, 2012.

[205]   F. Szoka and D. Papahadjopoulos. Procedure for preparation of liposomes with large
        internal aqueous space and high capture by reverse-phase evaporation (drug delivery/en-
        capsulation/lipid vesicles/encapsulated macromolecules). *PNAS of USA*, 75(9):4194–
        4198, 1978.

[206]   T. Lajunen, L. Viitala, L. Kontturi, T. Laaksonen, H. Liang, E. Vuorimaa-Laukkanen,
        T. Viitala, X. Le Guével, M. Yliperttula, L. Murtomäki, and A. Urtti. Light induced
        cytosolic drug delivery from liposomes with gold nanoparticles. *Journal of Controlled
        Release*, 203:85–98, 2015.

[207] A. M. Smith, M. C. Mancini, and S. Nie. Bioimaging: Second window for in vivo imaging. *Nature Nanotechnology*, 4(11):710–711, 2009.

[208] L. Roach, S. Ye, S. C. Moorcroft, K. Critchley, P. L. Coletta, and S. D. Evans. Morphological control of seedlessly-synthesized gold nanorods using binary surfactants. *Nanotechnology*, 29(13), Feb. 2018.

[209] E. Hemmer, A. Benayas, F. Légaré, and F. Vetrone. Exploiting the biological windows: Current perspectives on fluorescent bioprobes emitting above 1000 nm. *Nanoscale Horizons*, 1(3):168–184, 2016.

[210] S. Thamphiwatana, V. Fu, J. Zhu, D. Lu, W. Gao, and L. Zhang. Nanoparticle-stabilized liposomes for ph-responsive gastric drug delivery. *Langmuir*, 29(39):12228–12233, 2013.

[211] R. Michel, T. Plostica, L. Abezgauz, D. Danino, and M. Gradzielski. Control of the stability and structure of liposomes by means of nanoparticles. *Soft Matter*, 9(16):4167–4177, 2013.

[212] D. Pornpattananangkul, S. Olson, S. Aryal, M. Sartor, C. M. Huang, K. Vecchio, and L. Zhang. Stimuli-responsive liposome fusion mediated by gold nanoparticles. *ACS Nano*, 4(4):1935–1942, 2010.

[213] A. K. Rengan, M. Jagtap, A. De, R. Banerjee, and R. Srivastava. Multifunctional gold coated thermo-sensitive liposomes for multimodal imaging and photo-thermal therapy of breast cancer cells. *Nanoscale*, 6(2):916–923, Jan. 2014.

[214] A. K. Rengan, A. B. Bukhari, A. Pradhan, R. Malhotra, R. Banerjee, R. Srivastava, and A. De. In vivo analysis of biodegradable liposome gold nanoparticles as efficient agents for photothermal therapy of cancer. *Nano Letters*, 15(2):842–848, Feb. 2015.

[215] L. Zhang and S. Granick. How to stabilize phospholipid liposomes (Using nanoparticles). *Nano Letters*, 4(1):694–698, 2006.

[216] Y. Yu, S. M. Anthony, L. Zhang, S. C. Bae, and S. Granick. Cationic nanoparticles stabilize zwitterionic liposomes better than anionic ones. *Journal of Physical Chemistry C*, 111(23):8233–8236, 2007.

[217] W. Gao, D. Vecchio, J. Li, J. Zhu, Q. Zhang, V. Fu, J. Li, S. Thamphiwatana, D. Lu, and L. Zhang. Hydrogel Containing Nanoparticle-Stabilized Liposomes for Topical Antimicrobial Delivery. *ACS Nano*, 8(3):2900–2907, Mar. 2014.

[218] A. Bhat, L. W. Edwards, X. Fu, D. L. Badman, S. Huo, A. J. Jin, and Q. Lu. Effects of gold nanoparticles on lipid packing and membrane pore formation. *Applied Physics Letters*, 109(26), 2016.

[219] A. S. Urban, M. Fedoruk, M. R. Horton, J. O. Rädler, F. D. Stefani, and J. Feldmann. Controlled nanometric phase transitions of phospholipid membranes by plasmonic heating of single gold nanoparticles. *Nano Letters*, 9(8):2903–2908, 2009.

[220] G. A. Dichello, T. Fukuda, T. Maekawa, R. L. Whitby, S. V. Mikhalovsky, M. Alavijeh, A. S. Pannala, and D. K. Sarker. Preparation of liposomes containing small gold nanoparticles using electrostatic interactions. *European Journal of Pharmaceutical Sciences*, 105:55–63, 2017.

[221] D. V. Volodkin, A. G. Skirtach, and H. Mohwald. Near-IR Remote Release from Assemblies of Liposomes and Nanoparticles. *Angew Chem Int Ed Engl*, 48:1807–1809, 2009.

[222] Y. Jin and X. Gao. Spectrally tunable leakage-free gold nanocontainers. *Journal of the American Chemical Society*, 131(49):17774–17776, 2009.

[223] T. S. Troutman, J. K. Barton, and M. Romanowski. Biodegradable plasmon resonant nanoshells. *Advanced Materials*, 20(13):2604–2608, 2008.

[224] L. Luo, Y. Bian, Y. Liu, X. Zhang, M. Wang, S. Xing, L. Li, and D. Gao. Combined Near Infrared Photothermal Therapy and Chemotherapy Using Gold Nanoshells Coated Liposomes to Enhance Antitumor Effect. *Small*, 12(30):4103–4112, 2016.

[225] T. K. Sau, A. S. Urban, S. K. Dondapati, M. Fedoruk, M. R. Horton, A. L. Rogach, F. D. Stefani, J. O. Rädler, and J. Feldmann. Controlling loading and optical properties of gold nanoparticles on liposome membranes. *Colloids and Surfaces A: Physicochemical and Engineering Aspects*, 342(1-3):92–96, 2009.

[226] H. Guo and J. C. Kim. Photothermally induced release from liposome suspended in mixture solution of gold nanoparticle and thermo-sensitive polymer. *Colloids and Surfaces A: Physicochemical and Engineering Aspects*, 469:73–82, 2015.

[227] S. Thakur and O. Arotiba. Synthesis, characterization and adsorption studies of an acrylic acid-grafted sodium alginate-based TiO2 hydrogel nanocomposite. *Adsorption Science and Technology*, 36(1-2):458–477, 2018.

[228] H.-L. Tan, S.-Y. Teow, and J. Pushpamalar. Application of Metal NanoparticleHydrogel Composites in Tissue Regeneration. eng. *Bioengineering*, 6(1):17, 2019.

[229] R. Gupta and A. K. Bajpai. Magnetically guided release of ciprofloxacin from superparamagnetic polymer nanocomposites. *Journal of Biomaterials Science, Polymer Edition*, 22(7):893–918, 2011.

[230] M. Ghorbanloo, A. Heydari, and H. Yahiro. Ag-nanoparticle embedded p(AA) hydrogel as an efficient green heterogeneous Nano-catalyst for oxidation and reduction of organic compounds. *Applied Organometallic Chemistry*, 32(1), 2018.

[231] N. S. Capanema, A. A. Mansur, S. M. Carvalho, L. L. Mansur, C. P. Ramos, A. P. Lage, and H. S. Mansur. Physicochemical properties and antimicrobial activity of biocompatible carboxymethylcellulose-silver nanoparticle hybrids for wound dressing and epidermal repair. *Journal of Applied Polymer Science*, 135(6), 2018.

[232] Y. Zhan, Y. Pan, B. Chen, J. Lu, Z. Zhong, and X. Niu. Strain rate dependent hyperelastic stress-stretch behavior of a silica nanoparticle reinforced poly (ethylene glycol) diacrylate nanocomposite hydrogel. *Journal of the Mechanical Behavior of Biomedical Materials*, 75:236–243, 2017.

[233] E. A. Appel, M. W. Tibbitt, M. J. Webber, B. A. Mattix, O. Veiseh, and R. Langer. Self-assembled hydrogels utilizing polymer-nanoparticle interactions. *Nature Communications*, 6:6295–6304, 2015.

[234] E. Stalder and A. Zumbuehl. Liposome-Containing Mechanoresponsive Hydrogels. *Macromolecular Materials and Engineering*, 302(5), May 2017.

[235] L. Paasonen, T. Laaksonen, C. Johans, M. Yliperttula, K. Kontturi, and A. Urtti. Gold nanoparticles enable selective light-induced contents release from liposomes. *Journal of Controlled Release*, 122(1):86–93, Sept. 2007.

[236] L. Paasonen, T. Sipilä, A. Subrizi, P. Laurinmäki, S. J. Butcher, M. Rappolt, A. Yaghmur, A. Urtti, and M. Yliperttula. Gold-embedded photosensitive liposomes for drug delivery: Triggering mechanism and intracellular release. *Journal of Controlled Release*, 147(1):136–143, Oct. 2010.

[237] M. Mathiyazhakan, Y. Yang, Y. Liu, C. Zhu, Q. Liu, C. D. Ohl, K. C. Tam, Y. Gao, and C. Xu. Non-invasive controlled release from gold nanoparticle integrated photo-responsive liposomes through pulse laser induced microbubble cavitation. *Colloids and Surfaces B: Biointerfaces*, 126:569–574, 2015.

[238] L. J. Anderson, E. Hansen, E. Y. Lukianova-Hleb, J. H. Hafner, and D. O. Lapotko. Optically guided controlled release from liposomes with tunable plasmonic nanobubbles. *Journal of Controlled Release*, 144(2):151–158, 2010.

[239] L. Viitala. et al. Photothermally Triggered Lipid Bilayer Phase Transition and Drug Release from Gold Nanorod and Indocyanine Green Encapsulated Liposomes. *Langmuir*, 32(18):4554–4563, May 2016.

[240] N. Dave and J. Liu. Protection and promotion of UV radiation-induced liposome leakage via DNA-directed assembly with gold nanoparticles. *Advanced Materials*, 23(28):3182–3186, 2011.

[241] S. J. Leung, X. M. Kachur, M. C. Bobnick, and M. Romanowski. Wavelength-selective light-induced release from plasmon resonant liposomes. *Advanced Functional Materials*, 21(6):1113–1121, 2011.

[242] B. Radt, T. A. Smith, and F. Caruso. Optically addressable nanostructured capsules. *Advanced Materials*, 16(23-24):2184–2189, 2004.

[243] B. M. Geilich, I. Gelfat, S. Sridhar, A. L. van de Ven, and T. J. Webster. Superparamagnetic iron oxide-encapsulating polymersome nanocarriers for biofilm eradication. *Biomaterials*, 119:78–85, 2017.

[244] O. Bixner, S. Kurzhals, M. Virk, and E. Reimhult. Triggered release from thermoresponsive polymersomes with superparamagnetic membranes. *Materials*, 9(1), 2016.

[245] M. Amoli-Diva, R. Sadighi-Bonabi, and K. Pourghazi. Laser-assisted triggered-drug release from silver nanoparticles-grafted dual-responsive polymer. *Materials Science and Engineering C*, 76:536–542, 2017.

[246] S. Sirivisoot and B. S. Harrison. Magnetically stimulated ciprofloxacin release from polymeric microspheres entrapping iron oxide nanoparticles. *International Journal of Nanomedicine*, 10:4447–4458, 2015.

[247] M. Harris, H. Ahmed, B. Barr, D. LeVine, L. Pace, A. Mohapatra, B. Morshed, J. D. Bumgardner, and J. A. Jennings. Magnetic stimuli-responsive chitosan-based drug delivery biocomposite for multiple triggered release. *International Journal of Biological Macromolecules*, 104:1407–1414, 2017.

[248] A. Mohapatra, M. A. Harris, D. LeVine, M. Ghimire, J. A. Jennings, B. I. Morshed, W. O. Haggard, J. D. Bumgardner, S. R. Mishra, and T. Fujiwara. Magnetic stimulus responsive vancomycin drug delivery system based on chitosan microbeads embedded with magnetic nanoparticles. *Journal of Biomedical Materials Research - Part B Applied Biomaterials*, 106(6):2169–2176, 2018.

[249] D. G. Meeker, S. V. Jenkins, E. K. Miller, K. E. Beenken, A. J. Loughran, A. Powless, T. J. Muldoon, E. I. Galanzha, V. P. Zharov, M. S. Smeltzer, and J. Chen. Synergistic Photothermal and Antibiotic Killing of Biofilm-Associated Staphylococcus aureus Using Targeted Antibiotic-Loaded Gold Nanoconstructs. *ACS Infectious Diseases*, 2(4):241–250, Apr. 2016.

[250] D. Miranda and J. F. Lovell. Mechanisms of light-induced liposome permeabilization. *Bioengineering & Translational Medicine*, (3):267–276, 2016.

[251] Z. Izadifar, P. Babyn, and D. Chapman. Ultrasound cavitation/microbubble detection and medical applications. *Journal of Medical and Biological Engineering*, 39:259–276, 2019.

[252] P. A. Dijkmans, L. J. M. Juffermans, R. J. P. Musters, A van Wamel, F. J. ten Cate, W van Gilst, C. A. Visser, N de Jong, and O Kamp. Microbubbles and ultrasound: from diagnosis to therapy. *European Journal of Echocardiography*, 5(4):245–246, 2004.

[253] A. B. Karpiouk, S. R. Aglyamov, F. Bourgeois, A. Ben-Yakar, and S. Y. Emelianov. Ultrasound characterization of cavitation microbubbles produced by femtosecond laser pulses. *SPIE*, 7175(1):209 – 215, 2009.

[254] A. Mrozik, Z. Piotrowska-Seget, and S. Łabużek. Cytoplasmatic Bacterial Membrane Responses to Environmental Perturbations. *Polish Journal of Environmental Studies*, 13(5):487–494, 2004.

[255] X. Li, S. M. Robinson, A. Gupta, K. Saha, Z. Jiang, D. F. Moyano, A. Sahar, M. A. Riley, and V. M. Rotello. Functional Gold Nanoparticles as Potent Antimicrobial Agents against Multi-Drug-Resistant Bacteria. *ACS Nano*, 8(10):10682–10686, 2014.

[256] J.-W. Xu, K. Yao, and Z.-K. Xu. Nanomaterials with a photothermal effect for antibac-
       terial activities: an overview. *Nanoscale*, 11(18):8680–8691, 2019.

[257] B.-H. Lai and D.-H. Chen. Vancomycin-modified LaB6@SiO2/Fe3O4 composite nanopar-
       ticles for near-infrared photothermal ablation of bacteria. *Acta Biomaterialia*, 9(7):7573–
       7579, 2013.

[258] Z. Liu, J. Liu, R. Wang, Y. Du, J. Ren, and X. Qu. An efficient nano-based theranos-
       tic system for multi-modal imaging-guided photothermal sterilization in gastrointestinal
       tract. *Biomaterials*, 56:206–218, 2015.

[259] Y. Jin, J. Deng, J. Yu, C. Yang, M. Tong, and Y. Hou. Fe5C2 nanoparticles: a reusable
       bactericidal material with photothermal effects under near-infrared irradiation. *Journal
       of Materials Chemistry B*, 3(19):3993–4000, 2015.

[260] H. Suo, X. Zhao, Z. Zhang, Y. Wu, and C. Guo. Upconverting LuVO4:Nd3+/Yb3+/Er3+
       @SiO2@Cu2S Hollow Nanoplatforms for Self-monitored Photothermal Ablation. *ACS
       Applied Materials & Interfaces*, 10(46):39912–39920, 2018.

[261] C. Zhang, J. Wang, R. Chi, J. Shi, Y. Yang, and X. Zhang. Reduced graphene oxide
       loaded with MoS2 and Ag3PO4 nanoparticles/PVA interpenetrating hydrogels for im-
       proved mechanical and antibacterial properties. *Materials and Design*, 183:1–13, 2019.

[262] Y. Zhao, X. Wang, F. Gao, C. Wang, Z. Yang, H. Wu, C. Li, L. Cheng, and R. Peng.
       Facile Preparation of Cu2Se Nanosheets as Dual-Functional Antibacterial Agents. *ACS
       Applied Bio Materials*, 3(3):1418–1425, 2020.

[263] M. Zhu, X. Liu, L. Tan, Z. Cui, Y. Liang, Z. Li, K. W. Kwok Yeung, and S. Wu. Photo-
       responsive chitosan/Ag/MoS2 for rapid bacteria-killing. *Journal of Hazardous Materials*,
       383:121122, 2020.

[264] S. H. Kim, E. B. Kang, C. J. Jeong, S. M. Sharker, I. In, and S. Y. Park. Light Con-
       trollable Surface Coating for Effective Photothermal Killing of Bacteria. *ACS Applied
       Materials & Interfaces*, 7(28):15600–15606, July 2015.

[265] Y. Zhao, X. Dai, X. Wei, Y. Yu, X. Chen, X. Zhang, and C. Li. Near-Infrared Light-
       Activated Thermosensitive Liposomes as Efficient Agents for Photothermal and Antibi-
       otic Synergistic Therapy of Bacterial Biofilm. *ACS Applied Materials and Interfaces*,
       10(17):14426–14437, May 2018.

[266] Y. Ko, J. Kim, H. Y. Jeong, G. Kwon, D. Kim, M. Ku, J. Yang, Y. Yamauchi, H.-Y. Kim, C. Lee, and J. You. Antibacterial poly (3,4-ethylenedioxythiophene):poly(styrene-sulfonate)/agarose nanocomposite hydrogels with thermo-processability and self-healing. *Carbohydrate Polymers*, 203:26–34, 2019.

[267] C. Mao, Y. Xiang, X. Liu, Y. Zheng, K. W. K. Yeung, Z. Cui, X. Yang, Z. Li, Y. Liang, S. Zhu, and S. Wu. Local Photothermal/Photodynamic Synergistic Therapy by Disrupting Bacterial Membrane to Accelerate Reactive Oxygen Species Permeation and Protein Leakage. *ACS Applied Materials and Interfaces*, 11(19):17902–17914, 2019.

[268] G. Qing, X. Zhao, N. Gong, J. Chen, X. Li, Y. Gan, Y. Wang, Z. Zhang, Y. Zhang, W. Guo, Y. Luo, and X.-J. Liang. Thermo-responsive triple-function nanotransporter for efficient chemo-photothermal therapy of multidrug-resistant bacterial infection. *Nature Communications*, 10(1):4336, 2019.

[269] L.-X. Yan, L.-J. Chen, X. Zhao, and X.-P. Yan. pH Switchable Nanoplatform for In Vivo Persistent Luminescence Imaging and Precise Photothermal Therapy of Bacterial Infection. *Advanced Functional Materials*, 30(14):1909042, 2020.

[270] H. E. Karahan, C. Wiraja, C. Xu, J. Wei, Y. Wang, L. Wang, F. Liu, and Y. Chen. Graphene Materials in Antimicrobial Nanomedicine: Current Status and Future Perspectives. *Advanced Healthcare Materials*, 7(13):1701406, 2018.

[271] C. Yang, L. Xu, Y. Zhou, X. Zhang, X. Huang, M. Wang, Y. Han, M. Zhai, S. Wei, and J. Li. A green fabrication approach of gelatin/CM-chitosan hybrid hydrogel for wound healing. *Carbohydrate Polymers*, 82(4):1297–1305, 2010.

[272] M.-C. Wu, A. R. Deokar, J.-H. Liao, P.-Y. Shih, and Y.-C. Ling. Graphene-Based Photothermal Agent for Rapid and Effective Killing of Bacteria. *ACS Nano*, 7(2):1281–1290, Feb. 2013.

[273] M. P. Romero, V. S. Marangoni, C. G. de Faria, I. S. Leite, C. d. C. C. e. Silva, C. M. Maroneze, M. A. Pereira-da Silva, V. S. Bagnato, and N. M. Inada. Graphene Oxide Mediated Broad-Spectrum Antibacterial Based on Bimodal Action of Photodynamic and Photothermal Effects. *Frontiers in Microbiology*, 10:2995, 2020.

[274] N. Levi-Polyachenko, C. Young, C. MacNeill, A. Braden, L. Argenta, and S. Reid. Eradicating group A streptococcus bacteria and biofilms using functionalised multi-wall carbon nanotubes. *International Journal of Hyperthermia*, 30(7):490–501, 2014.

[275] L. Mocan, I. Ilie, F. A. Tabaran, C. Iancu, O. Mosteanu, T. Pop, C. Zdrehus, D. Bartos, T. Mocan, and C. Matea. Selective Laser Ablation of Methicillin-Resistant Staphylococcus Aureus with IgG Functionalized Multi-Walled Carbon Nanotubes. *Journal of Biomedical Nanotechnology*, 12(4):781–788, 2016.

[276] Y. Yang, L. Ma, C. Cheng, Y. Deng, J. Huang, X. Fan, C. Nie, W. Zhao, and C. Zhao. Nonchemotherapic and Robust Dual-Responsive Nanoagents with On-Demand Bacterial Trapping, Ablation, and Release for Efficient Wound Disinfection. *Advanced Functional Materials*, 28(21):1705708, 2018.

[277] J. C. Castillo-Martínez, G. A. Martínez-Castañón, F. Martínez-Gutierrez, N. V. Zavala-Alonso, N. Patiño-Marín, N. Niño-Martinez, V Zaragoza-Magaña, and C Cabral-Romero. Antibacterial and Antibiofilm Activities of the Photothermal Therapy Using Gold Nanorods against Seven Different Bacterial Strains. *Journal of Nanomaterials*, 2015:783671, 2015. A. Falqui, editor.

[278] N. N. Mahmoud, A. M. Alkilany, E. A. Khalil, and A. G. Al-Bakri. Nano-Photothermal ablation effect of Hydrophilic and Hydrophobic Functionalized Gold Nanorods on Staphylococcus aureus and Propionibacterium acnes. *Scientific Reports*, 8(1):6881, 2018.

[279] X. Hu, Y. Zhao, Z. Hu, A. Saran, S. Hou, T. Wen, W. Liu, Y. Ji, X. Jiang, and X. Wu. Gold nanorods core/AgPt alloy nanodots shell: A novel potent antibacterial nanostructure. *Nano Research*, 6(11):822–835, 2013.

[280] Y. Peng, Y. Liu, X. Lu, S. Wang, M. Chen, W. Huang, Z. Wu, G. Lu, and L. Nie. Ag-Hybridized plasmonic Au-triangular nanoplates: highly sensitive photoacoustic/Raman evaluation and improved antibacterial/photothermal combination therapy. *Journal of Materials Chemistry B*, 6(18):2813–2820, 2018.

[281] Z. Qiao, Y. Yao, S. Song, M. Yin, M. Yang, D. Yan, L. Yang, and J. Luo. Gold nanorods with surface charge-switchable activities for enhanced photothermal killing of bacteria and eradication of biofilm. *Journal of Materials Chemistry B*, 8(15):3138–3149, 2020.

[282] B. Hu, N. Wang, L. Han, M.-L. Chen, and J.-H. Wang. Core–shell–shell nanorods for controlled release of silver that can serve as a nanoheater for photothermal treatment on bacteria. *Acta Biomaterialia*, 11:511–519, 2015.

[283] X. Ding, P. Yuan, N. Gao, H. Zhu, Y. Y. Yang, and Q.-H. Xu. Au-Ag core-shell nanoparti-
       cles for simultaneous bacterial imaging and synergistic antibacterial activity. *Nanomedicine:
       Nanotechnology, Biology and Medicine*, 13(1):297–305, 2017.

[284] D. He, T. Yang, W. Qian, C. Qi, L. Mao, X. Yu, H. Zhu, G. Luo, and J. Deng. Combined
       photothermal and antibiotic therapy for bacterial infection via acidity-sensitive nanocar-
       riers with enhanced antimicrobial performance. *Applied Materials Today*, 12:415–429,
       2018.

[285] M. Liu, D. He, T. Yang, W. Liu, L. Mao, Y. Zhu, J. Wu, G. Luo, and J. Deng. An efficient
       antimicrobial depot for infectious site-targeted chemo-photothermal therapy. *Journal of
       Nanobiotechnology*, 16(1):23, 2018.

[286] I. Ocsoy, S. Yusufbeyoglu, V. Yılmaz, E. S. McLamore, N. Ildız, and A. Ülgen. DNA
       aptamer functionalized gold nanostructures for molecular recognition and photothermal
       inactivation of methicillin-Resistant Staphylococcus aureus. *Colloids and Surfaces B:
       Biointerfaces*, 159:16–22, 2017.

[287] L. Mocan, C. Matea, F. A. Tabaran, O. Mosteanu, T. Pop, C. Puia, L. Agoston-Coldea,
       D. Gonciar, E. Kalman, G. Zaharie, C. Iancu, and T. Mocan. Selective in vitro photother-
       mal nano-therapy of MRSA infections mediated by IgG conjugated gold nanoparticles.
       Scientific Reports, 6(1):39466, 2016.

[288] X. Zhang, Y. Li, J. Qiu, D. Zhou, M. Zhang, L. Tang, G. Xie, and H. Xiang. Hollow Au
       loaded with kanamycin for pharmacological and laser-triggered photothermal steriliza-
       tion. *RSC Advances*, 7(27):16836–16842, 2017.

[289] R. S. Norman, J. W. Stone, A. Gole, C. J. Murphy, and T. L. Sabo-Attwood. Targeted
       Photothermal Lysis of the Pathogenic Bacteria, Pseudomonas aeruginosa, with Gold
       Nanorods. *Nano Letters*, 8(1):302–306, 2008.

[290] S. Wang, A. Singh, D. Senapati, A. Neely, H. Yu, and P. Ray. Rapid Colorimetric Identi-
       fication and Targeted Photothermal Lysis of Salmonella Bacteria by Using Bioconjugated
       Oval-Shaped Gold Nanoparticles. *Chemistry – A European Journal*, 16(19):5600–5606,
       2010.

[291] V. P. Zharov, K. E. Mercer, E. N. Galitovskaya, and M. S. Smeltzer. Photothermal
       nanotherapeutics and nanodiagnostics for selective killing of bacteria targeted with gold
       nanoparticles. eng. *Biophysical journal*, 90(2):619–627, 2006.

[292] N. Yang, C. Wang, X. Wang, and L. Li. Synthesis of photothermal nanocomposites and their application to antibacterial assays. *Nanotechnology*, 29(17):175601, 2018.

[293] W.-C. Huang, P.-J. Tsai, and Y.-C. Chen. Multifunctional Fe3O4@Au Nanoeggs as Photothermal Agents for Selective Killing of Nosocomial and Antibiotic-Resistant Bacteria. *Small*, 5(1):51–56, 2009.

[294] H. Peng, R. E. Borg, L. P. Dow, B. L. Pruitt, and I. A. Chen. Controlled phage therapy by photothermal ablation of specific bacterial species using gold nanorods targeted by chimeric phages. *Proceedings of the National Academy of Sciences*, 117(4):1951, 2020.

[295] A. S. Nilsson. Pharmacological limitations of phage therapy. *Upsala Journal of Medical Sciences*, 124(4):218–227, 2019.

[296] W. Jo and M. J. Kim. Influence of the photothermal effect of a gold nanorod cluster on biofilm disinfection. *Nanotechnology*, 24(19):195104, 2013.

[297] M. A. Abdou Mohamed, V. Raeesi, P. V. Turner, A. Rebbapragada, K. Banks, and W. C. Chan. A versatile plasmonic thermogel for disinfection of antimicrobial resistant bacteria. *Biomaterials*, 97:154–163, Aug. 2016.

[298] C. Bermúdez-Jiménez, N. Niño-Martínez, N. Patiño-Marín, F. Martínez-Gutiérrez, F. Ruiz, H. Bach, and G. Martínez-Castañón. Effective control of biofilms by photothermal therapy using a gold nanorod hydrogel. *Journal of Biomedical Materials Research - Part B Applied Biomaterials*, 108(2):333–342, 2020.

[299] A. Pitto-Barry and N. P. E. Barry. Pluronic® block-copolymers in medicine: from chemical and biological versatility to rationalisation and clinical advances. *Polymer Chemistry*, 5(10):3291–3297, 2014.

[300] S. Krishnan. Biofilm Formation on Medical Devices and Infection: Preventive Approaches. In H. Kanematsu and D. Barry, editors, *Biofilm and Materials Science*. Pages 93–108. Springer, Cham, 2015.

[301] Z. Khatoon, C. D. McTiernan, E. J. Suuronen, T.-F. Mah, and E. I. Alarcon. Bacterial biofilm formation on implantable devices and approaches to its treatment and prevention. eng. *Heliyon*, 4(12):e01067–e01067, 2018.

[302] T. Yang, D. Wang, and X. Liu. Assembled gold nanorods for the photothermal killing of bacteria. *Colloids and Surfaces B: Biointerfaces*, 173:833–841, 2019.

[303] P. Pallavicini, A. Donà, A. Taglietti, P. Minzioni, M. Patrini, G. Dacarro, G. Chirico, L. Sironi, N. Bloise, L. Visai, and L. Scarabelli. Self-assembled monolayers of gold nanostars: a convenient tool for near-IR photothermal biofilm eradication. *Chemical Communications*, 50(16):1969–1971, 2014.

[304] I. de Miguel, I. Prieto, A. Albornoz, V. Sanz, C. Weis, P. Turon, and R. Quidant. Plasmon-Based Biofilm Inhibition on Surgical Implants. *Nano Letters*, 19(4):2524–2529, 2019.

[305] F. Varenne, A. Makky, M. Gaucher-Delmas, F. Violleau, and C. Vauthier. Multimodal Dispersion of Nanoparticles: A Comprehensive Evaluation of Size Distribution with 9 Size Measurement Methods. *Pharmaceutical Research*, 33(5):1220–1234, May 2016.

[306] R Pecora. Dynamic light scattering measurement of nanometer particles in liquids. *Journal of Nanoparticle Research*, 2:123–131, 2000.

[307] J. Wagner, W. Härtl, and R. Hempelmann. Characterization of monodisperse colloidal particles: comparison between SAXS and DLS. *Langmuir*, 16(9):4080–4085, May 2000.

[308] M. Jones. Diagram of zeta potential and slipping planeV2 [available online: https://en.wikipedia.org/wiki/Zeta_potential#/media/File:Diagram_of_zeta_potential_and_slipping_planeV2.svg], 2012.

[309] A. A. Barba, S. Bochicchio, A. Salmoro, D. Caccavo, S. Cascone, and G. Lamberti. Polymeric and lipid-based systems for controlled drug release: an engineering point of view. In *Nanomaterials for Drug Delivery and Therapy*. Volume 1, chapter 10, pages 267–304. William Andrew Publishers, 2019.

[310] A. Kumar and C. K. Dixit. Methods for characterization of nanoparticles. In *Advances in Nanomedicine for the Delivery of Therapeutic Nucleic Acids*, chapter 3, pages 43–58. Woodhead Publishing, 2017.

[311] E. Joseph and G. Singhvi. Multifunctional nanocrystals for cancer therapy: a potential nanocarrier. In *Nanomaterials for Drug Delivery and Therapy*, chapter 4, pages 91–116. William Andrew Publishers, 2019.

[312] M. Smoluchowski. Contribution a la theorie de l'endosmose electrique et de quelques phenomenes correlatifs. *Pisma Mariana Smoluchowskiego*, 1(1):403–420, 1924.

[313] P. Debye and E. Huckel. Zur Theorie der Elektrolyte. II. Grenzgesetz fu r die elektrische Leitfa higkeit [German] (On the theory of electrolytes. II. Limiting law for electric conductivity). *Physikalische Zeitschrift*, 24:305, 1923.

[314] M. Kaszuba, J. Corbett, F. M. N. Watson, and A. Jones. High-concentration zeta potential measurements using light-scattering techniques. *Philosophical Transactions of the Royal Society A: Mathematical, Physical and Engineering Sciences*, 368(1927):4439–4451, Sept. 2010.

[315] L. Zhai, J. Zhao, M. Zhao, Y. Chen, and L. Zhang. Encapsulation and releasing of calcein by spontaneously formed zwitterionic/anionic vesicle without separation. *Journal of Dispersion Science and Technology*, 28(3):455–461, Mar. 2007.

[316] R. Katoh, S. Sinha, S. Murata, and M Tachiya. Origin of the stabilization energy of perylene excimer as studied by fluorescence and near-IR transient absorption spectroscopy. *Journal of Photochemistry and Photobiology A: Chemistry*, 145(2):23–34, 2001.

[317] AAT Bioquest. The Spectra of Calcein and Its Variations, 2019.

[318] J. M. Walker. The Bicinchoninic Acid (BCA) Assay for Protein Quantitation. In *Basic Protein and Peptide Protocols*, pages 5–8. Humana Press, New Jersey, 1994.

[319] A. Banerjee and H. Onyuksel. Human pancreatic polypeptide in a phospholipid-based micellar formulation. *Pharmaceutical Research*, 29(6):1698–1711, 2012.

[320] O. Scherzer. The theoretical resolution limit of the electron microscope. *Journal of Applied Physics*, 20(1):20–29, 1949.

[321] B. Carter and D. B. Williams. *Transmission Electron Microscopy: Diffraction, Imaging, and Spectrometry*. Springer International Publishing, New York, 1st edition, 2016, pages 2–3.

[322] L. Reimer. Transmission Electron Microscopy. In *Transmission Electron Microscopy: Physics of Image Formation and Microanalysis*, chapter 1, pages 5–7. Springer-Verlag Berlin Heidelberg, New York, 4th edition, 1997.

[323] M. Müller. *Demonstration of Liposomes by Electron Microscopy*. A. Azzi, U. Brodbeck, and P. Zhaler, editors. Springer, Berlin, Heidelberg, 1st edition, 1981, pages 252–253.

[324] M. D. Amos and J. B. Wrtmst. Use of high-temperature pre-mixed flames in atomic absorption spectroscopy. *Spectrochimica Acta*, 22(7):23–24, 1966.

[325] *Coherent Ultrafast Laser Systems 2017 Catalogue.* Coherent, Santa Clara, 2017, page 14.

[326] D. P. Nair, M. Podgorski, S. Chatani, T. Gong, W. Xi, C. R. Fenoli, and C. N. Bow-
       man. The Thiol-Michael Addition Click Reaction: A Powerful and Widely Used Tool in
       Materials Chemistry. *Chemistry of Materials*, 26(1):724–744, 2014.

[327] H. Park, X. Guo, J. S. Temenoff, Y. Tabata, A. I. Caplan, F. K. Kasper, and A. G. Mikos.
       Effect of swelling ratio of injectable hydrogel composites on chondrogenic differentiation
       of encapsulated rabbit marrow mesenchymal stem cells in vitro. *Biomacromolecules*,
       10(3):541–546, 2009.

[328] J. Lai, L. Zhang, W. Niu, W. Qi, J. Zhao, Z. Liu, W. Zhang, and G. Xu. One-pot synthesis
       of gold nanorods using binary surfactant systems with improved monodispersity, dimen-
       sional tunability and plasmon resonance scattering properties. *Nanotechnology*, 25(12),
       Mar. 2014.

[329] L. Scarabelli, A. Sánchez-Iglesias, J. Pérez-Juste, and L. M. Liz-Marzán. A "Tips and
       Tricks" Practical Guide to the Synthesis of Gold Nanorods. *Journal of Physical Chem-
       istry Letters*, 6(21):4270–4279, Nov. 2015.

[330] B. C. Rostro-Kohanloo, L. R. Bickford, C. M. Payne, E. S. Day, L. J. E. Anderson,
       M. Zhong, S. Lee, K. M. Mayer, T. Zal, L. Adam, C. P. N. Dinney, R. A. Drezek,
       J. L. West, and J. H. Hafner. The stabilization and targeting of surfactant-synthesized
       gold nanorods. *IOP PUBLISHING NANOTECHNOLOGY Nanotechnology*, 20:434005–
       10, 2009.

[331] L. Vigderman, P. Manna, and E. R. Zubarev. Quantitative replacement of cetyl trimethy-
       lammonium bromide by cationic thiol ligands on the surface of gold nanorods and their
       extremely large uptake by cancer cells. *Angewandte Chemie*, 51(3):636–641, 2012.

[332] Yu, S.-S. Chang, C.-L. Lee, and C. R. C. Wang. Gold Nanorods: Electrochemical Syn-
       thesis and Optical Properties. *The Journal of Physical Chemistry B*, 101(34):6661–6664,
       1997.

[333] A Brioude, X. C. Jiang, and M. P. Pileni. Optical Properties of Gold Nanorods: DDA Sim-
       ulations Supported by Experiments. *The Journal of Physical Chemistry B*, 109(27):13138–
       13142, 2005.

[334] A. M. Alkilany, P. K. Nagaria, C. R. Hexel, T. J. Shaw, C. J. Murphy, and M. D. Wyatt. Cellular Uptake and Cytotoxicity of Gold Nanorods: Molecular Origin of Cytotoxicity and Surface Effects. *Small*, 5(6):701–708, 2009.

[335] T. S. Hauck, A. A. Ghazani, and W. C. Chan. Assessing the effect of surface chemistry on gold nanorod uptake, toxicity, and gene expression in mammalian cells. *Small*, 4(1):153–159, 2008.

[336] K. Nakata, T. Tsuchido, and Y. Matsumura. Antimicrobial cationic surfactant, cetyltrim ethylammonium bromide, induces superoxide stress in Escherichia coli cells. *Journal of Applied Microbiology*, 110(2):568–579, 2011.

[337] Y. Qiu, Y. Liu, L. Wang, L. Xu, R. Bai, Y. Ji, X. Wu, Y. Zhao, Y. Li, and C. Chen. Surface chemistry and aspect ratio mediated cellular uptake of Au nanorods. *Biomaterials*, 31(30):7606–7619, 2010.

[338] M. J. Datiles, E. A. Johnson, and R. E. McCarty. Inhibition of the ATPase activity of the catalytic portion of ATP synthases by cationic amphiphiles. *Biochimica et Biophysica Acta - Bioenergetics*, 1777(4):362–368, 2008.

[339] Y. Pan, Z. Wang, D. Shao, H. Zheng, Y. Chen, X. Zheng, M. Zhang, J. Li, F. Li, and L. Chen. CTAB induced mitochondrial apoptosis by activating the AMPK-p53 pathway in hepatocarcinoma cells. *Toxicology Research*, 4(5):1359–1365, 2015.

[340] C. Peetla and V. Labhasetwar. Effect of molecular structure of cationic surfactants on biophysical interactions of surfactant-modified nanoparticles with a model membrane and cellular uptake. *Langmuir*, 25(4):2369–2377, 2009.

[341] M Tanaka, Y Takahashi, L Roach, K Critchley, S. D. Evans, and M Okochi. Rational screening of biomineralisation peptides for colour-selected one-pot gold nanoparticle syntheses. *Nanoscale Advances*, 1(1):71–75, 2019.

[342] K. Simons. Cell membranes: A subjective perspective. *Biochimica et Biophysica Acta - Biomembranes*, 1858(10):2569–2572, 2016.

[343] A. Luchini and G. Vitiello. Understanding the nano-bio interfaces: Lipid-coatings for inorganic nanoparticles as promising strategy for biomedical applications. *Frontiers in Chemistry*, 7, May 2019.

[344] J. S. Suk, Q. Xu, N. Kim, J. Hanes, and L. M. Ensign. PEGylation as a strategy for improving nanoparticle-based drug and gene delivery. *Advanced Drug Delivery Reviews*, 99:28–51, 2016.

[345] J. R. Matthews, C. M. Payne, and J. H. Hafner. Analysis of Phospholipid Bilayers on Gold Nanorods by Plasmon Resonance Sensing and Surface-Enhanced Raman Scattering. *Langmuir*, 31(36):9893–9900, 2015.

[346] M. Ueno, S. Yoshida, and I. Horikoshi. Characteristics of the Membrane Permeability of Temperature-Sensitive Liposome. *Bulletin of the Chemical Society of Japan*, 64(5):1588–1593, 1991.

[347] R. L. Magin and M. R. Niesman. Temperature-Dependent Drug Release from Large Unilamellar Liposomes. *Cancer drug delivery*, 1(2), 1984.

[348] D. Marsh, A. Watts, and P. F. Knowles. Evidence for phase boundary lipid permeability of tempo-choline into dimyristoylphosphatidylcholine vesicles at the phase transition. *Biochemistry*, 15(1):3570–3578, 1976.

[349] Standard American Laser Institute. ANSI Z136.1 American national standard for safe use of lasers. [available online: https://webstore.ansi.org/Standards/LIA/A NSIZ1362014?source=blog]. Technical report, Orlando, FL, 2014.

[350] S. C. T. Moorcroft, L. Roach, D. G. Jayne, Z. Y. Ong, and S. D. Evans. Nanoparticle-Loaded Hydrogel for the Light-Activated Release and Photothermal Enhancement of Antimicrobial Peptides. *ACS Applied Materials & Interfaces*, 12(22):24544–24554, 2020.

[351] L. Otvos and J. D. Wade. Current challenges in peptide-based drug discovery. *Frontiers in Chemistry*, 2, 2014.

[352] A. Banerjee and H. Onyuksel. Peptide delivery using phospholipid micelles. *Wiley Interdisciplinary Reviews: Nanomedicine and Nanobiotechnology*, 4(5):562–574, Sept. 2012.

[353] A. Akbarzadeh, R. Rezaei-Sadabady, S. Davaran, S. W. Joo, N. Zarghami, Y. Hanifehpour, M. Samiei, M. Kouhi, and K. Nejati-Koshki. Liposome: Classification, preparation, and applications. *Nanoscale Research Letters*, 8(1), 2013.

[354] J. O. Eloy, M. Claro de Souza, R. Petrilli, J. P. A. Barcellos, R. J. Lee, and J. M. Marchetti. Liposomes as carriers of hydrophilic small molecule drugs: Strategies to en-

hance encapsulation and delivery. *Colloids and Surfaces B: Biointerfaces*, 123:345–363, 2014.

[355] A. M. Tedeschi, L. Franco, M. Ruzzi, L. Paduano, C. Corvaja, G. D'Errico, C. Corvaja, and V. Barone. Micellar aggregation of alkyltrimethylammonium bromide surfactants studied by electron paramagnetic resonance of an anionic nitroxide. *Physical Chemistry Chemical Physics*, 5(19):4204, 2003.

[356] S. Bibi, E. Lattman, A. R. Mohammed, and Y. Perrie. Trigger release liposome systems: local and remote controlled delivery? *Journal of Microencapsulation*, 29(3):262–276, 2012.

[357] Y. Lee and D. H. Thompson. Stimuli-responsive liposomes for drug delivery. *Wiley Interdisciplinary Reviews: Nanomedicine and Nanobiotechnology*, 9(5), 2017.

[358] T. Ta and T. M. Porter. Thermosensitive liposomes for localized delivery and triggered release of chemotherapy. *Journal of Controlled Release*, 169(2):112–125, 2013.

[359] S. Mura, J. Nicolas, and P. Couvreur. Stimuli-responsive nanocarriers for drug delivery. *Nature Publishing Group*, 12:991–1003, 2013.

[360] S. M. Lee and S. T. Nguyen. Smart nanoscale drug delivery platforms from stimuli-responsive polymers and liposomes. *Macromolecules*, 46(23):9169–9180, 2013.

[361] G. Adlakha-Hutcheon, M. B. Bally, C. R. Shew, and T. D. Madden. Controlled destabilization of a liposomal drug delivery system enhances mitoxantrone antitumor activity. *Nature Biotechnology*, 17(8):775–779, 1999.

[362] N. T. Thet, S. H. Hong, S. Marshall, M. Laabei, A. Toby, and A. Jenkins. Visible, colorimetric dissemination between pathogenic strains of Staphylococcus aureus and Pseudomonas aeruginosa using fluorescent dye containing lipid vesicles. *Biosensors and Bioelectronics*, 41(1):538–543, 2013.

[363] J. Li, X. Wang, T. Zhang, C. Wang, Z. Huang, X. Luo, and Y. Deng. A review on phospholipids and their main applications in drug delivery systems. *Asian Journal of Pharmaceutical Sciences*, 10(2):81–98, 2015.

[364] S. Mourtas, G. Diamanti, A. Foka, V. Dracopoulos, P. Klepetsanis, V. Stamouli, I. Spiliopoulou, and S. G. Antimisiaris. Inhibition of Bacterial Attachment on Surfaces

by Immobilization of Tobramycin-Loaded Liposomes. *Journal of Biomedical Nanotechnology*, 11(12):2186–2196, 2015.

[365] L. H. Lindner, M. E. Eichhorn, H. Eibl, N. Teichert, M. Schmitt-Sody, R. D. Issels, and M. Dellian. Novel Temperature-Sensitive Liposomes with Prolonged Circulation Time. *Clinical cancer research*, 10(6):2168–2178, 2004.

[366] N. Kučerka, M. P. Nieh, and J. Katsaras. Fluid phase lipid areas and bilayer thicknesses of commonly used phosphatidylcholines as a function of temperature. *Biochimica et Biophysica Acta - Biomembranes*, 1808(11):2761–2771, 2011.

[367] S. Bhattacharya and S. Haldar. Interactions between cholesterol and lipids in bilayer membranes. Role of lipid headgroup and hydrocarbon chain backbone linkage. *Biochima et Biophysica Acta*, 1467(1):39–53, 2000.

[368] S. Raffy and J. Teissié. Control of lipid membrane stability by cholesterol content. *Biophysical Journal*, 76(4):2072–2080, 1999.

[369] M. L. Briuglia, C. Rotella, A. McFarlane, and D. A. Lamprou. Influence of cholesterol on liposome stability and on in vitro drug release. *Drug Delivery and Translational Research*, 5(3):231–242, 2015.

[370] A. Mohan, S. Narayanan, S. Sethuraman, and U. M. Krishnan. Novel resveratrol and 5-fluorouracil coencapsulated in PEGylated nanoliposomes improve chemotherapeutic efficacy of combination against head and neck squamous cell carcinoma. *BioMed Research International*, 2014:424239, 2014.

[371] P. J. Patty and B. J. Frisken. The Pressure-Dependence of the Size of Extruded Vesicles. *Biophysical Journal*, 85(2):996–1004, 2003.

[372] F. C. O. Los, T. M. Randis, R. V. Aroian, and A. J. Ratner. Role of Pore-Forming Toxins in Bacterial Infectious Diseases. *Microbiology and Molecular Biology Reviews*, 77(2):173–207, 2013.

[373] L. Song, M. R. Hobaugh, C. Shustak, S. Cheley, H. Bayley, and J. E. Gouaux. Structure of Staphylococcal α-Hemolysin, a Heptameric Transmembrane Pore. *Science*, 274(5294):1859–1865, 1998.

[374] C. Potrich, H. Bastiani, D. A. Colin, S. Huck, G. Prévost, and M. Dalla Serra. The influence of membrane lipids in Staphylococcus aureus gamma-hemolysins pore formation. *Journal of Membrane Biology*, 227(1):13–24, 2009.

[375] Faudry E., Perdu C., and Attrée I. Pore Formation by T3SS Translocators: Liposome Leakage Assay. In A. Delcour, editor, *Methods in Molecular Biology (Methods and Protocols)*, chapter 1, pages 173–185. Humana Press, Totowa, NJ, 966th edition, 2013.

[376] N. T. Thet, D. R. Alves, J. E. Bean, S. Booth, J. Nzakizwanayo, A. E. Young, B. V. Jones, and A. T. A. Jenkins. Prototype Development of the Intelligent Hydrogel Wound Dressing and Its Efficacy in the Detection of Model Pathogenic Wound Biofilms. *ACS Applied Materials and Interfaces*, 8(24):14909–14919, 2016.

[377] M. Laabei, W. D. Jamieson, R. C. Massey, and A. T. A. Jenkins. Staphylococcus aureus interaction with phospholipid vesicles - A new method to accurately determine accessory gene regulator (agr) activity. *PLoS ONE*, 9(1), 2014.

[378] A. Stunova and L. Vistejnova. Dermal fibroblasts—A heterogeneous population with regulatory function in wound healing. *Cytokine & Growth Factor Reviews*, 39:137–150, 2018.

[379] W. V. Kraske and D. B. Mountcastle. Effects of cholesterol and temperature on the permeability of dimyristoylphosphatidylcholine bilayers near the chain melting phase transition. *Biochimica et Biophysica Acta*, 1514(2):159–164, 2001.

[380] A. Carruthers and D. L. Melchior. Studies of the Relationship between Bilayer Water Permeability and Bilayer Physical State. *Biochemistry*, 22(25):5797–5807, 1983.

[381] B. Kneidl, M. Peller, G. Winter, L. H. Lindner, and M. Hossann. Thermosensitive liposomal drug delivery systems: state of the art review. *International Journal of Nanomedicine*, 9:4387–4398, 2014.

[382] L. Redondo-Morata, M. I. Giannotti, and F. Sanz. Influence of cholesterol on the phase transition of lipid bilayers: A temperature-controlled force spectroscopy study. *Langmuir*, 28(35):12851–12860, 2012.

[383] M. Anderson and A. Omri. The Effect of Different Lipid Components on the in Vitro Stability and Release Kinetics of Liposome Formulations. *Drug Delivery: Journal of Delivery and Targeting of Therapeutic Agents*, 11(1):33–39, 2004.

[384] N. Rojko and G. Anderluh. How Lipid Membranes Affect Pore Forming Toxin Activity. *Accounts of Chemical Research*, 48(12):3073–3079, 2015.

[385] A. Barlič, I. Gutiérrez-Aguirre, J. M. M. Caaveiro, A. Cruz, M. Ruiz-Argüello, J. Pérez-Gil, and J. M. González-Mañas. Lipid Phase Coexistence Favors Membrane Insertion of Equinatoxin-II, a Poreforming Toxin from Actinia equina. *J. Biol. Chem.*, 279(1):34209–34216, 2004.

[386] L. N. Ribeiro, M. C. Breitkreitz, V. A. Guilherme, G. H. da Silva, V. M. Couto, S. R. Castro, B. O. de Paula, D. Machado, and E. de Paula. Natural lipids-based NLC containing lidocaine: from pre-formulation to in vivo studies. *European Journal of Pharmaceutical Sciences*, 106:102–112, 2017.

[387] J. M. Artigas, M. E. Garcia, M. R. Faure, and A. M. Gimeno. Serum trypsin levels in acute pancreatic and non-pancreatic abdominal conditions. eng. *Postgraduate medical journal*, 57(666):219–222, 1981.

[388] R. D. Sinclair and T. J. Ryan. Proteolytic enzymes in wound healing: the role of enzymatic debridement. *Australasian Journal of Dermatology*, 35(1):35–41, 1994.

[389] A. B. Wysocki. Evaluating and managing open skin wounds: colonization versus infection. *AACN clinical issues*, 13(3):382–397, 2002.

[390] K. Kirketerp-Møller, P. Jensen, M. Fazli, K. G. Madsen, J. Pedersen, C. Moser, T. Tolker-Nielsen, N. Høiby, M. Givskov, and T. Bjarnsholt. Distribution, organization, and ecology of bacteria in chronic wounds. *Journal of Clinical Microbiology*, 46(8):2717–2722, 2008.

[391] M. Fazli, T. Bjarnsholt, K. Kirketerp-Møller, B. Jørgensen, A. S. Andersen, K. A. Krogfelt, M. Givskov, and T. Tolker-Nielsen. Nonrandom distribution of Pseudomonas aeruginosa and Staphylococcus aureus in chronic wounds. *Journal of Clinical Microbiology*, 47(12):4084–4089, Dec. 2009.

[392] P. Bainbridge. Wound healing and the role of fibroblasts. *Journal of Wound Care*, 22(8):407–412, 2013.

[393] M. B. Witte and A. Barbul. General principles of wound healing. *Surgical clinics of north America*, 77(3):509–528, 1997.

[394] H. Takahashi, Y. Niidome, T. Niidome, K. Kaneko, H. Kawasaki, and S. Yamada. Modification of gold nanorods using phosphatidylcholine to reduce cytotoxicity. *Langmuir*, 22(1):2–5, 2006.

[395] P. B. Santhosh, N. Thomas, S. Sudhakar, A. Chadha, and E. Mani. Phospholipid stabilized gold nanorods: Towards improved colloidal stability and biocompatibility. *Physical Chemistry Chemical Physics*, 19(28):18494–18504, 2017.

[396] J. Koehler, F. P. Brandl, and A. M. Goepferich. Hydrogel wound dressings for bioactive treatment of acute and chronic wounds. *European Polymer Journal*, 100:1–11, 2018.

[397] J. Zhu and R. E. Marchant. Design properties of hydrogel tissue-engineering scaolds. *Expert review of medical devices*, 8(5):607–626, 2011.

[398] A. L. Rippa, E. P. Kalabusheva, and E. A. Vorotelyak. Regeneration of Dermis: Scarring and Cells Involved. *Cells*, 8(6):607, 2019.

[399] R. C. Op 't Veld, X. F. Walboomers, J. A. Jansen, and F. A. Wagener. Design considerations for hydrogel wound dressings; strategic and molecular advances. *Tissue Engineering Part B: Reviews*, 26(3):1–19, 2020.

[400] K. Jariashvili, B. Madhan, B. Brodsky, A. Kuchava, L. Namicheishvili, and N. Metreveli. Uv damage of collagen: Insights from model collagen peptides. *Biopolymers*, (3):189–198, 2012.

[401] M. C. Catoira, L. Fusaro, D. Di Francesco, M. Ramella, and F. Boccafoschi. Overview of natural hydrogels for regenerative medicine applications. *Journal of Materials Science: Materials in Medicine*, 30(115):1–10, 2019.

[402] X. Li, Q. Sun, Q. Li, N. Kawazoe, and G. Chen. Functional hydrogels with tunable structures and properties for tissue engineering applications. *Frontiers in Chemistry*, 6:1–20, 2018.

[403] L. E. Jansen, L. J. Negrón-Piñeiro, S. Galarza, and S. R. Peyton. Control of thiol-maleimide reaction kinetics in PEG hydrogel networks. *Acta Biomaterialia*, 70(1):120–128, 2018.

[404] F. M. Veronese and G. Pasut. PEGylation, successful approach to drug delivery. *Drug Discovery Today*, 10(21):1451–1458, 2005.

[405] J. Su. Thiol-Mediated Chemoselective Strategies for In Situ Formation of Hydrogels. *Gels*, 4(3):72, 2018.

[406] Y. Shtenberg, M. Goldfeder, A. Schroeder, and H. Bianco-Peled. Alginate modified with maleimide-terminated PEG as drug carriers with enhanced mucoadhesion. *Carbohydrate Polymers*, 175(1):337–346, 2017.

[407] E. Bakaic, N. M. Smeets, and T. Hoare. Injectable hydrogels based on poly(ethylene glycol) and derivatives as functional biomaterials. *RSC Advances*, 5(45):35469–35486, 2015.

[408] S. L. Chen, R. H. Fu, S. F. Liao, S. P. Liu, S. Z. Lin, and Y. C. Wang. A PEG-Based Hydrogel for Effective Wound Care Management. *Cell Transplantation*, 27(2):275–284, 2018.

[409] N. A. Peppas, K. B. Keys, M. Torres-Lugo, and A. M. Lowman. Poly(ethylene glycol)-containing hydrogels in drug delivery. *Journal of Controlled Release*, 62(2):81–87, 1999.

[410] C. C. Lin and A. T. Metters. Hydrogels in controlled release formulations: Network design and mathematical modeling. *Advanced Drug Delivery Reviews*, 58(12-13):1379–1408, 2006.

[411] B. H. Northrop, S. H. Frayne, and U. Choudhary. Thiol-maleimide "click" chemistry: Evaluating the influence of solvent, initiator, and thiol on the reaction mechanism, kinetics, and selectivity. *Polymer Chemistry*, 6(18):3415–3430, 2015.

[412] R. S. H. Wong, M. Ashton, and K. Dodou. Effect of crosslinking agent concentration on the properties of unmedicated hydrogels. *Pharmaceutics*, 7(3):305–319, 2015.

[413] L. Weng, X. Chen, and W. Chen. Rheological characterization of in situ crosslinkable hydrogels formulated from oxidized dextran and N-carboxyethyl chitosan. *Biomacromolecules*, 8(4):1109–1115, 2007.

[414] D. I. Wilson. What is rheology? *Eye*, 32(2):179–183, 2018.

[415] F. Ganji, S. V. Farahani, E. Vasheghani-Farahani, and S. Vasheghani-Farahani. Theoretical Description of Hydrogel Swelling: A Review Charge Acceptance of Advanced Lead Batteries View project Theoretical Description of Hydrogel Swelling: A Review. *Iranian Polymer Journal*, 19(5):375–398, 2010.

[416] M. P. Lutolf and J. A. Hubbell. Synthesis and physicochemical characterization of end-linked poly(ethylene glycol)-co-peptide hydrogels formed by Michael-type addition. *Biomacromolecules*, (3):713–722, 2003.

[417] S. Ye, A. P. Brown, A. C. Stammers, N. H. Thomson, J. Wen, L. Roach, R. J. Bushby, P. L. Coletta, K. Critchley, S. D. Connell, A. F. Markham, R. Brydson, and S. D. Evans. Sub-Nanometer Thick Gold Nanosheets as Highly Efficient Catalysts. *Advanced Science*, 6(21):1900911, 2019.

[418] M. Yanagioka and C. W. Frank. Defect generation surrounding nanoparticles in a cross-linked hydrogel network. *Langmuir*, 25(10):5927–5939, 2009.

[419] S. Santajit and N. Indrawattana. Mechanisms of Antimicrobial Resistance in ESKAPE Pathogens. eng. *BioMed research international*, 2016:2475067, 2016.

[420] World Health Organization. WHO publishes list of bacteria for which new antibiotics are urgently needed [available at: https://www.who.int/en/news-room/detail/27-02-2017-who-publishes-list-of-bacteria-for-which-new-antibiotics-are-urgently-needed], 2017.

[421] M. B. Yatvin, J. N. Weinstein, W. H Dennis, and R. Blumenthal. Design of Liposomes for Enhanced Local Release of Drugs by Hyperthermia. *Science*, 202(4374):1290–1293, 1978.

[422] R. L. Magin and M. R. Niesman. Temperature-dependent permeability of large unilamellar liposomes. *Chemistry and Physics of Lipids*, 34(1):245–256, 1984.

[423] L. Li, T. L. ten Hagen, D. Schipper, T. M. Wijnberg, G. C. van Rhoon, A. M. Eggermont, L. H. Lindner, and G. A. Koning. Triggered content release from optimized stealth thermosensitive liposomes using mild hyperthermia. *Journal of Controlled Release*, 143(2):274–279, 2010.

[424] T. Kaasgaard, C. Leidy, J. H. Crowe, O. G. Mouritsen, and K. Jørgensen. Temperature-controlled structure and kinetics of ripple phases in one- and two-component supported lipid bilayers. *Biophysical Journal*, 85(1):350–360, July 2003.

[425] O. G. Mouritsen and M. J. Zuckermann. Model of interfacial melting. *Physical Review Letters*, 58(4):389–392, 1987.

[426]   D Papahadjopoulos, K Jacobson, S Nir, and T Isac. Phase transitions in phospholipid vesicles fluorescence polarization and permeability measurement concerning the effect of temperature and cholesterol. *Biochimica et Biophysica Acta*, 311(3):330–348, 1973.

[427]   L. Cruzeiro-I-Iansson and O. G. Mouritsen. Passive ion permeability of lipid membranes modelled via Hpid-domain inteffacial area. *Biochimica et Biophysica Ata*, 944(1):63–72, 1988.

[428]   E. B. Ricker and E. Nuxoll. Synergistic effects of heat and antibiotics on Pseudomonas aeruginosa biofilms. *Biofouling*, 33(10):855–866, 2017.

[429]   K. Zarghooni, J. Bredow, J. Siewe, N. Deutloff, H. S. Mayer, and C. Lohmann. Is the use of modern versus conventional wound dressings warranted after primary knee and hip arthroplasty? Results of a Prospective Comparative Study. *Acta Orthop. Belg.*, 81(4):768–775, 2015.

[430]   S. P. Singh, S. B. Alvi, D. B. Pemmaraju, A. D. Singh, S. V. Manda, R. Srivastava, and A. K. Rengan. NIR triggered liposome gold nanoparticles entrapping curcumin as in situ adjuvant for photothermal treatment of skin cancer. *International Journal of Biological Macromolecules*, 110:375–382, 2018.

[431]   G. V. Orsinger, S. J. Leung, S. S. Knights-Mitchell, J. D. Williams, and M. Romanowski. Drug delivery with light-activated gold-coated liposomes. *NSTI-Nanotech*, 3(1):134–137, 2012.

[432]   X. Zou, E. Ying, and S. Dong. Seed-mediated synthesis of branched gold nanoparticles with the assistance of citrate and their surface-enhanced Raman scattering properties. *Nanotechnology*, 17(18):4758–4764, 2006.

[433]   A. U. Borwankar, B. W. Willsey, A. Twu, J. J. Hung, R. J. Stover, T. W. Wang, M. D. Feldman, T. E. Milner, T. M. Truskett, and K. P. Johnston. Gold nanoparticles with high densities of small protuberances on nanocluster cores with strong NIR extinction. *RSC Advances*, 5(127):104674–104687, 2015.

[434]   C. H. Kuo and M. H. Huang. Synthesis of branched gold nanocrystals by a seeding growth approach. *Langmuir*, 21(5):2012–2016, 2005.

[435] S. Barbosa, A. Agrawal, L. Rodríguez-Lorenzo, I. Pastoriza-Santos, R. A. Alvarez-Puebla, A. Kornowski, H. Weller, and L. M. Liz-Marzán. Tuning size and sensing properties in colloidal gold nanostars. *Langmuir*, 26(18):14943–14950, 2010.

[436] M. Wang, X. Cao, W. Lu, L. Tao, H. Zhao, Y. Wang, M. Guo, J. Dong, and W. Qian. Surface-enhanced Raman spectroscopic detection and differentiation of lung cancer cell lines (A549, H1229) and normal cell line (AT II) based on gold nanostar substrates. *RSC Advances*, 4(109):64225–64234, 2014.

[437] M. M. Phiri, D. W. Mulder, and B. C. Vorster. Seedless gold nanostars with seed-like advantages for biosensing applications. *Royal Society Open Science*, 6(2), 2019.

[438] C. G. Khoury and T. Vo-Dinh. Gold Nanostars For Surface-Enhanced Raman Scattering: Synthesis, Characterization and Optimization. *Phys. Chem. C Nanomater. Interfaces*, 2008(112):18849–18859, 2008.

[439] F. Liebig, R. Henning, R. M. Sarhan, C. Prietzel, C. N. Schmitt, M. Bargheer, and J. Koetz. A simple one-step procedure to synthesise gold nanostars in concentrated aqueous surfactant solutions. *RSC Advances*, 9(41):23633–23641, 2019.

[440] D. Maysinger, A. Moquin, J. Choi, M. Kodiha, and U. Stochaj. Gold nanourchins and celastrol reorganize the nucleo- and cytoskeleton of glioblastoma cells. *Nanoscale*, 10(4):1716–1726, 2018.

[441] O. M. Bakr, B. H. Wunsch, and F. Stellacci. High-yield synthesis of multi-branched urchin-like gold nanoparticles. *Chemistry of Materials*, 18(14):3297–3301, 2006.

[442] K. T. Kim, S. A. Meeuwissen, R. J. Nolte, and J. C. Van Hest. Smart nanocontainers and nanoreactors. *Nanoscale*, 2(6):844–858, 2010.

[443] G. W. Kim and J. W. Ha. Effect of adsorbate electrophilicity and spiky uneven surfaces on single gold nanourchin-based localized surface plasmon resonance sensors. *Chemical Physics Letters*, 697:38–42, 2018.

[444] L. Wang, G. Wei, C. Guo, L. Sun, Y. Sun, Y. Song, T. Yang, and Z. Li. Photochemical synthesis and self-assembly of gold nanoparticles. *Colloids and Surfaces A: Physicochemical and Engineering Aspects*, 312(2-3):148–153, 2008.

[445] F. Liebig, R. Henning, R. M. Sarhan, C. Prietzel, M. Bargheer, and J. Koetz. A new route to gold nanoflowers. *Nanotechnology*, 29(18), 2018.

[446] K. Sivasubramanian, M. Mathiyazhakan, C. Wiraja, P. K. Upputuri, C. Xu, and M. Pramanik. Near-infrared light-responsive liposomal contrast agent for photoacoustic imaging and drug release applications. *Journal of Biomedical Optics*, 22(4):041007, 2016.

[447] W. T. Ferrar, D. F. O'Brien, A. Warshawsky, and C. L. Voycheck. Metalization of Lipid Vesicles via Electroless Plating. *J. Am. Chem. Soc.*, 110:288–289, 1988.

[448] K. Ahmed, P. W. Muiruri, G. H. Jones, M. J. Scott, and M. N. Jones. The effect of grafted poly(ethylene glycol) on the electrophoretic properties of phospholipid liposomes and their adsorption to bacterial biofilms. *Colloid Surface A*, 194(3):287–296, 2001.

[449] R. Bajracharya, J. G. Song, S. Y. Back, and H.-K. Han. Recent Advancements in Non-Invasive Formulations for Protein Drug Delivery. *Computational and Structural Biotechnology Journal*, 17:1290–1308, 2019.

[450] H.-S. Joo, C.-I. Fu, and M. Otto. Bacterial strategies of resistance to antimicrobial peptides. *Philosophical Transactions of the Royal Society B: Biological Sciences*, 371(1695):20150292, 2016.